THREE-DIMENSIONAL MODELING OF COASTAL FLOWS USING UNSTRUCTURED GRIDS

André Bustorff Fortunato

B.Sc., Universidade Técnica de Lisboa, 1989

A dissertation submitted to the faculty of the

Oregon Graduate Institute of Science & Technology

in partial fulfillment of the

requirements for the degree

Doctor of Philosophy

in

Environmental Science and Engineering

January 1996

The dissertation "Three-Dimensional Modeling of Coastal Flows Using Unstructured Grids" by André Bustorff Fortunato has been examined and approved by the following committee:

António M. Baptista, Ph.D., Thesis Advisor

William Fish, Ph.D., Associate Professor

David Jay, Ph.D., Associate Professor

Michael G.G. Foreman, Ph.D., Institute of Ocean Sciences

Richard A. Luettich, Jr., Ph.D., University of North Carolina

To my wife, Anabela

ACKNOWLEDGEMENTS

This thesis is dedicated to my wife, Anabela Oliveira. During the last four years, she was a constant source of support. As a room-mate, she filled our apartment with furry animals that wake me up at night. As a colleague, she was my second advisor, discussing and questioning every detail of my work, giving me countless suggestions and proof-reading all my papers. As a friend, she shared the most enjoyable moments of my life. As a wife, she provided more love and attention than I deserved.

I would like to express my deepest gratitude to my parents for their support and encouragement, for doing all they could to make my life easier, and for having traveled from Portugal just to be with me on the day of my thesis defense. I would also like to thank Miguel Remédio and José Menaia for trying to make me feel at home during my first two years at OGI.

António Baptista has been an endless source of support and guidance during the last five years, and I could not have wished for a better advisor. His teaching skills are second to none. His scientific rigor, his attention to detail, his dedication to his students, made my experience at OGI extremely profitable, and his patience and good humor made it more bearable. His working habits set an example that will be hard to forget.

I am grateful to the members of my thesis committee, Drs. Richard Luettich, Jr., Michael Foreman, David Jay and William Fish for numerous suggestions and comments, which improved this thesis substantially.

I would like to acknowledge the support of the Laboratório Nacional de Engenharia Civil (Portugal), and in particular the heads of the Hydraulics Department, Jaime Melo Baptista, and of the Estuarine Division, Eduardo Oliveira. This work was made possible by the financial support from the Junta Nacional de Investigação Científica e Tecnológica (Portugal), grants BM-355/90-IG and BD-1786/91-IG.

TABLE OF CONTENTS

CHAPTER 3

Evaluation of Horizontal Gradients in Sigma-Coordinate Shallow Water Models 55

CHAPTER 4

Vertical Discretization in Tidal Flow Simulations 94

CHAPTER 5

CHAPTER 6

APPENDIX 1

APPENDIX 2

APPENDIX 3

LIST OF TABLES

LIST OF FIGURES

ABSTRACT

Three-Dimensional Modeling of Coastal Flows Using Unstructured Grids

André Bustorff Fortunato

Oregon Graduate Institute of Science & Technology, 1995

Supervising Professor: António M. Baptista

Although three-dimensional (3D) modeling of coastal and estuarine flows is becoming common, several limitations remain related to our ability both to describe and to numerically simulate the correct physics. Two key limitations concern vertical resolution: the lack of flexibility of current methods for vertical discretization prevents the optimal use of computational resources, and guidelines for vertical nodal placement are not available.

The major contribution of this thesis is the development, analysis and test of an approach that allows for an unprecedented flexibility in the vertical refinement of the domain. This approach, which we refer to as localized sigma coordinates (LSC), is the first to allow the number of nodes per vertical to vary horizontally, and can therefore be considered a natural extension to the use of unstructured grids in the horizontal.

To take advantage of the LSC, we perform the first systematic study for the vertical discretization in barotropic tidal flow simulations. The resulting optimal grid can reduce the errors relative to a uniform grid by over an order magnitude and compares favorably with non-uniform grids previously proposed. A criterion to guide the horizontal distribution of the total number of nodes is proposed and discussed in the context of simple one- and two-dimensional models, and is then extended to three dimensions. Accounting for advection in three dimensions forces modifications to the criterion, but the overall concept proved to be useful: using a variable number of nodes per vertical reduces the maximum velocity errors by a factor of two.

As part of our analysis of the LSC, we investigate the evaluation of the horizontal gradients in sigma-coordinate shallow water models. We show that horizontal gradients should be computed in sigma rather than z-coordinates, and that the so-called "hydrostatic inconsistency" typically associated with sigma coordinates does not correspond to a numerical inconsistency. The large errors associated with the evaluation of horizontal gradients can be by-passed through appropriate horizontal resolution, and a procedure to define this resolution is proposed based on results from a truncation error analysis.

An application to the Tagus estuary demonstrates the enhanced accuracy provided by the LSC, and provides new insights into the estuary's 3D barotropic circulation. Strong residual currents (depth-averaged eulerian residual velocities of up to 0.5 m/s) are generated by advective accelerations and have a major impact on the mixing characteristics at the mouth of the estuary. The asymmetry between ebbing and flooding promotes exchanges between marine and estuarine waters, while the interaction between tidal and residual flows leads to strong chaotic stirring.

The good performance of the LSC in a complex application establishes this method as an attractive alternative to the traditional sigma- and z-coordinates.

CHAPTER 1

Introduction

1.1 Modeling Physical Processes in Estuaries and Coasts

Estuaries and coastal seas are areas of great economic and ecological importance, given their potential for transportation, wastewater disposal, fishing and recreation. Due to industrial and wastewater discharges, pesticides and fertilizers, and atmospheric deposition of nitrate, the coastal environment has deteriorated rapidly for several decades, a trend that is seldom (and only slowly) being curbed. Major consequences of this deterioration include loss of habitat, invasions by exotic species, poisoning of commercially important species and eutrophication (LMER Coordinating Committee, 1992). Simultaneously, overpopulation in developing countries and over-consumption in developed countries call for an increasing exploitation of marine resources. The conflict between resources destruction and increasing needs can often be minimized by a science-based management of these resources. Numerical models have played an increasing role in this management, as tools that can integrate our knowledge of the physical, chemical and biological processes occurring in these areas (e.g., Dejak et al., 1990, Salomon and Pommepuy, 1990, Aikman et al., 1995).

Hydrodynamic models are an essential component of most computational structures to support estuarine management. Indeed, the simulation of velocity fields is usually a prerequisite for detailed water quality studies because estuaries and coastal seas are very dynamic areas, where transport is a very important process. Moreover, the velocity field influences the spatial and temporal distributions of salinity and temperature. In turn, both salinity and temperature can play a major role in both chemical and biological processes. For instance, salinity determines the ionic strength and microbial rates of survival depend on salinity and temperature.

Early models of estuarine dynamics were primarily driven by barotropic tides, typically the major forcing mechanism in these areas. Since the barotropic pressure gradient is uniform in the water column, depth-averaged models were extensively used, and water levels were simulated with some success. However, as demands for accuracy grew, more complex processes had to be simulated (e.g., Blumberg et al., 1993). Forcings such as wind stress and baroclinic pressure act unevenly along the water column, and therefore cannot be properly simulated with depth-averaged models. Density effects in particular can be very important in coastal systems: horizontal density gradients generate internal pressure forces and vertical gradients often damp turbulent mixing significantly. Also, the output from hydrodynamic models is used to force transport models, and the transported quantities are often not well mixed in the water column. For instance, sediments have higher concentrations near the bottom, and sewage water can spread in layers due to buoyancy effects. Finally, long term transport is mainly driven by residual transport. Since these residuals are extremely sensitive to non-linear effects, internal friction and baroclinic pressure, fully 3D simulations are recommended for long-term water quality studies. In this context, it is not surprising that a review of recent literature on coastal and estuarine modeling (e.g., Heaps, 1987, Nihoul and Jamart, 1987, Spaulding et al., 1992, 1994, Stevenson, 1995) shows that three-dimensional model applications are progressively replacing traditional depth-averaged simulations.

In spite of this evolution, recent reviews pointed out that three-dimensional models were still "in their infancy" (Cheng and Smith, 1990), or "in a development stage" (Westerink and Gray, 1990). An objective evaluation of state-of-the-art three-dimensional models compared simulations from two models (Blumberg and Mellor, 1987, Stole-Hansen and Slagstad, 1991) with field data from the Norwegian shelf (Hackett and Røed, 1994, Hackett et al., 1995). Figure 1.1 shows that both models were "unable to reproduce quantitatively the detailed vertical and horizontal structure seen in the observations" (Hackett et al., 1995), although some qualitative aspects were reproduced. This inability was attributed mainly to "the parameterization of subgrid scale turbulence, horizontal resolution and the initial and boundary conditions."

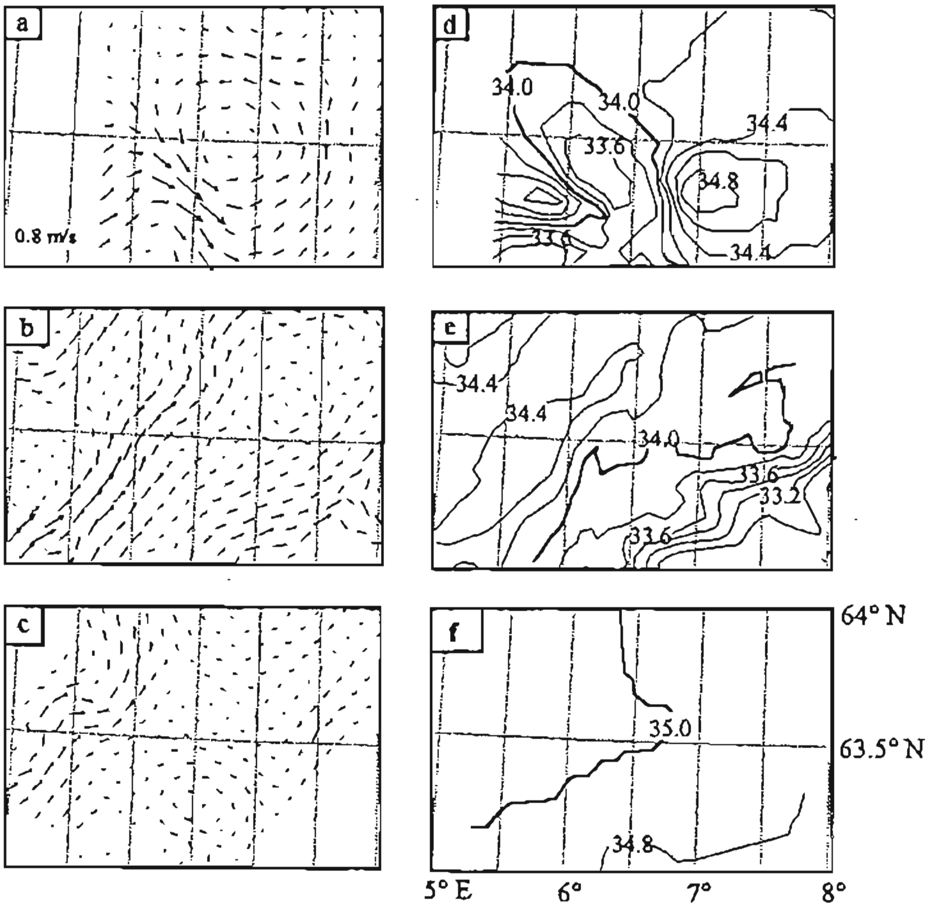

Figure 1.1 Horizontal distribution of velocity (a,b,c) and salinity (d,e,f) at a test area. (a,d) correspond to objectively analysed data, (b,e) and (c,f) to results from the Blumberg and Mellor (1987) and the Stole-Hansen and Slagstad (1991) models, respectively. Salinity contours are at 0.2 psu intervals. [from Hackett et al., 1995].

These conclusions illustrate three of the major limitations in three-dimensional simulations: insufficient data, insufficient grid resolution and insufficient understanding of some physical processes (in particular turbulence). In addition, we consider the incomplete understanding of the numerical methods properties to be another limitation.

The lack of quality data is often a major limitation to the accuracy of the simulations. Bathymetric data is often outdated (due to sediment deposition and erosion), of uneven quality (e.g., navigation channels are often better surveyed than shallower areas), or have too coarse a resolution. Velocity data records are often too short for meaningful harmonic analysis. Data needed to validate 3D models, such as detailed vertical profiles of velocity, temperature and salinity, are usually scarce. Fortunately, quality data sets are expected to become progressively more available, as measurement instruments become cheaper and more sophisticated, and satellite data becomes more broadly available (e.g., Foreman et al., 1992).

Grid resolution remains an issue despite the rapid growth in computing power (Lynch et al., 1995a). Unstructured grids and grid generation criteria provide the means and the knowledge for an efficient use of computational resources and are therefore critical to the solution of this problem.

In structured grids, each node is connected to a fixed number of its neighbors. Due to the rigidity in which each node is connected to its neighbors, these grids offer little or no flexibility for local refinement. In unstructured grids the connectivities between nodes can vary in space, enabling local refinement. While horizontally unstructured grids are well established, the first unstructured grids in the vertical are introduced in this work.

Existing grid generation criteria in the horizontal direction that impose a minimum dimensionless wavelength are based on simplistic assumptions (constant depth, linearity) and are therefore inappropriate near strong bathymetric gradients (e.g., Westerink et al., 1994). Convergence studies have provided useful insight (e.g., Westerink et al., 1992, Hannah and Wright, 1995, Lynch et al., 1995b), but failed to produce easy-to-use criteria. Grid refinement based on *a posteriori* error evaluation and adaptative grids have been used in other fields and appear as possible solutions (e.g., Carey, 1995, Hagen and Westerink, 1995).

Due to the strong vertical gradients present even in the simplest geophysical flows, the use of non-uniform grids in the vertical is probably even more important than in the horizontal. And yet, there have been very few attempts to develop grid-generation criteria for the vertical direction. Chapter 4 describes what is probably the first systematic study of this type, examining the effects of the relevant dimensionless numbers on the optimal placement of the nodes. This study only applies to barotropic tidal flows, though, and further studies are needed, in particular for flows involving stratification and wind effects.

Turbulence plays a major role in three-dimensional simulations, and our ability to model this phenomenon is still limited. Turbulence closure models are still not fully reliable because they depend heavily on the specification of too many empirical coefficients, and they are generally poorly tested. This lack of reliability increases when stratification plays an important role, as the number of empirical parameters and relationships increases. Turbulence closure models are discussed in Section 1.2.4.

Finally, choosing and applying a numerical method is a difficult task. The major difficulties include:

- Only marginal effort has been dedicated to systematic comparative research.[1] Even when comparisons exist, they often focus on accuracy and neglect cost. The cost issue is difficult to address because: a) comparisons are often made for very simple test cases where cost is not very meaningful (e.g., Baptista et al., 1995); b) the relative cost depends on the particular application (e.g., a frequency-domain model can be cheaper than a time-domain model in a long-term

---

[1] The Tidal Flow Forum (Werner, 1995) and the Metocean Modeling Project - MOMOP (Hackett and Røed, 1994, Røed et al., 1995, Hackett et al., 1995) were two noteworthy exceptions

application, but more expensive in a short-term one); and, c) the relative cost can depend strongly on the characteristics of the computer (e.g., some algorithms are particularly appropriate to certain computer architectures).

- The properties of the numerical methods are sometimes insufficiently understood, leading to errors in their application. For instance, it was believed for several years that σ-coordinates were only conditionally consistent. This belief, which we showed was incorrect (see Chapter 3), may have turned some modelers away from σ-coordinates. For instance, Casulli and Cheng (1994) justify their use of z-coordinates based on the problems of the σ-coordinates.
- There is a large number of issues on which modelers do not agree. For instance, there seems to be no consensus on whether finer vertical resolution is needed in shallow or in deep waters. Maybe for lack of guiding criteria, a constant grid spacing is often used in the vertical even though most models allow for a variable vertical resolution (e.g., Walters and Foreman, 1992). In Chapter 4 we present what is probably the first systematic study of the influence of relevant dimensionless numbers on the optimal vertical discretization.

In this context, the study of the numerical properties of methods currently used and the development of guidelines to apply those methods can greatly improve our ability to perform three-dimensional simulations of shallow water flow.

Due to these sources of errors, three-dimensional shallow water numerical models can be highly misleading if not used properly. Because errors can balance each other (e.g., peak values of the prognostic variable can be seriously reduced by numerical diffusion and increased by mass errors), and data are usually scarce, these errors often go undetected. Also, model results are easier to generate than to evaluate critically. As noted by Lynch and Davies (1995), "a single simulation exercise is easily capable of generating gigabytes of output in a matter of hours. Most of the data will necessarily go unexamined by its progenitors. Yet it is likely that disks full of simulation output will be used extensively [...] as a basis for operational decision-making."

Hence, the reliability of three-dimensional shallow water numerical models must be improved. The properties of the numerical methods (e.g., propagation factors), the effect of data errors and poor resolution, the error propagation from one model to another (e.g., the effect of flow errors on transport simulations), the limitation of empirical components of the model and the range of validity of the simplifying assumptions have to be understood and quantified. This knowledge can then conceivably be included into expert systems, which may eventually allow us to treat parts of the models as fool-proof "black boxes".

1.2 Three-Dimensional Shallow Water Models: a Brief Review

1.2.1 General Description

We concentrate here on models that solve the 3D form of the shallow water equations, which describe the conservation of mass and momentum under the assumptions of hydrostatic pressure and incompressibility. In addition, the Boussinesq approximation is generally invoked, given the small variations of density encountered in natural surface water systems.

Three-dimensional models typically decouple the horizontal and vertical directions, in an explicit recognition of the different scales involved in each direction. This decoupling is usually accomplished through the introduction of separate external and internal modes (Figure 1.2). The external mode solves depth-averaged equations for elevations (e.g., Lynch and Werner, 1991, Luettich et al., 1991), and, in most cases, depth-averaged velocities (e.g., Sheng, 1983, Blumberg and Mellor, 1987). The internal mode solves some form of the 3D momentum equations for the horizontal velocities, and, when needed, the continuity equation is solved for the vertical velocity. The internal and external modes constitute the flow module, which is the backbone of the model. Two additional modules can be added (Figure 1.2): a turbulence module which determines the eddy viscosity and diffusivity fields, and a density module which determines the density field by solving transport equations for salinity and/or temperature.

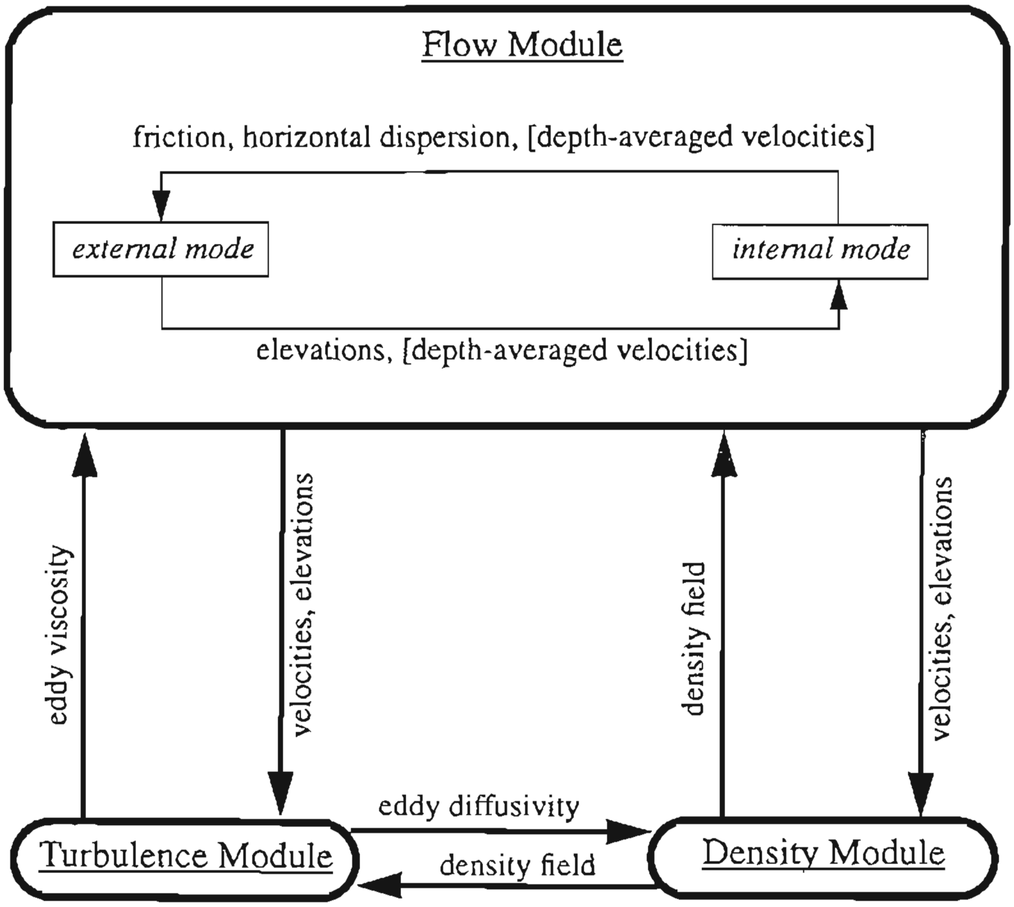

Figure 1.2 Information flow in a 3D shallow water model.

1.2.2 The External Mode

The external mode is akin to 2D depth-averaged models, and the solution procedures are very similar. Comparisons (e.g., Foreman, 1988, Werner, 1995, Oliveira et al., 1995) and reviews (e.g., Navon, 1988) of this type of models can be found in the literature so a detailed description will not be given here.

The major difference between models is probably the discretization method: some modelers resort to finite difference techniques, stressing their simplicity and low cost (on a per-node basis), while others prefer finite element techniques due to their superior ability for local refinement and shoreline description.

Within finite-element-based models, the Generalized Wave Continuity Equation (GWCE) formulation is probably the most popular (Lynch and Werner, 1991, Luettich and Westerink, 1991, Laible, 1992),[2] mainly due to its ability to minimize spurious oscillations. In addition, the solutions for elevations and for velocities are naturally decoupled, and the mass matrix for the wave equation is stationary. A drawback of GWCE models is their excessive dependence on the non-physical parameter G (see equation (2.14) on page 31). This problem is further discussed in Chapters 2, 5 and 6.

1.2.3 The Internal Mode

The solution of the internal mode varies widely. The major differences between existing models are probably the discretization procedure and the choice of the vertical coordinate.

Three techniques have been used to discretize the vertical direction: finite differences (e.g., Davies and Jones, 1990, Blumberg and Mellor, 1987, Casulli and Cheng, 1992), finite elements (e.g., Koutitas and O'Connor, 1980, Lynch and Werner, 1987, Luettich et al., 1994, Janin et al., 1994) and modal (or spectral) methods (e.g., Luettich and Westerink, 1991, Aldridge and Davies, 1993). The first two methods lead to very similar algorithms providing that the 3D problem can be transformed into a combination of a 2D (horizontal) and a set of 1D problems. This transformation, highly desirable for computational efficiency, is usually accomplished with a semi-implicit formulation: the vertical diffusion term is treated implicitly to allow a fine grid spacing in the vertical, and the terms involving horizontal gradients of depth-dependent quantities are treated explicitly

---

[2] Other type of wave equation formulations are also used in frequency domain models (Lynch and Werner, 1987, Walters, 1992).

(e.g., Blumberg and Mellor, 1987, Lynch and Werner, 1991) or with an Eulerian-Lagrangian technique (Casulli and Cheng, 1992, Janin et al., 1994). In addition, models using finite elements in the horizontal resort to lumping techniques (Lynch and Werner, 1991, Luettich et al., 1991, Li and Zhan, 1993) in order to remove horizontal connectivities between nodes. Modal methods express the vertical variation of dependent variables as a linear combination of shape functions. A review of this class of methods is given in Davies (1987), and a comparison with finite difference methods is given in Davies (1991).

The choice of the vertical coordinate is probably both more significant and more controversial. Several models (e.g., Leendertse and Liu, 1975, Casulli and Cheng, 1992) deal with the vertical dimension directly in cartesian form, using time-independent grids. This approach, known as the *z-coordinate* approach, has three important drawbacks: a) unless a very fine discretization is used, the shallow areas are generally under-resolved; b) the stepwise representation of the bottom topography can distort the bottom stress and flow (Sheng, 1983); and (c) the free surface must be treated as a moving boundary. Phillips (1957) proposed a domain-wide geometric mapping of the vertical coordinates, known as the *σ-coordinate* transformation, that satisfactorily addresses each of the three problems above. The σ-coordinate transformation introduces some additional terms in the equations, but solving for these terms has generally been considered a good trade-off relatively to the drawbacks of the z-coordinates. Sigma coordinates have therefore become increasingly popular, and are adopted in most three-dimensional models of coastal flows (e.g., see review by Cheng and Smith, 1990), and, in particular, in the Princeton Ocean Model (Blumberg and Mellor, 1987), probably the most widely used surface water model.

Sigma coordinates are not, however, free of drawbacks. In particular, the computation of horizontal gradients has received considerable attention in recent years because it can generate very large errors in presence of steep topography (see Chapter 3). Also, the number of nodes per vertical must remain constant over the entire computational domain, and the position of the vertical nodes in σ-coordinates must be the same for all verticals, i.e., the nodes must be located in planes of constant σ. This lack of flexibility leads to local under- and/or over-discretization of the vertical, particularly in domains including both deep and shallow regions. Attempts to overcome these problems include several complex transformations (e.g., Beckers, 1991, Gerdes, 1993, Song and Haidvogel, 1994, Huang and Spaulding, 1995) as well as the localized sigma coordinates (Fortunato and Baptista, 1994a) described in subsequent chapters.

An additional drawback of both σ- and z-coordinates is the potential for generation of diapycnical mixing. When isopycnic and coordinate surfaces do not coincide, and large horizontal diffusion is needed for numerical reasons (e.g., in deep ocean, coarse resolution simulations, or when advective accelerations are strong), both σ- and z-coordinate models generate numerical mixing across the isopycnic surfaces. Some models designed for deep ocean applications avoid this problem by using density as the vertical coordinate (e.g., Bleck and Smith, 1990). However, this approach fails in unstratified conditions.

Two interesting recent developments in 3D models relate to the choice of the unknowns in the momentum equation and to the solution of the continuity equation. Luettich and Westerink (1991) solve the momentum equations for stresses rather than velocities. Since stresses are known to vary almost linearly along the water column, this method can arguably lead to important computational savings relative to traditional methods. Also, the solution of the 3D continuity equation can be problematic because it is a first order equation with two boundary conditions (at the surface and at the bottom). To avoid having to drop one of the boundary conditions, Lynch and Naimie (1993) suggest solving the vertical derivative of the continuity equation (see also Fortunato and Baptista (1993) and Janin et al. (1994) for comparable approaches), while Muccino et al. (1994) use a least square approach, thereby enforcing both conditions in an approximate way.

1.2.4 Turbulence Closure Schemes

Turbulence closure schemes are generally classified according to the number of differential equations solved. The most common schemes are zero-, one- and two-equation models (see detailed reviews in Rodi, 1987, ASCE, 1988a,b and Davies et al., 1995). Alternatively, eddy viscosity can be directly specified based on local flow properties.

Two-equation models are the most complex currently used in geophysical flows. Like the other models presented below, they are based on the eddy viscosity/diffusivity concepts, i.e., turbulent transport of mass and momentum is assumed proportional to the mean velocity/concentration gradients. The proportionality coefficients are in turn assumed to be proportional to a velocity and a length scales.

Two-equation models solve two differential transport equations for a velocity and a length scale, or combinations of these scales. The traditional model (k-ε model) solves for turbulent energy (k) and dissipation (ε) (e.g., Nihoul et al., 1989). The k-ε model owes its popularity to the relatively simple form of the ε equation (Rodi, 1984). However, its critics claim that it is physically unrealistic because dissipation occurs at the smallest turbulent scales, whereas most turbulent energy is present at the largest scales (Mellor and Yamada, 1982). A very popular alternative in geophysical flows is the q^2-q^2l model, which solves equations for $q^2=2k$ and for q^2l, where l is the mixing length (Mellor and Yamada, 1982).[3] This approach is used in the Princeton Ocean Model and has also been adopted by others (e.g., Lynch et al., 1995b). The relative success of the Princeton Ocean Model model in the MOMOP exercise mentioned in the previous section helped establish the q^2-q^2l model as an unofficial reference in coastal ocean modeling.

One-equation models replace one of the transport equations by the direct specification of the mixing length, for which several empirical formulas are available (e.g., Blackadar, 1962, Vagar and Kagan, 1969, Johns, 1978). Applications of this approach can be found in Johns and Oguz (1987) and Davies and Jones (1990). Zero-equation models result from two-equation models by assuming local equilibrium, i.e., production of turbulent energy is locally compensated by dissipation. This approach is seldom used in surface water applications.

---

[3] A modification has later been introduced by Galperin et al. (1988).

A common alternative to these models is the direct specification of the eddy viscosity. For dimensional reasons, eddy viscosity is written as the product of a characteristic velocity (depth-averaged velocity, bottom velocity or stress velocity), a characteristic length scale (total depth, depth of the bottom boundary layer, roughness length) and an empirical constant. This approach provides a time variation of eddy viscosity which is very important as it makes the vertical diffusion term in the momentum equation non-linear, thus generating shallow water tidal constituents (Davies, 1990). Several vertical profiles have been tested by Davies and co-workers (e.g., Davies, 1993, Davies and Aldridge, 1993). The most commonly used profile varies linearly in the bottom 20% of the water column and is constant in the upper 80%.

Comparison between the direct specification of eddy viscosity and a one-equation model suggests that they yield comparable results for barotropic tidal flows when properly calibrated (Davies and Jones, 1990). However, there is no solid evidence that the same empirical constants are appropriate for all systems. There is therefore the risk that the improvements achieved by going from a two-dimensional to a three-dimensional model result mainly from the larger number of fitting parameters. Also, the direct specification of eddy viscosity is overly case-dependent (e.g., presence versus absence of wind), and unsatisfactory in the presence of buoyancy. Finally, this approach seems inadequate to fully explain the generation of some non-linear constituents (Grenier et al., 1995).

The trend in the modeling community has been towards two-equation models which are considered more accurate than one-equation models, and only slightly more expensive (Rodi, 1987). However, the direct specification approach is still often used due to its simplicity and low cost.

1.3 Objectives

Our ability to perform three-dimensional simulations of shallow water flow can be greatly improved by a better understanding of the numerical properties of methods currently used and by the development of guidelines to apply those methods. To accomplish our overall goal of enhanced guided three-dimensional simulations of shallow water flow, we examine two critical issues in detail: the computation of horizontal gradients of depth-dependent quantities, and the vertical discretization.

Coastal flow models assume that the characteristic horizontal scales are much larger than depth. Besides leading to the well-known hydrostatic approximation, this assumption leads to horizontal and vertical resolutions orders of magnitude apart. These different resolutions are needed and usually justified. However, when bottom slopes are very large, the meaning of "horizontal" in this context is ambiguous: should it mean "parallel to the bottom"? "perpendicular to the vertical"? Clearly, to be consistent with the assumption of different characteristic length scales, "horizontal" should mean "direction along which gradients are smallest". Unfortunately, this direction varies in space and time, and it is not possible to define *a priori* the right coordinate system to evaluate horizontal gradients. As a result, in presence of steep slopes, very sharp gradients are partly resolved with the horizontal grid, and very large errors develop. **Understanding and avoiding the generation of these errors was therefore the first goal of this study** (Fortunato and Baptista, 1994a, 1994b, 1995a).

The second goal of this study was to develop a flexible method to discretize the vertical direction. Two radically different approaches are used to discretize a spatial domain: structured and unstructured grids. The use of unstructured grids in the horizontal direction is well established in estuarine and coastal modeling, due to their superior ability to represent coastlines and areas of strong velocity gradients. Surprisingly, however, only structured grids have been used until now to represent the vertical direction. The method introduced here, the localized sigma coordinates - LSC (Fortunato and Baptista, 1994a), gives the modeler, for the first time, the ability to discretize each vertical independently from the other.

Our third goal was to develop solid guidelines for the vertical discretization of tidal models. Such guidelines were basically non-existent, and had to be developed to take advantage of the LSC's flexibility and make them more than an interesting curiosity. The case studied, a barotropic tidal flow (Fortunato and Baptista, 1995b), was chosen for its relative simplicity and for its practical interest. The criteria developed, both for the vertical placement of nodes in a single vertical and for the horizontal distribution of the total number of nodes, showed the advantages of the LSC even for very simple flows and can lead to important gains in accuracy even for structured grids. These criteria were then applied with some modifications to a complex estuarine system with excellent results (Fortunato et al., 1995).

Finally, we are involved in an ongoing effort to understand the tidal dynamics in the Tagus estuary, which should eventually lead to a prognostic water quality model for management purposes. Previous work had addressed the tidal propagation in the estuary using several depth-averaged models, and neglecting advective accelerations (Silva, 1994, Silva and Oliveira, 1995, Oliveira et al., 1995). **Our goal was to extend this work to include both advective accelerations and three-dimensional barotropic effects.** Both effects are particularly important in the lower estuary, and our work led to new insight into the circulation in this area (Fortunato et al., 1995).

1.4 Organization

This thesis includes six chapters and three appendices. Chapter 2 describes the governing equations and the numerical implementation of RITA_{2V} (Fortunato and Baptista, 1993), a two-dimensional, laterally-averaged, hydrodynamic model used extensively in subsequent chapters. In addition, the numerical properties of the GWCE and the LSC are also discussed.

Chapter 3[4] addresses the computation of horizontal gradients in surface water models. Two alternative techniques are compared through both truncation error analysis and numerical experimentation, and a method to define the horizontal resolution needed to avoid large errors is proposed.

In Chapter 4[5] we develop a criterion for vertical discretization in tidal flow simulations. This criterion addresses both the distribution of nodes within a single vertical and the distribution of the total number of nodes among different verticals. A two-dimensional application to a synthetic estuary illustrates the usefulness of the approach, and demonstrates the advantages of the LSC.

Chapter 5[6] describes a fully three-dimensional application of the concepts and methods developed in this study. This application, part of an on-going effort to understand the tidal dynamics to the Tagus estuary (Silva, 1994, Silva and Oliveira, 1995, Oliveira et al., 1995), evaluates the performance of the LSC in a real system. The criterion proposed in Chapter 4 for the distribution of the total number of nodes among verticals is shown to lead only to marginal gains when advective accelerations are important. An alternative criterion which leads to significant accuracy gains, even when advective accelerations are important, is proposed.

Chapter 6 contains a summary and some suggestions for future work. Appendix 1 and Appendix 2 describe the inputs and outputs of RITA_{2v}[7] and ADCIRC, respectively. Appendix 3[8] discusses the computation of advective acceleration in surface water models, and is a complement to Chapter 3.

---

[4] Fortunato and Baptista (1995a).

[5] Fortunato and Baptista (1995b).

[6] Fortunato et al. (1995).

[7] a more detailed application of RITA_{2v} can be found in Pearson et al. (1994).

[8] Fortunato and Baptista (1994b).

References

Aikman, F., G. L. Mellor, T. Ezer, D. Shenin, P. Chen, L. Breaker, K. Bosley, and D. B. Rao, 1995. Toward an Operational Nowcast/Forecast System for the U.S. East Coast, in *Modern Approaches to Data Assimilation in Ocean Modeling*, D. Halpern and P. Malanotte-Rizzoli (editors), Elsevier Publ., (in review).

Aldridge, J.N. and A.M. Davies, 1993. A High-Resolution Three-Dimensional Hydrodynamic Tidal Model of the Eastern Irish Sea, *J. Phys. Ocean.*, 23: 207-224.

ASCE Task Committee on Turbulence Models in Hydraulic Computations, 1988a. Turbulence Modeling of Surface Water Flow and Transport: Part I, *J. Hyd. Eng.*, 114: 970-991.

ASCE Task Committee on Turbulence Models in Hydraulic Computations, 1988b. Turbulence Modeling of Surface Water Flow and Transport: Part II, *J. Hyd. Eng.*, 114: 992-1014.

Baptista, A.M., E.E. Adams and P. Gresho, 1995. Benchmarks for the Transport Equation: the Convection-Diffusion Forum and Beyond, in *Quantitative Skill Assessment for Coastal Ocean Models*, D.R. Lynch and A.M. Davies (editors), Amer. Geoph. Union, Washington, 241-268.

Beckers, J.-M., 1991. Application of the GHER 3D General Circulation Model to the Western Mediterranean, *J. Mar. Syst.*, 1: 315-332.

Blackadar, A.K., 1962. The Vertical Distribution of Wind and Turbulent Exchange in a Neutral Atmosphere, *J. Geophys. Res.*, 67: 3095-3102.

Bleck, R. and L.T. Smith, 1990. A Wind-Driven Isopycnic Coordinate Model of the North and Equatorial Atlantic Ocean. 1. Model Development and Supporting Experiments, *J. Geophys. Res.*, 95: 3273-3285.

Blumberg, A.F. and G.L. Mellor, 1987. A Description of a Three-Dimensional Coastal Ocean Model, in *Three-Dimensional Coastal Ocean Models*, N.S. Heaps (editor), Amer. Geoph. Union, Washington, 1-16.

Blumberg, A.F., R.P. Signell and H.L. Jenter, 1993. Modelling Transport Processes in the Coastal Ocean, *J. Marine Env. Eng.*, 1: 31-52.

Carey, G.F., 1995. Mesh Generation, A Posteriori Error Estimation and Mesh Refinement, in *Quantitative Skill Assessment for Coastal Ocean Models*, D.R. Lynch and A.M. Davies (editors), Amer. Geoph. Union, Washington, 15-29.

Casulli, V. and R.T. Cheng, 1992. Semi-Implicit Finite Difference Methods for Three-Dimensional Shallow Water Equations, *Int. J. Num. Methods in Fluids*, 15: 629-648.

Casulli, V. and R.T. Cheng, 1994. Solutions of Primitive Equations for Three-Dimensional Tidal Circulation, in *Estuarine and Coastal Modeling III*, M.L. Spaulding, et al. (editors), Amer. Soc. Civ. Eng., 396-406.

Cheng, R.T. and P.E. Smith, 1990. A Survey of Three-Dimensional Numerical Estuarine Models, in *Estuarine and Coastal Modeling*, M.L. Spaulding (editor), Amer. Soc. Civ. Eng., 1-15.

Davies, A.M., 1987. Spectral Models in Continental Shelf Sea Oceanography, in *Three-Dimensional Coastal Ocean Models*, N.S. Heaps (editor), Amer. Geoph. Union, Washington, 71-106.

Davies, A.M., 1990a. On the Accuracy of Finite Difference and Modal Methods for Computing Tidal and Wind Wave Current Profiles, *Int. J. Num. Methods in Fluids*, 12: 101-124.

Davies, A.M., 1990b. On the Importance of Time Varying Eddy Viscosity in Generating Higher Tidal Harmonics, *J. Geophys. Res.*, 95: 20287-20312.

Davies, A.M., 1993. A Bottom Boundary Layer-Resolving Three-Dimensional Tidal Model: A Sensitivity Study of Eddy Viscosity Formulation, *J. Phys. Ocean.*, 23: 1437-1453.

Davies, A.M. and J.N. Aldridge, 1993. A Numerical Model Study of the Parameters Influencing Tidal Currents in the Irish Sea, *J. Geophys. Res.*, 98: 7049-7067.

Davies, A.M. and J.E. Jones, 1990. Application of a Three-Dimensional Turbulence Energy Model to the Determination of Tidal Currents on the Northwest European Shelf, *J. Geophys. Res.*, 95: 18143-18162.

Davies, A.M., P.J. Luyten and E. Deleersnijder, 1995. Turbulence Energy Models in Shallow Sea Oceanography, in *Quantitative Skill Assessment for Coastal Ocean Models*, D.R. Lynch and A.M. Davies (editors), Amer. Geoph. Union, Washington, 97-124.

Dejak, C., D. Franco, R. Pastres and G. Pecenik, 1990. A 3-D Eutrophication-Diffusion Model of the Venice Lagoon: Some Applications, in *Residual Currents and Long Term Transport*, R.T. Cheng (editor), Springer-Verlag, New York, 526-538.

Foreman, M.G.G., 1988. A Comparison of Tidal Models for the Southwest Coast of Vancouver Island, in *Proc. Int. Conf. on Computational Methods in Water Resources VII*, M.A. Celia, et al. (editors), Elsevier, Amsterdam, 231-236.

Foreman, M.G.G., A.F. Bennett, G.D. Egbert and C. Hagelberg, 1992. The Removal of Tidal Elevations from Satellite Altimeter Measurements, in *Proc. Int. Conf. on Computational Methods in Water Resources IX*, T.F. Russel, et al. (editors), Comp. Mech. Publications, Southampton, 637-648.

Fortunato, A.B. and A.M. Baptista, 1993. *RITA*$_{2v}$ *User's Manual. 2D Vertical Hydrodynamic Model for River and Tidal Analysis. Part I - Flow Model*, OGI-CCALMR Software Documentation Series SDS7, 93-3, Oregon Graduate Institute of Science & Technology, Portland, Oregon.

Fortunato, A.B. and A.M. Baptista, 1994a. Localized Sigma Coordinates for the Vertical Structure of Hydrodynamic Models, in *Estuarine and Coastal Modeling III*, M.L. Spaulding, et al. (editors), Amer. Soc. Civ. Eng., 323-335.

Fortunato, A.B. and A.M. Baptista, 1994b. Modeling Near-Bottom Advective Accelerations in Surface Water Models, in *Proc. Int. Conf. on Computational Methods in Water Resources X*, A. Peters, et al. (editors), Kluwer Academic Publishers, 1045-1052.

Fortunato, A.B. and A.M. Baptista, 1995a. Evaluation of Horizontal Gradients in SIgma-Coordinate Shallow Water Models, *Atmosphere-Ocean* (in review).

Fortunato, A.B. and A.M. Baptista, 1995b. Vertical Discretization in Tidal Flow Simulations, *Int. J. Num. Methods in Fluids* (in press).

Fortunato, A.B., A.M. Baptista and R.A. Luettich, Jr., 1995. Tidal Dynamics in the Mouth of the Tagus Estuary (Portugal), (in preparation).

Galperin, B., L.H. Kantha, S. Hassid and A. Rosati, 1988. A Quasi-Equilibrium Turbulent Energy Model for Geophysical Flows, *J. Atmos. Sciences*, 45: 55-62.

Gerdes, R., 1993. A Primitive Equation Ocean Circulation Model Using a General Vertical Coordinate Transformation. 1. Description of the Model, *J. Geophys. Res.*, 98: 14683-14701.

Grenier, Jr., R.R., R.A. Luettich, Jr. and J.J. Westerink, 1995. A Comparison of the Nonlinear Frictional Characteristics of Two-Dimensional and Three-Dimensional Models of a Shallow Water Embayment, *J. Geophys. Res.*, 100: 13,719-13,735.

Hackett, B. and L.P. Røed, 1994. Numerical Modeling of the Halten Bank Area: a Validation Study, *Tellus*, 46A: 113-133.

Hackett, B., L.P. Røed, B. Gjevik, E.A. Martinsen and L.I. Eide, 1995. A Review of the Metocean Modeling Project (MOMOP). Part 2: Model Validation Study, in *Quantitative Skill Assessment for Coastal Ocean Models*, D.R. Lynch and A.M. Davies (editors), Amer. Geoph. Union, Washington, 307-328.

Hagen, S.C. and J.J. Westerink, 1995. Finite Element Grid Resolution Based on Second and Fourth Order Truncation Error Analysis, in *Proc. 2nd Int. Conf. Computer Modeling of Seas and Coastal Regions* (to appear).

Hannah, C.G. and D.G. Wright, 1995. Depth Dependent Analytical and Numerical Solutions of Wind-Driven Flow in the Coastal Ocean, in *Quantitative Skill Assessment for Coastal Ocean Models*, D.R. Lynch and A.M. Davies (editors), Amer. Geoph. Union, Washington, 125-152.

Heaps, N.S. (editor), 1987. *Three-Dimensional Coastal Ocean Models*, Amer. Geoph. Union, Washington.

Huang, W. and M. Spaulding, 1995. 3D Model of Estuarine Circulation and Water Quality Induced by Surface Water Discharges, *J. Hyd. Eng.*, 121: 300-311.

Johns, B., 1978. The Modeling of Tidal Flow in a Channel Using a Turbulence Energy Closure Scheme, *J. Phys. Ocean.*, 8: 1042-1049.

Johns, B. and T. Oguz, 1987. Turbulent Energy Closure Schemes, in *Three-Dimensional Coastal Ocean Models*, N.S. Heaps (editor), Amer. Geoph. Union, Washington, 17-39.

Janin, J.M., F. Lepeintre and P. Péchon, 1994. TELEMAC-3D: A Finite Element Code to Solve 3D Free Surface Flow Problems, in *Computer Modelling of Seas and Coastal Regions*, P.W. Partridge (editor), Comp. Mech. Pub., 489-506.

Koutitas, C. and B. O'Connor, 1980. Finite Element-Fractional Steps Solution of the 3D Coastal Circulation Model, in *Finite Elements in Water Resources III, Vol. 2*, S.Y. Wang, et al., University of Mississipi, Oxford, Mississipi.

Laible, J.P., 1992. On the Solution of the Three-Dimensional Shallow Waters Equations Using the Wave Equation Formulation, in *Computational Methods in Water Resources IX, Vol. 2*, T.F. Russel, et. al. (editors), Computational Mechanics Publications, 545-552.

Leendertse, J.J. and S.K. Liu, 1975. *A Three-Dimensional Model for Estuaries and Coastal Seas. II, Aspects of Computation.* Rand Corporation Report R-1764-OWRT.

Li, Y.S. and J.M. Zhan, 1993. An Efficient Three-Dimensional Semi-Implicit Finite-Element Scheme for Simulation of Free Surface Flows, *Int. J. Num. Methods in Fluids*, 16: 187-198.

LMER Coordinating Committee, 1992. Understanding Changes in Coastal Environments: the LMER Program, *EOS*, 73: 481-488.

Luettich, R.A. and J.J. Westerink, 1991. A Solution for the Vertical Variation of Stress, Rather than Velocity, in a Three-Dimensional Circulation Model, *Int. J. Num. Methods in Fluids*, 12: 911-928.

Luettich, R.A., J.J. Westerink and N.W. Scheffner, 1991. *ADCIRC: An Advanced Three-Dimensional Circulation Model for Shelves, Coasts and Estuaries. Report 1: Theory and Methodology of ADCIRC-2DDI and ADCIRC-3DL.* Prepared for Department of the Army, U.S. Army Corps of Engineers.

Luettich, R.A. S. Hu and J.J. Westerink, 1994. Development of the Direct Stress Solution Technique for Three-Dimensional Hydrodynamic Models Using Finite Elements, *Int. J. Num. Methods in Fluids*, 19: 295-319.

Lynch, D.R. and A.M. Davies, 1995. Preface, in *Quantitative Skill Assessment for Coastal Ocean Models*, D.R. Lynch and A.M. Davies (editors), Amer. Geoph. Union, Washington.

Lynch, D.R. and C.E. Naimie, 1993. The M2 Tide and its Residual on the Outer Banks of the Gulf of Maine, *J. Phys. Ocean.*, 23: 2222-2253.

Lynch, D.R. and F.E. Werner, 1987. Three-Dimensional Hydrodynamics on Finite Elements: Part I: Linearized Harmonic Model, *Int. J. Num. Methods in Fluids*, 7: 871-909.

Lynch, D.R. and F.E. Werner, 1991. Three-Dimensional Hydrodynamics on Finite Elements: Part II: Non-Linear Time Stepping Model, *Int. J. Num. Methods in Fluids*, 12: 507-533.

Lynch, D.R., A.M. Davies, H. Gerritsen and C.N.K. Mooers, 1995a. Closure: Quantitative Skill Assessment for Coastal Ocean Models, in *Quantitative Skill Assessment for Coastal Ocean Models*, D.R. Lynch and A.M. Davies (editors), Amer. Geoph. Union, Washington, 501-506.

Lynch, D.R., J.T.C. Ip, C.E. Naimie and F.E. Werner, 1995b. Convergence Studies of Tidally-Rectified Circulation on Georges Bank, in *Quantitative Skill Assessment for Coastal Ocean Models*, D.R. Lynch and A.M. Davies (editors), Amer. Geoph. Union, Washington, 153-174.

Mellor, G.L. and T. Yamada, 1982. Development of a Turbulence Closure Model for Geophysical Fluid Problems, *Reviews of Geophys. and Space Phys.*, 20: 851-875.

Muccino, J.C., W.G. Gray and M.G.G. Foreman, (1994). Calculation of Vertical Velocity in a 3D Model Using a Least Squares Approach, in *Proc. Int. Conf. on Computational Methods in Water Resources X*, A. Peters, et al. (editors), Kluwer Academic Publishers, 1105-1112.

Navon, I.M., 1988. A Review of Finite Element Methods for Solving the Shallow Water Equations, in *Proc. of an Int. Conf. on Computer Modelling in Ocean Engineering*, B.A. Schreffer and O.C. Zienkiewicz (editors), A.A. Balkema Publishers, Rotterdam, Netherlands.

Nihoul, J.C.J. and B.M. Jamart (editors), 1987. *Three-Dimensional Models of Marine and Estuarine Dynamics*, Elsevier, Amsterdam.

Nihoul, J.C.J., E. Deleersnijder and S. Djenidi, 1989. Modeling the General Circulation of Shelf Seas by 3D k-ε Models, *Earth-Science Reviews*, 26: 163-189.

Oliveira, A.P., A.B. Fortunato, and A.M. Baptista, 1995. Tidal Propagation in the Tagus Estuary (Portugal), (in preparation).

Pearson, P., P.J. Turner, A.B. Fortunato and A.M. Baptista, 1994. *Hydrodynamic Modeling of the Snake and Columbia Rivers*, Technical Report, Center for Coastal and Land-Margin Research, Oregon Graduate Institute of Science & Technology, Portland, Oregon.

Phillips, N.A., 1957. A Coordinate System Having Some Special Advantages for Numerical Forecasting. *J. Meteor.* 14: 184-185.

Rodi, W., 1984. *Turbulence Models and Their Application in Hydraulics - a State of the Art Review*, International Association for Hydraulic Research, Delft, Netherlands.

Rodi, W., 1987. Examples of Calculation Methods for Flow and Mixing in Stratified Fluids, *J. Geophys. Res.*, 92: 5305-5328.

Røed, L.P., B. Hackett, B. Gjevik, E.A. Martinsen and L.I. Eide, 1995. A Review of the Metocean Modeling Project (MOMOP). Part 1: Model Comparison Study, in *Quantitative Skill Assessment for Coastal Ocean Models*, D.R. Lynch and A.M. Davies (editors), Amer. Geoph. Union, Washington, 285-305.

Salomon, J.C. and M. Pommepuy, 1990. Mathematical Model of Bacterial Contamination of the Morlaix Estuary (France), *Wat. Res.*, 24: 983-994.

Sheng, Y.P., 1983. *Mathematical Modeling of Three-Dimensional Coastal Currents and Sediment Dispersion*, Technical Report CERC-83-2, U.S. Army Engineer Waterway Experiment Station, Vicksburg, Mississippi.

Silva, M.C., 1994. *EXPO'98: Hydrodynamic Modeling. Progress Report.* Report LNEC 215/94 - NET, Laboratório Nacional de Engenharia Civil, Lisbon, Portugal (in Portuguese).

Silva, M.C. and E.M. Oliveira, 1995. *EXPO'98: Hydrodynamic Modelling of the Tagus Estuary*, Report 174/95 - NET, Laboratório Nacional de Engenharia Civil, Lisbon, Portugal (in Portuguese).

Song, Y. and D. Haidvogel, 1994. A Semi-Implicit Ocean Circulation Model Using a Generalized Topography-Following Coordinate System, *J. Comp. Phys.*, 115: 228-244.

Spaulding, M.L., K. Bedford, A. Blumberg, R. Cheng and C. Swanson (editors), 1992, *Estuarine and Coastal Modeling II*, Amer. Soc. Civ. Eng.

Spaulding, M.L., K. Bedford, A. Blumberg, R. Cheng and C. Swanson (editors), 1994, *Estuarine and Coastal Modeling III*, Amer. Soc. Civ. Eng.

Stevenson, R.E. (editor), 1995. *Abstracts from the XXI General Assembly for the International Association for the Physical Sciences of the Oceans*, Int. Assoc. for the Phys. Sc. of the Oceans.

Stole-Hansen, K. and D. Slagstad, 1991. Simulation of Currents, Ice Melting and Vertical Mixing in the Barents Sea Using a 3-D Baroclinic Model, in *Proc. of the ProMare Symp. on Polar Marine Ecology*, Sakshaug et al. (editors), *Polar Res.*, 10: 33-44.

Vager, B.G. and B.A. Kagan, 1969. Dynamics of Turbulent Boundary Layer In Tidal Current, *Bull. Acad. Sci. USSR, Atmos. Oceanic Y Phys. Ser. (USA)*, 5: 168-179.

Walters, R.A., 1992. A 3D, Finite Element Model for Coastal and Estuarine Circulation, *Cont. Shelf Res.*, 12: 83-102.

Walters, R.A. and M.G.G. Foreman. 1992. A 3D, Finite Element Model for Baroclinic Circulation on the Vancouver Island Continental Shelf, *J. Mar. Syst.*, 3: 507-518.

Westerink, J.J. and W.G. Gray, 1990. Progress in Surface Water Modeling, *Rev. Geophys.*, supplement, 210-217.

Westerink, J.J., J. Muccino and R.A. Luettich, Jr., 1992. Resolution Requirements for a Tidal Model of the Western North Atlantic and Gulf of Mexico, *Computational Methods in Water Resources IX, Vol. 2*, in T.F. Russel, et al. (editors), Computational Mechanics Publications, 667-674.

Westerink, J.J., R.A. Luettich, Jr. and J. Muccino, 1994. Modeling Tides in the Western North Atlantic Using Unstructured Graded Grids, *Tellus*, 46A, 178-199.

Werner, F.E., 1995. A Field Test Case for Tidally Forced Flows: a Review of the Tidal Flow Forum, in *Quantitative Skill Assessment for Coastal Ocean Models*, D.R. Lynch and A.M. Davies (editors), Amer. Geoph. Union, Washington, 269-284.

CHAPTER 2

RITA$_{2v}$: a Two-Dimensional Laterally-Averaged Hydrodynamic Model

2.1 Introduction

This chapter describes the formulation and numerical properties of *RITA*$_{2v}$ (Fortunato and Baptista, 1993). *RITA*$_{2v}$ (River and Tidal Analysis 2D vertical) is a two-dimensional, vertical hydrodynamic model based on the shallow water equations. The main characteristics of the model are as follows:

- fully non-linear;
- one- or two-dimensional modes available;
- the width is variable, although the cross-section is assumed to be rectangular;
- forcings include boundary elevations or flows, wind, bottom deformation and baroclinic pressure (treated diagnostically);
- time- and space-dependent vertical eddy viscosity;
- the external mode is solved with the Generalized Continuity Wave Equation with linear finite elements;
- the internal mode can use either domain wide sigma coordinates (DWSC), or localized sigma coordinates (LSC);
- the time step for the internal mode can be a multiple of the time step for the external mode.

This chapter includes three sections besides this Introduction. Section 2.2 describes the basic equations used in the model, and the assumptions made in their derivation. Section 2.3 describes the numerical procedures used to solve the equations. The final section discusses the basic characteristics of the numerical methods used.

2.2 Mathematical Model

2.2.1 Basic Equations and Approximations

The Reynolds equations are obtained by averaging the Navier-Stokes equations over the time scales of turbulence (e.g., see White, 1974). Assuming incompressibility, the momentum and continuity equations are:

$$\frac{Du_i}{Dt} = F_i - \frac{1}{\rho}\frac{\partial p}{\partial x_i} + \frac{1}{\rho}\frac{\partial \tau_{ji}}{\partial x_j} + \nu\frac{\partial^2 u_i}{\partial x_i^2} \qquad i, j = 1, 2, 3 \tag{2.1}$$

and:

$$\frac{\partial u_i}{\partial x_i} = 0 \tag{2.2}$$

where u_i are the cartesian components of the Reynolds averaged velocities, x_j are the cartesian coordinates, t is time, p is pressure, ρ is density, ν is the kinematic molecular viscosity, τ_{ij} are the Reynold stresses, and F_i are the body forces.

Two approximations are invoked to derive the shallow water equations: the hydrostatic and Boussinesq approximations. When the wavelength is much larger than depth, vertical accelerations are negligible, and the vertical momentum equation collapses into the hydrostatic condition, i.e.:

$$\frac{1}{\rho}\frac{\partial p}{\partial z} + g = 0 \tag{2.3}$$

where g represents the gravitational acceleration. By integrating (2.3) from a generic position z to the surface η, pressure can be determined and eliminated in the horizontal momentum equations:

$$\frac{\partial p}{\partial x_i} = \frac{\partial p_a}{\partial x_i} + g\rho\frac{\partial \eta}{\partial x_i} + g\int_z^{\eta}\frac{\partial \rho}{\partial x_i}dz \qquad i = 1, 2 \tag{2.4}$$

where p_a represents the pressure at the water surface.

The Boussinesq approximation states that density variations in space and time are negligible, except in terms multiplied by gravity. With this set of assumptions, the Reynolds equations are transformed into the shallow water equations:

$$\begin{aligned} \frac{Du}{Dt} &= fv - \frac{1}{\rho_0}\frac{\partial p_a}{\partial x} - g\frac{\partial \eta}{\partial x} - \frac{g}{\rho_0}\int_z^{\eta}\frac{\partial \rho}{\partial x}dz + \frac{1}{\rho_0}\frac{\partial \tau_{j1}}{\partial x_j} + \upsilon\nabla^2 u \\ \frac{Dv}{Dt} &= -fu - \frac{1}{\rho_0}\frac{\partial p_a}{\partial y} - g\frac{\partial \eta}{\partial y} - \frac{g}{\rho_0}\int_z^{\eta}\frac{\partial \rho}{\partial y}dz + \frac{1}{\rho_0}\frac{\partial \tau_{j2}}{\partial x_j} + \upsilon\nabla^2 v \end{aligned} \tag{2.5}$$

where ρ_0 is the reference density and f is the Coriolis parameter.

2.2.2 Laterally Averaged Equations

The momentum and continuity equations are now laterally averaged, assuming a rectangular cross-section. Integrating each term of the continuity equation (2.2) over width using the Leibnitz rule[1] and the kinematic boundary conditions,[2] we get (Figure 2.1):

---

[1] $$\frac{\partial}{\partial x_1}\int_{h_1(x_1)}^{h_2(x_1)} f(x_1, x_2, x_3)\,dx_3 = \int_{h_1(x_1)}^{h_2(x_1)} \frac{\partial}{\partial x_1}f(x_1, x_2, x_3)\,dx_3 + f|_{h_2}\frac{\partial h_2}{\partial x_1} - f|_{h_1}\frac{\partial h_1}{\partial x_1}$$

[2] $$-u\frac{\partial y}{\partial x} + v - w\frac{\partial y}{\partial z}\bigg|_i = 0 \qquad i = 1, 2$$

$$\int_{y_1}^{y_2} \frac{\partial u_i}{\partial x_i} dy =$$

$$\left(\frac{\partial}{\partial x}\int_{y_1}^{y_2} u\,dy - u|_{y_2}\frac{\partial y_2}{\partial x} + u|_{y_1}\frac{\partial y_1}{\partial x}\right) + \left(v|_{y_2} - v|_{y_1}\right) + \left(\frac{\partial}{\partial z}\int_{y_1}^{y_2} w\,dy - w|_{y_2}\frac{\partial y_2}{\partial z} + w|_{y_1}\frac{\partial y_1}{\partial z}\right) = \tag{2.6}$$

$$\frac{\partial}{\partial x}\tilde{u}B + \frac{\partial}{\partial z}\tilde{w}B = 0$$

where B represents the width of the channel and the tildes represent lateral averages.

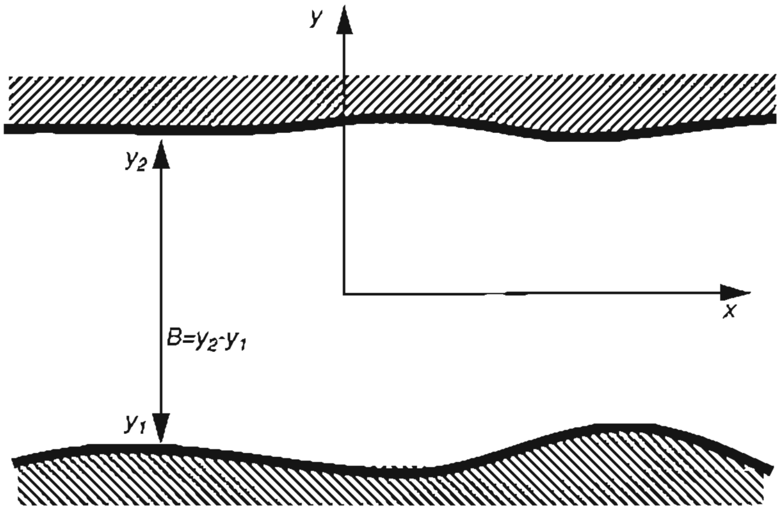

Figure 2.1 Channel geometry.

Likewise, the x-momentum equation becomes:

$$\frac{\partial \tilde{u}}{\partial t} + \tilde{u}\frac{\partial \tilde{u}}{\partial x} + \tilde{w}\frac{\partial \tilde{u}}{\partial z} + \frac{1}{\rho_0}\frac{\partial \tilde{p}_a}{\partial x} + \frac{g}{\rho_0}\int_z^{\eta}\frac{\partial \tilde{\rho}}{\partial x}dz + g\frac{\partial \tilde{\eta}}{\partial x} - \frac{\partial}{\partial z}\left(A_v\frac{\partial \tilde{u}}{\partial z}\right) - \frac{1}{B}\frac{\partial}{\partial x}\left(BA_h\frac{\partial \tilde{u}}{\partial x}\right) = 0 \tag{2.7}$$

where once more the variables are laterally averaged, and A_h and A_v are the horizontal and vertical dispersion coefficients, respectively. The dispersion terms include the molecular viscosity, the eddy dispersion and the lateral dispersion effects. To derive (2.7) the pressure gradient in the Y direction was neglected. This approximation is valid if the curvature of the river and the lateral salinity gradients are small. Also, the lateral stresses at the walls were neglected, a reasonable assumption if the width is significantly larger than depth.

The validity of the laterally averaged equations depends on two fundamental quantities (Ianniello, 1977): the Kelvin number,

$$Ke = \frac{fB}{\sqrt{gh}} \tag{2.8}$$

and the horizontal aspect ratio,

$$\delta = \frac{B}{T\sqrt{gh}} \tag{2.9}$$

where f is the Coriolis parameter and T the tidal period. These two dimensionless numbers, Ke and δ, are measures of the importance of, respectively, the Coriolis terms and the cross-channel velocities in the momentum equation. Equations (2.6) and (2.7) are valid when both Ke and δ are much smaller than unity.

For clarity, the tildes will be dropped from now on.

2.2.3 *Laterally and Depth Averaged Equations*

The one dimensional equations can now be obtained by integrating (2.6) and (2.7) from the bottom to the free surface. The kinematic boundary conditions at the bottom and free surface are, respectively:

$$u_b \frac{\partial h}{\partial x} + w_b = 0 \tag{2.10}$$

and

$$-\frac{\partial \eta}{\partial t} - u_s \frac{\partial \eta}{\partial x} + w_s = 0 \tag{2.11}$$

Using Equations (2.10) and (2.11), as well as the Leibnitz rule, the continuity equation becomes:

$$L \equiv \frac{\partial}{\partial x} HB\bar{u} + B\frac{\partial \eta}{\partial t} = 0 \tag{2.12}$$

where $H=h+\eta$ is the total depth and an overbar indicates a depth average. The width, B, was assumed to be depth-independent. The momentum equation becomes, in conservative form:

$$M_c \equiv \frac{\partial}{\partial t} HB\bar{u} + \frac{\partial}{\partial x} HB\overline{uu} + gBH\frac{\partial \eta}{\partial x} + \frac{gB}{\rho_0}\int_{-h}^{\eta}\left(\int_{z}^{\eta}\frac{\partial \rho}{\partial x}dz\right)dz - \frac{B\tau_b}{\rho_0} - \frac{B\tau_w}{\rho_0} - H\frac{\partial}{\partial x}(BA_h\frac{\partial \bar{u}}{\partial x}) = 0 \tag{2.13}$$

where τ_b and τ_w represent the friction and wind stresses, respectively.

2.3 Numerical Model

2.3.1 External Mode

The elevation solution

The Generalized Wave Continuity Equation, GWCE, (Kinnmark, 1985) is obtained by combining Equations (2.12) and (2.13) as:

$$W \equiv \frac{\partial L}{\partial t} - \frac{\partial M_c}{\partial x} + GL = 0 \tag{2.14}$$

where G [s^{-1}] is an arbitrary constant. The result is:

$$W \equiv B\frac{\partial^2 \eta}{\partial t^2} + BG\frac{\partial \eta}{\partial t} -$$

$$\frac{\partial}{\partial x}\left(\frac{\partial}{\partial x}(\overline{uu}BH) + gBH\frac{\partial \eta}{\partial x} + \frac{gB}{\rho_0}\int_{-h}^{\eta}\left(\int_{z}^{\eta}\frac{\partial \rho}{\partial x}dz\right)dz - GBH\bar{u} - \frac{B\tau_b}{\rho_0} - \frac{B\tau_w}{\rho_0} - H\frac{\partial}{\partial x}(BA_h\frac{\partial \bar{u}}{\partial x})\right) = 0 \tag{2.15}$$

Following the approach of Kolar and Gray (1990), the continuity equation is used to transform the diffusion term as:

$$H\frac{\partial}{\partial x}(BA_h\frac{\partial \bar{u}}{\partial x}) = -\frac{\partial}{\partial x}(A_hB\frac{\partial \eta}{\partial t}) - \frac{\partial}{\partial x}(A_h\bar{u})\frac{\partial}{\partial x}(HB) - A_h\bar{u}\frac{\partial^2}{\partial x^2}(HB) - A_hB\frac{\partial H}{\partial x}\frac{\partial \bar{u}}{\partial x} \quad (2.16)$$

The bottom stress can be parametrized as a linear function of the depth-averaged velocity:

$$\frac{\tau_b}{\rho_0} = -\lambda H\bar{u} \quad (2.17)$$

where λ is the linear friction coefficient, or the more conventional quadratic formulation can be used:

$$\frac{\tau_b}{\rho_0} = -C_f|\bar{u}|\bar{u} \quad (2.18)$$

When the model is run in 1D mode, a Manning-type formulation is used for C_f:

$$C_f = \frac{n^2 g}{H^{1/3}} \quad (2.19)$$

where n is the Manning coefficient ($[m^{-1/3}s]$).

When the full 2Dv model is being applied, τ_b is parametrized directly in terms of the bottom velocity. The bottom stress is computed in the internal mode and kept constant while solving the external steps. Friction is then computed as:

$$\frac{\tau_b}{\rho_0} = -C_D|u_b|u_b \quad (2.20)$$

where C_D is a friction coefficient, and u_b the bottom velocity.

The wind stress is assumed to be constant in time and space. It is computed as:

$$\tau_w = C_d\rho_a|W|W \quad (2.21)$$

where ρ_a is the air density, W is the wind velocity 10 meters above the water surface *(m/s)* and C_d is a drag coefficient given by (Amorocho and DeVries, 1980):

$$C_d = 0.0015\,(1 + exp\,(\frac{12.5 - W}{1.56}))^{-1} + 0.00104 \tag{2.22}$$

Baroclinic pressure is treated diagnostically and linearized:

$$\int_{-h}^{\eta}\left(\int_{z}^{\eta}\frac{\partial\rho}{\partial x}dz\right)dz \approx \int_{-h}^{0}\left(\int_{z}^{0}\frac{\partial\rho}{\partial x}dz\right)dz \tag{2.23}$$

A Galerkin finite element (FE) technique with linear elements is used for the space discretization. The weighted residual statement (weak formulation) is:

$$\begin{gathered}
\langle B\left(\frac{\partial^2\eta}{\partial t^2} + G\frac{\partial\eta}{\partial t}\right)\phi_i\rangle + \\
\langle\left(\frac{\partial}{\partial x}\overline{uu}BH + gBH\frac{\partial\eta}{\partial x} + \frac{gB}{\rho_0}\int_{-h}^{\eta}\left(\int_{z}^{\eta}\frac{\partial\rho}{\partial x}dz\right)dz - GBH\bar{u} - \frac{B\,(\tau_b + \tau_w)}{\rho_0} + \frac{\partial}{\partial x}(A_h B\frac{\partial\eta}{\partial t})\right)\frac{\partial\phi_i}{\partial x}\rangle + \\
\langle\frac{\partial}{\partial x}(A_h\bar{u})\frac{\partial}{\partial x}(HB) + A_h\bar{u}\frac{\partial^2}{\partial x^2}(HB) + A_h B\frac{\partial H}{\partial x}\frac{\partial\bar{u}}{\partial x}\Bigg)\frac{\partial\phi_i}{\partial x}\rangle = \\
-(\frac{\partial}{\partial t}BH\bar{u} + GBH\hat{u})\Big|_0^L
\end{gathered} \tag{2.24}$$

where L is the length of the domain, and <> represents an integration over the horizontal domain. The momentum equation was used to simplify the boundary terms, displaying the hydrodynamic transport $HB\bar{u}$ as a natural boundary condition.

The term $\overline{uu}$ is written as:

$$\overline{uu} = \bar{u}\cdot\bar{u} + I \tag{2.25}$$

where I is defined as:

$$\begin{gathered}
I = \frac{1}{H}\int_{-h}^{\eta}(u')^2 dz \\
u' = u - \bar{u}
\end{gathered} \tag{2.26}$$

When the full 2D model is running, the value of I is computed in the internal mode and held constant until the next internal step. When only the external mode is being used, the horizontal dispersion is parametrized as:

$$\frac{\partial}{\partial x}(IBH) \approx -A_h B \frac{\partial H}{\partial x}\frac{\partial \bar{u}}{\partial x} \tag{2.27}$$

In order to obtain a stationary matrix while treating part of the gravitic term implicitly, this term is split in two. The linear part is treated implicitly, and the non-linear part is treated explicitly.

Applying the Galerkin method to the weighted residual statement (2.24):

$$\begin{gathered}\sum_{j=1}^{N}\left[\langle B\phi_i,\phi_j\rangle\left(\frac{\partial^2\eta_j}{\partial t^2}+G\frac{\partial\eta_j}{\partial t}\right)+\langle gBh\frac{\partial\phi_i}{\partial x}\frac{\partial\phi_j}{\partial x}\rangle\eta_j+\langle\frac{\partial}{\partial x}(A_hB\phi_j)\frac{\partial\phi_i}{\partial x}\rangle\frac{\partial\eta_j}{\partial t}\right]= \\ -\langle\left(\frac{\partial}{\partial x}(\bar{u}\cdot\bar{u}+I)\,BH+gB\eta\frac{\partial\eta}{\partial x}+\frac{gB}{\rho_0}\int_{-h}^{\eta}\left(\int_{z}^{\eta}\frac{\partial\rho}{\partial x}dz\right)dz+(\lambda-G)\,BH\bar{u}-\frac{B\tau_w}{\rho_0}\right)\frac{\partial\phi_i}{\partial x}\rangle- \\ \langle\left(\frac{\partial}{\partial x}(A_h\bar{u})\frac{\partial}{\partial x}(HB)+A_h\bar{u}\frac{\partial^2}{\partial x^2}(HB)+A_hB\frac{\partial H}{\partial x}\frac{\partial\bar{u}}{\partial x}\right)\frac{\partial\phi_i}{\partial x}\rangle-\left(\frac{\partial}{\partial t}BH\bar{u}+GBH\bar{u}\right)\Big|_0^L\end{gathered} \tag{2.28}$$

where the N is the total number of horizontal nodes in the domain. Space dependent variables are assumed linear within each element, except the longitudinal dispersion that uses an element based formulation. The integrals are evaluated either analytically or with a three point Gauss Quadrature. A three time level semi-implicit scheme is used for the time discretization. All the terms are centered at n, while solving for $n+1$:

$$\begin{gathered}B\frac{\eta^{n+1}-2\eta^{n}+\eta^{n-1}}{\Delta t^2}+GB\frac{\eta^{n+1}-\eta^{n-1}}{2\Delta t}-\frac{\partial^2}{\partial x^2}\left(A_hB\frac{\partial\eta}{\partial t}\right) \\ gBh\left(\frac{\theta}{2}\left(\frac{\partial}{\partial x}\eta^{n+1}+\frac{\partial}{\partial x}\eta^{n-1}\right)+(1-\theta)\frac{\partial}{\partial x}\eta^{n}\right)=R^n\end{gathered} \tag{2.29}$$

where R represents the non-linear and boundary terms, and $\theta \in [0,1]$ is a time-discretization coefficient.

The depth-averaged velocity solution

The depth-averaged velocity is obtained from the horizontal momentum equation, with known gravitic forcing at time $n+1$. The equation reads:

$$\frac{\partial\bar{u}}{\partial t}+\bar{u}\frac{\partial\bar{u}}{\partial x}+\frac{\partial I}{\partial x}+\frac{I}{HB}\frac{\partial}{\partial x}HB+g\frac{\partial\eta}{\partial x}+\frac{g}{H\rho_0}\int_{-h}^{0}\left(\int_{z}^{0}\frac{\partial\rho}{\partial x}dz\right)dz-\frac{\tau_b}{H\rho_0}-\frac{\tau_w}{H\rho_0}$$
$$-\frac{1}{B}\frac{\partial}{\partial x}\left(BA_h\frac{\partial\bar{u}}{\partial x}\right)=0 \qquad (2.30)$$

Equation (2.30) is discretized in space with a Galerkin FE method, with a weak formulation applied to the diffusion term. The weighted residual statement reads:

$$\sum_{j=1}^{N}\left[\langle\phi_i\phi_j\rangle\frac{\partial\bar{u}_j}{\partial t}\right]=\langle Q\frac{\partial}{\partial x}\frac{\phi_i}{B}\rangle+\langle R\phi_i\rangle+\langle S\phi_i\rangle+\Gamma \qquad (2.31)$$

where Q, R, S and Γ are defined as:

$$Q=-BA_h\frac{\partial\bar{u}}{\partial x}$$
$$R=-g\frac{\partial\eta}{\partial x}+\frac{\tau_w}{H\rho_0}$$
$$S=-\left(\bar{u}\frac{\partial\bar{u}}{\partial x}+\frac{\partial I}{\partial x}+\frac{I}{HB}\frac{\partial}{\partial x}HB-\frac{\tau_b}{H\rho_0}+\frac{g}{H\rho_0}\int_{-h}^{0}\left(\int_{z}^{0}\frac{\partial\rho}{\partial x}dz\right)dz\right) \qquad (2.32)$$
$$\Gamma=A_h\frac{\partial\bar{u}}{\partial x}\bigg|_0^L$$

A semi-implicit scheme is used for the time discretization. All terms are centered at $n+1/2$, except Q and S which are lagged behind at n. When friction is linearized, the bottom stress term is also centered at $n+1/2$. The time-discretized equation reads:

$$\frac{\bar{u}^{n+1}-\bar{u}^{n}}{\Delta t}=Q^n+\frac{R^{n+1}+R^n}{2}+S^n+\frac{\Gamma^n+\Gamma^{n+1}}{2} \qquad (2.33)$$

2.3.2 Boundary conditions

Three types of boundary conditions are available in the model: specified elevation, specified flux or transmissive boundary. In the first two cases the conditions can be specified either as a time series or as a sum of sinusoidal functions.

When elevation is specified, the corresponding row in the GWCE matrix is set to zero, except for the diagonal term which is replaced by a constant. The corresponding term in the vector is set to the specified elevation multiplied by this constant. This constant, used to ensure the good conditioning of the matrix, is such that the absolute value of the diagonal term in the matrix is at least as large as the non-diagonal terms in the same row and column. The depth-averaged velocity is determined by solving the GCWE (rather than the momentum equation) for the flux. Theoretical and numerical studies (Lynch, 1985, Kolar et al., 1992) suggest that using some form of the continuity equation at the boundary improves mass preservation.

When the total flux is specified, it is enforced as a natural boundary condition in the GCWE (see equation (2.28)), and as an essential boundary for the momentum equation.

Finally, when transmissive boundaries are specified, the elevation is computed with a form of the Sommerfeld radiation boundary condition (Sommerfeld, 1949):

$$\frac{\partial \eta}{\partial t} \pm c\frac{\partial \eta}{\partial x} = 0 \tag{2.34}$$

where $c = \sqrt{gH}$ is the celerity. The time derivative is centered at $n+1/2$ while celerity term is taken at n. The velocity is then computed with the GCWE, as before.

2.3.3 Internal Mode

Coordinate transformation

One of the problems associated with 3D and 2Dv models is the fact that the free surface constitutes a moving boundary, and therefore the physical domain changes in time. The most common approach is to map the vertical domain $z \in [-h, \eta]$ into a fixed interval $\sigma \in [a, b]$. Several types of transformations have been used (see Davies, 1991), the linear being the most common (e.g. Blumberg and Mellor, 1987).

Sigma is defined as:

$$\sigma = \frac{z-\eta}{H} \tag{2.35}$$

where $\sigma \in [-1,0]$, η is the free surface elevation, and H the total depth. The derivatives in the coordinate systems (x,z,t) and (s,σ,τ) are related by:

$$\frac{\partial}{\partial x} \equiv \frac{\partial}{\partial s} - \left(\frac{\sigma}{H}\frac{\partial H}{\partial s} + \frac{1}{H}\frac{\partial \eta}{\partial s}\right)\frac{\partial}{\partial \sigma} \tag{2.36}$$

$$\frac{\partial}{\partial z} \equiv \frac{1}{H}\frac{\partial}{\partial \sigma} \tag{2.37}$$

$$\frac{\partial}{\partial t} \equiv \frac{\partial}{\partial \tau} - \frac{\sigma+1}{H}\frac{\partial \eta}{\partial \tau}\frac{\partial}{\partial \sigma} \tag{2.38}$$

For depth-independent quantities,

$$\begin{aligned} \frac{\partial}{\partial x} &\equiv \frac{\partial}{\partial s} \\ \frac{\partial}{\partial t} &\equiv \frac{\partial}{\partial \tau} \end{aligned} \tag{2.39}$$

Evaluation of terms involving horizontal gradients

Neglecting gradients of atmospheric pressure, the horizontal Reynolds equation (2.7) can be rewritten as:

$$\frac{\partial}{\partial t}u' + \frac{\partial \bar{u}}{\partial t} + Ad + g\frac{\partial \eta}{\partial x} + \frac{g}{\rho_0}\int_z^0 \frac{\partial \rho}{\partial x}dz - \frac{\partial}{\partial z}\left(A_v\frac{\partial}{\partial z}u'\right) - Diff = 0 \tag{2.40}$$

or, in sigma coordinates:

$$\frac{\partial}{\partial \tau}u' + \frac{\partial \bar{u}}{\partial \tau} + Ad - \frac{\sigma+1}{H}\frac{\partial \eta}{\partial \tau}\frac{\partial}{\partial \sigma}u' + g\frac{\partial \eta}{\partial x} + \frac{gh}{\rho_0}\int_\sigma^0 \frac{\partial \rho}{\partial x}d\sigma - \frac{1}{BH^2}\frac{\partial}{\partial \sigma}\left(BA_v\frac{\partial}{\partial \sigma}u'\right) - Diff = 0 \tag{2.41}$$

where the horizontal velocity u was split as the sum of a depth-averaged part, $\bar{u}$, and a deviation from this mean, u'. Consistent with the external mode, we assume $\eta \ll h$ in the baroclinic pressure term. *Ad* and *Diff* represent the advective acceleration and the horizontal diffusion, respectively.

Several formulations have been implemented to deal with terms involving horizontal gradients of depth-dependent quantities. Formulation 1 assumes the horizontal gradient of u' is much smaller than that of $\bar{u}$. *Ad* and *Diff* thus become:

$$\begin{gathered} Ad \approx \bar{u}\frac{\partial \bar{u}}{\partial x} + u'\frac{\partial \bar{u}}{\partial x} - u\left(\frac{\sigma}{H}\frac{\partial H}{\partial x} + \frac{1}{H}\frac{\partial \eta}{\partial x}\right)\frac{\partial}{\partial \sigma}u' + \frac{w}{H}\frac{\partial}{\partial \sigma}u' \\ Diff \approx \frac{1}{B}\frac{\partial}{\partial x}\left(BA_h\frac{\partial \bar{u}}{\partial x}\right) \end{gathered} \tag{2.42}$$

In formulation 2, the velocity is written as the product of the depth-averaged velocity and a shape function. The shape function is then assumed to change slowly in space compared with the depth-averaged velocity. This shape function is defined as:

$$X_v(z) = \frac{u'(x,z)}{\bar{u}(x)} \tag{2.43}$$

The advective terms become:

$$Ad \approx \bar{u}\frac{\partial \bar{u}}{\partial x} + u'\frac{\partial \bar{u}}{\partial x} + \frac{uu'}{U}\frac{\partial \bar{u}}{\partial x} - u\left(\frac{\sigma}{H}\frac{\partial H}{\partial x} + \frac{1}{H}\frac{\partial \eta}{\partial x}\right)\frac{\partial}{\partial \sigma}u' + \frac{w}{H}\frac{\partial}{\partial \sigma}u' \tag{2.44}$$

where U is defined as:

$$U = \begin{cases} \bar{u} & |\bar{u}| \geq u_l \\ \pm u_l & |\bar{u}| < u_l \end{cases} \tag{2.45}$$

and u_l is a limit value taken as 0.01 m/s. The use of U rather than $\bar{u}$ in (2.44) is needed to avoid a division by zero. For simplicity, the horizontal diffusion term keeps the same form as in formulation 1 (Equation (2.42)).

Formulation 3 corresponds to the traditional sigma transformation. *Ad* and *Diff* are defined as:

$$Ad = \bar{u}\frac{\partial \bar{u}}{\partial x} + u'\frac{\partial \bar{u}}{\partial x} + u\frac{\partial}{\partial s}u' - \frac{u}{H}\left(\sigma\frac{\partial H}{\partial x} + \frac{\partial \eta}{\partial x}\right)\frac{\partial}{\partial \sigma}u' + \frac{w}{H}\frac{\partial}{\partial \sigma}u'$$
$$Diff \approx \frac{1}{BH}\frac{\partial}{\partial s}\left(BHA_h\frac{\partial u}{\partial s}\right) \tag{2.46}$$

The diffusion term was simplified, following Blumberg and Mellor (1985). The necessary values of u' at neighboring verticals can either be taken at specific nodes, if DWSC are used, or obtained by interpolation when LSC are used.

Finally, formulation 4 follows Laible (1992), and computes the horizontal gradients directly in the cartesian coordinate system. *Ad* and *Diff* are thus given by:

$$Ad = \left(\bar{u}\frac{\partial \bar{u}}{\partial x} + u'\frac{\partial \bar{u}}{\partial x} + u\frac{\partial}{\partial x}u'\right) + \frac{w}{H}\frac{\partial}{\partial \sigma}u'$$
$$Diff = \frac{1}{B}\frac{\partial}{\partial x}\left(BA_h\frac{\partial u}{\partial x}\right) \tag{2.47}$$

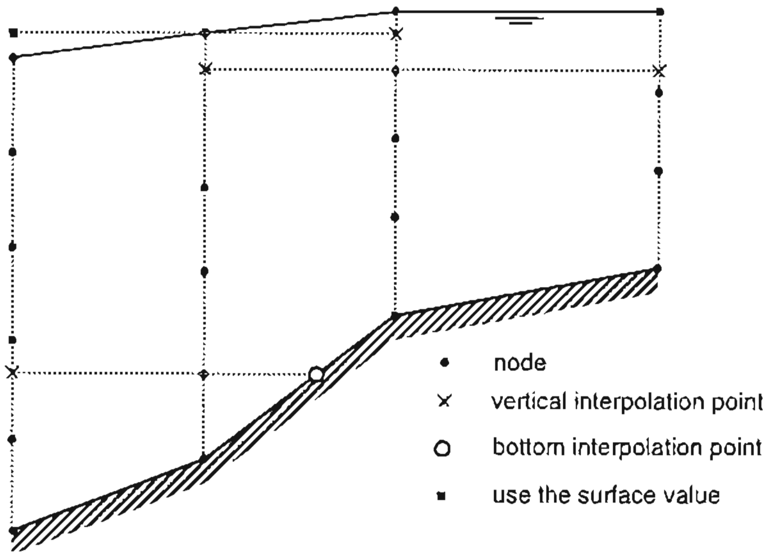

Figure 2.2 Interpolation of u' and ρ at neighboring verticals for the evaluation of gradients in cartesian coordinates.

The necessary values of u' at neighboring verticals are obtained by interpolation (Figure 2.2). When only two values of u' are available at the bottom node, horizontal diffusion is neglected at that point.

The baroclinic pressure term can be computed using formulations 3 or 4.

The horizontal velocity solution

The momentum equation is discretized in space with 1D linear finite elements, leading to a tridiagonal matrix which is solved with the Thomas algorithm. A weak formulation is used for the vertical diffusion to allow the representation of second derivatives.

The terms known from the external mode (e.g., gravitic forcing, mean advection) are centered in time. The term $u'\frac{\partial \bar{u}}{\partial x}$ is treated with an alpha method. The vertical diffusion term is treated implicitly, since a semi-implicit formulation led to $2\Delta t$ oscillations in some cases. All other terms are fully explicit.

Once the solution for u' is found, the closure error (the integral of u' from the bottom to the free surface) is evaluated and subtracted from u'. This procedure aims at avoiding imbalances between the external and internal mode solutions (Blumberg and Mellor, 1987).

Initial and boundary conditions

In order to minimize the initial transients when the internal mode is activated, the internal mode velocities are initialized with an analytical solution for permanent flow (see below).

Bottom and surface stresses are enforced as natural boundary conditions:

$$\left.\frac{A_v}{H^2}\frac{\partial}{\partial\sigma}u'\right|_b = \frac{\tau_b}{H\rho_0} \qquad \left.\frac{A_v}{H^2}\frac{\partial}{\partial\sigma}u'\right|_s = \frac{\tau_w}{H\rho_0} \tag{2.48}$$

A quadratic formulation is used for the bottom stress:

$$\tau_b = -\rho_0 C_D |u_b| u_b \tag{2.49}$$

where C_D is a dimensionless coefficient. The time discretization is particularly important to avoid $2\Delta t$ oscillations when the grid is very refined (Davies and Aldridge, 1992). In our experience, the following semi-implicit formulation appears to have good stability properties:

$$\frac{A_v}{H^2}\frac{\partial}{\partial\sigma}u'\Bigg|_b^{n+\frac{1}{2}} \approx \frac{C_D\left|\bar{u}^{n+\frac{1}{2}} + (u')^n\right|\left(\bar{u}^{n+\frac{1}{2}} + (u')^{n+1}\right)}{H^{n+\frac{1}{2}}} \tag{2.50}$$

The Vertical Velocity Solution

The vertical velocity is obtained, for formulations 1 through 4, by integrating the continuity equation (2.6) from the bottom up. The velocity at the bottom is first determined from the kinematic boundary condition:

$$w_b = -u_b\frac{\partial h}{\partial x} \tag{2.51}$$

The velocities at the others nodes are then computed as:

- formulation 1:

$$\begin{aligned} w_{i+1} = w_i - H\Delta\sigma_i\left(\frac{\partial\bar{u}}{\partial x} + \frac{1}{B}\frac{\partial B}{\partial x}\left(\bar{u} + \frac{u'_{i+1}+u'_i}{2}\right)\right) + \\ (u'_{i+1} - u'_i)\left(\frac{\partial\eta}{\partial x} + \frac{\partial H}{\partial x}\frac{\sigma_{i+1}+\sigma_i}{2}\right) \end{aligned} \tag{2.52}$$

- formulation 2:

$$\begin{aligned} w_{i+1} = w_i - H\Delta\sigma_i\left(\frac{\partial\bar{u}}{\partial x} + \frac{1}{B}\frac{\partial B}{\partial x}\left(\bar{u} + \frac{u'_{i+1}+u'_i}{2}\right)\right) + \\ (u'_{i+1} - u'_i)\left(\frac{\partial\eta}{\partial x} + \frac{\partial H}{\partial x}\frac{\sigma_{i+1}+\sigma_i}{2}\right) - \frac{H}{U}\left(\frac{u'_{i+1}+u'_i}{2}\right)\Delta\sigma_i\frac{\partial\bar{u}}{\partial x} \end{aligned} \tag{2.53}$$

- formulation 3:

$$w_{i+1} = w_i - H\Delta\sigma_i\left(\frac{\partial\bar{u}}{\partial x} + \frac{1}{B}\frac{\partial B}{\partial x}\left(\bar{u} + \frac{u'_{i+1} + u'_i}{2}\right)\right) + (u'_{i+1} - u'_i)\left(\frac{\partial\eta}{\partial x} + \frac{\partial H}{\partial x}\frac{\sigma_{i+1} + \sigma_i}{2}\right) - H\int_{\sigma_i}^{\sigma_{i+1}}\frac{\partial}{\partial r}u'd\sigma \tag{2.54}$$

- formulation 4:

$$w_{i+1} = w_i - H\Delta\sigma_i\left(\frac{\partial\bar{u}}{\partial x} + \frac{1}{B}\frac{\partial B}{\partial x}\left(\bar{u} + \frac{u'_{i+1} + u'_i}{2}\right)\right) - H\int_{\sigma_i}^{\sigma_{i+1}}\frac{\partial}{\partial x}u'd\sigma \tag{2.55}$$

As with the computation of u', a closure error ε is computed in the end:

$$\varepsilon = w_s - \frac{\partial\eta}{\partial t} - u_s\frac{\partial\eta}{\partial x} \tag{2.56}$$

The vertical velocity is then corrected to obey the boundary conditions both at the bottom and at the surface:

$$w_c(\sigma) = w(\sigma) - (\sigma + 1)\varepsilon \tag{2.57}$$

This method is similar to the method of Lynch and Naimie (1993) which solves the vertical derivative of the continuity equation.

Analytical solution for internal mode initialization

For simplicity, the solution is derived for the velocity shape X_v (2.43). For an uniform flow, and assuming a constant eddy viscosity coefficient, the 2D horizontal momentum equation reduces to:

$$\frac{\partial^2 X_v}{\partial\sigma^2} = \frac{H^2 g}{\bar{u}A_v}\frac{\partial\eta}{\partial x} \tag{2.58}$$

X_v is therefore a quadratic function of sigma:

$$X_v = \frac{1}{2}\left(\frac{H^2 g}{\bar{u}A_v}\frac{\partial\eta}{\partial x}\right)\sigma^2 + b\sigma + c \tag{2.59}$$

where b and c are determined by the boundary conditions. We consider here a quadratic slip boundary condition at the bottom, and no stress at the surface. The equations are:

$$\left.\frac{\partial}{\partial\sigma}u'\right|_{\sigma=0} = 0$$
$$\left.\frac{\partial}{\partial\sigma}u'\right|_{\sigma=-1} = d \tag{2.60}$$

Using also the fact that the integral of X_v from the bottom to the free surface is zero, we get:

$$X_v = \frac{d}{2}\left(\frac{1}{3}-\sigma^2\right) \tag{2.61}$$

where:

$$d = -\frac{H^2 g}{A_v \bar{u}}\frac{\partial\eta}{\partial x} \tag{2.62}$$

Using the boundary condition at the bottom, d can be expressed as a function of $\bar{u}$ alone:

$$d = \frac{\partial X_v}{\partial\sigma}(-1) = \frac{C_D|1+X_{vb}|\,(1+X_{vb})}{A_v}|\bar{u}|H = \frac{C_D\left|1-\frac{d}{3}\right|\left(1-\frac{d}{3}\right)}{A_v}|\bar{u}|H \tag{2.63}$$

Solving for d, we get:

$$d = \frac{6\frac{|\bar{u}|}{u_s}+9-9\sqrt{1+\frac{4}{3}\frac{|\bar{u}|}{u_s}}}{2\frac{|\bar{u}|}{u_s}} \tag{2.64}$$

where:

$$u_s = \frac{A_v}{C_D H} \tag{2.65}$$

Recovering u' from the definition of X_v, we get:

$$u' = \frac{\bar{u}d}{2}\left(\frac{1}{3} - \sigma^2\right) \tag{2.66}$$

2.4 Numerical Properties

2.4.1 The Generalized Wave-Continuity Equation

Early hydrodynamic finite element models, based on the primitive equations, were plagued by severe spurious oscillations. Damping these oscillations, with either unrealistic values of the diffusion coefficient or dissipative numerical schemes, also damped the physical waves, thus compromising the accuracy of the solution. It was the introduction of the Continuity Wave equation (Lynch, 1978), and later the Generalized Continuity Wave Equation (Kinnmark, 1985), that established the use of finite element models as reliable alternatives to their finite difference counterparts. Formal analysis shows that this method propagates and damps the $2\Delta x$ waves while being highly accurate for the longer waves (e.g., Kinmark, 1985). From a computational perspective, the GCWE also has three major advantages relative to the primitive equations. First, the solutions of the elevation and the velocities are naturally uncoupled, thus the equations can be solved sequentially. Second, the GCWE mass matrix is time-independent, and therefore only needs to be inverted once. Finally, when nodal quadrature is used, the momentum equation mass matrix is diagonal and its inversion is trivial. The GCWE formulation is therefore accurate, stable and efficient as compared to other methods to solve the shallow water equations.

However, the GCWE formulation also has two major problems. First, the solutions can be very sensitive to the choice of GCWE parameter - G (e.g., Myers and Baptista, 1995). This parameter has no physical meaning and there is no consensus on how to define its optimal value, other than it should be loosely related to the linear friction coefficient. In general, increasing the weight of the continuity equation in the GCWE makes the equations more primitive, thus improving mass conservation but also increasing $2\Delta x$ oscillations. Finding the right balance between a pure wave equation and the primitive continuity equation has proved a difficult task although both theoretical (Kinnmark, 1985) and numerical (e.g., Remédio, 1992, Myers and Baptista, 1995) studies have been done. A commonly used rule of thumb (e.g., Luettich et al., 1991) is to set G similar to the largest equivalent linear friction coefficient across the domain. Kolar et al. (1994) proposed using dispersion analysis to define the largest value of G that, for given values of depth and horizontal resolution, will not lead to the aliasing of tidal frequencies. This approach will be further discussed in Chapter 5.

The second problem of the GCWE is its potential for mass conservation problems. Consider the 2D versions of the GCWE (2.14) and the non-conservative momentum equation (2.30):

$$W \equiv \frac{\partial L}{\partial t} - \nabla M_c + GL = 0 \tag{2.67}$$

$$M \equiv \frac{M_c - \vec{u}L}{H} = 0 \tag{2.68}$$

Kinnmark (1985) showed that combining (2.68) and (2.67) gives:

$$L(s) = L(s|_{t=0})\, exp\left(-\int_0^s (G - \nabla \vec{u})\, ds\right) \tag{2.69}$$

where s is a trajectory, given by:

$$\begin{aligned} \frac{dx}{dt}(s) &= -u(x(s), y(s), s) \\ \frac{dy}{dt}(s) &= -v(x(s), y(s), s) \end{aligned} \tag{2.70}$$

Equation (2.70) shows that mass errors introduced in the solution at some point in space and time will propagate and dissipate as the simulation progresses, as long as:

$$G - \nabla \vec{u} > 0 \tag{2.71}$$

Neglecting the velocity gradient, the mass error will tend to zero in a time scale of $1/G$. Since G is typically of the order of 10^{-3}-$10^{-4}\ s^{-1}$, this time scale is large compared to the time step, and errors can accumulate.

Approaches to improve mass conservation can therefore be classified in two categories: reduction of the error generation, and improvement of the error dissipation. Error generation can have different sources, thus requiring different treatments. Two local sources of errors have been identified. Lynch (1985) observed localized mass unbalances at boundaries where the elevations are imposed, and found that this was due to the continuity wave equation being discarded at these nodes. He proposed discarding the normal component of the momentum equation instead, thus enforcing continuity at the boundary. His work was confirmed later by Kolar et al. (1992) who further increased the weight of the continuity equation at the boundary. We also found that errors in the imposition of initial conditions could seriously compromise the accuracy of the solution in tsunami simulations. This problem can be avoided either by imposing tsunami initial conditions at both initial time steps, or by including a bottom deformation term in the equations (e.g., Myers and Baptista, 1995).

However, mass errors are not always generated at precise points in space or time. As an example, Figure 2.3 illustrates the presence of mass errors in a permanent flow over a schematic continental slope. The errors develop all along the continental slope, and are clearly not related to the initial or boundary conditions. For errors such as this one, the only available option is to improve error dissipation. Kolar et al. (1994) proposed casting the advective terms in the GCWE in their non-conservative form. This is equivalent to redefining the GCWE as:

$$W \equiv \frac{\partial L}{\partial t} - \nabla\ (HM) + GL = 0 \tag{2.72}$$

Combining (2.72) with (2.68) now leads to:

$$L\,(x, y, t) \ = \ L\,(x, y, 0)\, exp\,(-Gt) \tag{2.73}$$

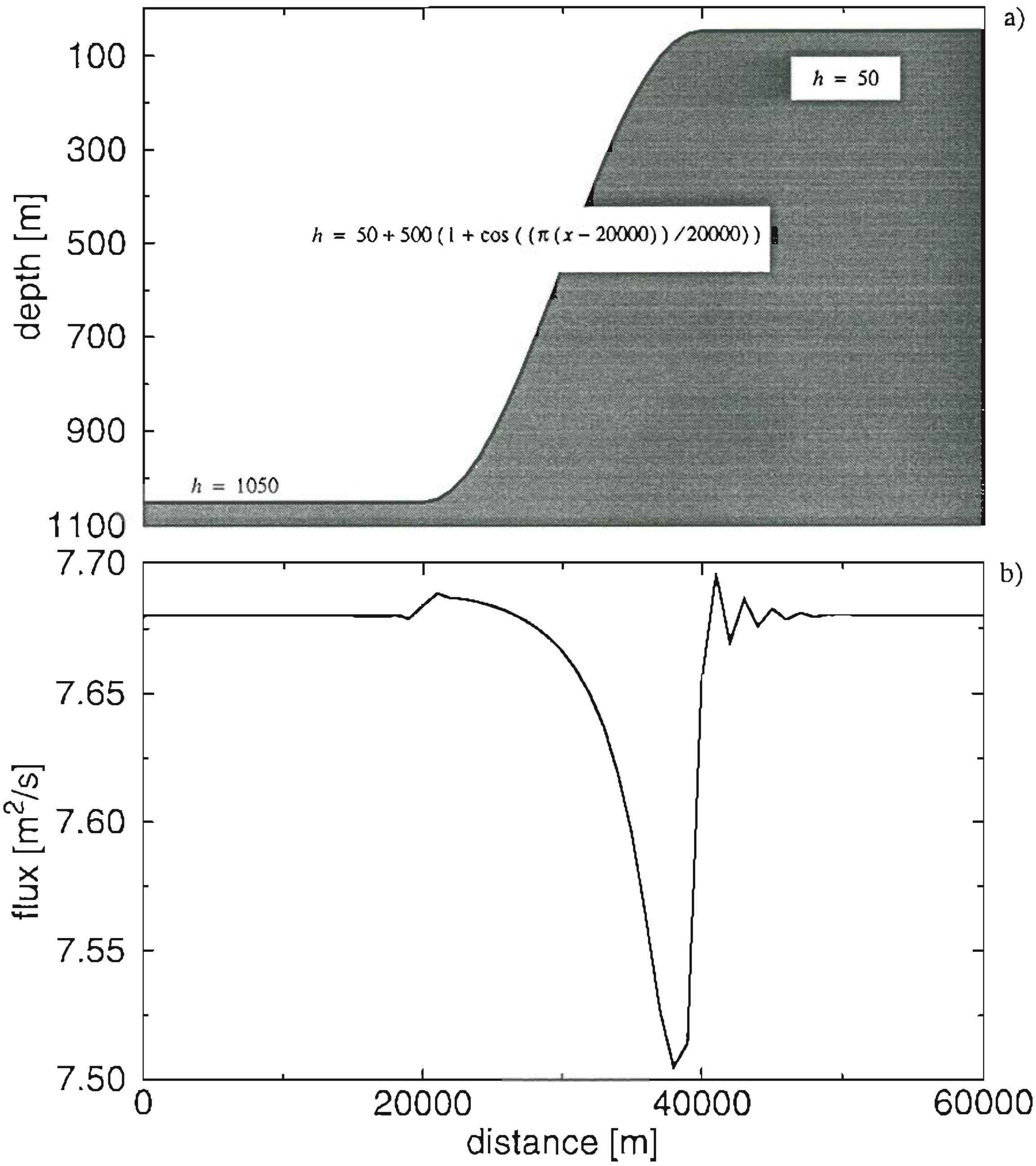

Figure 2.3 Example of mass errors generation inside the domain. a) Bathymetry; b) flux per unit width. The flow is forced by a constant setup of 0.1 m at the ocean boundary. At steady state, the flux should be constant for mass to be conserved. Friction was linearized and we set $G=\lambda=0.00025\ \mathrm{s}^{-1}$.

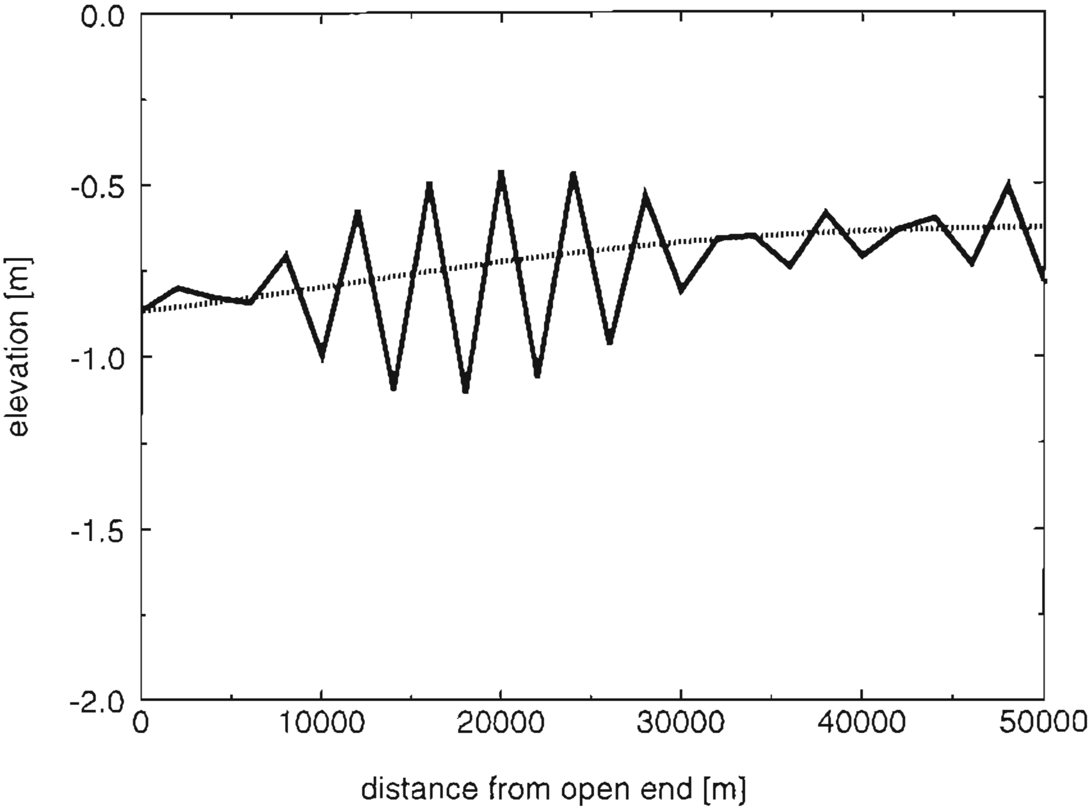

Figure 2.4 Illustration of the different stability properties of the two GCWE formulations. Elevations along the channel at t = 521640 s are shown for the original formulation (equation (2.67) - dotted line), and the modified formulation (equation (2.72) - solid line). The parameters are given in the text.

When velocity gradients are non-negligible compared to G, this new formulation should therefore dissipate mass errors faster than the standard form of the GCWE. Unfortunately our experience indicates that (2.72) is less stable than (2.67), which may be due to part of the advective term in the new formulation not being centered in time. To illustrate the different behavior of the two approaches we ran a simple case of a one-dimensional wave propagating in a flat channel. The parameters are:

• channel length:	50,000 m;
• channel depth:	5 m;
• eddy viscosity:	0 m^2/s;

• time step:	74.52 s;
• grid spacing:	2,000 m;
• boundary conditions:	h(0,t) = sin(2πt/12.42 h) m;
	$\overline{u}$(50,000,t) = 0 m/s;
• initial conditions:	cold start;
• bottom friction:	λ=0.0001s^{-1} (linear);
• GCWE parameter:	G=λ.

The model based on the original formulation (equation (2.67)) ran for 24 tidal cycles without any signs of instabilities, while the model based on (2.72) became unstable after about 12 tidal cycles (Figure 2.4). $RITA_{2v}$ is therefore based on (2.67).

2.4.2 The Localized Sigma Coordinates

The development of the Localized Sigma Coordinates (LSC) was motivated by the rigidity of the traditional, domain-wide, sigma coordinates (DWSC). In DWSC models nodes are defined at the intersection between constant sigma planes and vertical lines defined by the position of horizontal nodes. As a result, all verticals must have the same number of nodes, and with the same distribution. This rigidity is clearly undesirable. As an example, consider a wind-driven flow in a domain including both shallow and deep areas. In the deep regions, the flow will be restricted to the surface layer, where sharp vertical gradients of velocity will occur; in shallow regions, the surface boundary layer will occupy the whole water column, and gradients will be smeared by higher levels of turbulence. Optimal discretizations will therefore vary strongly with the horizontal position: in deep waters a very fine resolution will be needed near the surface, whereas in shallow waters a more uniform grid will be appropriate. Clearly, LSC will be at an advantage to simulate this type of flow. Also, LSC can improve accuracy relative the to DWSC for simple density driven flows (Fortunato and Baptista, 1994a) and for tidal flows (Fortunato and Baptista, 1995).

Unfortunately, LSC also have their drawbacks: they increase the CPU time and memory requirements for the simulation (on a node per node basis) and are only conditionally consistent. The conditional consistency arises from the truncation errors introduced by the interpolation needed to compute horizontal gradients (Fortunato and Baptista, 1994a). Referring to the stencil in Figure 2.5 and assuming a rigid lid approximation, the truncation error for (2.36) reads:

$$\begin{aligned} E = {} & \frac{\Delta_1}{4\Delta x}\frac{\partial^2}{\partial\sigma^2} + \frac{(\Delta x)^2}{6}\frac{\partial^3}{\partial s^3} + \frac{\Delta_2}{4}\frac{\partial^3}{\partial s\partial\sigma^2} + \\ & \left(\frac{\Delta_3}{12\Delta x} - \frac{\sigma(\Delta\sigma)^2}{6h}\frac{\partial h}{\partial s}\right)\frac{\partial^3}{\partial\sigma^3} \end{aligned} \tag{2.74}$$

where:

$$\begin{aligned} \Delta_1 &= \Delta\sigma_3\Delta\sigma_4 - \Delta\sigma_1\Delta\sigma_2 \\ \Delta_2 &= \Delta\sigma_3\Delta\sigma_4 + \Delta\sigma_1\Delta\sigma_2 \\ \Delta_3 &= \Delta\sigma_3\Delta\sigma_4(\Delta\sigma_3 - \Delta\sigma_4) - \Delta\sigma_1\Delta\sigma_2(\Delta\sigma_1 - \Delta\sigma_2) \end{aligned} \tag{2.75}$$

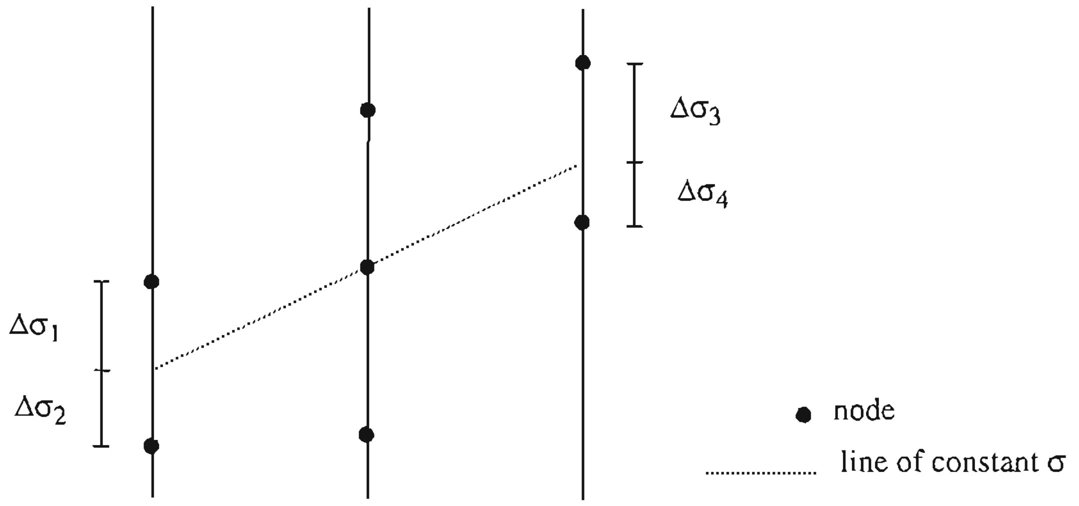

Figure 2.5 Stencil for the evaluation of horizontal gradients in LSC.

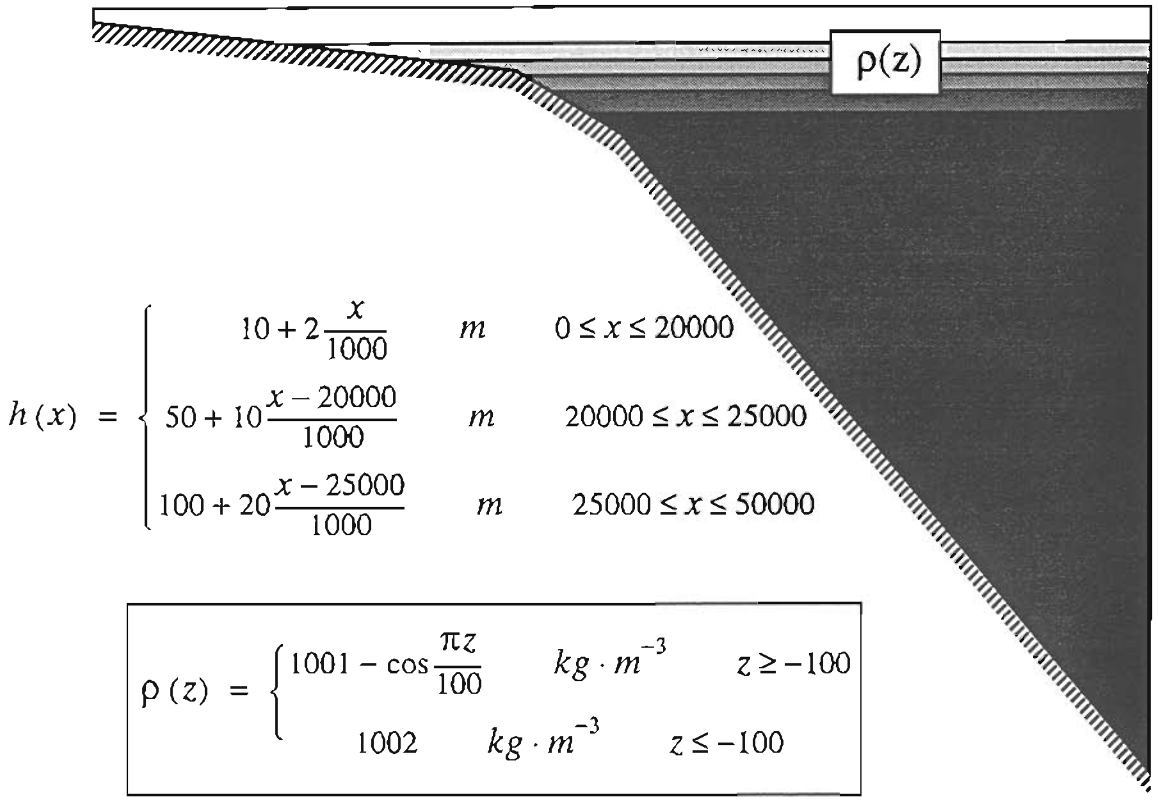

$$h(x) = \begin{cases} 10 + 2\dfrac{x}{1000} & m \quad 0 \le x \le 20000 \\ 50 + 10\dfrac{x-20000}{1000} & m \quad 20000 \le x \le 25000 \\ 100 + 20\dfrac{x-25000}{1000} & m \quad 25000 \le x \le 50000 \end{cases}$$

$$\rho(z) = \begin{cases} 1001 - \cos\dfrac{\pi z}{100} \quad kg \cdot m^{-3} & z \ge -100 \\ 1002 \quad kg \cdot m^{-3} & z \le -100 \end{cases}$$

Figure 2.6 Bathymetry and density field to illustrate the LSC conditional consistency.

The truncation error shows that the method will only converge if $\Delta\sigma^2$ goes to zero faster than Δx. To illustrate the effect of the conditional consistency of the method, we examine the variation of velocity errors with Δx for the bathymetry and density field shown in Figure 2.6. No-flow and zero elevations are imposed at the landward and seaward boundaries, respectively, and a no-slip condition is used at the bottom. The number of horizontal nodes is varied between 11 and 641. The number of nodes per vertical nv is given by:

$$nv = n - int((n-1)/3) + 19 \tag{2.76}$$

where n is the horizontal node index and int represents the integer part. Figure 2.7 shows that the error can indeed increase when Δx is reduced.

Overall, we consider this conditional consistency an acceptable payoff for the advantages of the LSC. However, the user should keep this potential problem in mind when refining his grid.

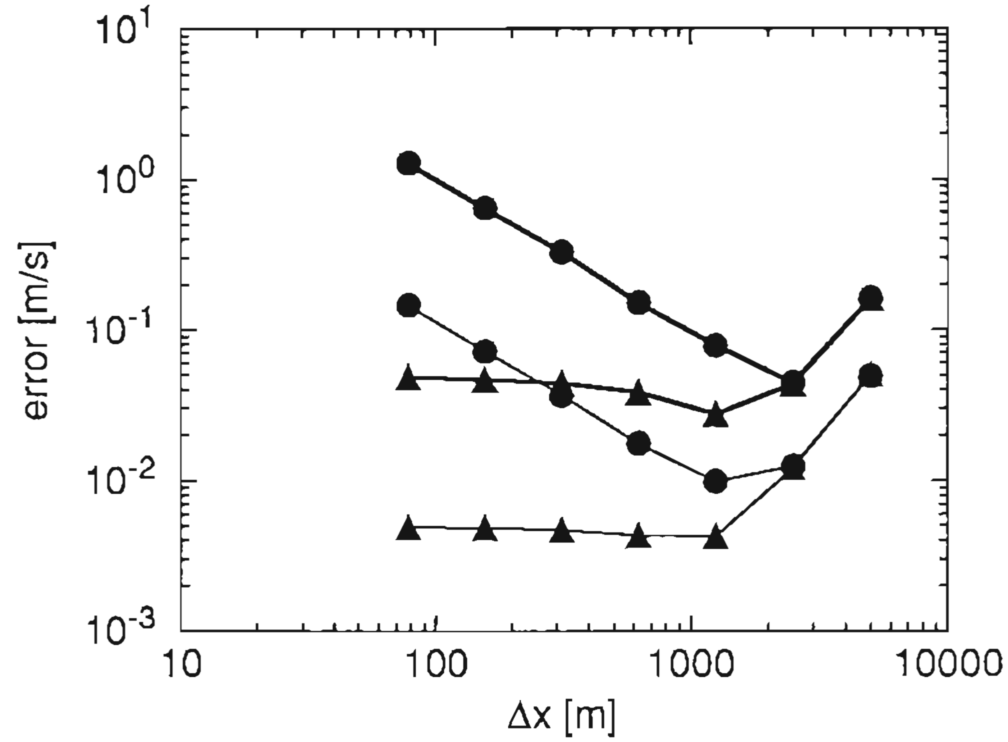

Figure 2.7 Conditional consistency of the LSC (circles). Maximum error (thick lines) and standard deviation of the errors (thin lines) are shown as a function of the horizontal resolution. Results for sigma coordinates with 21 nodes per vertical are shown for comparison (triangles).

References

Amorocho, J. and J.J. DeVries, 1980. A New Evaluation of the Wind Stress Coefficient Over Water Surfaces, *J. Geoph. Res.*, 85: 433-442.

Blumberg, A.F. and G.L. Mellor, 1985. Modeling Vertical and Horizontal Diffusivities with the Sigma Coordinate System, *Monthly Weather Review*, 113: 1379-1383.

Blumberg, A.F. and G.L. Mellor, 1987. A Description of a Three-Dimensional Coastal Ocean Model, in *Three-Dimensional Coastal Ocean Models*, N.S. Heaps (editor), American Geophysical Union, Washington, D.C, 1-16.

Davies, A.M., 1991. On the Accuracy of Finite Difference and Modal Methods for Computing Tidal and Wind Wave Current Profiles, *Int. J. for Numerical Methods in Fluids*, 12: 101-124.

Davies, A.M. and J.N. Aldridge, 1992. A Stable Algorithm for Bed Friction in Three-Dimensional Shallow Sea Modal Models, *Int. J. for Num. Methods in Fluids*, 14: 477-493.

Fortunato, A.B. and A.M. Baptista, 1993. *$RITA_{2v}$ User's Manual. 2D Vertical Hydrodynamic Model for River and Tidal Analysis. Part I - Flow Model*, OGI-CCALMR Software Documentation Series SDS7, 93-3, Oregon Graduate Institute of Science & Technology, Portland, Oregon.

Fortunato, A.B. and Baptista, A.M., 1994a. Localized Sigma Coordinates for the Vertical Structure of Hydrodynamic Models, in *Estuarine and Coastal Modeling III*, M.L. Spaulding, et al. (editors), Amer. Soc. Civ. Eng., 323-335.

Fortunato, A.B. and Baptista, A.M., 1995. Vertical Discretization in Tidal Flow Simulations, *Int. J. Num. Methods in Fluids* (in press).

Ianniello, J.P., 1977. Tidally Induced Residual Currents in Estuaries of Constant Breadth and Depth, *J. of Marine Research*, 35: 755-786.

Kinnmark, I.P.E., 1985. *The Shallow Water Equations: Formulation, Analysis and Application*, Lecture Notes in Engineering, 15, C.A. Brebia and S.A. Orszag (editors), Springer-Verlag, Berlin, 187 p.

Kolar, R.L. and W.G. Gray, 1990. Shallow Water Modelling in Small Water Bodies, in *Proc. Computational Methods in Surface Hydrology*, G. Gambolati, et al. (editors), 149-155.

Kolar, R.L., W.G. Gray and J.J. Westerink, 1992. An Analysis of the Mass Conserving Properties of the Generalized Continuity Wave Equation, in *Proc. Computational Methods in Water Resources IX, Vol. 2*, T.F. Russel, et. al. (editors), 537-544.

Kolar, R.L., J.J. Westerink, M.E. Cantekin and C.A. Blain, 1994. Aspects of Nonlinear Simulations Using Shallow Water Models Based on the Wave Continuity Equation, *Computers and Fluids*, 23: 523-538.

Laible, J.P., 1992. On the Solution of the Three-Dimensional Shallow Waters Equations Using the Wave Equation Formulation, in *Proc. Computational Methods in Water Resources IX, Vol. 2*, T.F. Russel, et. al. (editors), 545-552.

Luettich, R.A., J.J. Westerink and N.W. Scheffner, 1991. *ADCIRC: An Advanced Three-Dimensional Circulation Model for Shelves, Coasts and Estuaries. Report 1: Theory and Methodology of ADCIRC-2DDI and ADCIRC-3DL.* Prepared for Department of the Army, U.S. Army Corps of Engineers.

Lynch, D.R., 1978. *Finite Element Solution of the Shallow Water Equations*, Ph.D. Thesis, Princeton University.

Lynch, D.R., 1985. Mass Balance in Shallow Water Simulations, *Communications in Applied Numerical Methods*, 1: 153-159.

Lynch, D.R. and C.E. Naimie, 1993. The M2 Tide and its Residual on the Outer Banks of the Gulf of Maine, *J. Phys. Ocean.*, 23: 2222-2253.

Myers, E.P. and A.M. Baptista, 1995. Finite Element Modeling of the July 12, 1993 Hokkaido Nansei-Oki Tsunami, *Pure and Applied Geophysics*, 144 (3/4): 1070-1103.

Remédio, J.M.R., 1992. *RITA$_1$ - A Tool for Education and Exploratory Research on Shallow Waters*, M.S. Thesis, Department of Environmental Science and Engineering, Oregon Graduate Institute of Science & Technology, Portland, Oregon.

Sommerfeld, A., 1949. *Partial Differential Equations in Physics*, Academic Press, New York.

White, F.R., 1974. *Viscous Fluid Flow*, McGraw-Hill, New York.

CHAPTER 3[1]

Evaluation of Horizontal Gradients in Sigma-Coordinate Shallow Water Models

Abstract

Evaluating horizontal gradients in three-dimensional shallow water models that use bottom-following sigma coordinates can lead to large errors near steep bathymetry. A technique that has been proposed to minimize this problem involves computing horizontal gradients in cartesian coordinates, while treating all other terms in a sigma coordinate framework. We study this technique through both truncation error analysis and numerical experimentation, and compare it to the direct application of sigma coordinates. While the cartesian coordinate method has better convergence properties and generally smaller truncation errors when horizontal gradients are zero, the sigma coordinate method can be more accurate in other physically relevant situations. Also, the cartesian coordinate method introduces significant numerical diffusion of variable sign near the bottom (where physical diffusion is particularly small), thus potentially leading to instabilities. Overall, we consider the sigma coordinates to be the best approach.

3.1 Introduction

Three-dimensional numerical models of shallow water flow and transport have become common tools in coastal and estuarine studies, largely due to the rapid increase in

---

[1] submitted to Atmosphere-Ocean.

computer performance and to the development of efficient computational techniques. These models generally decouple the horizontal and vertical dimensions, in an explicit recognition of the different space and time scales involved. The decoupling is usually accomplished by the introduction of a global solution for elevation and depth-averaged velocity, and a local solution for the vertical structure of velocity.

The representation of the vertical direction still introduces a number of numerical difficulties. Models using cartesian grids in the vertical (e.g., Casulli and Cheng, 1992) have three major problems: shallow areas are in general poorly resolved; the stepwise representation of the bottom topography can distort the near bottom flow and transport; and the treatment of the surface boundary is complex. Models based on the bottom-following sigma coordinates avoid these problems, and are therefore generally preferred (see review by Cheng and Smith, 1990).

Unfortunately, sigma coordinate models have their own drawbacks, associated with the evaluation of horizontal gradients of depth-dependent quantities (Leendertse, 1989; Johnson et al., 1990; Haney, 1991; Paul, 1994). In particular, the evaluation of the baroclinic pressure gradient has received considerable attention in recent years. Even though atmospheric modelers have long known the potential for very large errors in the evaluation of horizontal gradients in sigma coordinates (e.g., Rousseau and Pham, 1971; Janjic, 1977), only recently did ocean modelers recognize this issue as a major problem. In the presence of steep slopes and strong stratification, the evaluation of baroclinic pressure can lead to very large truncation errors (Haney, 1991). These errors are particularly troubling because they can generate moderate currents in systems that should otherwise be at rest (Walters and Foreman, 1992).

The source of these large truncation errors can be understood qualitatively by examining the expression for the horizontal gradients in sigma coordinates. The sigma coordinate system (s_1,s_2,σ) is defined as:

$$\begin{cases} s_i \equiv x_i & i = 1, 2 \\ \sigma = \dfrac{z - \eta}{h + \eta} \end{cases} \tag{3.1}$$

where (x_1, x_2, z) is the cartesian coordinate system, h is the depth relative to mean sea level, and η is the elevation of the water surface. The horizontal derivatives in the two coordinate systems are related by:

$$\frac{\partial}{\partial x_i} \equiv \frac{\partial}{\partial s_i} - \frac{1}{H}\left(\sigma\frac{\partial H}{\partial s_i} + \frac{\partial \eta}{\partial s_i}\right)\frac{\partial}{\partial \sigma} \qquad i = 1, 2 \tag{3.2}$$

where $H=h+\eta$.

If the left-hand side is small compared to the two terms on the right hand side, using (3.2) corresponds to evaluating a small term as the subtraction of two large ones, which can lead to large errors (Haney, 1991). On the other hand, if the derivative along s_i is small relative to the other terms, evaluating horizontal gradients in σ-coordinates should lead to the best accuracy, since the vertical grid spacing is typically much finer than the horizontal (Fortunato and Baptista, 1994a).

In general, one expects salinity and temperature to fit the first situation described above, and velocity to fit the second. The sigma coordinate system would then be the "natural" system to evaluate velocity gradients (as argued by Mellor and Blumberg, 1985), whereas the cartesian system would be more appropriate for density gradients. However, the density field can also exhibit small derivatives along s_i (e.g., density fields determined by near-bottom suspended sediments, upwelling in continental slopes), in which case sigma coordinates would also be the most appropriate to evaluate baroclinic pressure gradients.

Several solutions have been proposed to avoid the large truncation errors in sigma coordinates. Expressing the density field as a deviation from a reference density profile, independent of time and horizontal position, can reduce the errors (Phillips, 1973; Blumberg and Mellor, 1987; Signell et al., 1994). This approach, however, is cumbersome and ineffective in estuaries, where the position of the pycnoclines varies strongly in time and space. Spall and Robinson (1990) proposed a hybrid coordinate system that uses z-coordinates in the surface layer, where the stratification occurs, and sigma coordinates below a certain depth. Beckers (1991) uses a similar approach, but discretizes both layers independently with sigma coordinates. Both these approaches are attractive for large scale ocean modeling, but may lead to a coarse refinement in shallow areas. A fourth-order approximation of the horizontal gradients (McCalpin, 1994) produces good results, but is practical only for horizontally structured grids.

The *cartesian coordinate method* (CCM) investigated in this paper has potential appeal due to its simplicity and general applicability. This method keeps the general framework of the sigma coordinates, but computes the horizontal gradients in cartesian coordinates by interpolating the necessary values at neighboring verticals (Laible, 1992; Beckmann and Haidvogel, 1993; Fortunato and Baptista, 1994b). While shown to be more accurate than the direct application of the sigma coordinates in some particular situations (Beckmann and Haidvogel, 1993; Fortunato and Baptista, 1994b), the CCM has not been systematically analyzed.

The purpose of this paper is to examine the evaluation of horizontal gradients in shallow water models. We compare the evaluation of horizontal gradients in cartesian (CCM) and sigma coordinates (SCM, standing for *sigma coordinate method*). The numerical properties of the two methods are first examined using truncation error analysis, and then illustrated with numerical examples for both density and velocity gradients. While the analysis is performed for finite element shallow-water models, the main conclusions should extend both to other numerical techniques (e.g., finite-differences) and to other types of models (e.g., transport models).

While none of the two methods emerges as clearly optimal, the drawbacks of the CCM appear to outweigh its advantages. In general, the CCM is more accurate than the SCM when the dependent variable (e.g., velocity, density) depends only on the vertical cartesian coordinate. However, the reverse happens when the isolines of the dependent variable tend to follow the bottom. Also, when used to evaluate advective accelerations or transport, the CCM introduces significant (positive or negative) numerical diffusion near the bottom, which can lead to significant errors and potentially to instabilities.

3.2 Formulations

The shallow-water equations express the conservation of mass and momentum assuming incompressibility, hydrostatic pressure and the Boussinesq approximation:

$$\frac{\partial u_j}{\partial x_j} = 0 \qquad j = 1, 2, 3 \tag{3.3}$$

$$\frac{\partial u_i}{\partial t} + u_j \frac{\partial u_i}{\partial x_j} = F_i - g\frac{\partial \eta}{\partial x_i} - \frac{g}{\rho_0}\int_z^{\eta} \frac{\partial \rho}{\partial x_i} dz + \frac{\partial}{\partial x_j}\left(A_j \frac{\partial u_j}{\partial x_j}\right) \qquad i = 1, 2; \qquad j = 1, 2, 3 \tag{3.4}$$

where t is time, u is the velocity vector, F is the Coriolis term, g is gravity, ρ is density, ρ_0 is a reference density, and A is the eddy viscosity vector. In addition, if density is treated as a prognostic variable, one or two transport equations must also be solved for salinity and/or temperature.

The formulations presented below are restricted to the treatment of horizontal gradients. They can be applied to most three-dimensional hydrodynamic finite element models based on linear triangular elements (e.g., Lynch and Werner, 1991; Luettich et al., 1991; Walters, 1992; Laible, 1992; Janin et al., 1994).

In a finite element framework using linear triangular elements, the gradients along s_i for a generic variable θ can be approximated as:

$$\left.\frac{\partial\theta}{\partial s_i}\right|_{n,j} \approx \frac{\sum_{e=1}^{nel(n)} \sum_{k=1}^{3} A_e \frac{\partial\phi_{ke}}{\partial s_i}\theta_{ke}}{\sum_{e=1}^{nel(n)} A_e} \qquad i = 1, 2 \tag{3.5}$$

where *nel(n)* represents the number of horizontal elements containing node n, A_e are their area, ϕ_{ke} are the corresponding shape functions and j is the vertical index of the node. The nodal values θ_{ke} are taken in a constant sigma plane (Figure 3.1).

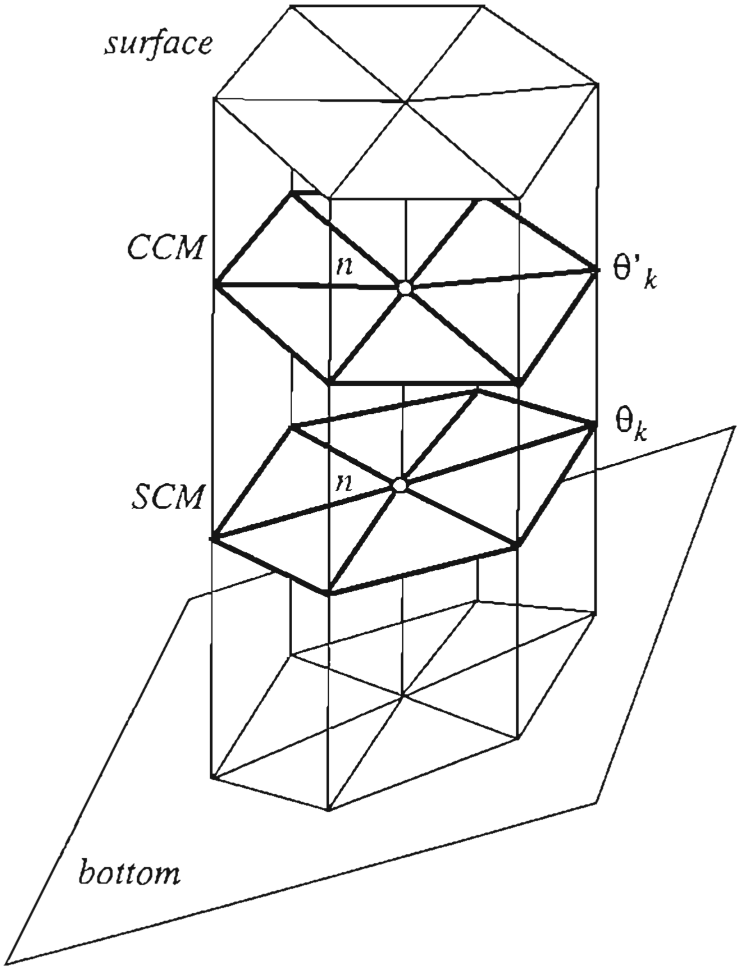

Figure 3.1 Evaluation of horizontal gradients of a generic variable θ, at node n, for the SCM and CCM.

In the CCM, the governing equations are still written in sigma coordinates, except for the terms involving horizontal gradients, which remain in their cartesian form. Since the nodes are not defined in horizontal planes, the values needed to evaluate the gradients at neighboring verticals are interpolated between adjacent vertical nodes. Consistent with the use of linear finite elements, a linear interpolation is used. Horizontal gradients are evaluated as:

$$\left.\frac{\partial\theta}{\partial x_i}\right|_{n,j} \approx \frac{\sum\limits_{e=1}^{nel(n)} \sum\limits_{k=1}^{3} A'_e \frac{\partial\phi'_{ke}}{\partial x_i} \theta'_{ke}}{\sum\limits_{e=1}^{nel(n)} A'_e} \qquad i = 1, 2 \tag{3.6}$$

where the values θ'_{ke} are defined in a fixed horizontal plane (Figure 3.1). While in most of the water column the areas A'_e and the shape functions ϕ'_{ke} coincide with the elemental areas and shape functions, near the bottom the evaluation of (3.6) requires special treatment. Two alternatives were considered. The first alternative, loosely based on Beckmann and Haidvogel (1993), uses an extrapolation along the vertical (Figure 3.2a), while the second (Fortunato and Baptista, 1994b) uses an interpolation along the bottom (Figure 3.2b). The first alternative is computationally simpler and may be more stable for deep ocean applications, but the second formulation appears to be more stable for coastal applications (see Appendix A). The second formulation is retained in the remaining of this paper, leading to, in (3.6):

$$\theta'_{ke} = \begin{cases} \theta_n & if\ n = k \\ \theta_{nb} + \alpha_{njk}(\theta_{kb} - \theta_{nb}) & if\ n \neq k \end{cases} \tag{3.7}$$

$$A'_e = A_e \alpha_{nji} \alpha_{njk} \tag{3.8}$$

where the subscript b refers to bottom values (Figure 3.2b), element e is defined by nodes n, i and k, and,

$$\alpha_{njk} = \frac{H_n + z_{n,j}}{H_n - H_k} \tag{3.9}$$

where k and j are the horizontal and vertical node indexes, respectively.

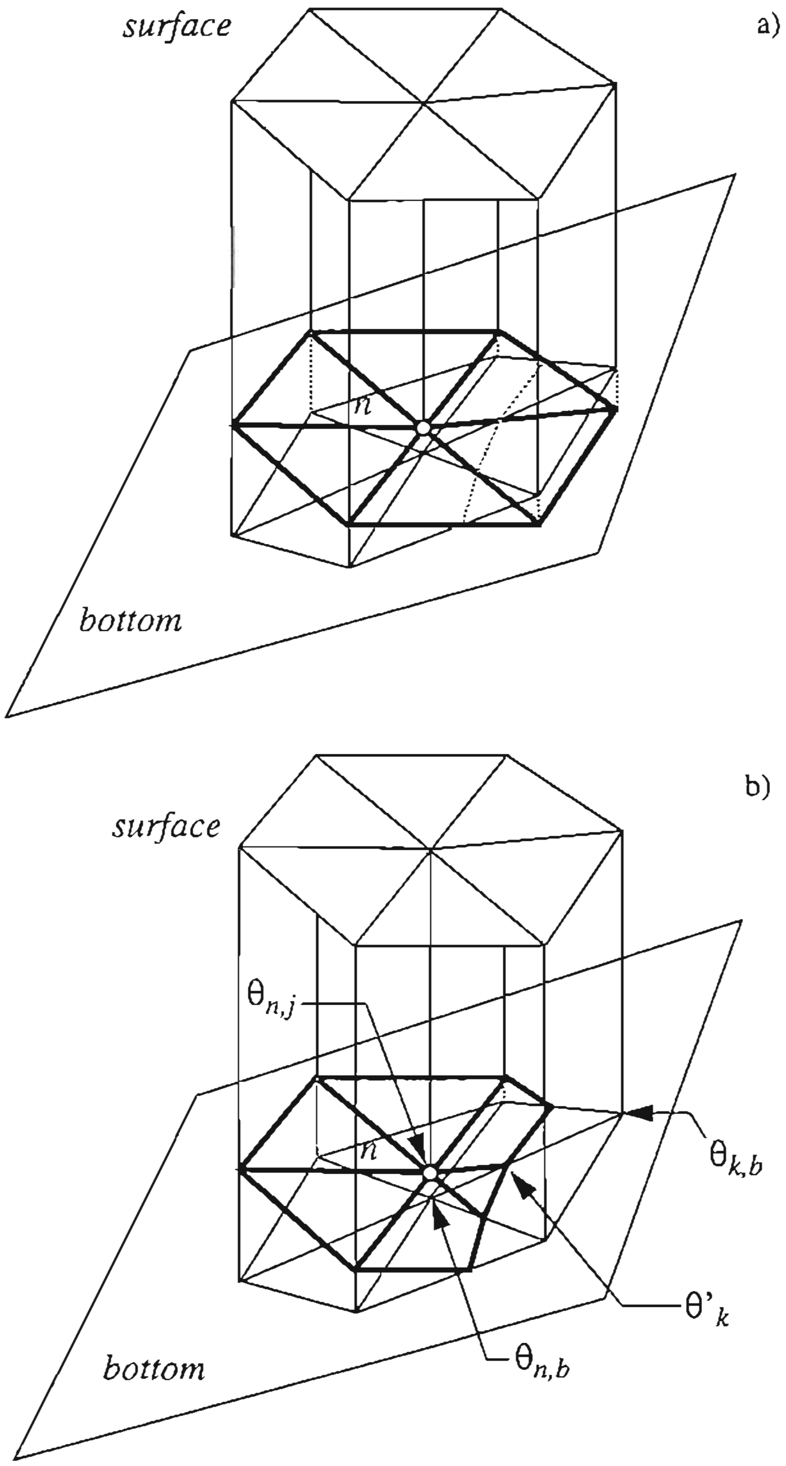

Figure 3.2 Evaluation of near-bottom horizontal gradients of a generic variable θ, at node n, for the CCM. a) extrapolation; b) interpolation. The subscript b indicates a bottom node.

3.3 Truncation errors

Truncation errors for CCM and SCM are compared in this section. For simplicity, we restrict the analysis to 2D and assume a rigid-lid approximation. Finite difference analogs for both methods (Table 3.1) and associated truncation errors (Table 3.2) are used below to discuss consistency, convergence, and stability. Truncation errors were developed by expansion in Taylor series of the finite difference analogs. In addition, truncation errors for the SCM were written in cartesian coordinates using the relations developed in Appendix B.

3.3.1 Consistency

Both methods are unconditionally consistent. Simple examination of Table 3.2 shows that this is true for the SCM. However, for the CCM, Δx appears in the denominator of truncation terms introduced by interpolation errors, and a closer examination is needed to demonstrate unconditional consistency.

Table 3.1 Finite difference analogs (see stencils in Figure 3.3).

Method	Finite differences analog
SCM	$\frac{\partial\theta}{\partial x} \equiv \frac{\partial\theta}{\partial s} - \frac{\sigma\partial h\partial\theta}{h\partial s\partial\sigma} \approx \frac{\theta_{i+1,k} - \theta_{i-1,k}}{2\Delta x} - \frac{\sigma\partial h}{h\partial s}\frac{\theta_{i,k+1} - \theta_{i,k-1}}{2\Delta\sigma}$
CCM	$\frac{\partial\theta}{\partial x} \approx \frac{(\theta_{i+1,k'-1}\Delta\sigma_3 + \theta_{i+1,k'}\Delta\sigma_4) - (\theta_{i-1,k-1}\Delta\sigma_1 + \theta_{i-1,k}\Delta\sigma_2)}{2\Delta x\Delta\sigma}$

We examine, for illustration, the limits of the two leading terms that have Δx in the denominator (Table 3.2), when Δx and $\Delta\sigma$ approach zero. While three cases (Δx approaching zero faster, slower, and at the same rate as $\Delta\sigma$) had to be analyzed, the second and third cases are relatively straightforward, and we discuss here only the first and least intuitive case.

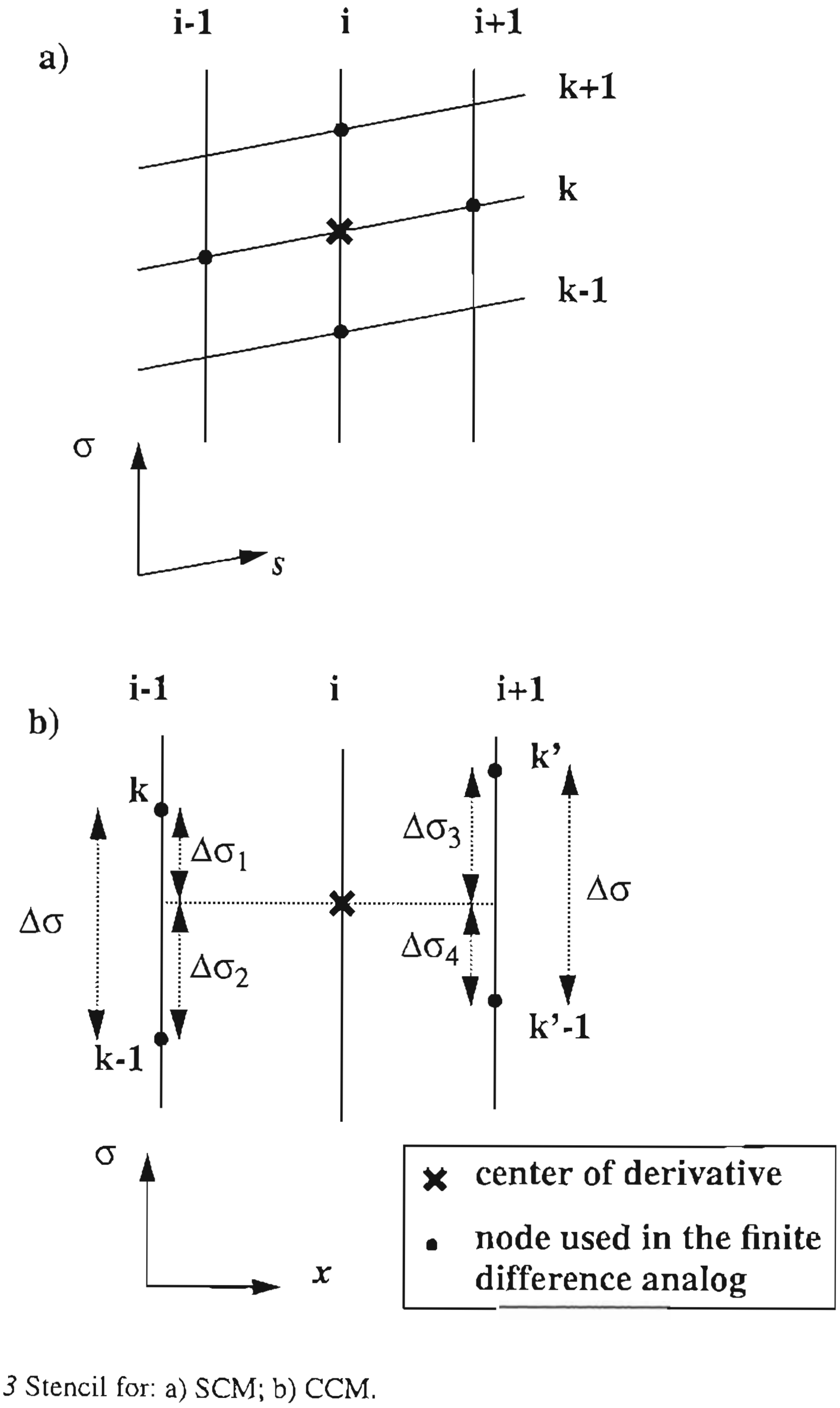

Figure 3.3 Stencil for: a) SCM; b) CCM.

For the first term:

$$\lim_{(\Delta x, \Delta \sigma) \to 0}\left(\frac{\Delta_1}{4\Delta x} h^2 \frac{\partial^2 \theta}{\partial z^2}\right) = \left(\frac{h^2}{4}\frac{\partial^2 \theta}{\partial z^2}\right)\lim_{(\Delta x, \Delta \sigma) \to 0}\left(\frac{\Delta_1}{\Delta x}\right) \tag{3.10}$$

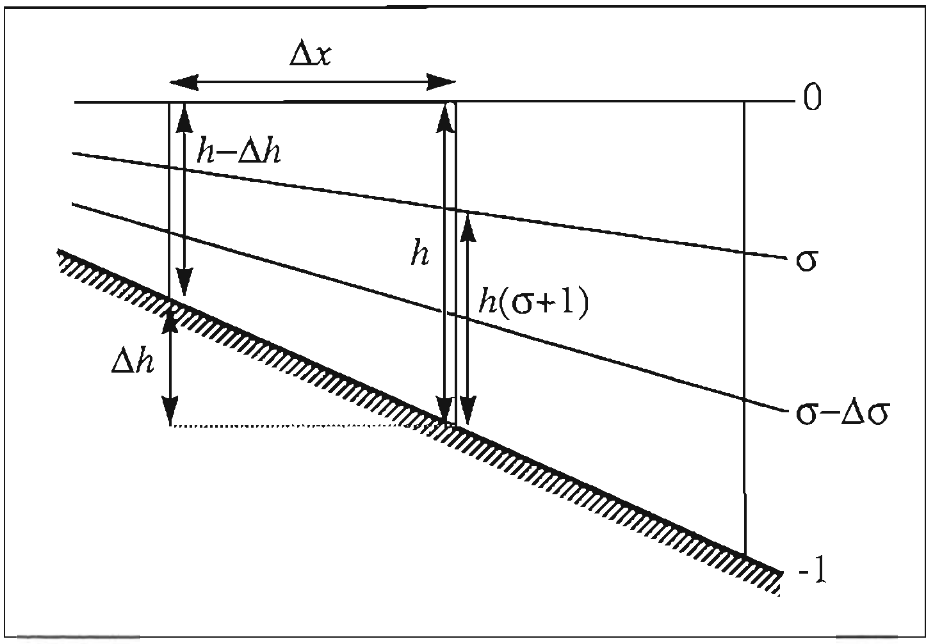

Figure 3.4 Evaluation of $\Delta\sigma_1$, $\Delta\sigma_2$, $\Delta\sigma_3$ and $\Delta\sigma_4$ (see Table 3.2) for a small Δx.

Using geometric arguments (Figure 3.4) Δ_1 can, for a constant slope, be related to $\Delta\sigma$ and Δx as:

$$\Delta_1 = \frac{2\Delta h\sigma}{h^2 - \Delta h^2}\left|\frac{\partial h}{\partial x}\right|\left(\Delta\sigma + \frac{2h|\Delta h|\sigma}{h^2 - \Delta h^2}\right)\Delta x \tag{3.11}$$

with

$$\Delta h = \Delta x\frac{\partial h}{\partial x} \qquad \lim_{\Delta x \to 0} \Delta h = 0 \tag{3.12}$$

and, therefore:

Table 3.2 Truncation errors.

Method	Truncation Error
SCM	$\left(\frac{\sigma i}{6}\frac{\partial^3\theta}{\partial z^3}\right)[(\sigma i\Delta x)^2-(h\Delta\sigma)^2]+$ $\frac{(\Delta x)^2}{2}\left[\frac{1}{3}\frac{\partial^3\theta}{\partial x^3}+\sigma i\cdot\frac{\partial^3\theta}{\partial x^2\partial z}+(\sigma i)^2\frac{\partial^3\theta}{\partial x\partial z^2}\right]+ higher\ order\ terms$
CCM	$\frac{\Delta_1}{4\Delta x}h^2\frac{\partial^2\theta}{\partial z^2}+\frac{(\Delta x)^2}{6}\frac{\partial^3\theta}{\partial x^3}+\frac{\Delta_2}{4}h^2\frac{\partial^3\theta}{\partial x\partial z^2}+\frac{\Delta_3}{12\Delta x}h^3\frac{\partial^3}{\partial z^3}\theta+$ *higher order terms*
CCM (near bottom)	$\frac{\Delta x}{2}\frac{1-\alpha}{1+\alpha}\frac{\partial^2\theta}{\partial x^2}+\alpha i\Delta x\frac{1-\alpha}{1+\alpha}\frac{\partial^2\theta}{\partial x\partial z}-\frac{i^2\alpha\Delta x}{2}\frac{1-\alpha}{1+\alpha}\frac{\partial^2\theta}{\partial z^2}+$ $\frac{(\Delta x)^2}{6}\frac{\partial^3\theta}{\partial x^3}-\frac{i\alpha(\Delta x)^2}{2}\frac{1-\alpha}{1+\alpha}\frac{\partial^3\theta}{\partial x^2\partial z}+\frac{i^2\alpha(\Delta x)^2}{2}\frac{(1-\alpha)^2}{1+\alpha}\frac{\partial^3\theta}{\partial x\partial z^2}$ $-\frac{i^3\alpha(\Delta x)^2}{6}\frac{(1-\alpha)(1-2\alpha)}{1+\alpha}\frac{\partial^3\theta}{\partial z^3}+ higher\ order\ terms$
$\Delta_1=\Delta\sigma_3\Delta\sigma_4-\Delta\sigma_1\Delta\sigma_2$ $\quad\Delta_3=\Delta\sigma_3\Delta\sigma_4(\Delta\sigma_3-\Delta\sigma_4)-\Delta\sigma_1\Delta\sigma_2(\Delta\sigma_1-\Delta\sigma_2)$ $\Delta_2=\Delta\sigma_3\Delta\sigma_4+\Delta\sigma_1\Delta\sigma_2$ $\quad i=\frac{\partial h}{\partial x}$ $\quad\alpha=\frac{\sigma h}{i\Delta x}$	

$$\lim_{(\Delta x,\Delta\sigma)\to 0}\left(\frac{\Delta_1}{\Delta x}\right)=\lim_{(\Delta x,\Delta\sigma)\to 0}\left[\frac{2\Delta h\sigma}{h^2-\Delta h^2}\left|\frac{\partial h}{\partial x}\right|\left(\Delta\sigma+\frac{2h\left|\Delta h\right|\sigma}{h^2-\Delta h^2}\right)\right]=0 \tag{3.13}$$

Hence, the limit in (3.10) is zero.

Similarly,

$$\frac{\Delta_3}{\Delta x} = ((-2\Delta h\sigma)/(h^2-\Delta h^2)^3)\left|\frac{\partial h}{\partial x}\right| \times [\Delta\sigma h(h^2+3\Delta h^2)(2\Delta\sigma h+3|\Delta h|\sigma) - (3h^2+\Delta h^2)(\Delta\sigma^2(h^2+\Delta h^2)+3\Delta\sigma h|\Delta h|\sigma+2\Delta h^2\Delta\sigma^2)] \tag{3.14}$$

and,

$$\lim_{(\Delta x,\Delta\sigma)\to 0}\left(\frac{\Delta_3 h^3}{12\Delta x}\frac{\partial^3\theta}{\partial z^3}\right) = \frac{h^3}{12}\frac{\partial^3\theta}{\partial z^3}\lim_{(\Delta x,\Delta\sigma)\to 0}\left(\frac{\Delta_3}{\Delta x}\right) = 0 \tag{3.15}$$

3.3.2 Convergence

The SCM has higher order accuracy than the CCM (Table 3.2). However, the convergence of the two methods has a particular behavior in two special situations (Table 3.3): zero horizontal gradients, and zero gradients along planes of constant sigma. Both situations are important from a physical viewpoint: the first represents a state of equilibrium for density, and the second closely mimics the case of a long-wave velocity field.

When the horizontal gradients are zero, the CCM truncation error in the water column converges to zero with $\Delta\sigma$ alone, since $\Delta_1 \le \Delta\sigma^2/4$ and $\Delta_3 < \Delta\sigma^3/10$. This is not surprising since only vertical gradients are being resolved. However, near the bottom, the truncation errors depend on Δx. The truncation error for the SCM depends on both $\Delta\sigma$ and Δx, and unless the "hydrostatic consistency" condition (Haney, 1991) is observed:

$$\left|\frac{\sigma}{h}\frac{\partial h}{\partial x}\right|\Delta x < \Delta\sigma \tag{3.16}$$

the error in Δx is dominant, and further vertical refinement will not improve accuracy. In presence of steep slopes (3.16) can be a very stringent condition, making horizontal refinement the primary mechanism to reduce errors in the SCM. In this case, the CCM becomes more attractive than the SCM. Conversely, if the gradient along s is zero, the error for the SCM depends on $\Delta\sigma$ alone, while for the CCM it also depends on Δx (Table 3.3). In this case, the SCM is a more suitable choice.

Table 3.3 Truncation errors in special cases. Symbols are defined in Table 3.2

case	method	truncation error
$\frac{\partial\theta}{\partial x} = 0$	SCM	$\left(\frac{\sigma i}{6}\cdot\frac{\partial^3\theta}{\partial z^3}\right)[(\sigma i\Delta x)^2-(h\Delta\sigma)^2] + higher\ order\ terms$
	CCM	$\frac{\Delta_1}{4\Delta x}h^2\frac{\partial^2\theta}{\partial z^2}+\frac{\Delta_3}{12\Delta x}h^3\frac{\partial^3}{\partial z^3}\theta + higher\ order\ terms$
$\frac{\partial\theta}{\partial s} = 0$	SCM	$-\left(\frac{\sigma i}{6h}(\Delta\sigma)^2\cdot\frac{\partial^3\theta}{\partial\sigma^3}\right) + higher\ order\ terms$
	CCM	$-\sigma(\Delta x)^2(\frac{i}{h})^3\frac{\partial\theta}{\partial\sigma}+(\frac{\Delta_1}{4\Delta x}-\frac{\Delta_2}{2h}i-\sigma^2(\Delta x)^2(\frac{i}{h})^3)\frac{\partial^2\theta}{\partial\sigma^2}$ $\left(\frac{\Delta_3}{12\Delta x}-\frac{(\Delta x)^2}{6}(\frac{\sigma i}{h})^3-\frac{\Delta_2}{4h}\sigma i\right)\frac{\partial^3\theta}{\partial\sigma^3} + higher\ order\ terms$

The particular form of the SCM truncation error has led to some confusion. When horizontal gradients are zero, decreasing Δx while keeping $\Delta\sigma$ fixed reduces the truncation error until the factor associated with the third derivative vanishes. Further reducing Δx increases the truncation error asymptotically because this error involves the subtraction of two positive quantities. This growth has led to the erroneous idea that sigma coordinate models would be non-convergent unless (3.16) was verified (e.g. Haney, 1991). The term "hydrostatic inconsistency", introduced by Janjic (1977) for atmospheric models, is misleading and may have fuelled this misconception about sigma coordinate models: it indicates the sequential use of two different approximations of the hydrostatic equation, rather than a numerical inconsistency. In the context of shallow-water models, different approximations of the density field may be used in the vertical integration of the density field and in the evaluation of the baroclinic pressure gradient. The use of two different approximations corresponds to hydrostatic inconsistency, but the truncation error for the evaluation of horizontal derivatives shows the consistency of the scheme and explains the error growth (Mellor et al., 1994, Fortunato and Baptista, 1994b). The truncation error for the baroclinic pressure gradient term (third term on the right-hand side in (3.4), involving both the vertical integral and the horizontal gradient), is qualitatively similar (Appendix C). A similar effect in (3.11) can also lead to a non-monotonic convergence for the CCM.

3.3.3 Numerical diffusion

Unlike for the SCM, the CCM truncation error includes a second vertical derivative. Therefore, when this formulation is used to compute advective accelerations or transport (in the transport equation), it will introduce vertical numerical diffusion. Since horizontal gradients are multiplied by velocity in the advective terms, the numerical diffusion coefficient is proportional to velocity and can be either positive or negative. In regions where eddy viscosity is small (e.g., highly stratified regions), numerical diffusion can therefore lead to instabilities. The worst problems should occur near the bottom, where numerical vertical diffusion can be very large (Table 3.2), while physical eddy viscosity decreases sharply.

3.4 Numerical tests

Three tests are presented next to illustrate the properties discussed above. Tests 1 and 2 demonstrate that the convergence of CCM and SCM depends largely on the prevailing horizontal gradients: CCM performs better in Test 1, which represents an equilibrium state, with zero horizontal gradients of density; both methods perform similarly, and rather poorly, in Test 2, which represents a case of upwelling forced by wind and baroclinic pressure. Test 3 simulates a tidal wave propagating over a step, and illustrates the role of numerical diffusion.

The tests were conducted with $RITA_{2v}$ (River and Tidal Analysis 2D vertical), a two-dimensional, width-averaged hydrodynamic model (Fortunato and Baptista, 1993).

The tests are therefore non-rotating and strictly two-dimensional, with one of the horizontal velocity components neglected. $RITA_{2v}$ uses a mode splitting technique in time: the depth-averaged equations are solved first for the elevations and depth-averaged velocities, and then the 2D momentum and continuity equations are solved for the horizontal and vertical velocities. The depth-averaged solution is based on the Generalized Continuity Wave Equation (Kinmark, 1985), and the domain is discretized with linear finite elements both in the horizontal and vertical directions. Baroclinic pressure is treated diagnostically.

3.4.1 Free baroclinic flow

Test 1, adapted from Walters and Foreman (1992), consists of an idealized continental shelf, shelf break and continental slope (Figure 3.5a). No-flow and zero elevations are imposed at the landward and seaward boundaries, respectively. A no-slip condition is used at the bottom, and the vertical eddy viscosity is set to $H/2400$ [m^2/s]. Since there are no boundary forcings and the density field is only a function of z (Figure 3.5a), the fluid should be at rest. In the numerical model, the flow is forced by the truncation errors in the evaluation of the baroclinic pressure. To focus our attention on these truncation errors, as well as for stability reasons, advection is neglected. Furthermore, the depth-averaged solution is replaced by the analytical solution to avoid error feedbacks.

The behavior of the velocity errors with Δx and $\Delta\sigma$ (Figure 3.6) confirms the conclusions from the truncation error analysis: CCM converge rapidly with $\Delta\sigma$, while SCM convergence requires decreasing both Δx and $\Delta\sigma$, and horizontal resolution appears as the primary error reduction mechanism.

The location of the largest errors further confirms the formal analysis. For the SCM, and for small Δx, the hydrostatic consistency condition is verified and the truncation error is dominated by $\Delta\sigma$. Maximum errors occur therefore in the deepest region at the surface, where vertical discretization ($h\Delta\sigma$) is coarsest. For $(\Delta x,\Delta\sigma) \sim (1500,0.05)$ (Figure 3.6a) and $(\Delta x,\Delta\sigma) \sim (2500,0.08)$ (Figure 3.6b), truncation errors due to Δx and $\Delta\sigma$ cancel in this area, and the error curves reach a minimum. For larger ratios of $\Delta x/\Delta\sigma$, the maximum error occurs over the shelf break near the bottom, suggesting that the curvature of the bathymetry, neglected in the truncation error (Appendix B), may have an important effect in some cases. For the CCM, the largest errors occur generally in the deep areas near the surface, again where vertical discretization is coarsest. However, for Δx = 2500 m and $\Delta\sigma$ smaller than 0.025, the largest errors occur over the shelf break and close to the bottom, and simultaneously the convergence in $\Delta\sigma$ stops (Figure 3.6b). This behavior reflects the truncation error in the second vertical derivative near the bottom (Table 3.2), which is only a function of Δx. In this particular test, this error only affects the continental shelf and shelf break, since the near bottom density is constant on the continental slope.

For this test, and within the restrictions of uniform grids, an appropriate spatial discretization may consist of 60 nodes in the vertical ($\Delta\sigma \approx 0.017$) and 11 nodes in the horizontal (Δx=5000m). The vertical resolution allows 10 nodes within the pycnocline, which extends for half the wavelength of the density field and occupies one sixth of the water column in the deepest region of the domain. The horizontal resolution corresponds to a dimensionless wavelength between 30 and 200, for a sixth-diurnal wave, and therefore can be considered acceptable for tidal simulations. For this level of discretization, Figure 3.6 suggests that the CCM represents a considerable gain in accuracy relative to the SCM. Indeed:

- for $(\Delta x,\Delta\sigma)=(5000,0.05)$, the standard deviations of the errors are ten times smaller for the CCM than for the SCM (Figure 3.6a), and reducing $\Delta\sigma$ would further increase the difference (Figure 3.6b);
- for $(\Delta x,\Delta\sigma)=(2500,0.017)$, the maximum error for the CCM is more than an order of magnitude smaller than for the SCM (Figure 3.6b), and increasing Δx would again increase the difference (Figure 3.6a).

This test confirms that, for the particular situation where the density field is a function of z alone, the SCM can lead to very large errors for typical horizontal resolutions. The CCM avoids these large errors, and converges rapidly with $\Delta\sigma$.

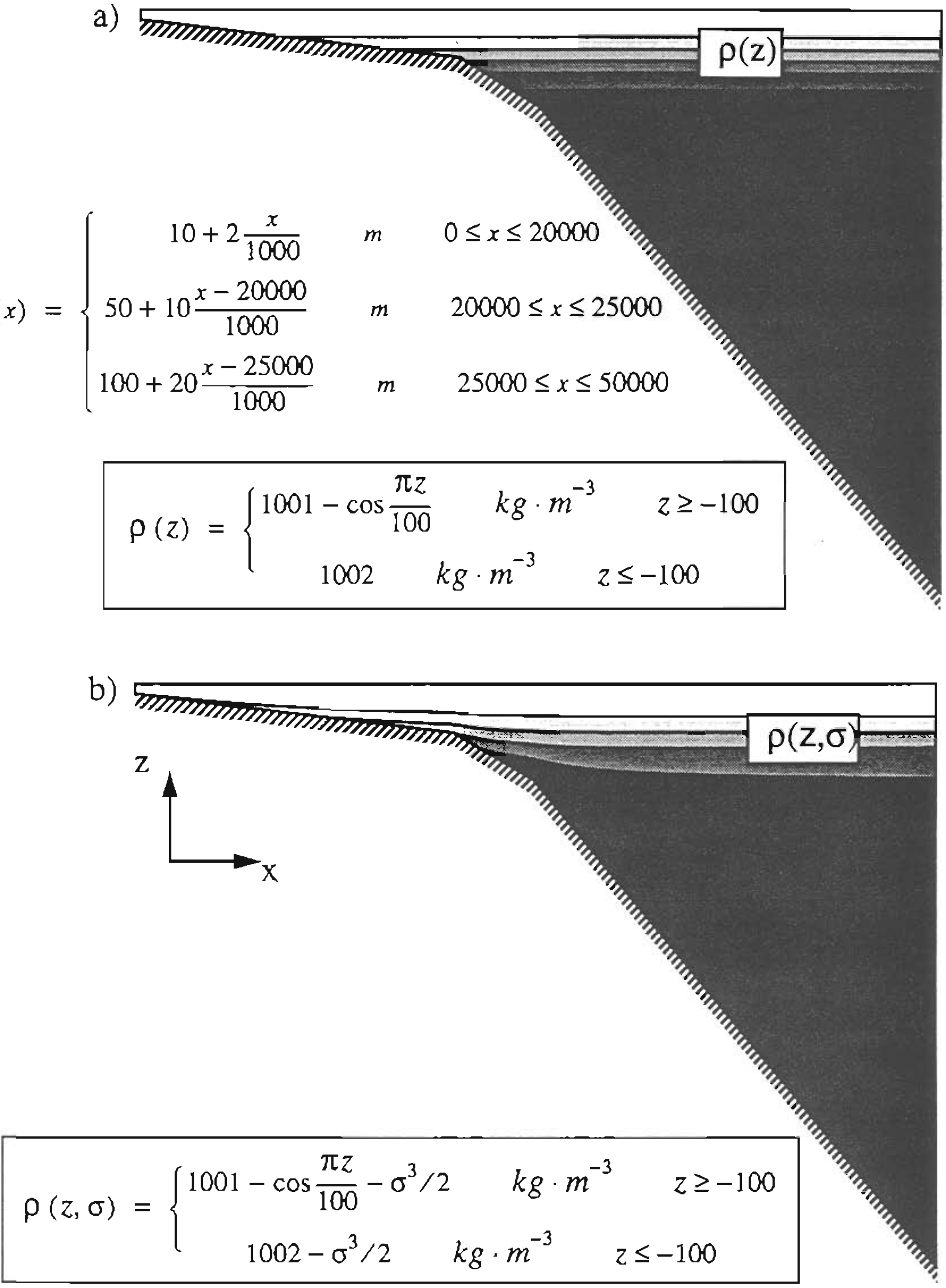

$$h(x) = \begin{cases} 10 + 2\dfrac{x}{1000} & m \quad 0 \le x \le 20000 \\ 50 + 10\dfrac{x-20000}{1000} & m \quad 20000 \le x \le 25000 \\ 100 + 20\dfrac{x-25000}{1000} & m \quad 25000 \le x \le 50000 \end{cases}$$

$$\rho(z) = \begin{cases} 1001 - \cos\dfrac{\pi z}{100} \quad kg \cdot m^{-3} & z \ge -100 \\ 1002 \quad kg \cdot m^{-3} & z \le -100 \end{cases}$$

$$\rho(z,\sigma) = \begin{cases} 1001 - \cos\dfrac{\pi z}{100} - \sigma^3/2 \quad kg \cdot m^{-3} & z \ge -100 \\ 1002 - \sigma^3/2 \quad kg \cdot m^{-3} & z \le -100 \end{cases}$$

Figure 3.5 Bathymetry (h) and density fields (ρ) for: a) Test 1 (contour interval 0.375 kg/m^3); b) Test 2 (contour interval 0.5kg/m^3).

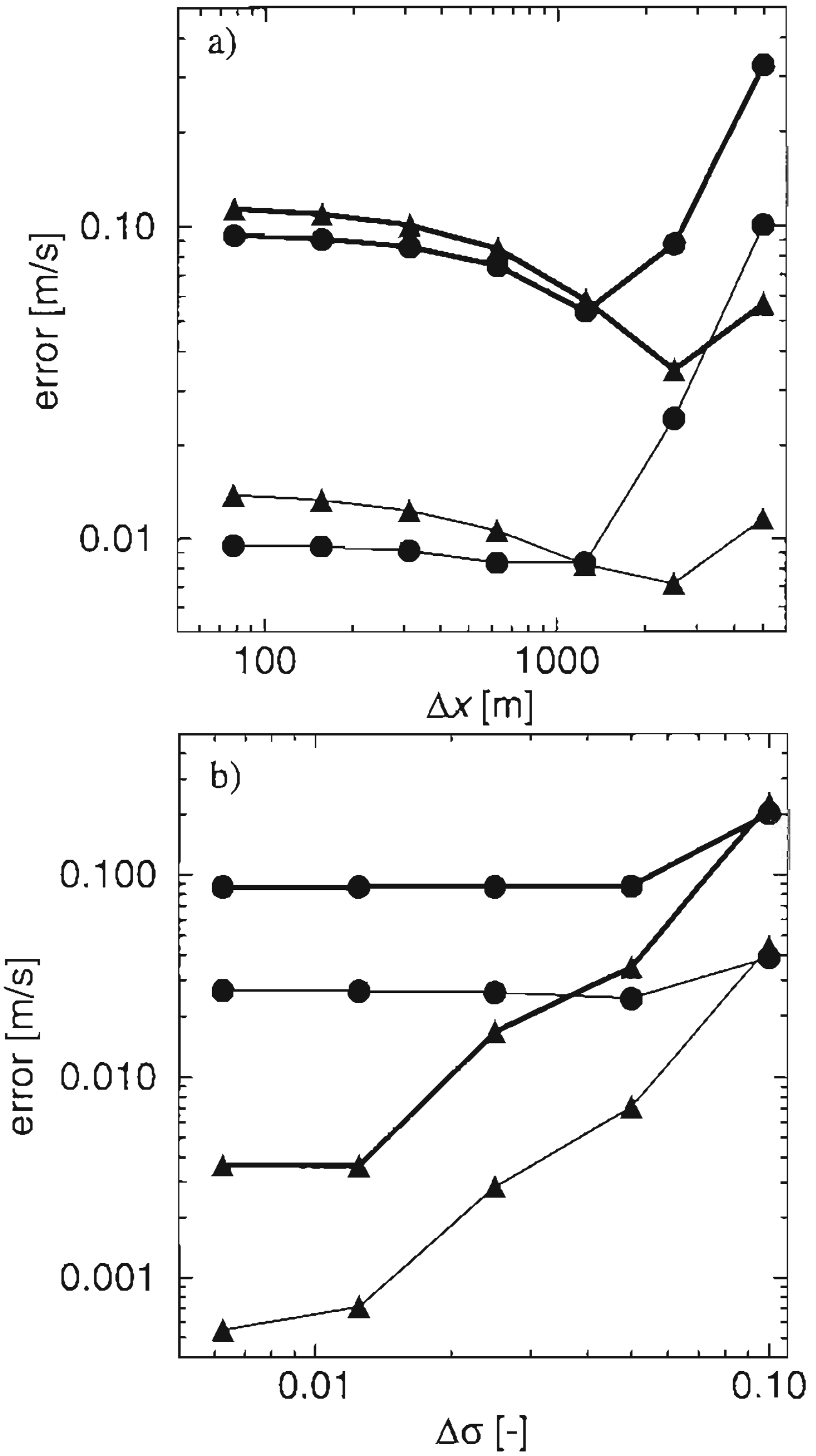

Figure 3.6 Test 1. Comparison between the SCM (circles) and the CCM (triangles). a) Convergence in Δx ($\Delta\sigma = 0.05$); b) convergence in $\Delta\sigma$ ($\Delta x = 2500$ m). Maximum errors are shown in thick lines and standard deviations in thin lines.

Direct extrapolation of the actual magnitude of the errors to real simulations is discouraged, since the solution of this test is very sensitive to the friction parameterization and to the vertical and horizontal diffusion coefficients. Also, we are neglecting the feedback loop between errors in the calculation of the velocity and density fields, which may attenuate both errors as time progresses (Mellor et al., 1994).

3.4.2 Forced baroclinic flow

As shown by the truncation error analysis and confirmed by numerical tests (not shown), when the density field is a function of σ alone, the performance of the two methods is the reverse of that observed in Test 1. Test 2 illustrates a case of upwelling where the density field is a function of both z and σ (Figure 3.5b). The bathymetry and boundary conditions are the same as in Test 1. A surface stress of 1 N/m^2 in the positive x direction

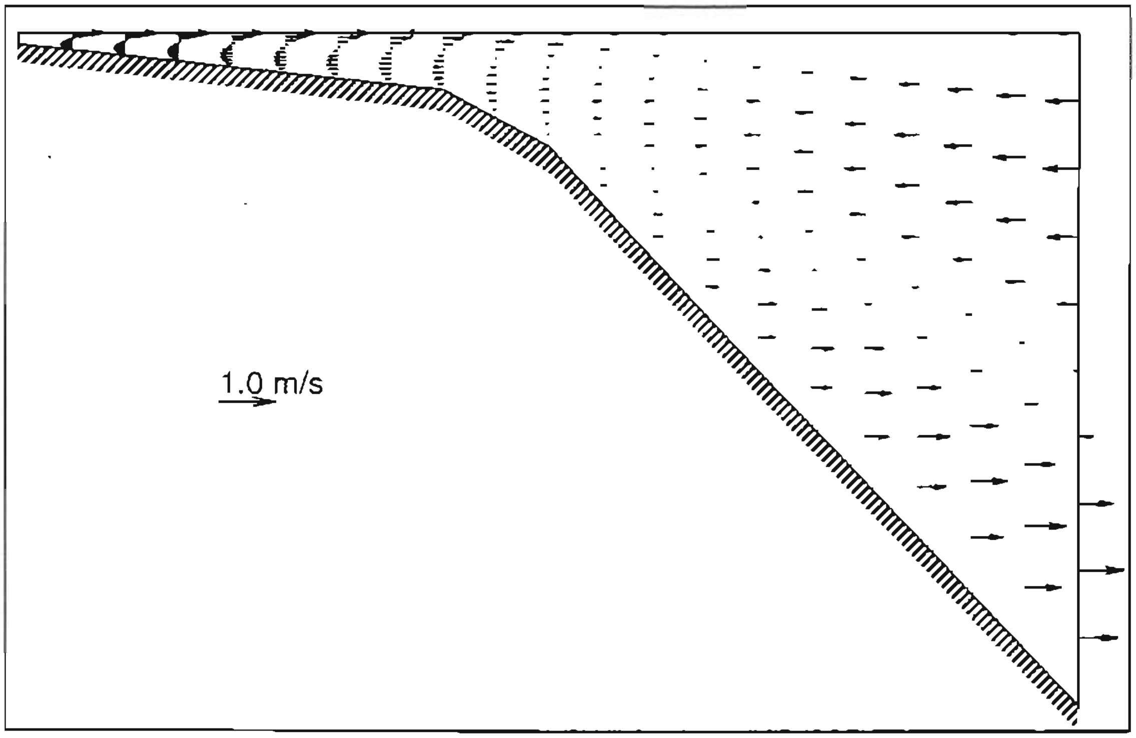

Figure 3.7 Analytical solution used in Test 2.

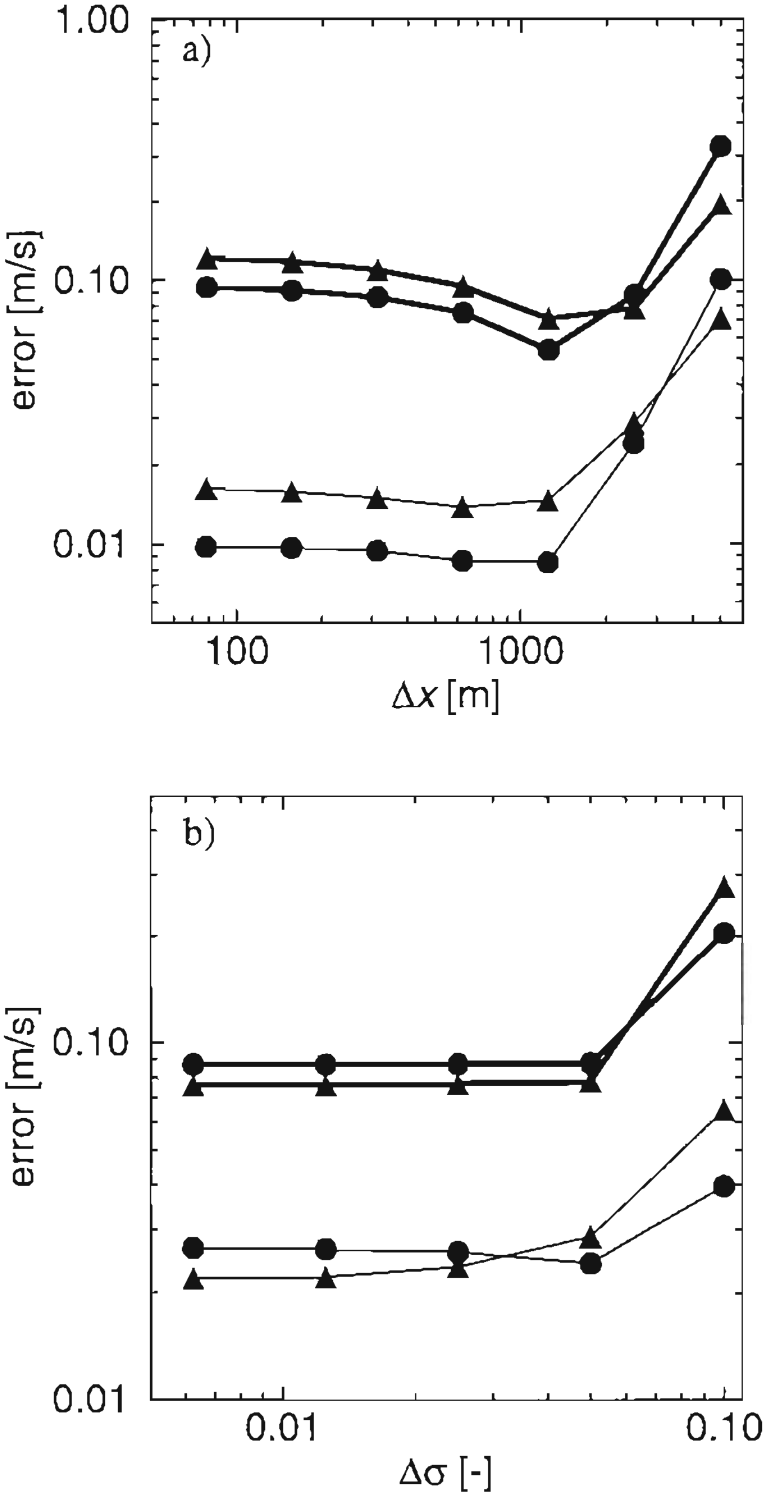

Figure 3.8 Test 2. Comparison between the SCM (circles) and the CCM (triangles). a) Convergence in Δx ($\Delta\sigma = 0.05$); b) convergence in $\Delta\sigma$ ($\Delta x = 2500$ m). Maximum errors are shown in thick lines and standard deviations in thin lines.

is imposed, corresponding to a wind speed of about 20 m/s. To define the vertical eddy viscosity coefficient, we set the surface velocity to 3% of the wind speed in the absence of baroclinic forcing, obtaining $A_v = H/2400$ m^2/s. Numerical results are compared with a semi-analytical solution (Figure 3.7) derived in Appendix D. The depth-averaged solution is again replaced by the exact solution and advection is neglected.

Test 1 grids are again used to examine the convergence both in Δx and in $\Delta\sigma$ (Figure 3.8). Results show that significant errors can now occur for both formulations. While Test 1 suggested that the CCM reduces the large errors introduced by the SCM, Test 2 shows that this conclusion is not general. When the density field is a function of both z and σ, either formulation can be more accurate, depending on the relative strength of each part of the density field. Relying on the good accuracy of the CCM based on simple tests like Test 1 can therefore be misleading.

3.4.3 Barotropic flow over a step

Test 3 examines the performance of the two methods to evaluate advective accelerations, by simulating a tidal wave propagating over a bottom step. The bathymetry is given by:

$$h\,[m] = \begin{cases} 5 + (3x)/5000 & 0 \le x < 7000 \\ 30 + (3x)/5000 - 25\cos\left(\left(\pi\,(x - 7000)\right)/5000\right) & 7000 \le x < 12000 \\ 55 + (3x)/5000 & 12000 \le x < 15000 \end{cases} \tag{3.17}$$

The wave has a period of 12 hours (S_2) and an amplitude of 1 m at the open boundary. The horizontal domain was discretized with 31 evenly spaced nodes. In the vertical, the nodes were distributed as (Fortunato and Baptista, 1995):

$$\sigma_i = \left(\frac{1-i}{1-n}\right)^4 - 1 \tag{3.18}$$

with n=20 nodes per vertical.

Two eddy viscosity parameterizations proposed by Davies (1993a) were used. Eddy viscosity profile A is depth independent and defined as:

$$A_v = K|\bar{u}|\Delta \qquad with \qquad \Delta = min\left(H, 2000\sqrt{|\tau_b|/\rho_0}\right) \tag{3.19}$$

where K is a dimensionless coefficient taken as 0.0025, $\bar{u}$ is the depth averaged velocity, Δ is the depth of the bottom boundary layer and τ_b is the bottom stress.

Eddy viscosity profile B is given by (3.19) in the upper 80% of the water column, then decreases linearly to:

$$A_{vb} = \kappa z_0\sqrt{|\tau_b|/\rho_0} \tag{3.20}$$

at the bottom. Here κ is the von Kármán constant (0.4) and z_0 is the roughness length taken as 0.01 m. A quadratic bottom stress with a friction coefficient of 0.01 was imposed.

The time step was set to 10 s. The horizontal diffusion coefficient was set to 1 m^2/s in the depth-averaged solution (to avoid spurious oscillations) and was neglected in the vertical solution. The model was run for six tidal cycles in 1D mode, plus four cycles in 2D mode. At the last tidal cycle, velocities at $x = 9500$ m were harmonically analyzed for S_2 and its major harmonics (Z_0, S_4 and S_6), and the results were compared with those obtained with a very finely discretized grid (301 horizontal nodes, 60 nodes per vertical distributed according to (3.18), and a time step of 1 s). The reference solution was computed with the SCM.

For profile A, the eddy viscosity (3.19) is of the same order of magnitude as the numerical diffusion introduced by the CCM near the bottom (Table 3.2). Numerical problems can therefore be masked by the large viscosity, and the S_2 results compare reasonably well with the reference solution (Figure 3.9a). Still, the CCM fails to reproduce the nonlinear components satisfactorily (Figure 3.9b). For the more realistic profile B, the near-bottom eddy viscosity (3.20) can be two orders of magnitude smaller than the numerical diffusion, leading to visible errors even in the main tidal constituent (Figure 3.9c). The introduction of numerical diffusion is therefore a major drawback of the CCM.

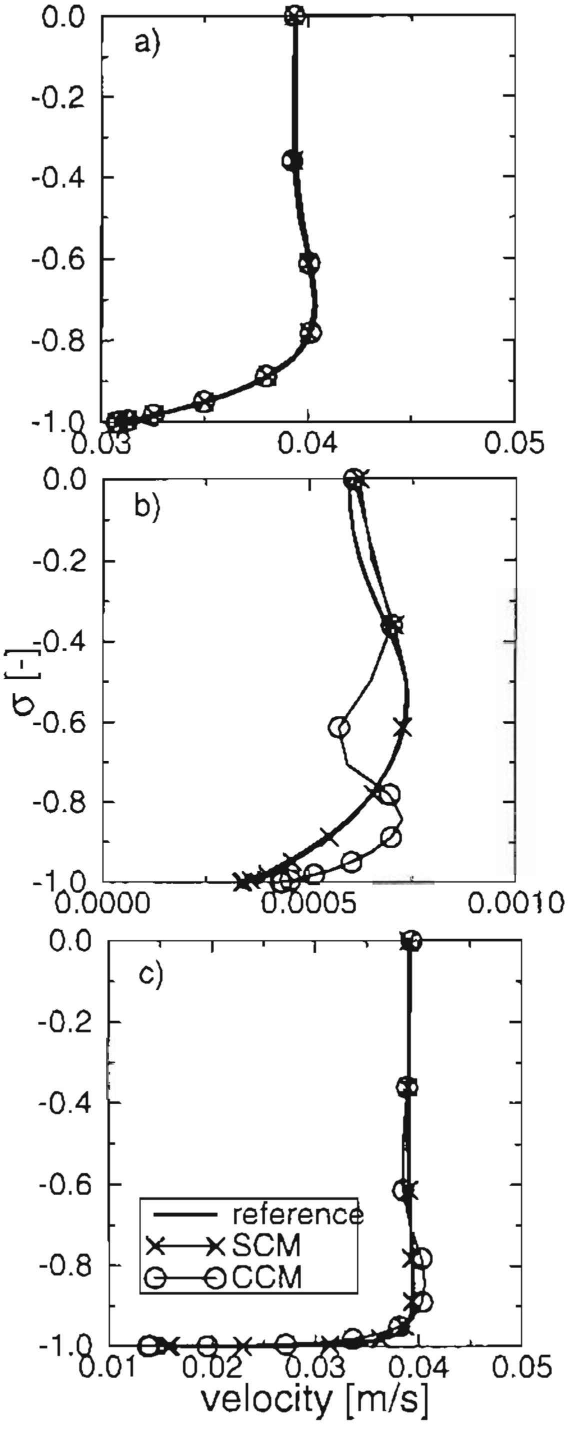

Figure 3.9 Vertical profiles of velocity amplitudes at x = 9500 m. a) S_2, eddy viscosity profile A; b) S_4, eddy viscosity profile A; c) S_2, eddy viscosity profile B.

3.5 Final considerations

Two methods to evaluate horizontal gradients in shallow water models were compared. Both methods use finite-element sigma-coordinate grids, but the SCM evaluates the horizontal gradients in a sigma-coordinate system (the traditional approach), while the CCM evaluates the gradients directly in cartesian coordinates, interpolating the necessary values at neighboring verticals. The comparison was performed through truncation error analysis and illustrated with simple numerical examples (2D, diagnostic) for both density and velocity gradients.

As shown earlier by Beckmann and Haidvogel (1993) and Fortunato and Baptista (1994b), the CCM is more accurate than the SCM when the horizontal gradients are zero. However, relying on such a simple test to assess the relative accuracy of CCM and SCM is misleading, because either method can be more accurate than the other depending on the direction of the smaller gradients. Furthermore, when advective accelerations are computed with the CCM, positive or negative numerical diffusion is introduced near the bottom, which can lead to distortions of the bottom flow and potentially to instabilities. Similarly, if the CCM was used to compute advective transport, numerical diffusion would also be introduced with analogous consequences.

Overall, the drawbacks of the CCM outweigh its advantages, and we recommend the evaluation of horizontal derivatives in sigma coordinates. For velocity gradients, the SCM represents a better approach regardless of horizontal grid discretization (Fortunato and Baptista 1994a). For density gradients, the use of SCM will require keeping truncation errors under control, either with a fine horizontal grid spacing near steep slopes or through one of the methods described in Section 3.1.

For finite element-based models, which have capability for flexible local refinement, the use of a fine horizontal grid spacing near steep slopes is particularly attractive. The difficulty is choosing the appropriate horizontal resolution for a given system. Based on a lose truncation error analysis, Deleersnijder and Beckers (1992) proposed:

$$\Delta x \ll h / \left| \frac{\partial h}{\partial x} \right| \tag{3.21}$$

Our results suggest that the following alternative approach is feasible:

Step 1: Choose the horizontal resolution needed to resolve barotropic processes (e.g., using dimensionless wavelength criteria, or *a posteriori* truncation error estimation as proposed by Hagen and Westerink, 1995);

Step 2: Choose the vertical resolution that is needed to represent properly the density field, as in Test 1;

Step 3: Choose the local horizontal resolution by forcing truncation errors in Δx and $\Delta\sigma$ to be similar, i.e.:

$$\Delta x \sim (\Delta\sigma h) / \left| \sigma \frac{\partial h}{\partial x} \right| \tag{3.22}$$

where σ should be characteristic of the position of the pycnocline.

Step 4: Adjust the vertical resolution to account for expected vertical gradients in the velocity field, from tides (Fortunato and Baptista, 1995), wind (Davies, 1985), or vertical stratification (Davies, 1993b).

We note that if Δx is larger than in (3.22), horizontal truncation errors will dominate, and vertical resolution will be ineffective. Following the three steps outlined above rather than applying the hydrostatic consistency condition will in general allow for less refined horizontal grids because the definition of the horizontal resolution will not be affected by the extra vertical resolution potentially required by vertical gradients in the velocity field (e.g., as needed to resolve surface or bottom boundary layers). Our approach is also more rigorous than (3.21) since it takes into account the vertical resolution. However, the two approaches should be comparable for typical vertical resolutions ($\Delta\sigma$~0.01-0.1).

The horizontal grid refinements will not necessarily be a major burden on the computations. Near strong topographic changes, barotropic tidal models already require finer grids than those based on wavelength criteria (Westerink et al., 1992, 1994a and 1994b). In many cases, the horizontal resolution required to simulate barotropic waves may therefore be sufficient to lead to an acceptable accuracy in the evaluation of baroclinic pressure.

Appendix A: Evaluation of Near-Bottom Gradients in the CCM

We compare two alternative approaches to evaluate near-bottom horizontal derivatives in cartesian coordinates. A fictitious value can be obtained below the bottom by extrapolation (Figure 3.10a), or a value can be interpolated at the bottom (Figure 3.10b). The first alternative is apparently the most attractive: it is simpler from a computational viewpoint, and it is centered in space, thus avoiding truncation errors in the second horizontal derivative. However, the combined findings of Beckmann and Haidvogel (1993) and Fortunato and Baptista (1994a) suggest that the extrapolation method can lead to instabilities in the evaluation of gradients of both density and velocity. To investigate this possibility, we look at the error amplification for the two formulations. The goal is to estimate the effect of a small error in a nodal value on the evaluation of the derivative. If this effect is small, the method will be robust; if the effect is large, errors can grow rapidly and instabilities can occur.

Consider the 2D finite difference analogs of (3.6), assuming a rigid lid approximation. Referring to the stencils in Figure 3.10, we have for the extrapolation:

$$\left.\frac{\partial\theta}{\partial x}\right|_{n,j} \approx \frac{\theta'_{n+1,j} - \dfrac{\Delta z + \Delta x\,(1-\alpha)\,i}{\Delta z}\theta_{n-1,b} + \dfrac{\Delta x\,(1-\alpha)\,i}{\Delta z}\theta_{n-1,b+1}}{2\Delta x} \tag{3.23}$$

and for the interpolation:

$$\left.\frac{\partial\theta}{\partial x}\right|_{n,j} \approx \frac{\theta'_{n+1,j} - (1-\alpha)\,\theta_{n,b} - \alpha\theta_{n-1,b}}{\Delta x\,(1+\alpha)} \tag{3.24}$$

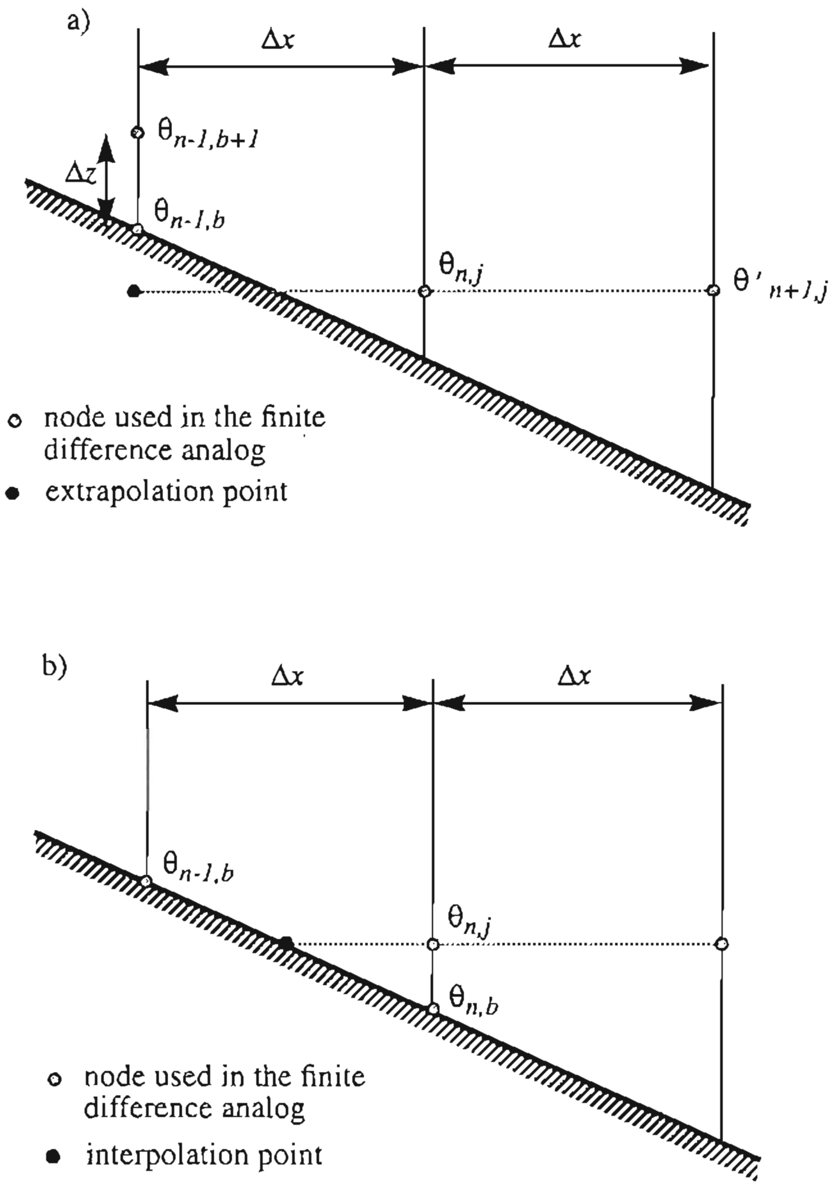

Figure 3.10 Stencil for: a) extrapolation; b) interpolation.

We then assume that each nodal variable, at a given time step, can be written:

$$\tilde{\theta}_x = \theta_x + \varepsilon_x \tag{3.25}$$

where θ_x is the exact value, ε_x is the error, and the tilde indicates a numerical value. Substituting (3.25) into (3.23) and (3.24), and taking the derivative of the resulting expression relative to the error at each node, we obtain:

$$\frac{\partial\tilde{\theta}}{\partial\varepsilon_{n+1,j}} = \frac{1}{2\Delta x} \qquad \frac{\partial\tilde{\theta}}{\partial\varepsilon_{n-1,b}} = -\left(\frac{1}{2\Delta x} + \frac{i(1-\alpha)}{2\Delta z}\right) \qquad \frac{\partial\tilde{\theta}}{\partial\varepsilon_{n-1,b-1}} = \frac{i(1-\alpha)}{2\Delta z} \tag{3.26a-c}$$

$$\frac{\partial\tilde{\theta}}{\partial\varepsilon_{n+1,j}} = \frac{1}{\Delta x(1+\alpha)} \qquad \frac{\partial\tilde{\theta}}{\partial\varepsilon_{n,b}} = -\frac{1-\alpha}{\Delta x(1+\alpha)} \qquad \frac{\partial\tilde{\theta}}{\partial\varepsilon_{n-1,b}} = -\frac{\alpha}{\Delta x(1+\alpha)} \tag{3.27a-c}$$

for the extrapolation and interpolation, respectively.

In coastal and estuarine applications, where friction is often an important process, the near-bottom vertical grid spacing must be very small to resolve the bottom boundary layer (Fortunato and Baptista, 1994c). Error amplifications (3.26b-c) then become very large, potentially leading to instabilities. Also, the extrapolation introduces slightly more vertical numerical diffusion than the interpolation (Fortunato and Baptista, 1994a). Interpolation is therefore the best option for coastal applications. For deep ocean applications, however, friction is unimportant and the near-bottom vertical resolution is usually coarse. Moreover, the horizontal resolution is also relatively coarse, increasing the truncation error in the second horizontal derivative for the interpolation formulation (Table 3.2). In this case, the extrapolation may be the most appropriate choice.

Appendix B: Derivatives in σ-Coordinates

In order to compare the evaluation of horizontal gradients in sigma and in cartesian coordinates, it is convenient to convert the truncation errors in σ-coordinates to the cartesian coordinate system. For this conversion, we need to relate derivatives in the two coordinate systems. First derivatives in the sigma and cartesian coordinate systems, using a rigid-lid approximation, are related as:

$$\frac{\partial\theta}{\partial s} = \frac{\partial\theta}{\partial x} + \frac{zi}{h}\frac{\partial\theta}{\partial z} \qquad \frac{\partial\theta}{\partial\sigma} = h\frac{\partial\theta}{\partial z} \tag{3.28}$$

where i = ∂h/∂x. Applying expressions (3.28) successively, and assuming a constant bottom slope, we can relate higher order derivatives in the two systems:

$$\frac{\partial^2\theta}{\partial s^2} = \frac{\partial^2\theta}{\partial x^2} + \frac{2zi}{h}\frac{\partial^2\theta}{\partial x\partial z} + \left(\frac{zi}{h}\right)^2\frac{\partial^2\theta}{\partial z^2} \tag{3.29}$$

$$\frac{\partial^3\theta}{\partial s^3} = \frac{\partial^3\theta}{\partial x^3} + \frac{3zi}{h}\frac{\partial^3\theta}{\partial x^2\partial z} + 3\left(\frac{zi}{h}\right)^2\frac{\partial^3\theta}{\partial x\partial z^2} + \left(\frac{zi}{h}\right)^3\frac{\partial^3\theta}{\partial z^3} \tag{3.30}$$

$$\frac{\partial^2\theta}{\partial s\partial\sigma} = h\frac{\partial^2\theta}{\partial x\partial z} + zi\frac{\partial^2\theta}{\partial z^2} + i\frac{\partial\theta}{\partial z} \tag{3.31}$$

$$\frac{\partial^3\theta}{\partial s^2\partial\sigma} = h\frac{\partial^3\theta}{\partial x^2\partial z} + 2zi\frac{\partial^3\theta}{\partial x\partial z^2} + \frac{(zi)^2}{h}\frac{\partial^3\theta}{\partial z^3} + 2i\frac{\partial^2\theta}{\partial x\partial z} + \frac{2zi^2}{h}\frac{\partial^2\theta}{\partial z^2} \tag{3.32}$$

$$\frac{\partial^3\theta}{\partial s\partial\sigma^2} = h^2\frac{\partial^3\theta}{\partial x\partial z^2} + hzi\frac{\partial^3\theta}{\partial z^3} + 2hi\frac{\partial^2\theta}{\partial z^2} \tag{3.33}$$

Appendix C: Truncation Error for the Evaluation of Baroclinic Pressure

We want to evaluate:

$$\begin{gathered}\int_{\sigma_i}^{0}\frac{\partial\rho}{\partial x}d\sigma = \sum_{j=i}^{n-1}\int_{\sigma_j}^{\sigma_{j+1}}\frac{\partial\rho}{\partial x}d\sigma = \sum_{j=i}^{n-1}\int_{\sigma_j}^{\sigma_{j+1}}\left(\frac{\partial\rho}{\partial s} - \frac{\sigma}{h}\frac{\partial h}{\partial x}\frac{\partial\rho}{\partial\sigma}\right)d\sigma = \\ \sum_{j=i}^{n-1}\left(\int_{\sigma_j}^{\sigma_{j+1}}\frac{\partial\rho}{\partial s}d\sigma - \frac{1}{h}\frac{\partial h}{\partial x}\int_{\sigma_j}^{\sigma_{j+1}}\sigma\frac{\partial\rho}{\partial\sigma}d\sigma\right) = \sum_{j=i}^{n-1}\left(\int_{\sigma_j}^{\sigma_{j+1}}\frac{\partial\rho}{\partial s}d\sigma - \frac{1}{h}\frac{\partial h}{\partial x}\left(\sigma\rho\Big|_{\sigma_j}^{\sigma_{j+1}} - \int_{\sigma_j}^{\sigma_{j+1}}\rho d\sigma\right)\right)\end{gathered} \tag{34}$$

where we used a rigid-lid approximation. The two of the terms that cannot be evaluated exactly are:

$$X_j = \int_{\sigma_j}^{\sigma_{j+1}}\frac{\partial\rho}{\partial s}d\sigma \tag{35}$$

and:

$$Y_j = \int_{\sigma_j}^{\sigma_{j+1}} \rho d\sigma \tag{36}$$

The truncation error for the integral of a generic function a is obtained by expanding the integral in Taylor series:

$$\int_{x}^{(x+\Delta x)} a dx = 0 + a\Delta x + \frac{a' (\Delta x)^2}{2} + \frac{a'' (\Delta x)^3}{6} + \frac{a''' (\Delta x)^4}{24} + \dots \tag{37}$$

The integral is approximated as:

$$\begin{gathered} \frac{a(x) + a(x+\Delta x)}{2} \Delta x = \frac{\Delta x}{2} \left(a + a + a' \Delta x + \frac{a'' (\Delta x)^2}{2} + \frac{a''' (\Delta x)^3}{6} + \dots \right) = \\ a\Delta x + \frac{a' (\Delta x)^2}{2} + \frac{a'' (\Delta x)^3}{4} + \frac{a''' (\Delta x)^4}{12} + \dots \end{gathered} \tag{38}$$

The truncation error is therefore:

$$TE_I = -\frac{a'' (\Delta x)^3}{12} - \frac{a''' (\Delta x)^4}{24} + \dots \tag{39}$$

The truncation errors will be evaluated assuming zero horizontal derivatives for simplicity (as in Mellor et al, 1994). The numerical approximation of X_j is:

$$\langle X_j \rangle = \langle \int_{\sigma_j}^{\sigma_{j+1}} \frac{\partial \rho}{\partial r} d\sigma \rangle = int \left(\langle \frac{\partial \rho}{\partial r} \rangle \right) \Big|_j^{j+1} \tag{40}$$

where the brackets indicate a numerical value in general, and *int* indicates a numerical integration. Calling TE_r the truncation error in the evaluation of the derivative, (40) can be written:

$$\langle X_j \rangle = int \left(\frac{\partial \rho}{\partial s} - TE_r \right) \Big|_j^{j+1} = int \left(\frac{\partial \rho}{\partial s} \right) \Big|_j^{j+1} - int (TE_r) \Big|_j^{j+1} \tag{41}$$

or, using (39):

$$\langle X_j\rangle = \int_{\sigma_j}^{\sigma_{j+1}} \frac{\partial\rho}{\partial s}\,d\sigma - \left(-\frac{(\Delta\sigma)^3}{12}\frac{\partial^3\rho}{\partial s\partial\sigma^2} - \frac{(\Delta\sigma)^4}{24}\frac{\partial^4\rho}{\partial s\partial\sigma^3} + \dots\right) - int(TE_r)\Big|_j^{j+1} \qquad (42)$$

The truncation error for the derivative along s is:

$$TE_r = \frac{\sigma}{6}\frac{\partial h}{\partial x}\frac{\partial^3\rho}{\partial z^3}\left(\sigma\frac{\partial h}{\partial x}\Delta x\right)^2 \qquad (43)$$

The truncation error for X_j is therefore:

$$\begin{aligned} TE_{X_j} = {} & \left(\frac{\sigma}{6}\frac{\partial h}{\partial x}\frac{\partial^3\rho}{\partial z^3}\left(\sigma\frac{\partial h}{\partial x}\Delta x\right)^2\bigg|_j + \frac{\sigma}{6}\frac{\partial h}{\partial x}\frac{\partial^3\rho}{\partial z^3}\left(\sigma\frac{\partial h}{\partial x}\Delta x\right)^2\bigg|_{j+1}\right)\frac{\Delta\sigma}{2} + \\ & \left(-\frac{(\Delta\sigma)^3}{12}\frac{\partial^3\rho}{\partial s\partial\sigma^2} - \frac{(\Delta\sigma)^4}{24}\frac{\partial^4\rho}{\partial s\partial\sigma^3} + \dots\right) \end{aligned} \qquad (44)$$

or, in cartesian coordinates:

$$\begin{aligned} TE_{X_j} = {} & \left(\frac{\sigma}{6}\frac{\partial h}{\partial x}\frac{\partial^3\rho}{\partial z^3}\left(\sigma\frac{\partial h}{\partial x}\Delta x\right)^2\bigg|_j + \frac{\sigma}{6}\frac{\partial h}{\partial x}\frac{\partial^3\rho}{\partial z^3}\left(\sigma\frac{\partial h}{\partial x}\Delta x\right)^2\bigg|_{j+1}\right)\frac{\Delta\sigma}{2} + \\ & - h\frac{\partial h}{\partial x}\frac{(\Delta\sigma)^3}{6}\frac{\partial^2\rho}{\partial z^2} - h^2\sigma\frac{\partial h}{\partial x}\frac{(\Delta\sigma)^3}{12}\frac{\partial^3\rho}{\partial z^3} - h^2\frac{\partial h}{\partial x}\frac{3(\Delta\sigma)^4}{24}\frac{\partial^3\rho}{\partial z^3} + \dots = \\ & \left(\frac{\sigma}{6}\frac{\partial h}{\partial x}\frac{\partial^3\rho}{\partial z^3}\left(\sigma\frac{\partial h}{\partial x}\Delta x\right)^2\bigg|_j + \frac{\sigma}{6}\frac{\partial h}{\partial x}\frac{\partial^3\rho}{\partial z^3}\left(\sigma\frac{\partial h}{\partial x}\Delta x\right)^2\bigg|_{j+1}\right)\frac{\Delta\sigma}{2} + \\ & - h\frac{\partial h}{\partial x}\frac{(\Delta\sigma)^3}{6}\frac{\partial^2\rho}{\partial z^2} - h^2\frac{\partial h}{\partial x}\frac{(\Delta\sigma)^3}{12}\frac{\partial^3\rho}{\partial z^3}\left(\sigma + \frac{3\Delta\sigma}{2}\right) + \dots \end{aligned} \qquad (45)$$

The truncation error for Y_j is simply:

$$TE_{Y_j} = -\frac{(\Delta\sigma)^3}{12}h^2\frac{\partial^2\rho}{\partial z^2} - \frac{(\Delta\sigma)^4}{24}h^3\frac{\partial^3\rho}{\partial z^3} + \dots \qquad (46)$$

Adding TE_{X_j} and TE_{Y_j} multiplied by $\frac{1}{h}\frac{\partial h}{\partial x}$:

$$
\begin{aligned}
& TE_j = TE_{X_j} + TE_{Y_j} = \\
& \left(\frac{\sigma}{6}\frac{\partial h}{\partial x}\frac{\partial^3\rho}{\partial z^3}\left(\sigma\frac{\partial h}{\partial x}\Delta x\right)^2\bigg|_j + \frac{\sigma}{6}\frac{\partial h}{\partial x}\frac{\partial^3\rho}{\partial z^3}\left(\sigma\frac{\partial h}{\partial x}\Delta x\right)^2\bigg|_{j+1}\right)\frac{\Delta\sigma}{2} + \\
& -\left(h\frac{\partial h}{\partial x}\frac{(\Delta\sigma)^3}{6} + h\frac{\partial h}{\partial x}\frac{(\Delta\sigma)^3}{12}\right)\frac{\partial^2\rho}{\partial z^2} - \left(h^2\frac{\partial h}{\partial x}\frac{(\Delta\sigma)^3}{12}\left(\sigma + \frac{3\Delta\sigma}{2}\right) + h^2\frac{\partial h}{\partial x}\frac{(\Delta\sigma)^4}{24}\right)\frac{\partial^3\rho}{\partial z^3} + \ldots = \\
& \left(\frac{\sigma}{6}\frac{\partial h}{\partial x}\frac{\partial^3\rho}{\partial z^3}\left(\sigma\frac{\partial h}{\partial x}\Delta x\right)^2\bigg|_j + \frac{\sigma}{6}\frac{\partial h}{\partial x}\frac{\partial^3\rho}{\partial z^3}\left(\sigma\frac{\partial h}{\partial x}\Delta x\right)^2\bigg|_{j+1}\right)\frac{\Delta\sigma}{2} + \\
& -h\frac{\partial h}{\partial x}\frac{(\Delta\sigma)^3}{4}\frac{\partial^2\rho}{\partial z^2} - h^2\frac{\partial h}{\partial x}\frac{(\Delta\sigma)^3}{12}(\sigma + \Delta\sigma)\frac{\partial^3\rho}{\partial z^3} + \ldots
\end{aligned}
\tag{47}
$$

The difficulty now is to make the summation of the TE_j from a generic position to the surface. We concentrate here on the third derivative terms (for which the truncation error depends both on Δx and Δσ), and we note that $\sigma_j+\Delta\sigma=\sigma_{j+1}$.

$$
\begin{aligned}
& \sum_{j=i}^{n-1} TE_j \approx \\
& \sum_{j=i}^{n-1}\left(\left(\frac{\sigma}{6}\frac{\partial h}{\partial x}\frac{\partial^3\rho}{\partial z^3}\left(\sigma\frac{\partial h}{\partial x}\Delta x\right)^2\bigg|_j + \frac{\sigma}{6}\frac{\partial h}{\partial x}\frac{\partial^3\rho}{\partial z^3}\left(\sigma\frac{\partial h}{\partial x}\Delta x\right)^2\bigg|_{j+1}\right)\frac{\Delta\sigma}{2} - h^2\frac{\partial h}{\partial x}\frac{(\Delta\sigma)^3}{12}\sigma_{j+1}\frac{\partial^3\rho}{\partial z^3}\right) = \\
& \left(\frac{\Delta\sigma}{12}\frac{\partial h}{\partial x}\frac{\partial^3\rho}{\partial z^3}\right)\sum_{j=i}^{n-1}\left(\sigma\left(\sigma\frac{\partial h}{\partial x}\Delta x\right)^2\bigg|_j + \sigma\left(\sigma\frac{\partial h}{\partial x}\Delta x\right)^2\bigg|_{j+1} - h^2(\sigma_{j+1})(\Delta\sigma)^2\right) = \\
& \left(\frac{\Delta\sigma}{12}\frac{\partial h}{\partial x}\frac{\partial^3\rho}{\partial z^3}\right)\sum_{j=i}^{n-1}\left(\sigma\frac{\partial h}{\partial x}\Delta x\right)^2\sigma\bigg|_j + \left(\left(\sigma\frac{\partial h}{\partial x}\Delta x\right)^2 - (h\Delta\sigma)^2\right)\sigma\bigg|_{j+1}
\end{aligned}
\tag{48}
$$

Clearly, the method is unconditionally consistent. The error is proportional to Δσ, which should mean that it would converge with Δσ alone. However, when we sum over depth, the sum of Δσ becomes σ.

Appendix D: Semi-Analytical Solution for Steady-State, Baroclinic, Wind-Driven Flow

In order to compute errors in Section 3.4.2, a semi-analytical solution for a forced baroclinic flow is derived here. Neglecting advective accelerations, horizontal diffusion and rotation, the steady state one-dimensional momentum equation (3.4) reduces to:

$$g\frac{\partial\eta}{\partial x} + \frac{gH}{\rho_0}\int_{\sigma}^{0}\frac{\partial\rho}{\partial x}d\sigma = \frac{A_v}{H^2}\frac{\partial^2 u}{\partial\sigma^2} \tag{3.49}$$

Equation (3.49) is solved with the boundary conditions:

$$\left.\frac{\partial u}{\partial\sigma}\right|_{\sigma=0} = \frac{H\tau_w}{A_v\rho_0} \qquad u|_{\sigma=-1} = 0 \tag{3.50}$$

where τ_w is the wind stress. The density field is fixed in time as:

$$\rho = \rho(z) + \rho_1\sigma^3 \tag{3.51}$$

where a cubic dependency on σ was chosen to give non-zero truncation errors for both the SCM and the CCM. Integrating (3.49) twice in the vertical and using the boundary conditions (3.50), we get:

$$u(\sigma) = \frac{gH^2}{A_v}\left(\frac{1}{2}\frac{\partial\eta}{\partial x}(\sigma^2-1) + \frac{1}{20}\frac{\partial\eta}{\partial x}\frac{\rho_0}{\rho_1}(\sigma^5+1) + \frac{1}{40}\frac{\partial H}{\partial x}\frac{\rho_0}{\rho_1}(\sigma^6-1)\right) + \frac{H\tau_w}{A_v\rho_0}(\sigma+1) \tag{3.52}$$

If one of the lateral boundaries is closed, continuity forces the depth-averaged velocity to be zero in the whole domain. Integrating (3.52) over depth and equating the result with zero, we can solve for the surface gradient:

$$\frac{\partial\eta}{\partial x} = \frac{1260\frac{\tau_w}{gH} - 54\frac{\partial h}{\partial x}\rho_1}{840\rho_0 - 51\rho_1} \tag{3.53}$$

Replacing (3.53) in (3.52), the velocity can be written:

$$u(\sigma) = \frac{H\tau_w}{A_v}\left\{\frac{1}{\rho_0}(\sigma+1) + \frac{630}{840\rho_0 - 51\rho_1}\left[(\sigma^2-1) + \frac{\rho_1}{20\rho_0}(\sigma^6+2\sigma^5+1)\right]\right\} +$$
$$\frac{g\rho_1 H^2}{A_v}\frac{\partial h}{\partial x}\left\{\frac{27}{840\rho_0 - 51\rho_1}\left[(\sigma^2-1) + \frac{\rho_1}{20\rho_0}(\sigma^6+2\sigma^5+1)\right] + \frac{1}{40\rho_0}(\sigma^6-1)\right\} \tag{3.54}$$

The model used in this paper treats baroclinic pressure diagnostically, i.e., this force is computed in the beginning of the run assuming η=0 and held constant in time. With this simplification, (3.53) and (3.54) become:

$$\frac{\partial\eta}{\partial x} \approx \frac{3\tau_w}{2gH\rho_0} - \frac{9}{140}\frac{\partial h}{\partial x}\frac{\rho_1}{\rho_0} \tag{3.55}$$

and,

$$u(\sigma) \approx \frac{H\tau_w}{4A_v\rho_0}(3\sigma^2+4\sigma+1) + \frac{g\rho_1 H^2}{280\rho_0 A_v}\frac{\partial h}{\partial x}(7\sigma^6-9\sigma^2+2) \tag{3.56}$$

Equation (3.55) is solved for η numerically, starting from the boundary where elevation is known. The total depth is then computed at each point, and (3.56) is solved for velocity.

References

Beckers, J.-M., 1991. Application of the GHER 3D General Circulation Model to the Western Mediterranean, *J. Mar. Syst.*, 1: 315-322.

Beckmann, A. and D.B. Haidvogel, 1993. Numerical Simulation of Flow Around a Tall Isolated Seamount. Part I: Problem Formulation and Model Accuracy, *J. Phys. Oceanogr.*, 23: 1736-1753.

Blumberg, A.F. and G.L. Mellor, 1987. A Description of a Three-Dimensional Coastal Ocean Circulation Model, in *Three-Dimensional Coastal Ocean Models*, N.S. Heaps (editor), Amer. Geoph. Union, Washington, D.C., 1-16.

Casulli, V. and R.T. Cheng, 1992. Semi-Implicit Finite Difference Methods for Three-Dimensional Shallow Water Flow, *Int. J. for Num. Met. in Fluids*, 15: 629-648.

Cheng, R.T. and P.E. Smith, 1990. A Survey of Three-Dimensional Numerical Estuarine Models, in *Estuarine and Coastal Modeling*, M.L. Spaulding (editor), Amer. Soc. Civ. Eng., 1-15.

Davies, A.M., 1985. Application of a Sigma Coordinate Sea Model to the Calculation of Wind-Induced Currents, *Cont. Shelf Res.*, 4: 389-423.

Davies, A.M., 1993a. A Bottom Boundary Layer-Resolving Three-Dimensional Tidal Model: a Sensitivity Study of Eddy Viscosity Formulation, *J. Phys. Oceanogr.*, 23: 207-224.

Davies, A.M., 1993b. Numerical Problems in Simulating Tidal Flows with a Frictional-Dependent Eddy Viscosity and the Influence of Stratification, *Int. J. for Num. Met. in Fluids*, 16: 105-131.

Deleersnijder, E. and J.-M. Beckers, 1992. On the Use of the σ-Coordinate System in Regions of Large Bathymetric Variations, *J. Mar. Syst.*, 3: 381-390.

Fortunato, A.B. and A.M. Baptista, 1993. *RITA2v User's Manual. 2D Vertical Hydrodynamic Model for River and Tidal Analysis. Part I - Flow Model*, OGI-CCALMR Software Documentation Series SDS7, 93-3, Oregon Graduate Institute of Science & Technology, Portland, Oregon.

Fortunato, A.B. and A.M. Baptista, 1994a. Modeling Near-Bottom Advective Acceleration in Surface Water Models, in *Computational Methods in Water Resources X*, Vol. 2, A. Peters, et al. (editors), Kluwer Academic Publishers, 1045-1052.

Fortunato, A.B. and A.M. Baptista, 1994b. Localized Sigma Coordinates for the Vertical Structure of Hydrodynamic Models, in *Estuarine and Coastal Modeling III*, M.L. Spaulding, et al. (editors), Amer. Soc. Civ. Eng., 323-335.

Fortunato, A.B. and A.M. Baptista, 1995. Vertical Discretization in Tidal Flow Simulations, *Int. J. for Num. Met. in Fluids* (in press).

Hagen, S.C. and J.J. Westerink, 1995. Finite Element Grid Resolution Based on Second and Fourth Order Truncation Error Analysis, in *Proc. 2nd Int. Conf. Computer Modeling of Seas and Coastal Regions* (to appear).

Haney, R.L., 1991. On the Pressure Gradient Force over Steep Topography in Sigma Coordinate Models, *J. Phys. Oceanogr.*, 21: 610-619.

Janin, J.M., F. Lepeintre and P. Péchon, 1994. TELEMAC-3D: A Finite Element Code to Solve 3D Free Surface Flow Problems, in *Computer Modelling of Seas and Coastal Regions*, P.W. Partridge, et al. (editors), Computational Mechanics Publications, 489-506.

Janjic, Z.I., 1977. Pressure Gradient Force and Advection Scheme Used for Forecasting with Steep and Small Scale Topography, *Contrib. Atmospheric Phys.*, 50: 186-199.

Jonhson, B.H., K.W. Kim, Y.P. Sheng and R.E. Heath, 1990. Development of a Three-Dimensional Hydrodynamic Model of Chesapeake Bay, in *Estuarine and Coastal Modeling*, M.L. Spaulding (editor), Amer. Soc. Civ. Eng., 162-171.

Kinmark, I.P.E., 1985. *The Shallow Water Equations: Formulation, Analysis and Application*, Lecture Notes in Engineering, 15, C.A. Brebia and S.A. Orszag (editors), Springer-Verlag, Berlin, 187 pp.

Laible, J.P., 1992. On the Solution of the Three-Dimensional Shallow Waters Equations Using the Wave Equation Formulation, in *Computational Methods in Water Resources IX, Vol. 2*, T.F. Russel, et. al. (editors), Computational Mechanics Publications, 545-552.

Leendertse, J.J., 1989. Discussion of "Turbulence Modeling of Surface Water Flow and Transport: Part IV", *J. Hydraulic Engrg.*, 115: 603-606.

Luettich, R.A., J.J. Westerink and N.W. Sheffner, 1991. *ADCIRC: An Advanced Three-Dimensional Circulation Model for Shelves, Coasts and Estuaries. Report 1: Theory and Methodology of ADCIRC 2DDI and ADCIRC-3DL*, Department of the Army, US Army Corps of Engineers.

Lynch, D.R. and F.E. Werner, 1991. Three-Dimensional Hydrodynamics on Finite Elements. Part II: Non-Linear Time-Stepping Model, *Int. J. for Num. Met. in Fluids*, 12: 507-533.

McCalpin, J.D., 1994. A Comparison of Second Order and Fourth-Order Pressure Gradient Algorithms in a σ-Co-ordinate Ocean Model, *Int. J. for Num. Met. in Fluids*, 18: 361-383.

Mellor, G.L., and A.F. Blumberg, 1985. Modeling Vertical and Horizontal Diffusivities with the Sigma Coordinate System, *Mon. Weather Rev.*, 113: 1379-1383.

Mellor, G.L, T. Ezer and L.-Y. Oey, 1994. The Pressure Gradient Conundrum of Sigma Coordinates Ocean Models, *J. Atmos. Oceanic. Technol.*, 11, 4: 1126-1134.

Paul, J.F., 1994. Observations Related to the Use of the Sigma Coordinate Transformation for Estuarine and Coastal Modeling Studies, in *Estuarine and Coastal Modeling III*, M.L. Spaulding, et al. (editors), Amer. Soc. Civ. Eng., 336-350.

Phillips, N.A., 1973. Principles of Large Scale Numerical Weather Prediction, in *Dynamic Meteorology*, P. Morel (editor), Reidel, Dordrecht, 1-96.

Rousseau, D. and H.L. Pham, 1971. Premiers Résultats d'un Modèle de Prévision Numérique à Courte Echéance sur l'Europe, *La Météorologie*, 20: 1-12.

Signell, R.P., H.L. Jenter and A.F. Blumberg, 1994. Modeling the Seasonal Circulation in Massachusetts Bay, in *Estuarine and Coastal Modeling III*, M.L Spaulding, et al. (editors), Amer. Soc. Civ. Eng., 578-590.

Spall, M.A. and A.R. Robinson, 1990. Regional Primitive Equation Studies of the Gulf Stream Meander and Ring Formation Region, *J. Phys. Ocean.*, 20: 985-1016.

Walters, R.A., 1992. A 3D, Finite Element Model for Coastal and Estuarine Circulation, *Cont. Shelf Res.*, 12: 83-102.

Walters, R.A. and M.G.G. Foreman, 1992. A 3D, Finite Element Model for Baroclinic Circulation on the Vancouver Island Continental Shelf, *J. Mar. Syst.*, 3: 507-518.

Westerink, J.J., J.C. Muccino and R.A. Luettich, Jr., 1992. Resolution Requirements for a Tidal Models of the Western North Atlantic and Gulf of Mexico, in *Computational Methods in Water Resources IX, Vol. 2*, T.F. Russel, et al. (editors), Computational Mechanics Publications, 667-674.

Westerink, J.J., R.A. Luettich, Jr. and J.C. Muccino, 1994a. Modeling Tides in the Western North Atlantic Using Graded Unstructured Grids, *Tellus*, Special Issue of JONS-MOD'92: 178-199.

Westerink J.J., R.A. Luettich, Jr. and S.C. Hagen, 1994b. Meshing Requirements for Large Scale Coastal Ocean Tidal Models, in *Computational Methods in Water Resources X, Vol. 2*, A. Peters, et al. (editors), Kluwer Academic Publishers, 1323-1330.

CHAPTER 4[1]

Vertical Discretization in Tidal Flow Simulations

Abstract

We propose an empirical law for vertical nodal placement in tidal simulations that depends on a single parameter, p. The influence of dimensionless numbers on the optimal value of p is analysed through a series of numerical experiments for an individual vertical, and a single value of p is found to be adequate for all cases. The proposed law can lead to gains in accuracy of over two orders of magnitude relative to a uniform grid, and compares favorably with non-uniform grids previously used in the literature. In practical applications, the most effective use of this law may require each vertical to have a different number of nodes. Criteria for the distribution of the total number of nodes among different verticals are also proposed, based on the concept of equalizing errors across the domain. The usefulness of the overall approach is demonstrated through a two-dimensional laterally-averaged application to a synthetic estuary.

4.1 Introduction

Two general approaches have been used for the horizontal discretization of the flow and transport equations in estuarine and coastal models: unstructured (typically finite elements) and structured (primarily finite differences) grids. While finite elements allow

---

1. Accepted for publication in the International Journal for Numerical Methods in Fluids.

for far superior flexibility in the description of irregular boundaries and in the placement of local refinements, finite difference grids lead to simpler and arguably more efficient (in a node per node basis) algorithms.

By contrast, structured grids have been the norm for vertical discretization. Methods using both orthogonal (z-coordinate, Leendertse and Liu, 1975, Casulli and Cheng, 1992) and curvilinear (sigma coordinate, Blumberg and Mellor, 1987, Lynch and Werner, 1991, Walters, 1992) grids have been extensively used. Sigma coordinates are probably the most popular (see review by Cheng and Smith, 1990), offering three main advantages relative to the z-coordinates: a) a better resolution of shallow areas; b) a smooth representation of the bottom topography; and, c) a simpler treatment of the free surface. The major disadvantage associated with the sigma coordinates is the potential for generation of large errors in the evaluation of horizontal gradients near steep slopes (e.g., Gary, 1973, Haney, 1991, Deleersnijder and J.M. Beckers, 1992). However, several techniques can be used to reduce these errors considerably (Signell et al., 1994, McCalpin, 1994, Stelling, G.S. and J.A.TH.M. Van Kester, 1994). Moreover, z-coordinate models can also suffer from similar problems (Fortunato and Baptista, 1994a, 1995).

Recently, we proposed what can be seen as the loose vertical equivalent to horizontal unstructured grids (Fortunato and Baptista, 1994b). Denoted *localized sigma coordinates* (LSC), this approach combines the main advantages, as well as disadvantages, of the traditional *domain-wide sigma coordinates* (DWSC) with a higher flexibility to discretize the vertical direction: the nodal placement is independent for each vertical, thus local refinements do not carry over to the rest of the domain.

The concept behind LSC is simple. As in DWSC, the height of the water column is linearly mapped into a fixed interval. However, LSC recognize the solution of the internal mode as an essentially one-dimensional, *localized* problem, rather than divide the domain in levels. Therefore, each vertical is discretized independently from the others. Horizontal gradients of depth dependent quantities, which constitute the only direct link between nodes in adjacent verticals, can be computed either in cartesian or in sigma coordinates, by interpolating the necessary quantities at neighboring verticals (Laible, 1992, Fortunato and Baptista, 1994a, 1994b, 1995). Interpolations increase slightly the computational costs (Fortunato and Baptista, 1994b), and may make LSC more awkward to implement on some computer architectures. In the examples presented in this paper, these interpolations are avoided by considering only barotropic flows and neglecting advection and horizontal diffusion.

The use of unstructured grids in the vertical direction can lead to important computational savings relative to the methods currently used. For instance, stratified areas require a fine local discretization (Davies, 1993a), which cannot be achieved efficiently using unstructured grids. Also, one of the trends in ocean modeling is to simulate increasingly larger domains, including simultaneously both deep ocean areas and shallow coastal seas (Westerink et al., 1994a). Clearly, different areas will typically require a different vertical resolution. In deep areas, friction is unimportant, and a coarse resolution is sufficient near the bottom as long as a slip bottom boundary condition is used; in contrast, a good representation of the bottom boundary layer is needed in shallow areas.

Still, one cannot take full advantage of the flexibility of the LSC without appropriate criteria to discretize the vertical dimension. The primary purpose of this paper is to develop a criterion for vertical nodal placement. Because a very large number of parameters can potentially influence an optimal discretization, this study is restricted to unstratified tidal flows. In spite of the relative simplicity of these flows, the criterion proposed herein can greatly reduce the errors in tidal simulations relative to vertically uniform grids, and provide useful guidelines for the simulation of more complex flows.

The criterion developed here addresses both the nodal distribution in a single vertical and the horizontal distribution of the total number of nodes among different verticals. This criterion can be applied on three different levels of complexity. While the two more complex forms lead to a varying number of nodes per vertical (thus requiring the use of LSC), the simplest form can also be applied to DWSC models.

Previous work on vertical discretization strategies is surprisingly scarce. Noye (1984) proposed the use of a "kappa grid", which allows a higher resolution near the bottom. Errors relative to a uniform grid are significantly reduced, while maintaining second-order accuracy in $\Delta\sigma$ (Noye and Stevens, 1987). However, optimal kappa grids vary strongly with frictional parameters, making the method difficult to use in practice. Davies (1991) compared four approaches to discretize the vertical (a kappa grid, logarithmic and log-linear grids, and a spectral method), and found the spectral method and the log-linear grid to provide the fastest convergence. However, either one or two parameters need to be specified in all these four methods, and no criteria for their specification were proposed. The method presented herein compares favorably with the logarithmic and log-linear grids.

This paper includes five sections in addition to the introduction. ***Numerical Formulation and Dimensionless Numbers*** describes the model used in the numerical tests, and introduces the relevant dimensionless numbers. ***Nodal Distribution in a Single Vertical*** introduces two types of grids, and establishes the optimal distribution of the nodes in a single vertical based on the effect of the dimensionless numbers. ***Horizontal Nodal Distribution*** addresses the distribution of the total number of nodes among the different verticals. ***Application*** presents an application to a two-dimensional laterally-averaged synthetic estuary, to illustrate the gains in accuracy achieved with the optimized grids. The final section presents a summary and some concluding remarks.

4.2 Numerical Formulation and Dimensionless Numbers

The propagation of tides is generally modeled with the shallow water equations, which describe the conservation of mass and momentum under the conventional hydrostatic pressure and Boussinesq approximations. Here we further neglect advective accelerations and rotation effects, in order to decouple the two horizontal momentum equations. Advective accelerations can be neglected because they are usually small compared to the gravity term, and rotation was shown to have little effect on the convergence of several numerical methods to solve the vertical structure of tidal flows (Davies, 1991). With these simplifications, each momentum equation can be written:

$$\frac{\partial u}{\partial t} = -g\frac{\partial \eta}{\partial x} + \frac{\partial}{\partial z}\left(A_v \frac{\partial u}{\partial z}\right) \tag{4.1}$$

where:

x,z are the cartesian coordinates;

t is time;

u is the horizontal velocity;

η is the elevation of the water surface;

g is the gravitic acceleration; and,

A_v is the vertical eddy viscosity.

Most three-dimensional shallow water numerical models decouple the treatment of the horizontal and vertical dimensions, in an explicit recognition of the different space and time scales involved. The decoupling is usually accomplished by the introduction of external and internal modes. Loosely stated, the external mode determines the elevations (and, in some case, the depth-averaged velocities), while the internal mode resolves the vertical structure of the flow.

Consistent with the objectives of this paper, we will concentrate here on the internal mode. To isolate this mode, we assume an elevation field of the form:

$$\eta = A\cos\left(\frac{2\pi t}{T} + \phi\right) \tag{4.2}$$

where A, T and ϕ are the wave amplitude, period and phase, respectively. The gravity forcing can then be written as:

$$g\frac{\partial\eta}{\partial x} = g\frac{\partial A}{\partial x}\cos\left(\frac{2\pi t}{T}+\phi\right) - gA\frac{\partial\phi}{\partial x}\sin\left(\frac{2\pi t}{T}+\phi\right) \tag{4.3}$$

or, after re-arrangement:

$$g\frac{\partial\eta}{\partial x} = -\frac{2\pi U}{T}\cos\left(\frac{2\pi t}{T}+\phi+\phi'\right) \tag{4.4}$$

where we introduce a free stream velocity U and a phase ϕ' defined as:

$$U = \frac{gT}{2\pi}\sqrt{\left(\frac{\partial A}{\partial x}\right)^2 + \left(A\frac{\partial\phi}{\partial x}\right)^2} \tag{4.5}$$

and:

$$\phi' = \operatorname{atan}\left(\left(A\frac{\partial\phi}{\partial x}\right)/\frac{\partial A}{\partial x}\right) \tag{4.6}$$

Physically, the free stream velocity represents the velocity amplitude in the absence of friction. In deep waters, where the effect of dissipation is restricted to the bottom layer, U represents closely the actual velocity amplitude near the surface.

Equation (4.1) is solved assuming a zero stress at the surface, and using a quadratic bottom slip condition:

$$\left.\frac{\partial u}{\partial z}\right|_{z=0} = 0 \qquad \left.\frac{\partial u}{\partial z}\right|_{z=-h} = c_d|u_b|u_b \tag{4.7}$$

Here c_d is a dimensionless friction coefficient, h is depth and the subscript b represents values at the bottom. A rigid-lid approximation is used for simplicity.

In order to reduce the number of physical parameters involved, (4.1) and (4.7) are written in dimensionless form. Dimensionless quantities are defined as:

$$\begin{array}{ccc} v = u/U & \tau = t/T & \sigma = z/h \\ E = A_v/(hU) & \Gamma = (UT)/h & \end{array} \tag{4.8}$$

The momentum equation becomes:

$$\frac{\partial v}{\partial \tau} = 2\pi\cos(2\pi\tau + \phi + \phi') + \Gamma\frac{\partial}{\partial\sigma}\left(E\frac{\partial v}{\partial\sigma}\right) \tag{4.9}$$

and the boundary conditions:

$$\left.\frac{\partial v}{\partial\sigma}\right|_{\sigma = 0} = 0 \qquad E_b\left.\frac{\partial v}{\partial\sigma}\right|_{\sigma = -1} = c_d|v_b|v_b \tag{4.10}$$

Examination of the above equations suggests that three dimensionless numbers determine the behavior of the solution: Γ, c_d and E. While Γ and c_d are relatively simple to determine, E can vary both in time and along the vertical. For simplicity, E is assumed to be time-independent, an assumption that will be relaxed later. Furthermore, a simple (yet realistic) vertical profile is used to keep the number of parameters to a minimum:

$$E = \begin{cases} E_b + (1+\sigma)\left(\dfrac{E_c - E_b}{0.2}\right) & -1 \le \sigma \le -0.8 \\ E_c \quad -0.8 \le \sigma \le 0 \end{cases} \tag{4.11}$$

where E_b and E_c represent the dimensionless eddy viscosity at the bottom and in the bulk of the water column, respectively. This form of eddy viscosity profile is supported by observations (Bowden and Fergussen, 1980) and has been used by a number of modelers (Walters, 1992, Davies, 1993b).

The numerical solution of (4.9) and (4.10) forms the basis of our vertical model. The momentum equation is discretized in space with linear finite elements. All terms are centered in time except the viscosity term which is treated implicitly for stability.

4.3 Nodal Distribution in a Single Vertical

The optimization of the nodal distribution for a single vertical is accomplished in four steps. First, we define physically relevant ranges for the dimensionless numbers introduced in the previous Section (Γ, c_d, E_b and E_c). Then, we select a general expression for nodal placement, controlled by a single parameter (p) for simplicity. Next, several experiments are carried out to study the effect of each dimensionless number on the optimal value of p. Finally, the results from the optimal grid are compared against those obtained with previously proposed vertical discretizations (Davies, 1991).

4.3.1 Dimensionless Numbers

The free stream velocity scales as $U \sim A\sqrt{g/h}$ (Equation (4.5)), and Γ can be scaled as $\Gamma \sim AT\sqrt{g/h^3}$. Assuming ranges of T, h and A of 10^4-10^5s, 1-1000m and 0.1-10m respectively, Γ varies between 10^{-1} and 10^5. (The combination A=10m, h=1m was not considered realistic.) Values of the friction coefficient c_d used in the literature vary between 0.0025 (minimum recommended by Blumberg and Mellor, 1987) and 0.05 (as an extreme case, Walters (1992) uses up to 0.07 in Delaware Bay). The dimensionless bottom eddy viscosity scales as $E_b \sim (\kappa z_0\sqrt{|\tau_b|/\rho})/(hU) \sim (\kappa z_0\sqrt{c_f})/h$, where κ is the von Kármán constant, z_0 is the roughness length, τ_b is the bottom friction and c_f is a dimensionless friction coefficient for depth-averaged models. Using values of z_0 between 0.001 and 0.1 m, and values of c_f between 10^{-3} and 5×10^{-3} suggests a range of E_b between 10^{-8} and 10^{-3}. Finally, Davies and Aldridge (1993) suggest $E_c = 0.0025(\bar{u}/U)$, where u represents the depth-averaged velocity. We will therefore take E_c between 10^{-3} and 10^{-2}.

One should distinguish between the physically meaningful parameters, Γ and E_b, and those that arise from numerical considerations. Γ represents the dimensionless forcing period, while E_b is related to the dimensionless bottom roughness. The friction coefficient c_d arises from the non-consideration of the high-shear near-bottom layer in many numerical models. If a no-slip bottom boundary condition is used, c_d is set to infinity and thus eliminated as a controlling number. Finally, E_c is physically determined by the other numbers. However, in a numerical model it can be set independently, and therefore it was kept here for completeness. An additional parameter governing wave properties in channels relates to the rate of variation of the cross-sectional area (Prandle and Rahman, 1980, Jay, 1991). This parameter is not considered here because it does not affect the vertical structure of the flow.

4.3.2 Vertical Grids

Two expressions for nodal placement which allow a finer grid spacing near the bottom are studied. The first expression ("grid α") was originally proposed for baroclinic flows (Haney, 1991):

$$\sigma_i = -\left(\frac{i-n}{1-n}\right)^p \qquad i = 1, n \tag{4.12}$$

where n is the number of nodes, and p determines the degree of near-bottom resolution. A uniform grid in the σ domain corresponds to $p=1$, and decreasing (increasing) values of p lead to increasingly finer grids near the bottom (surface). The second expression ("grid β") is given by:

$$\sigma_i = \left(\frac{1-i}{1-n}\right)^{1/p} - 1 \qquad i = 1, n \tag{4.13}$$

Grid β represents an adjustment introduced in this work to better reflect the physics of tidal flows. The variation of vertical profiles of velocity in tidal flows is very rapid near the bottom, and decreases upward. In order to obtain accurate results efficiently, the vertical grid spacing should vary in a similar manner. As a first order approximation, the vertical grid spacing is given by the derivatives of the continuous forms of (4.12) and (4.13), for α and β, respectively:

$$a'(x) = \frac{p}{n-1}\left(\frac{x-n}{1-n}\right)^{p-1} \qquad b'(x) = \frac{1}{p}\left(\frac{1-x}{1-n}\right)^{\frac{1}{p}-1} \tag{4.14}$$

where $x \in [1,n]$ and $p \in]0,1[$. Function b' is parabolic and can therefore represent a typical velocity profile much better than a' which is hyperbolic.

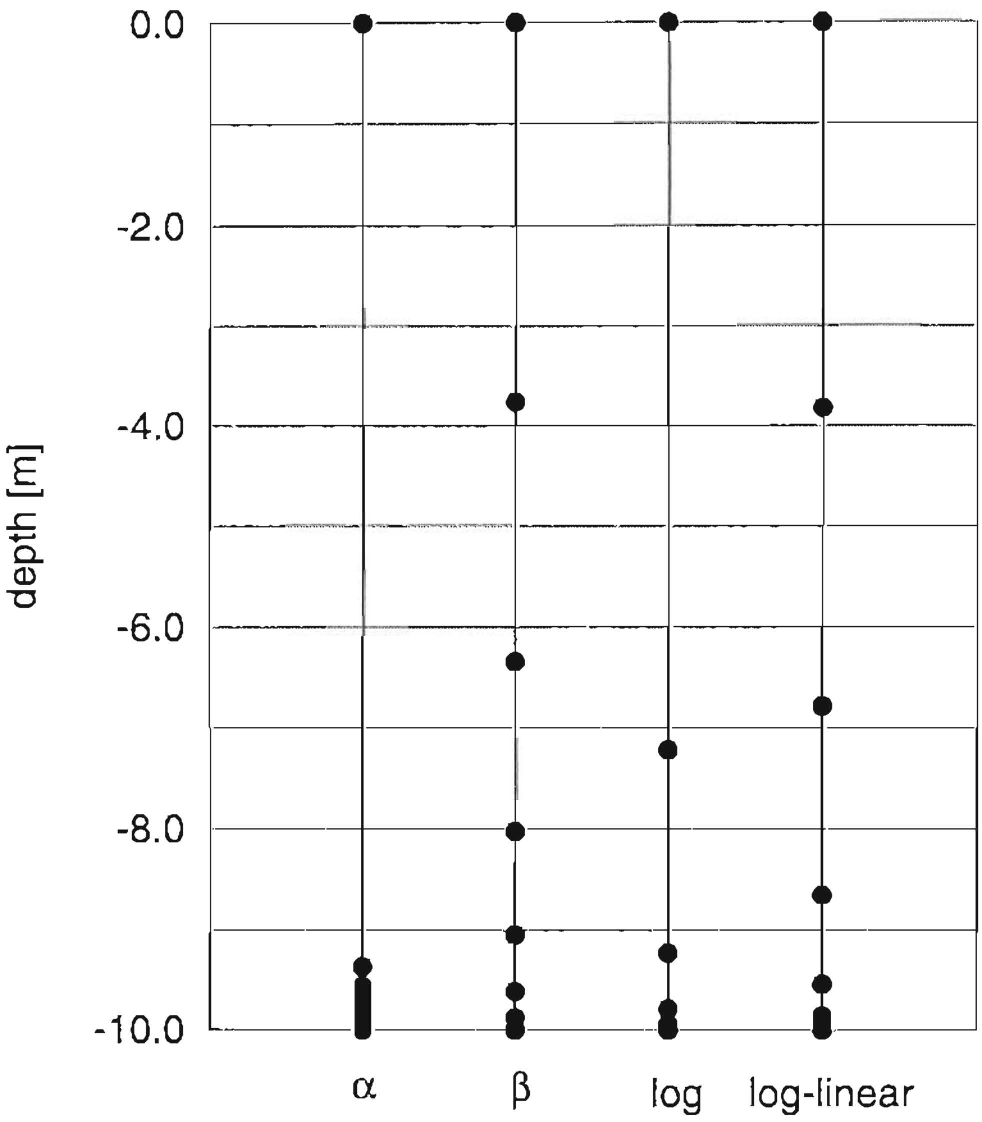

Figure 4.1 Examples of 10-node α (p=0.03) and β (p=0.25) grids, for 10 m depth. Logarithmic and log-linear grids (Davies, 1991) are also included for comparison.

The difference between grids α and β is illustrated in Figure 4.1. In grid α, the reduction of spatial resolution near the bottom is slower than the corresponding increase of resolution near the surface, while the reverse occurs with formulation β. As a result, properly resolving the bottom layer with grid α can lead to too coarse a resolution near the surface, a problem that grid β avoids. Relative to the logarithmic and log-linear grids proposed by Davies (1991), both the α and β grids have two convenient advantages: they include the uniform grid as a particular case, and the first node (i=1) is naturally placed at the bottom. Although the log-linear and β grids appear very similar at the scale shown in Figure 4.1, the β grid is fairly coarser near the bottom.

The performance of grids α and β is compared using the default values of the dimensionless numbers (Table 4.1). A dimensionless time step of 10^{-3} is used in all simulations. The model is run for ten tidal cycles and the time series of velocity at each node from the last cycle are harmonically analyzed to extract the amplitudes and phases of the two relevant dimensionless frequencies, F_1 (the forcing frequency) and F_3 (the third harmonic, generated by non-linear friction). Results are compared with those obtained using a very fine reference grid, with 10^4 nodes and a time step of 10^{-4}. We chose a β grid with p=0.6 as reference, because uniform grids did not provide enough resolution near the bottom, even for as many as 10^4 nodes. The accuracy of the reference grid was verified by running one of the tests with a 10^5 nodes grid and comparing the results. L2-norms of amplitudes and phases are computed for each frequency as:

$$L_2(\theta_r) = \sqrt{\int_{-1}^{0} (\theta_r - \tilde{\theta}_r)^2 d\sigma} \tag{4.15}$$

where θ represents a generic variable, the subscript r represents either amplitudes or phases, and the tilde stands for the reference solution. Note that only relative amplitude errors can be computed since U is not known.

Amplitude and phase errors for Test 1 are shown in Figure 4.2 as a function of p for both grid types. Grid β is much better than grid α: not only is the optimal value of p, p_{opt}, only weakly dependent on the number of nodes, but errors are much smaller. The weak dependence of p_{opt} on the number of nodes will prove very convenient to establish criteria for node placement. Because of the need to resolve properly the bottom layer, p_{opt}

for the α grids tends to be very small, resulting in grids much too coarse in most of the water column (e.g., n=30 and p=0.05 leads to $\Delta\sigma$=0.845 at the surface). This is similar to the behavior reported by Davies (1991) for the kappa grid, and explains the poorer accuracy relative to grids β. Grid α is therefore abandoned hereafter.

Table 4.1 Parameters used in Tests 1-5. Default values are shown in bold.

Test	Γ	c_d	E_b	E_c
1	**10^4**	**0.005**	**10^{-5}**	**0.0025**
2	10^{-1}, 10^0, 10^1, 10^2, 10^3, **10^4**, 10^5	0.005	10^{-5}	0.0025
3	**10^4**	0.0025, **0.005**, 0.01, 0.05	10^{-5}	**0.0025**
4	**10^4**	**0.005**	10^{-8}, 10^{-7}, 10^{-6}, 10^{-5}, 10^{-4}, 10^{-3}	**0.0025**
5	**10^4**	**0.005**	10^{-5}	0.001, **0.0025**, 0.01

Test 1 illustrates the importance of using non-uniform grids. Not only are the errors with regular grids very large (p=1 in Figure 4.2), but the convergence of the solutions is slow relative to an optimized β grid. In particular, insufficient resolution near the bottom can lead to a serious underprediction of velocities in the entire water column (Figure 4.3).

The results for the β grid (Figure 4.2) also suggest that p_{opt} is the same for both F_1 and F_3, and for both amplitudes and phases. We will take advantage of these two properties in the discussion of remaining 1D tests, where we will only show results for the amplitudes of the primary constituents.

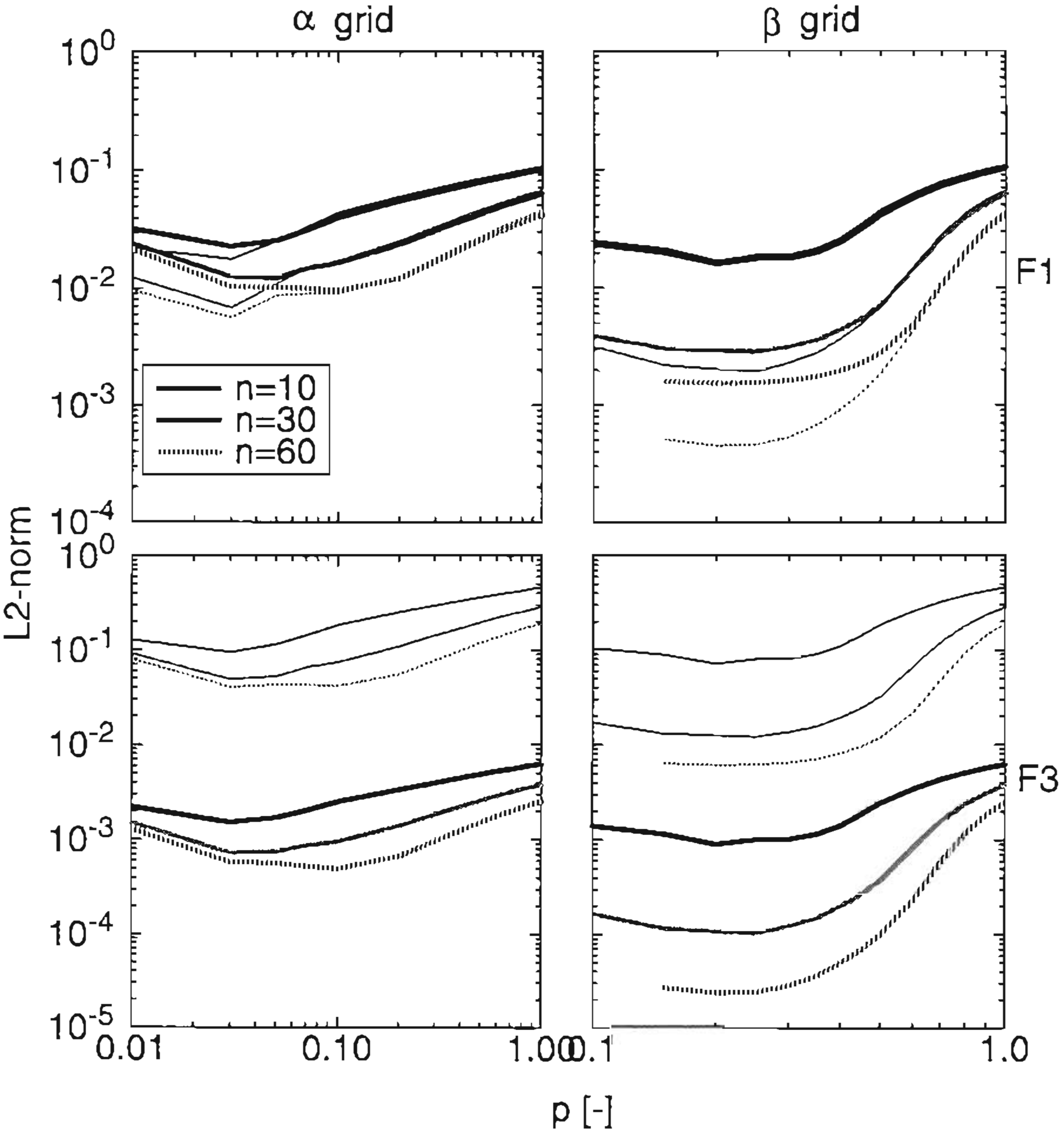

Figure 4.2 Test 1. L_2-norms of velocities for α and β grids. Thick lines: amplitudes [-]; thin lines: phases [rad].

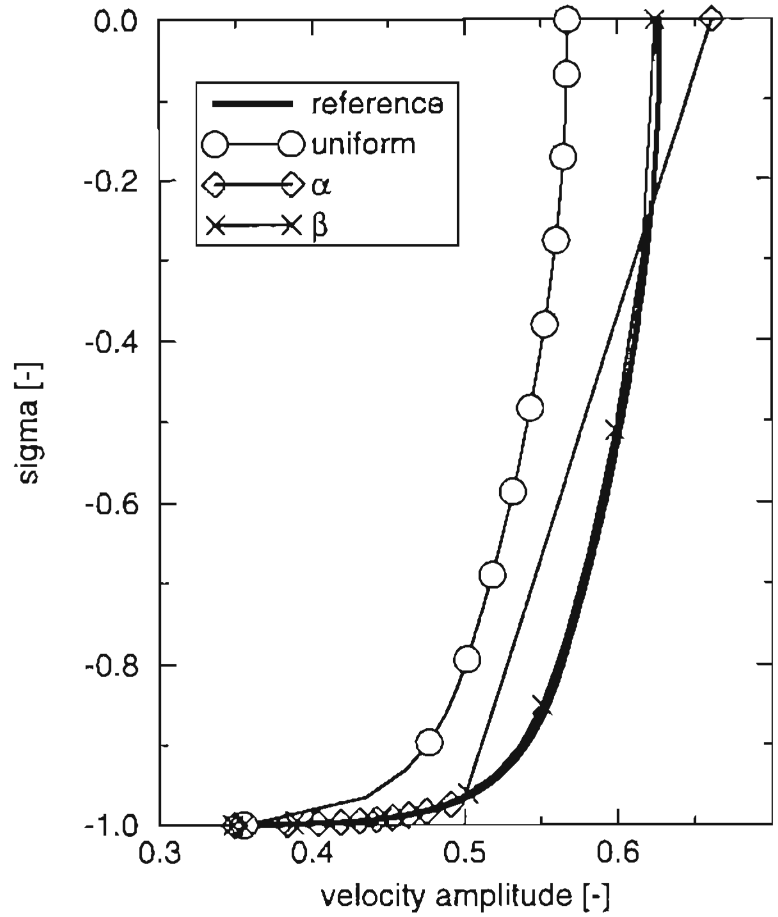

Figure 4.3 Test 1. Profiles of F_1 velocity amplitude obtained with different 30 node grids. The α and β grids are the optimal for this test (p equals 0.05 and 0.25, respectively).

We note, however, that the independence of p_{opt} from the frequency does not necessarily extend to more complex conditions, including higher dimensions. Indeed, we believe that this independence results, in our 1D tests, from two reasons. First, F_3 is generated by F_1, thus errors in the primary constituent will be reflected in the overtides. Secondly, profiles for both F_1 and F_3 have very large gradients near the bottom, although for different reasons: the primary constituent decreases sharply near this boundary due to friction, while the non-linear constituent is generated at the bottom, and diffuses slowly upward. In more realistic simulations, F_3 may have smaller gradients near the bottom, both because it can be forced directly by gravity, and because it is also generated in the water column by the interaction between velocity and the time-dependent eddy viscosity (Davies, 1990). Under these circumstances, p_{opt} may depend more strongly on the specific constituent than implied by our tests.

4.3.3 Optimization

Tests 2-5 examine the effect of the dimensionless numbers Γ, c_d, E_b, and E_c on p_{opt}. In each test, a number is varied while the others are held constant (Table 4.1). The vertical profiles of the F_1 amplitude (Figure 4.4) suggest that the various dimensionless numbers have very different effects on p_{opt}:

- As Γ increases, the bottom boundary layer includes a growing portion of the water column, which should increase p_{opt}. Still, significant shear remains near the bottom even for the larger values of Γ, thus p_{opt} should remain small.
- The friction coefficient c_d controls the magnitude of the velocities but has very little effect on the shape of the velocity profile, and therefore should not affect p_{opt} significantly.
- Increasing E_b has two effects. First, it reduces velocities just like decreasing c_d does (see Equation (4.10)); secondly, it reduces shear at the bottom by making eddy viscosity more uniform over depth. This second effect will make p_{opt} increase with E_b, as fewer nodes will be needed to resolve the bottom layer.
- Reducing E_c also leads to a more uniform eddy viscosity, thus to a larger p_{opt}.

This qualitative analysis is supported by the results of numerical experimentation. Indeed, concentrating on the variation of the L2-norms of velocity amplitudes with p, we observe that:

- When Γ increases, p_{opt} rises very mildly (Figure 4.5). Still, the error curves are almost flat in a large region around p_{opt} (around 0.15-0.3), thus the effect of Γ on p_{opt} is secondary. The major consequence of increasing Γ is the error growth: the minimum L2-norm grows by about two orders of magnitude when Γ goes from 10^{-1} to 10^4. For $\Gamma=10^5$ the errors decrease, possibly because the friction becomes a dominant process and the dimensionless velocities decrease by almost an order of magnitude (Figure 4.4).
- The effect of c_d on the errors is very mild (Figure 4.6). The L2-norms decrease slightly with c_d due to the reduction of the velocity, but p_{opt} remains unchanged.

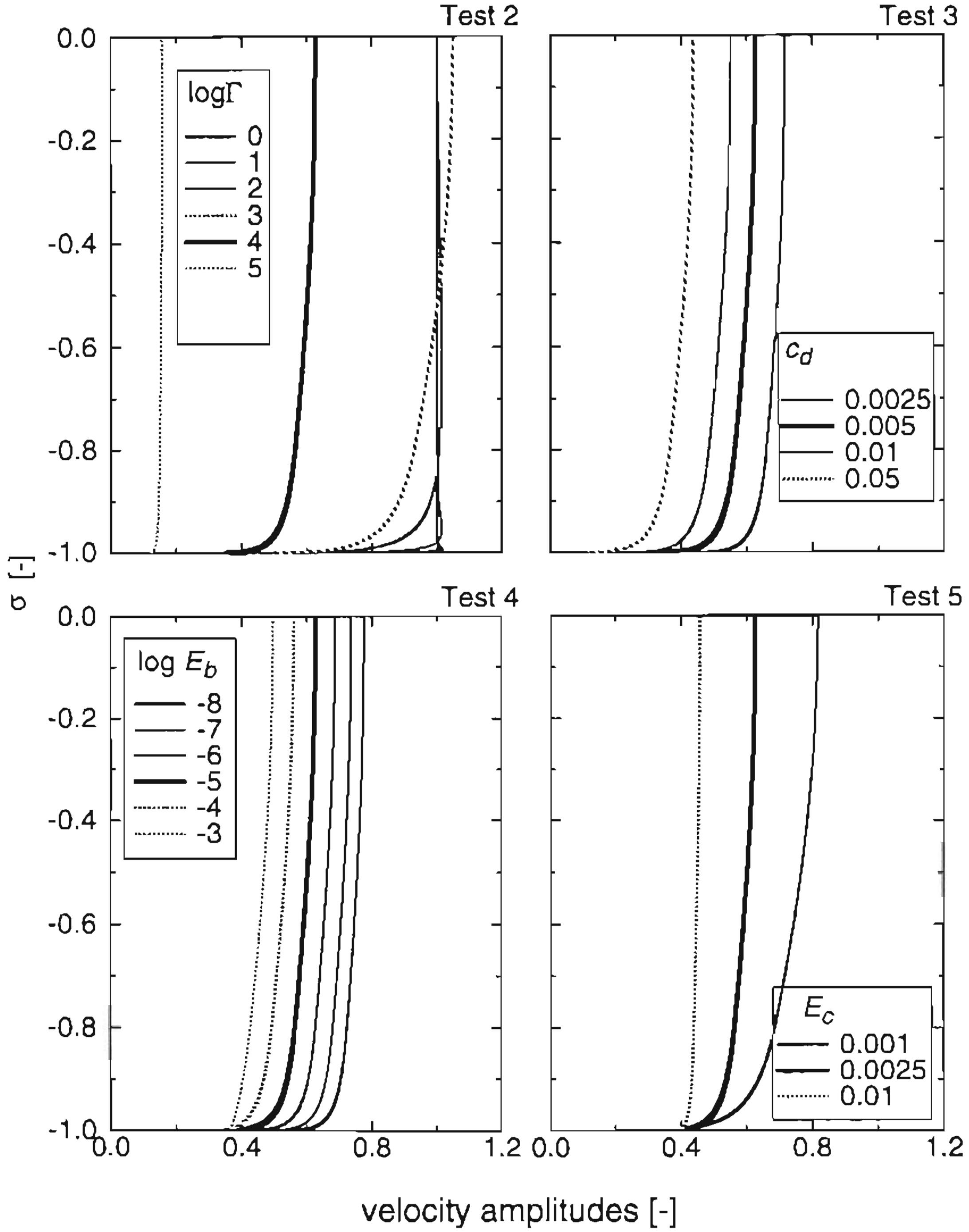

Figure 4.4 Tests 2-5. Velocity amplitudes (reference simulations).

- The bottom dimensionless eddy viscosity has a dramatic impact on the L2-norm behavior (Figure 4.7), just as it had on the velocity profiles. The value of p_{opt} tends to increase with E_b due to a reduction of shear. However, the main effect of the loss of vertical structure of the flow is the flattening of the L2-norm curves. As an example, for $E_b=10^{-3}$ and $n=30$, the difference between the maximum and minimum L2-norms is less than 20%. Therefore, using a small value of p for large E_b will not affect the errors significantly.
- E_c has only a minor effect on the error curves, perhaps due to the small range of variation of this number (Figure 4.8). Again, these curves tend to flatten as E_c approaches E_b, but p_{opt} remains mostly unchanged.

In general, Tests 2-5 suggest that a single value of p_{opt} (around 0.2-0.3) may be retained. Even though it seems possible to determine a relationship between p_{opt} and the four dimensionless numbers using some kind of optimization technique, eventual gains in accuracy should be marginal. Furthermore, in practical applications with complex turbulence models, the determination of E_b and E_c is difficult, if at all possible. Last but not least, DWSC models require a constant p_{opt}. Therefore, we suggest 0.25 as an appropriate value for p_{opt}. This value will be used from here on.

While p_{opt} is fairly independent from the controlling dimensionless numbers, one must realize that actual errors are not. Indeed, the L2-norms in tests 2-5 show a significant dependency on Γ (Figure 4.5) and, to a lesser extent, on E_b (Figure 4.7); only the dependence on c_d (Figure 4.6) and E_c (Figure 4.8) is weak.

The strong dependence of the errors with Γ is consistent with previous analysis. Ianniello (1977) shows that velocity profiles depend most strongly on $d_0 = h/(\sqrt{(2A_v)/w})$. Scaling A_v as Uh, $\Gamma=1/d_0^2$. Similarly, Luettich et al. (1994) show that velocity profiles and bottom stress depend mainly on $\Omega=h(w\pm f)/U_{*b}$, where f is the Coriolis parameter and U_{*b} is the bottom friction velocity. This suggests that our analysis can easily be extended to include rotation effects.

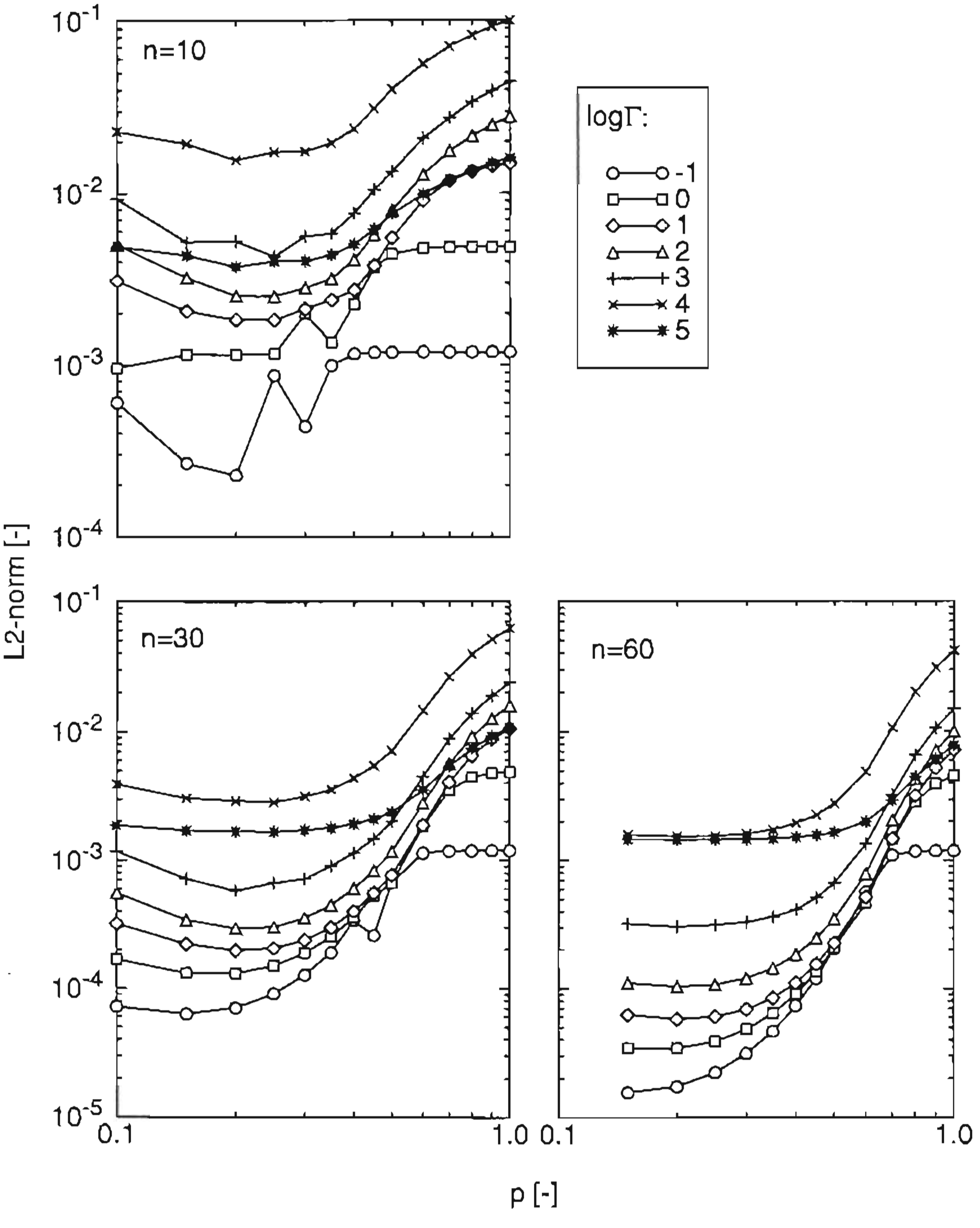

Figure 4.5 Test 2. Influence of Γ on p_{opt} for three different numbers of nodes *n*.

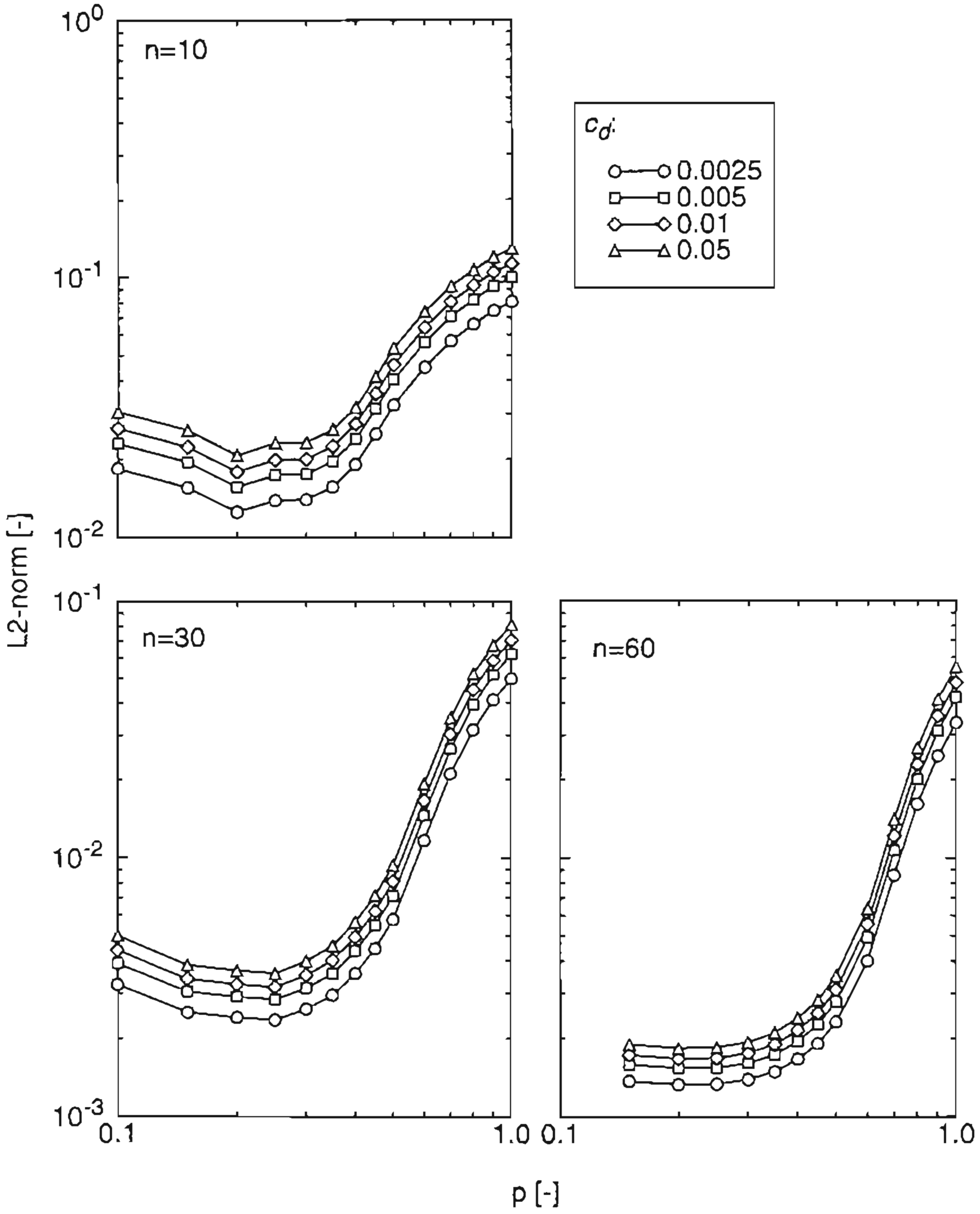

Figure 4.6 Test 3. Influence of c_d on p_{opt} for three different numbers of nodes n.

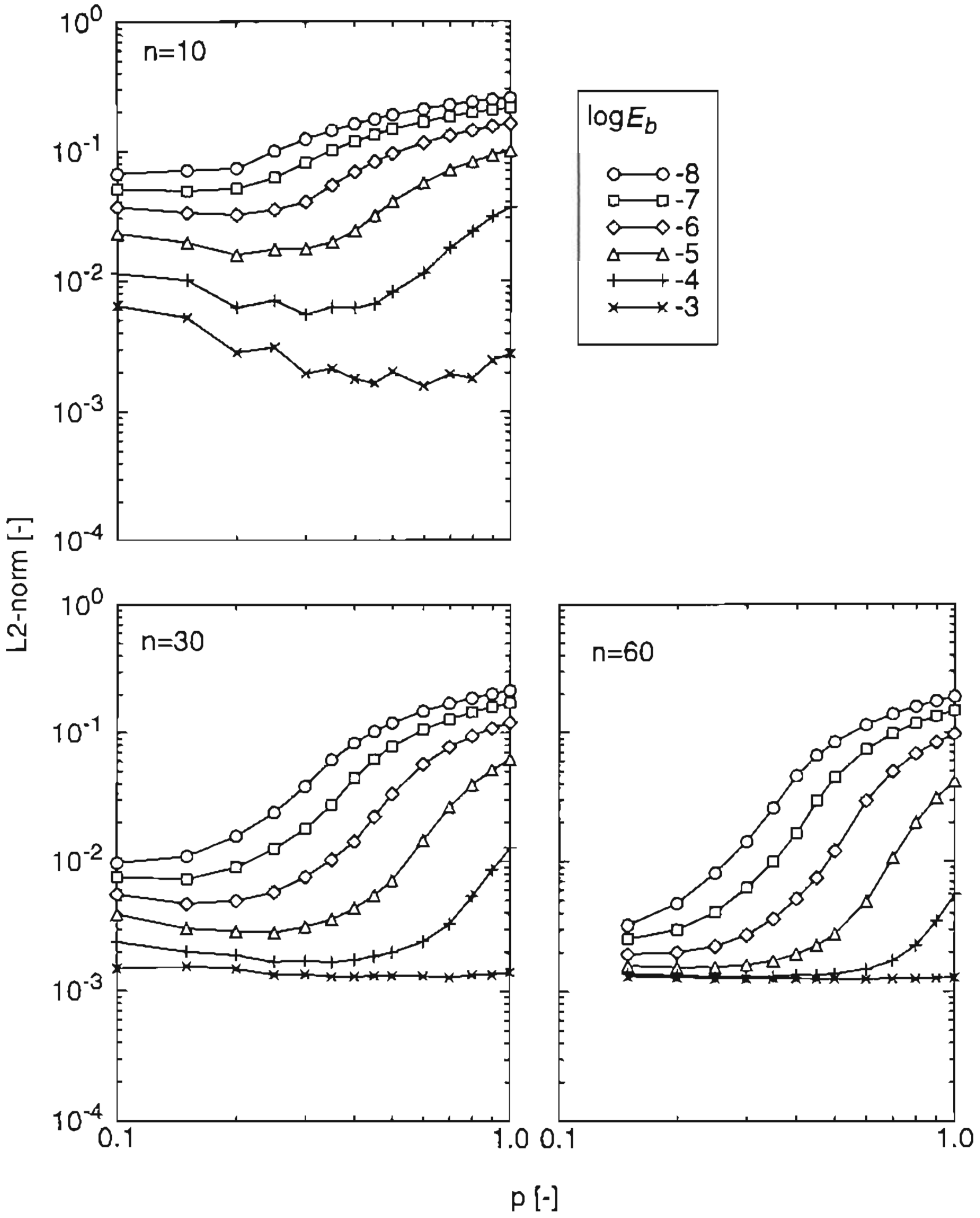

Figure 4.7 Test 4. Influence of E_b on p_{opt} for three different numbers of nodes *n*.

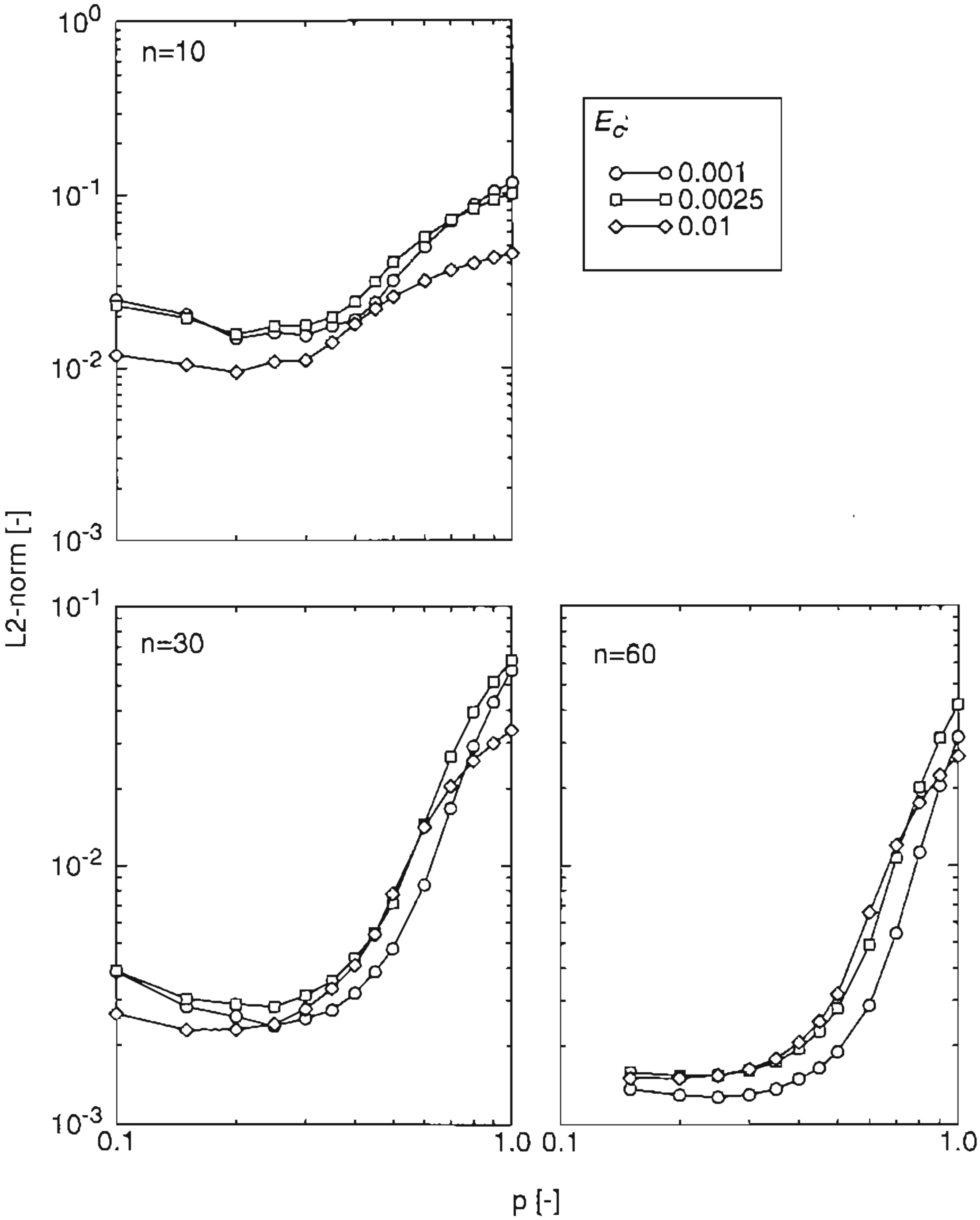

Figure 4.8 Test 5. Influence of E_c on p_{opt} for three different numbers of nodes n.

4.3.4 Verification

In Test 6, we repeat a 1D experiment reported by Davies (1991). Our purpose is twofold. First, the optimized β grid (p=0.25) is compared against previously available grids. Secondly, its performance is assessed for conditions different from the ones for which it was derived. Namely, a no-slip condition is used at the bottom and the eddy viscosity varies in time:

$$A_v = 0.2\frac{e(\sigma)}{\bar{e}}\bar{u}^2 \qquad e(\sigma) = \begin{cases} e_b + (1+\sigma)\dfrac{e_c - e_b}{0.2} & -1 \leq \sigma \leq -0.8 \\ e_b & -0.8 \leq \sigma \leq 0 \end{cases} \tag{4.16}$$

where $(e_b, e_c, \bar{e})$=(0.0001,0.1,0.09001) and $\bar{u}$ is the depth averaged velocity. The free stream velocity is 1m/s, and the wave period 12 hours (S_2 tide).

Velocity amplitudes and phases at selected points in the vertical were compared with results from the reference grid (Table 4.2). Grid β with 30 nodes and the logarithmic and log-linear grids with 60 nodes have a similar accuracy. For the same number of nodes, the results from grid β are clearly better than those from both the logarithmic and log-linear grids. Grid β therefore represents an improvement over other available discretization approaches.

Results also suggest that β grids and the optimization criterion derived in the previous section are robust (or at least lead to accurate numerical solutions), beyond the original conditions of friction parameterization. Experiments were repeated with p=0.2 and p=0.3. The results were very similar, further suggesting that 0.25 is an appropriate value for p_{opt}, even for time dependent eddy viscosity profiles.

Table 4.2 Test 6. Results from the reference grid and differences between the results from the various test grids and the reference grid. Velocity amplitudes are in m/s, (phases) are in degrees. Results from the logarithmic and log-linear grids are from Davies (1991).

sigma	reference (104 nodes)	log-linear (60 nodes)	logarithmic (60 nodes)	β (10 nodes)	β (30 nodes)	β (60 nodes)
S_2, h=10m						
-0.995	0.215 (211)	-0.019 (-2)	0.008 (0)	-0.040 (-2)	-0.007 (-1)	-0.004 (0)
-0.99	0.259 (211)	-0.018 (-2)	0.009 (0)	-0.038 (-2)	-0.007 (0)	-0.004 (0)
-0.9	0.402 (213)	-0.012 (-1)	0.015 (0)	-0.030 (-2)	-0.009 (0)	-0.006 (0)
-0.75	0.453 (214)	-0.010 (-1)	0.016 (0)	-0.029 (-2)	-0.009 (0)	-0.007 (0)
-0.5	0.502 (215)	-0.008 (-1)	0.015 (0)	-0.026 (-1)	-0.009 (0)	-0.008 (0)
S_6, h=10m						
-0.995	0.026 (121)	-0.002 (-8)	0.000 (0)	-0.003 (-11)	0.000 (-3)	0.001 (-2)
-0.99	0.031 (124)	-0.001 (-8)	0.001 (0)	-0.002 (-10)	0.001 (-3)	0.001 (-2)
-0.9	0.049 (136)	0.001 (-7)	0.002 (0)	-0.001 (-8)	0.000 (-2)	0.000 (-1)
-0.75	0.055 (143)	0.003 (-7)	0.004 (-1)	-0.001 (-7)	0.001 (-3)	0.001 (-2)
-0.5	0.062 (150)	0.004 (-8)	0.005 (-2)	0.000 (-6)	0.000 (-2)	0.000 (-2)
S_2, h=100m						
-0.995	0.554 (244)	-0.007 (-1)	-0.011 (0)	-0.065 (-4)	-0.008 (0)	-0.002 (0)
-0.99	0.654 (246)	-0.006 (0)	-0.011 (0)	-0.048 (-3)	-0.005 (0)	-0.001 (0)
-0.9	0.928 (256)	-0.003 (0)	-0.005 (1)	-0.013 (-1)	-0.004 (0)	-0.002 (1)
-0.75	0.991 (261)	-0.002 (0)	-0.002 (1)	-0.009 (-1)	-0.003 (0)	-0.002 (0)
-0.5	1.023 (267)	-0.002 (-1)	-0.001 (0)	-0.004 (-1)	-0.003 (-1)	-0.003 (0)
S_6, h=100m						
-0.995	0.070 (218)	0.001 (0)	0.000 (-9)	0.003 (-4)	0.001 (0)	0.001 (1)
-0.99	0.069 (226)	0.001 (-1)	-0.001 (-8)	0.004 (-3)	0.001 (0)	0.001 (1)
-0.9	0.036 (278)	0.000 (-1)	-0.003 (-6)	0.005 (-2)	0.000 (1)	-0.001 (1)
-0.75	0.023 (319)	-0.001 (0)	-0.003 (0)	0.004 (-3)	0.000 (1)	-0.001 (1)
-0.5	0.013 (13)	0.001 (5)	0.000 (32)	0.004 (1)	0.001 (3)	0.000 (3)

4.4 Horizontal Nodal Distribution

We now address the issue of distributing among verticals the total number of nodes available for the domain. Within DWSC formulations, this problem is inexistent, as all verticals must have the same number of nodes. However, LSC formulations allow more nodes to be placed in the verticals where finer resolution is necessary for accuracy reasons.

We have shown earlier that $L_2(v)$ depends very significantly on Γ, and less significantly on the other controlling dimensionless numbers. Γ is also fairly straightforward to evaluate. It is therefore both reasonable and convenient to argue that criteria to guide the distribution of the number of nodes among verticals should account for the spacial distribution of Γ. The difficulty is to define a relationship between n and Γ that leads to optimal accuracy, within a chosen constraint (e.g., a certain total number of nodes in the entire domain, or a certain maximum error).

A possible approach, which we will explore below, is to assume that errors are exclusively a function of n and Γ, and look for a distribution of nodes that keeps errors constant with regard to these two parameters, i.e:

$$d\log\Theta = \left(\frac{\partial}{\partial\log\Gamma}\log\Theta\right) d\log\Gamma + \left(\frac{\partial}{\partial\log n}\log\Theta\right) d\log n = 0 \tag{4.17}$$

where Θ denotes an error measure. Only error measures that display the functional dependence identified above for $L_2(v)$ should be retained. An example that will be used in the next section is:

$$L_2(u) = UL_2(v) = \frac{\Gamma h}{T} L_2(v) \tag{4.18}$$

From (4.17) we can now derive the desired relationship between n and Γ:

$$\frac{d\log n}{d\log\Gamma} = -\frac{\dfrac{\partial}{\partial\log\Gamma}\log\Theta}{\dfrac{\partial}{\partial\log n}\log\Theta} \tag{4.19}$$

For this relationship to be of any practical significance, however, we need to be able to quantify the RHS. This is non-trivial. While it can be argued that $d\log\Theta/d\log n$ is approximately a constant (e.g., see Figure 4.9 for $\Theta=L_2(v)$), linked to the order of accuracy of the numerical solution method, the behavior of $d\log\Theta/d\log\Gamma$ is unknown a priori, is likely very sensitive to the choice of Θ, and may be impossible to characterize even experimentally.

It is however reasonable to assume a functional form for the RHS of (4.19), based on "best available information", construct the grid, and evaluate errors *a posteriori* to assess how well (4.17) is observed. We will experiment with this concept in the next section, making the simple assumption that the right hand side is a constant (based on Figure 4.9, for $\Theta=L_2(\nu)$), and re-writing (4.19) as:

$$n = n_{min}\left(\frac{n_{max}}{n_{min}}\right)^{\frac{\log(\Gamma/\Gamma_{min})}{\log(\Gamma_{max}/\Gamma_{min})}} \tag{4.20}$$

where n_{min} and n_{max} are user-specified maximum and minimum numbers of nodes per vertical, and Γ_{max} and Γ_{min} are maximum and minimum values of Γ in the domain. The choice of n_{min} and n_{max} dictates the value of $d\log\Theta/d\log\Gamma$, which is convenient from the user viewpoint, but does not necessarily represent the true behavior of this term.

The use of (4.20) requires that Γ, which is not known a priori, be estimated. Three levels of decreasing complexity are considered here for the estimation of Γ, all based on the combination of (4.5) and (4.8). If the amplitudes and phases of the main tidal constituent are known (say, from a depth-averaged simulation), Γ can be evaluated as (level 3):

$$\Gamma = \frac{gT^2}{2\pi h}\sqrt{(\nabla A)^2 + (A\nabla\phi)^2} \tag{4.21}$$

The gradient operator is used here because we are interested in the maximum value of Γ in each vertical.

A simpler alternative (level 2), which does not require a preliminary run, is to neglect amplitude variations in the domain, and estimate Γ as:

$$\Gamma \approx AT\sqrt{g/h^3} \tag{4.22}$$

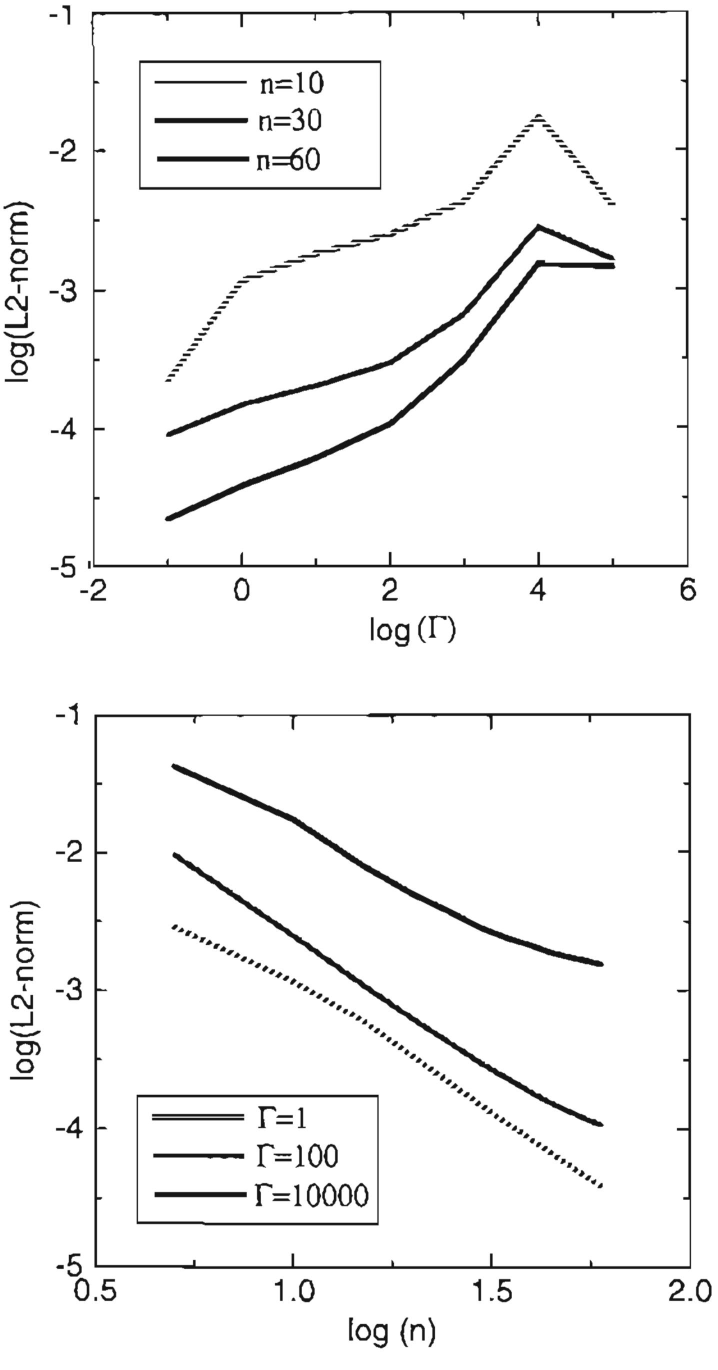

Figure 4.9 Variation of $L_2(v_A)$ with n and Γ. Default values of c_d, E_b and E_c were used (Table 4.1).

In this case, only depth effects are considered in the variation of Γ. While these effects are generally dominant in deep waters, they can be secondary in estuarine conditions (e.g., relative to lateral constraints).

Finally (level 1), we can ignore the variations of Γ altogether, leading to a constant number of nodes per vertical. This level is the only one that can be applied with DWSC models.

The performance of each level is illustrated in the next section.

4.5 Application

The criteria and concepts developed in Sections 4.3 and 4.4 are now applied in the context of a synthetic but relatively complex estuary. Our primary objective is to evaluate whether the overall approach is useful beyond the very narrow limits of the adopted simplifying assumptions. For this purpose, we choose a case where the rigid-lid approximation does not apply, we use a time-dependent eddy viscosity, and we solve both the internal and external modes.

The application consists of a tidal wave propagating from deep into shallow waters. The domain (Figure 4.10) schematically represents a shallow embayment connected by a narrow mouth to a continental shelf and continental slope. A two-dimensional laterally averaged model, $RITA_{2v}$ (Fortunato and Baptista, 1993), is used, to make Γ vary due to both topographic and geometric effects. $RITA_{2v}$ solves the external mode with the Generalized Wave Continuity Equation (Kinmark, 1986), using linear finite elements. The internal mode equations are discretized as described in Section 4.2.

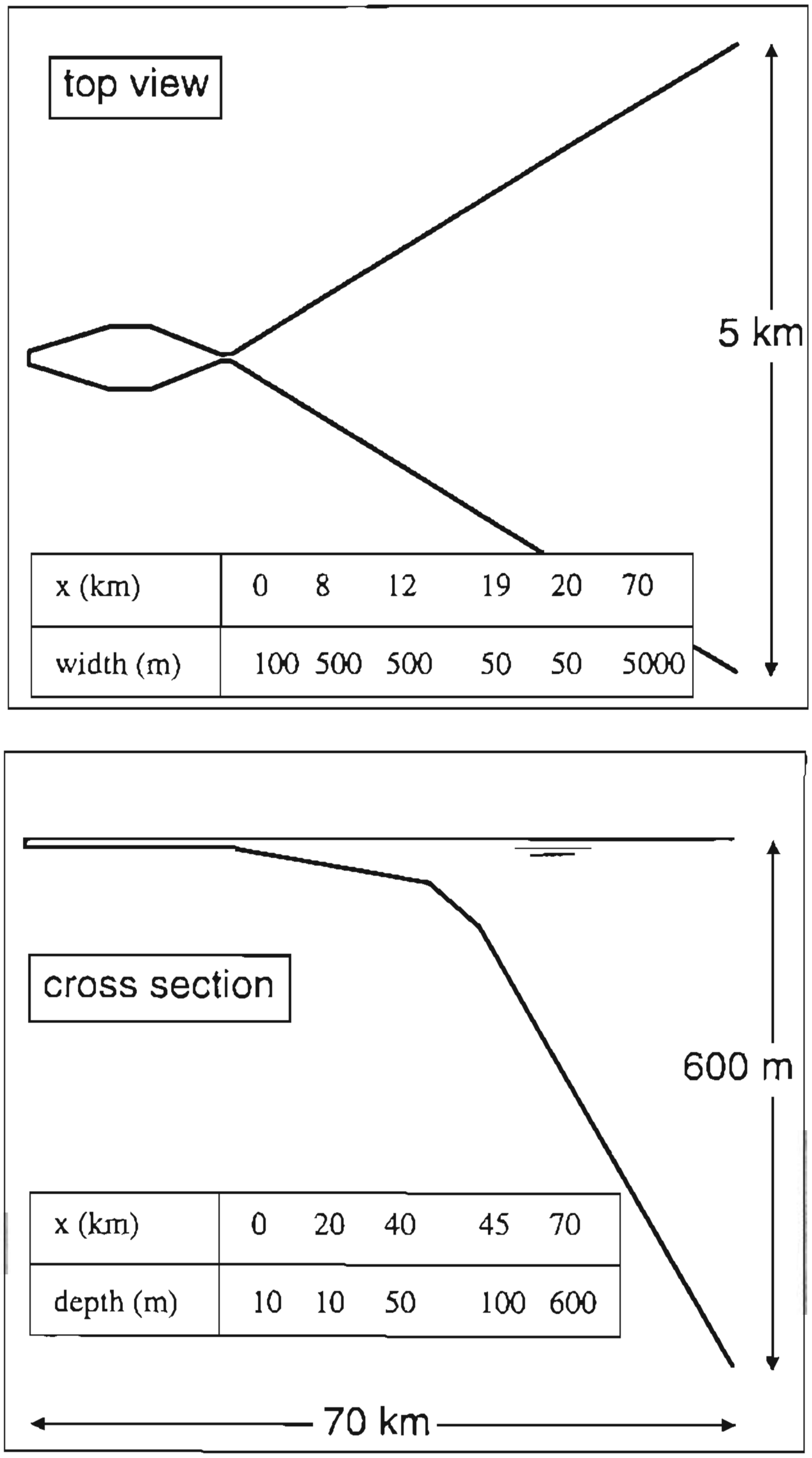

x (km)	0	8	12	19	20	70
width (m)	100	500	500	50	50	5000

x (km)	0	20	40	45	70
depth (m)	10	10	50	100	600

Figure 4.10 Domain for the synthetic application

A time-dependent eddy viscosity parameterization proposed by Davies and Lawrence (1994) is used. In the upper 80% of the water column, the eddy viscosity coefficient is given by:

$$A_v = K|\bar{u}|\Delta \tag{4.23}$$

where $\bar{u}$ is the depth averaged velocity, K is a dimensionless coefficient taken as 0.0025, and the depth of the bottom boundary layer, Δ, is computed as:

$$\Delta = min\left(h, 2000\sqrt{|\tau_b|/\rho}\right) \tag{4.24}$$

In the bottom 20% of the water column, A_v decreases linearly to:

$$A_{vb} = max\left(\kappa z_0\sqrt{|\tau_b|/\rho}, \mu\right) \tag{4.25}$$

where μ is the molecular viscosity of water (10^{-6}m^2/s). The friction coefficient c_d is set to 0.01.

Four grids were built (Figure 4.11), all using the same horizontal nodal spacing (Δx=1000m), but each having different vertical discretizations: G0 is uniform, while G1 through G3 are β grids and correspond respectively to levels 1 through 3 of the criterion discussed in the previous section. The total number of nodes is roughly the same for all grids, but their distribution varies: G0 and G1 have 10 nodes per vertical, while in G2 and G3 n varies according to (4.20), with Γ computed with (4.22) and (4.21), respectively (Figure 4.12). For the last two grids we set n_{min}=5, which lead to n_{max} =15 for G2 and n_{max} =24 for G3. To build G3, a preliminary depth-averaged simulation was performed for a single constituent (S_2), and the resulting amplitudes and phases were used to evaluate Γ (Figure 4.13).

The comparison between the four grids implicitly assumes similar costs, i.e., a CPU time for the internal mode directly related to the total number of nodes. This assumption is valid since the internal mode matrices are tridiagonal, requiring only O(n) operations to invert (Press et al., 1988).

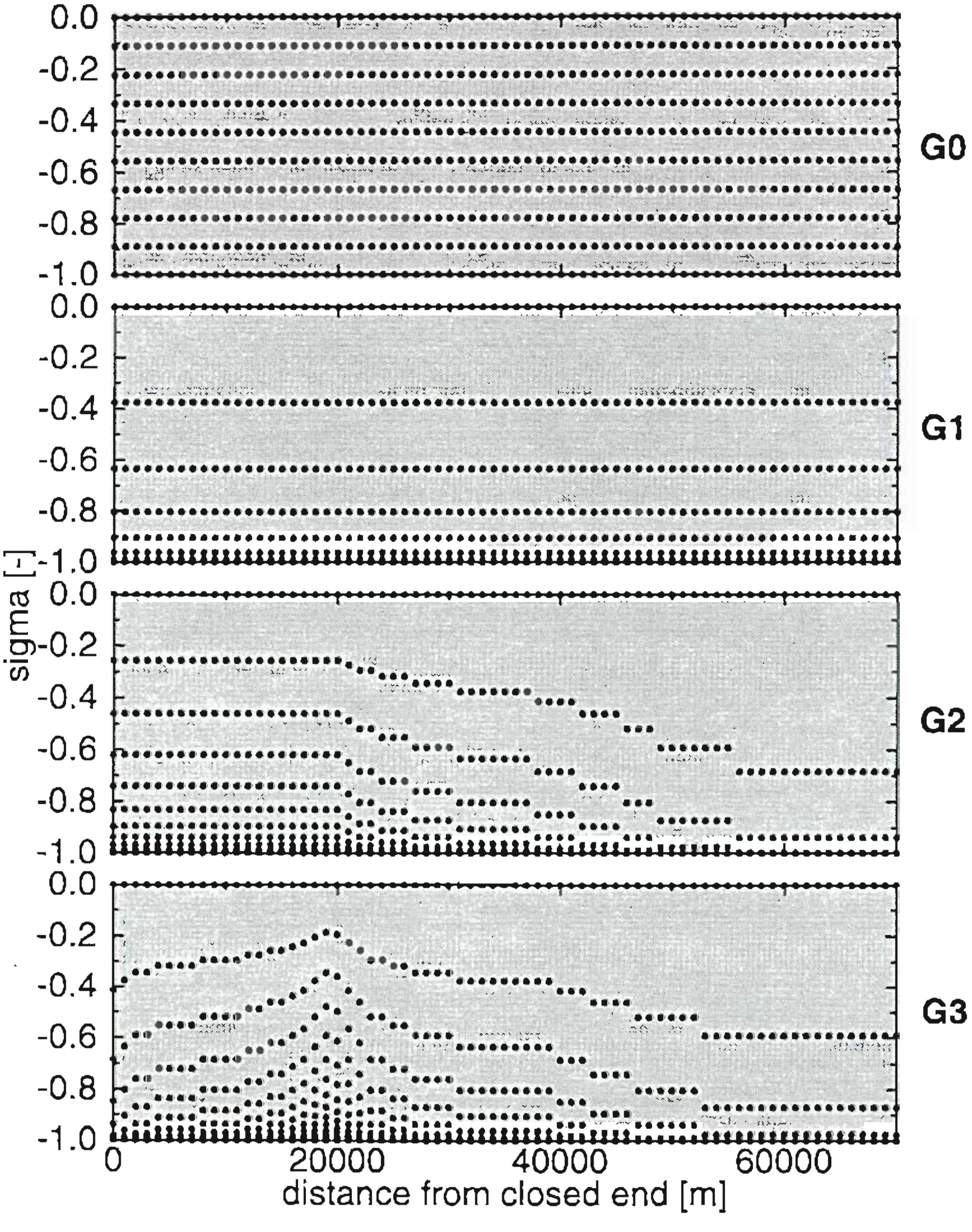

Figure 4.11 Grids used in the application.

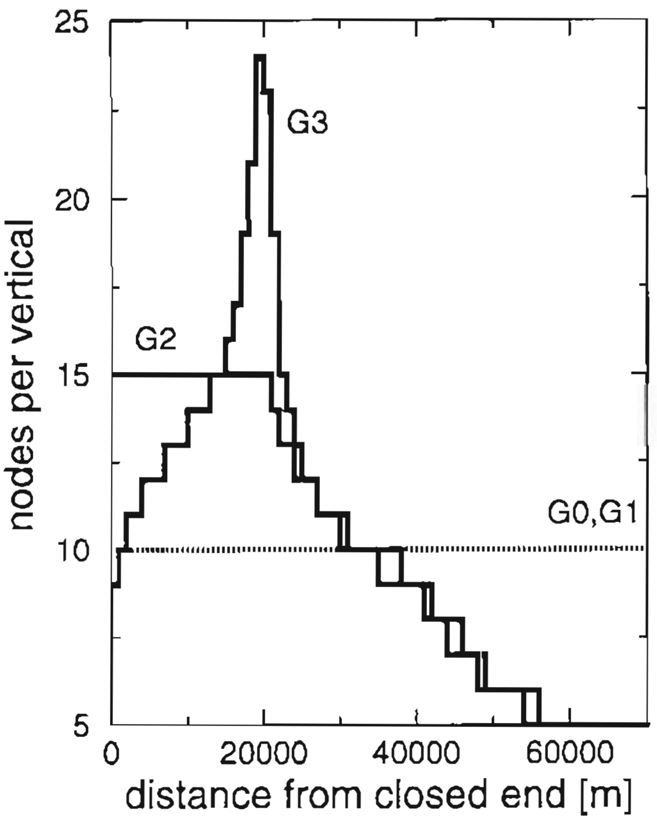

Figure 4.12 Number of nodes per vertical. The total number of nodes is 710 for G0 and G1, 711 for G2, and 703 for G3.

The model is forced at the ocean boundary with S_2 (T=12 hours) and S_1 (T=24 hours) waves with amplitudes of 1 and 0.5 meters, respectively. All non-linear terms are included, except advective accelerations. The model is run for ten S_1 tidal cycles in depth-averaged mode, plus five cycles in 2D mode. The time step is 60s. Results from the last cycle are harmonically analyzed at regularly spaced verticals, where the L2-norms of the velocity amplitudes, $L_2(u_A)$, are evaluated. The reference grid has the same horizontal resolution as the test grids, and a β grid with 60 nodes per vertical. The time step of the reference simulation is 30s.

Figure 4.14 shows $L_2(u_A)$ along the channel, for representative constituents (S_0, S_1, S_2 and S_6). Results for other constituents (S_3, S_4 and S_5) show similar trends, and are not shown here.

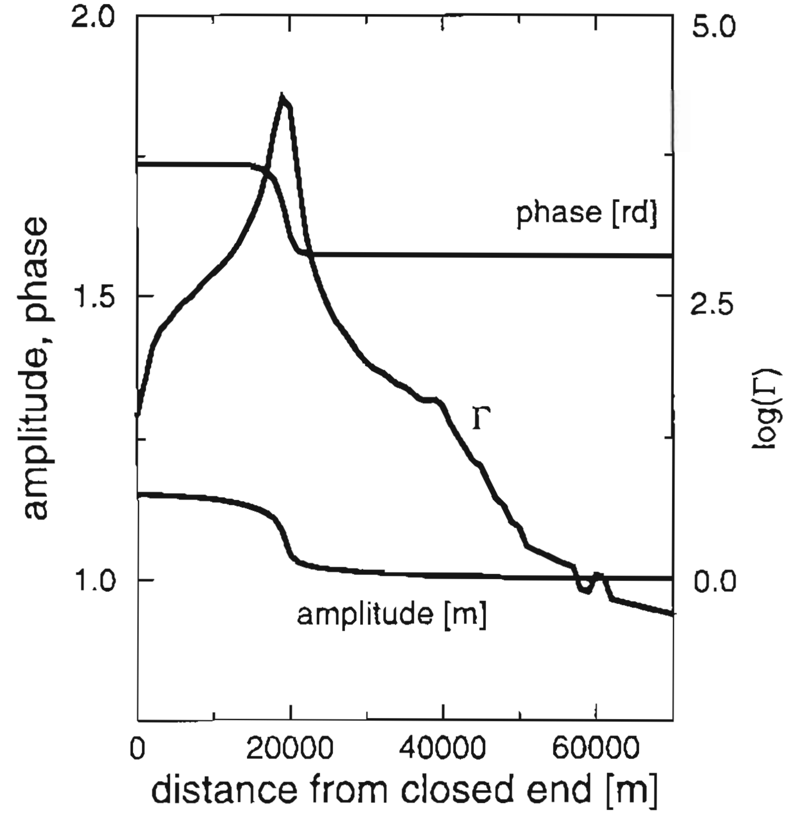

Figure 4.13 S_2 characteristics: Γ and elevation amplitudes and phases (1D simulation).

For G0, errors typically present a maximum in the channel (e.g., 0.1 m/s for the $S_{2)}$, and are smallest in deep water ($2x10^{-5}$ m/s for the same constituent). The error peak should be attributed both to larger velocities and to a rapid change in the waves amplitudes and phases (Figure 4.13). This change in wave characteristics corresponds to a maximum in the value of Γ, which, as shown in the 1D tests, leads to the largest errors.

The use of grid G1 dramatically improves the results, with L2-norms decreasing almost uniformly for all frequencies by a factor of ten (Figure 4.14). Still, the difference between maximum and minimum errors persists, indicating a relative over-refinement in deep water. This difference suggests that the LSC can further improve the overall accuracy.

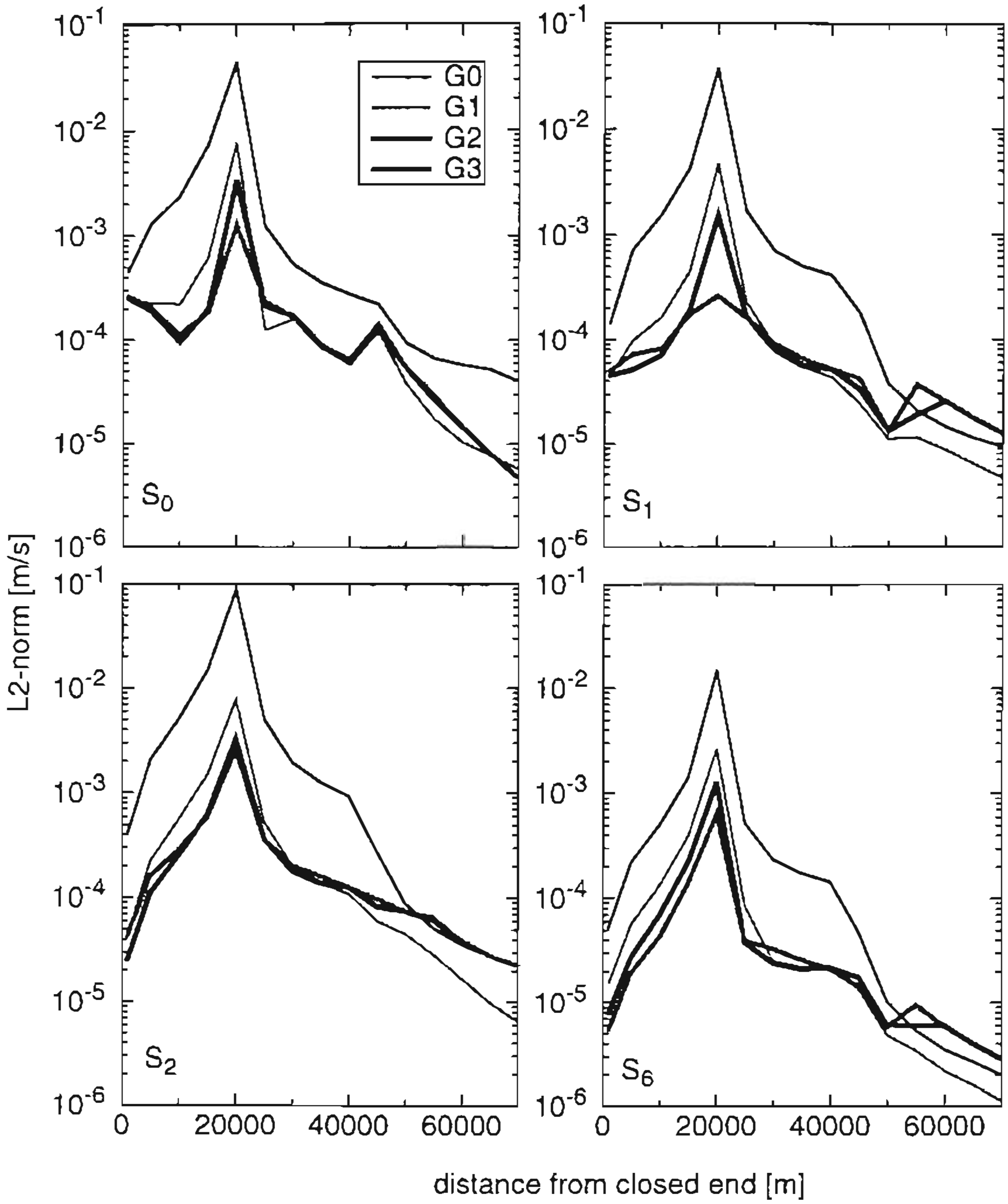

Figure 4.14 $L_2(u_A)$ for grids G0 through G3.

The errors for grid G2 decrease in the estuary and increase in the continental slope, because this grid concentrates more nodes in shallow water. As a result, the errors are more uniform than those obtained with G1. However, not enough resolution is provided in the channel because G2 ignores geometry effects on Γ, and the already small errors observed with G1 near the closed boundary are further decreased. As discussed in the previous section, level 2 of the criterion is not well suited for estuarine applications because lateral constraints are not accounted for.

Grid G3 leads to the best results. Relative to G1, it typically reduces the maximum, mean and standard deviation of the L2-norms by a factor of 3 to 6. Inside the estuary, the errors are similar to G2's, even though G2 has more nodes in this area; in the channel, G3 leads to better results than G2. As a result, the L2-norms for G3 are the smallest and the most uniform.

We note (Figure 4.15) that $\log(L_2(u))$ varies approximately linearly with $\log(\Gamma)$, as assumed in our discussion of (4.19). However, the value of the slope inherently assumed in (4.20) with n_{min}=5 and n_{max}=24 is 0.13, against an observed slope of 0.61 (Figure 4.15). Our interpretation is that we could make $L_2(u)$ further uniform in G3 by adjusting n_{min} in order to obtain a larger imposed slope.

It is also interesting to observe the variation of $\log(L_2(v))$ with $\log(\Gamma)$ - Figure 4.15. For this error measure, the assumption of a linear variation breaks down. Coincidentally (results not shown), mean $L_2(v)$ are not significantly better for grids G2 and G3 than for grid G1. Our interpretation is that to optimize the distribution of $L_2(v)$ in the domain, we would need to use in (4.20) an higher order function to describe the dependency of $\log(L_2(v))$ on $\log(\Gamma)$.

The choice of the error norm that we want to equalize over the domain is somewhat ambiguous and will impact the outcome. Norms based on absolute errors can lead to large erroneous fluxes in deep waters, which can be amplified in shallow waters. Norms based on relative errors can be overly stringent in deep waters, leading to errors far below the detection limits of current instruments. Our choices in this paper were pragmatic: in the 1D tests, only relative errors ($L_2(v)$) could be computed; in the 2D application, absolute errors ($L_2(u)$) led to overall best results.

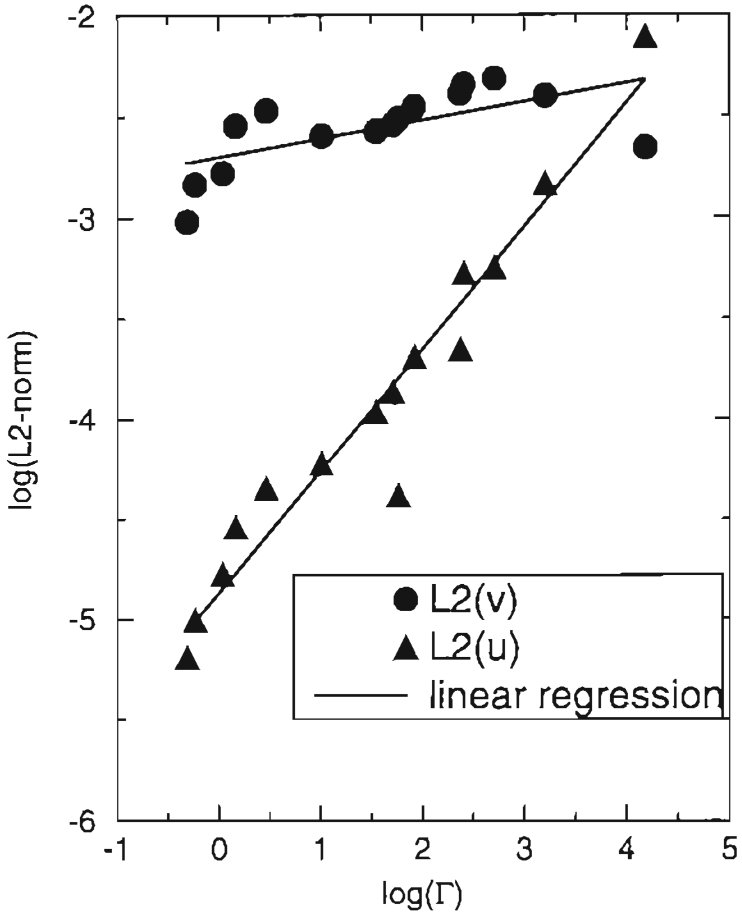

Figure 4.15 Linear regression for $\log(L_2(v_A))$ (slope 0.09, correlation coefficient 0.62) and $\log(L_2(u_A))$ (slope 0.61, correlation coefficient 0.97) versus $\log(\Gamma)$ for grid G1.

4.6 Final Considerations

This paper addressed the vertical discretization in barotropic tidal models. Criteria for both the nodal distribution within a given vertical and for the horizontal distribution of the total number of nodes were developed and showed promising results in a synthetic application.

Our analysis demonstrated the strong dependency of errors on local flow properties. An efficient vertical discretization should take those properties into account, which is not possible with either DWSC or z-coordinates. Thanks to their flexibility, LSC appear therefore to be a strong alternative to the previous methods.

The usefulness of LSC should extend well beyond the cases explored in this paper. For instance, a method recently developed, in which the momentum equations are solved for Reynold stresses rather than velocities (Luettich and Westerink, 1991) can also highly benefit from the LSC. Numerical experiments with a barotropic tidal model showed that the number of nodes per vertical needed to achieve a 1% error in the bottom friction varied from 2 to 52, depending on the physical parameters (Luettich et al., 1994). Clearly, using the same number of vertical nodes throughout the domain will lead to large errors and/or over-refinements.

The degree of refinement adequate for a given vertical was shown to depend on a dimensionless number Γ which characterizes the local changes in wave properties. This number may also prove useful to derive criteria for the horizontal discretization of tidal models. Indeed, the usual criterion for horizontal discretization based on the dimensionless wavelength is inadequate in areas of rapid change of the wave properties, due to its inability to take into account the two-dimensional structure of the flow and the rate of change in wavelength (Westerink et al., 1992, 1994b). The number Γ, based on horizontal gradients of the wave amplitude and phase, may provide a good indication as to where horizontal resolution is most needed.

This paper constitutes only a first step towards the development of solid guidelines to discretize the vertical dimension in surface water models, and certainly leaves many questions unanswered. Out of necessity, several simplifying assumptions were made that may eventually have to be revisited. Important open questions include:

- the dependency of p_{opt} on the chosen turbulence closure scheme;
- the extension of the proposed criteria to other types of vertical grids;

- the validity of the proposed criteria in 3D barotropic flows;
- the implications of stratification on the choice of the grid type and on the development of optimization criteria.

The extension of the proposed criteria to fully 3D barotropic is described in Chapter 5.

References

Blumberg, A.F. and G.L. Mellor, 1987. A Description of a Three-Dimensional Coastal Ocean Model, in *Three-Dimensional Coastal Ocean Models*, N.S. Heaps (editor), Amer. Geoph. Union, Washington, D.C, 1-16.

Bowden, K.W. and S.R. Ferguson, 1980. Variations with Height of the Turbulence in a Tidally Induced Bottom Boundary Layer, in *Proc. 11th Liege Colloq. on Ocean Hydrodynamics*, J.C.J. Nihoul (editor), Elsevier Oceanography Series, Vol. 28, Marine Turbulence, Elsevier, Amsterdam, 259-286.

Casulli, V. and R.T. Cheng, 1992. Semi-Implicit Finite Difference Methods for Three-Dimensional Shallow Water Flow, *Int. J. for Num. Met. in Fluids*, 15: 629-648.

Cheng, R.T. and P.E. Smith, 1990. A Survey of Three-Dimensional Numerical Estuarine Models, *Estuarine and Coastal Modeling*, M.L. Spaulding (editor), Amer. Soc. Civ. Eng., 1-15.

Davies, A.M., 1990. On the Importance of Time Varying Eddy Viscosity in Generating Higher Tidal Harmonics, *J. Geophys. Res.*, 95 (C11): 20287-20312.

Davies, A.M., 1991. On the Accuracy of Finite Difference and Modal Methods for Computing Tidal and Wind Waves Current Profiles, *Int. J. for Num. Met. in Fluids*, 12: 101-124.

Davies, A.M., 1993a. Numerical Problems in Simulating Tidal Flows with a Frictional-Velocity-Dependent Eddy Viscosity and the Influence of Stratification, *Int. J. for Num. Met. in Fluids*, 16: 105-131.

Davies, A.M., 1993b. A Bottom Boundary Layer Resolving Three-Dimensional Tidal Model: A Sensitivity Study of Eddy Viscosity Formulation, *J. Phys. Ocean.*, 23: 1437-1453.

Davies A.M., and J. Aldridge, 1993. A Numerical Model Study of Parameters Influencing Tidal Currents in the Irish Sea, *J. Geophys. Res.*, 98 (C4): 7049-7067.

Davies A.M., and J. Lawrence, 1994. Modelling the Non-linear Interaction of Wind and Tide: its Influence on Current Profiles, *Int. J. for Num. Met. in Fluids*, 18: 163-188.

Deleersnijder, E. and J.M. Beckers, 1992. On the Use of the σ-Coordinate System in Regions of Large Bathymetric Variation, *J. Marine Syst.*, 3: 381-390.

Fortunato, A.B. and A.M. Baptista, 1993. *RITA*$_{2v}$ *User's Manual. 2D Vertical Hydrodynamic Model for River and Tidal Analysis. Part I - Flow Model*, OGI-CCALMR Software Documentation Series SDS7, 93-3, Oregon Graduate Institute of Science & Technology, Portland, Oregon.

Fortunato, A.B. and A.M, Baptista, 1994a. Modeling Near-Bottom Advective Acceleration in Surface Water Models, *Proc. Int. Conf. on Computational Methods in Water Resources X*, A. Peters, et al. (editors), Kluwer Academic Publishers, 1045-1052.

Fortunato, A.B. and A.M. Baptista, 1994b. Localized Sigma Coordinates for the Vertical Structure of Hydrodynamic Models, in *Estuarine and Coastal Modeling III*, M.L. Spaulding, et al. (editors), Amer. Soc. Civ. Eng., 323-335.

Fortunato, A.B. and A.M, Baptista, 1995. Evaluation of Horizontal Gradients in Sigma-Coordinate Shallow Water Models, *Atmos.-Ocean* (in review).

Gary, J.M., 1973. Estimate of Truncation Error in Transformed Coordinate, Primitive Equation Atmospheric Models, *J. Atmos. Sci.*, 30: 223-233.

Haney, R.L., 1991. On the Pressure Gradient Force over Steep Topography in Sigma Coordinate Ocean Models, *J. Phys. Ocean.*, 21: 610-619.

Ianniello, J.P., 1977. Tidally Induced Residual Currents in Estuaries of Constant Breadth and Depth, *J. Mar. Res.*, 35: 755-786.

Jay, D.A., 1991. Green's Law Revisited: Tidal Long-Wave Propagation in Channels with Strong Topography, *J. Geophys. Res.*, 96: 20,585-20,598.

Kinmark, I.P.E., 1985. *The Shallow Water Equations: Formulation, Analysis and Application*, Lecture Notes in Engineering, 15, C.A. Brebia and S.A. Orszag (editors), Springer-Verlag, Berlin.

Laible, J.P., 1992. On the Solution of the Three-Dimensional Shallow Water Equations Using the Wave Equation Formulation, in *Proc. Int. Conf. on Computational Methods in Water Resources IX*, T.F. Russel, et al. (editors), Computational Mechanics Publications, 545-552.

Leendertse, J.J. and S.K. Liu, 1975. *A Three-Dimensional Model for Estuaries and Coastal Seas. II, Aspects of Computation.* Rand Corporation Report R-1764-OWRT.

Luettich, Jr., R.A. and J.J. Westerink, 1991. A Solution for the Vertical Variation of Stress, Rather than Velocity, in a Three-Dimensional Circulation Model, *Int. J. for Num. Met. in Fluids*, 12: 911-928.

Luettich, Jr., R.A., S. Hu and J.J. Westerink, 1994. Development of the Direct Stress Solution Technique for Three-Dimensional Hydrodynamic Models Using Finite Elements, *Int. J. for Num. Met. in Fluids*, 19: 295-319.

Lynch, D.R. and F.E. Werner, 1991. Three-Dimensional Hydrodynamics on Finite Elements. Part II: Non-Linear Time-Stepping Model, *Int. J. for Num. Met. in Fluids*, 12: 507-533.

McCalpin, J.D., 1994. A Comparison of Second-Order and Fourth-Order Pressure Gradient Algorithms in a σ-Coordinate Ocean Model, *Int. J. Num. Methods in Fluids*, 18: 361-383.

Noye, B.J., 1984. Finite Difference Techniques for Partial Differential Equations, in *Computational Techniques for Differential Equations*, B.J. Noye (editor), North-Holland, Amsterdam, 95-354.

Noye, B.J. and M. Stevens, 1987. A Three-Dimensional Model of Tidal Propagation Using Transformations and Variable Grids, in *Three-Dimensional Coastal Ocean Models*, Coastal and Estuarine Sciences, Vol. 4, N.S. Heaps (editor), Amer. Geoph. Union, Washington, D.C., 41-69.

Prandle, D. and M. Rahman, 1980. Tidal Response in Estuaries, *J. Phys. Ocean.*, 10: 1552-1573.

Press,W.H., S.A. Teukolsky, W.T. Vetterling and B.P. Flannery, 1988. *Numerical Recipes in C*, Cambridge University Press.

Signell, R.P., H.L. Jenter and A.F. Blumberg, 1994. Modeling the Seasonal Circulation in Massachusetts Bay, in *Estuarine and Coastal Modeling III*, M.L. Spaulding, et al. (editors), Amer. Soc. Civ. Eng., 578-590.

Stelling, G.S. and J.A.TH.M. Van Kester, 1994. On the Approximation of Horizontal gradients in Sigma Coordinates for Bathymetry with Steep Bottom Slopes, *Int. J. Num. Methods in Fluids*, 18: 915-935.

Walters, R.A., 1992. A 3D, Finite Element Model for Coastal and Estuarine Circulation, *Continental Shelf Res.*, 12: 83-102.

Westerink, J.J., J.C. Muccino and R.A. Luettich, Jr., 1992. Resolution Requirements for a Tidal Model of the Western North Atlantic and the Gulf of Mexico, in *Proc. Int. Conf. on Computational Methods in Water Resources IX*, in T.F. Russel, et al. (editors), Elsevier Applied Science.

Westerink, J.J., R.A. Luettich, Jr. and J.C. Muccino, 1994a. Modeling Tides in the Western North Atlantic Using Unstructured Graded Grids, *Tellus*, 46A (2): 178-199.

Westerink, J.J., R.A. Luettich, Jr. and S.C. Hagen, 1994b. Meshing Requirements for Large Scale Coastal Ocean Tidal Models, in *Proc. Int. Conf. on Computational Methods in Water Resources X*, A. Peters, et al. (editors), Kluwer Academic Publishers.

CHAPTER 5

Tidal Dynamics in the Mouth of the Tagus Estuary (Portugal)

Abstract

Three-dimensional simulations of barotropic tides are used to investigate the complex circulation at the mouth of the Tagus estuary. Comparison with field data shows that elevations are well represented in the main area of interest, but velocities are slightly overpredicted due to a simplified treatment of intertidal flats. Model results show the existence of strong velocity phase lags (up to 1.75 hours for the semi-diurnal constituents) between the shallow areas and the deep channel. These phase lags are partially responsible for the generation by advective accelerations of a strong residual velocity field (velocities reach 0.5 m/s) with well defined eddies. The interaction between the residual and tidal velocity fields in turn generates strong chaotic stirring.

Localized sigma coordinates (LSC), a recently proposed method which allows the number of nodes per vertical to vary horizontally, are used for the first time in a three-dimensional application. A previously proposed criterion for the horizontal distribution of the total number of vertical nodes is shown to be inadequate when advective accelerations are important. However, with an alternative criterion, the use of LSC reduces maximum errors by a factor of two relative to traditional sigma coordinates.

5.1 Introduction

This paper is part of an ongoing effort to understand the tidal dynamics in the Tagus estuary and ultimately build a prognostic water quality model to support management decisions. Important water quality issues in the Tagus estuary include contamination by heavy metals (e.g., Andreae et al., 1983, Lima et al., 1986) and fecal material, and problems arising from dredging and engineering modifications of the estuary (e.g., Vieira, 1988, Silva and Oliveira, 1995). Our general strategy is to use models of increasing complexity to improve the description of the physics and progressively enhance our understanding of the system. In this paper we extend previous investigations of tidal propagation in the estuary using depth-averaged models (Oliveira et al. (1995), hereafter OFB95) by including both advective accelerations and three-dimensional barotropic effects. At the mouth of the estuary, large velocities and a complex coastline and topography make both effects particularly important in the generation of strong residual currents. These residual currents are in turn responsible for strong mixing by chaotic advection and "tidal pumping", and therefore can not be ignored in water quality studies.

Grids that are unstructured both horizontally and vertically are used because they enhance computational efficiency. Triangular finite elements are used in the horizontal, allowing for the representation of some small-scale geometric features and eddies. In the vertical direction, localized sigma coordinates (Fortunato and Baptista, 1994) allow the number of nodes per vertical to vary horizontally. Hence, areas requiring a finer vertical resolution can be refined efficiently.

The Tagus estuary on the west coast of Portugal has two very distinct regions (Figure 5.1). The upper estuary, from Vila Franca de Xira to Cacilhas, is wide (over 10 km in some places) and shallow (maximum depths of 15 m). It is characterized by extensive tidal flats, small islands, and a web of narrow channels, sometimes only tens of meters wide. Intense sediment deposition and erosion in this area is changing the bathymetry (Castanheiro, 1986) and strongly damping and retarding the tides (OFB95). The lower estuary is a channel about 30 m deep, 2 km wide and 12 km long that opens into a large bay, limited by the Cabo Raso to the North, and the Cabo Espichel to the South. The mouth is characterized by two small scale features: the island of Bugio and the cape of S. Julião. The morphology of the bay is deeply marked by the historically strong discharge from the Tagus river. The channel is prolonged by a canyon about 20 m deep, limited on both sides by sand banks with depths of the order of 5 m: the Bugio Bank to the South, and the Bico do Pato to the North. The morphology of the mouth has been changing over recent years (Oliveira, 1993): between 1929 and 1985, the Bugio Bank has extended 700 m to the north and the Bico do Pato has shifted 850 m south-east.

Tides are primarily semi-diurnal. The tidal form number, defined as the ratio between amplitudes of the main diurnal (K_1+O_1) and the main semidiurnal (M_2+S_2) constituents (Defant, 1960), is 0.10 at Cascais, below the limit for mixed tides. This number decreases upstream (e.g, 0.08 at Pta. da Erva) due to a resonant mode that increases the amplitudes of semi-diurnal waves by roughly 40% in the upper estuary, leaving the diurnal waves mostly unchanged (OFB95). The phase lag of semi-diurnal constituents between the outermost station (Cascais) and Vila Franca de Xira is 1 hour and 20 minutes (Table 5.1).

The water column is generally well mixed during spring tides but it is partially stratified during neap tides where residual currents were observed to be landward near the bottom and seaward near the surface (Vale and Sundby, 1987). In addition, strong stratification can occur in the upper estuary under large river flow and low tidal range conditions. Bottom-to-surface salinity differences over 20 ppt were observed in the upper estuary on neap tides for a river flow of 900 m^3/s (Martins et al., 1983). The same differences near the mouth and under the same conditions varied between 5 and 10 ppt. The importance of baroclinic effects is therefore expected to grow landward, and then decrease as one approaches the limit of salinity intrusion (around V.F. Xira). For lack of quality data, and because our focus is on the flow near the mouth of the estuary, we will neglect baroclinic effects.

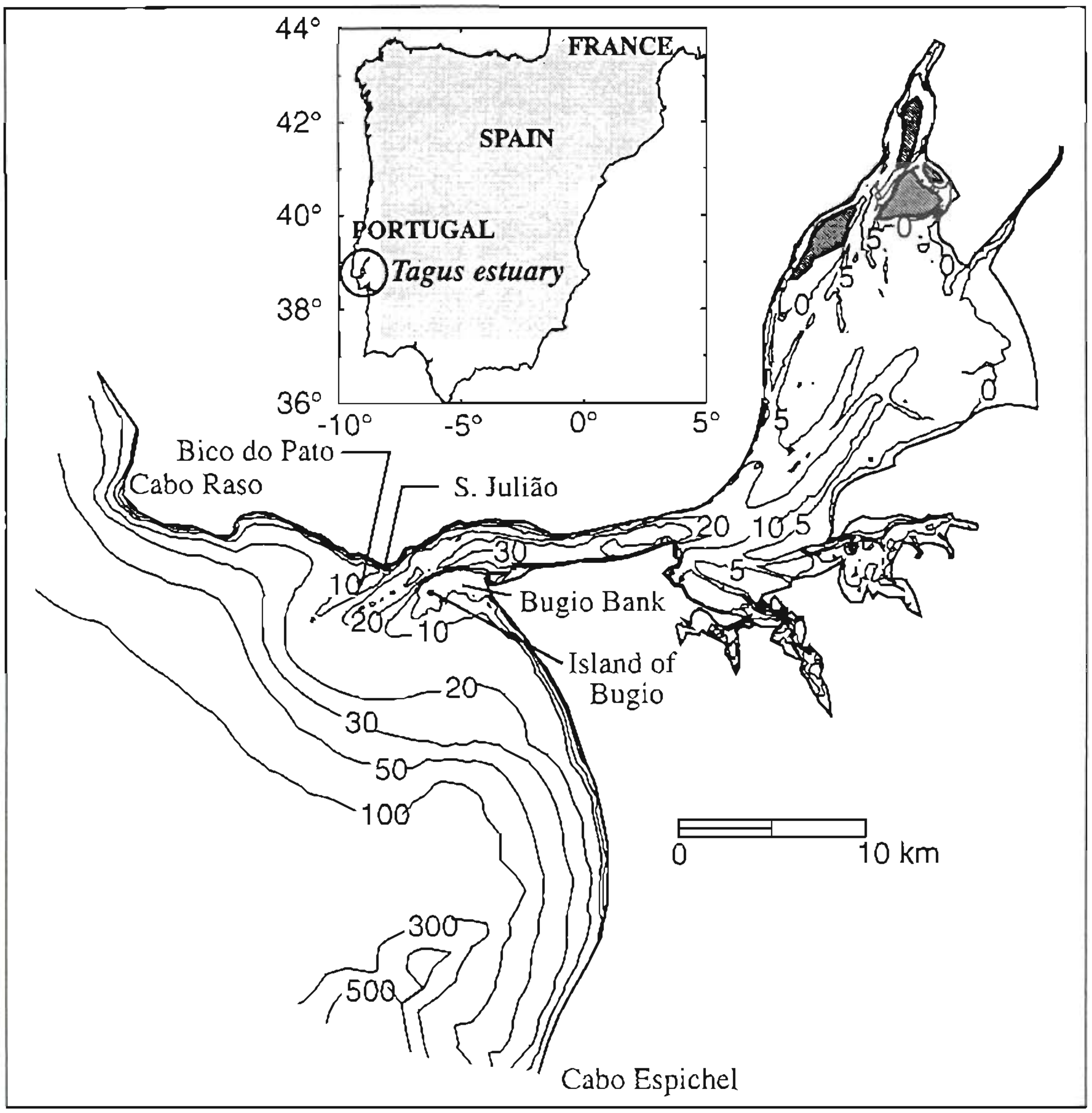

Figure 5.1 The Tagus estuary: location, place names and bathymetry (isolines (in meters) relative to the mean sea level; islands are represented in gray).

Comprehensive bathymetric data are available from a 1964/67 survey, but only localized updates were conducted since. Thirteen tidal gauges were in operation in 1972, providing an excellent coverage of the estuary (Figure 5.2). Three of the stations (Cascais, Lisboa and VF Xira) are still in operations. Velocity data are available for seven current meters (Figure 5.2) deployed near the mouth of the estuary in October and November

1987, where velocities were measured 70% below the water surface (Vieira, 1988). Statistics of the Tagus river flow are also available (e.g., DGRAH, 1986). Other inflows to the estuary are small compared to the Tagus (OFB95) and were not considered. A detailed description of the data used in this study is given in OFB95 and will not be repeated here.

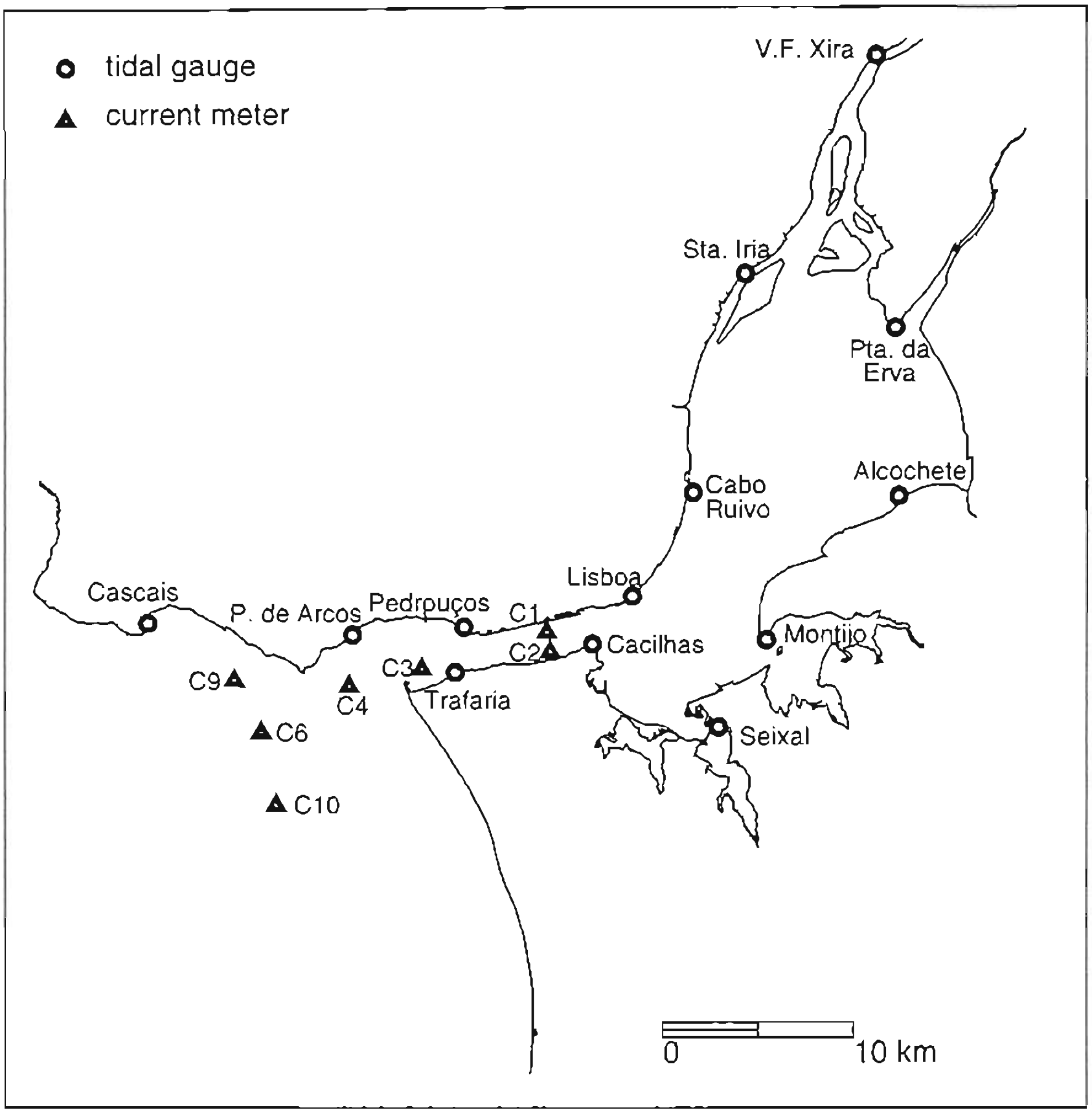

Figure 5.2 The Tagus estuary: tide gauges and current meter stations.

Unstructured grids are an attractive way to combine long-term simulations (over one month) with a fine grid resolution at an acceptable computational cost. The model used in this study uses a finite element technique in the horizontal and localized sigma coordinates (LSC) in the vertical. LSC, applied here for the first time in a complex three-dimensional situation, combine the main advantages of the traditional σ-coordinates (Phillips, 1957) with a higher flexibility to discretize the vertical direction: the nodal placement is independent for each vertical, thus local refinements do not carry over to the rest of the domain. To take advantage of the flexibility of this method, we proposed a criterion to distribute the total number of nodes among verticals, based on simple one-dimensional experiments (Fortunato and Baptista, 1995a). Although this criterion led to significant accuracy improvements in a two-dimensional (in the vertical) simulation, it has not been validated in a fully 3D simulation. Two secondary goals of this paper are therefore to test the criterion and to illustrate the advantages of the LSC in a complex, fully three-dimensional situation.

5.2 Numerical Model

The model used in this study, a modified version of ADCIRC (Luettich et al., 1991, Westerink et al., 1992), is based on the shallow waters equations which express the conservation of mass and momentum assuming incompressibility and hydrostatic pressure. In this version, density variations are neglected and nodes are not allowed to dry. The general procedure consists of a global solution for elevations and a local solution for velocities. The Generalized Wave Continuity equation (GWCE, Kinmark, 1986, Kolar et al., 1994a) is solved first for elevations using linear triangular finite elements. The three-dimensional momentum and continuity equations are then solved for velocities using localized sigma coordinates (LSC).

The depth-averaged continuity and non-conservative momentum equations are written, respectively:

$$L \equiv \frac{\partial \eta}{\partial t} + \frac{\partial}{\partial x}HU + \frac{\partial}{\partial y}HV = 0 \qquad (5.1)$$

and,

$$\begin{aligned} M_x \equiv \frac{\partial U}{\partial t} + U\frac{\partial U}{\partial x} + V\frac{\partial U}{\partial y} + \frac{\partial}{\partial x}\left(\frac{1}{H}\int_{-h}^{\eta} (u-U)^2 dz\right) + \frac{\partial}{\partial y}\left(\frac{1}{H}\int_{-h}^{\eta} (u-U)\,(v-V)\,dz\right) + \\ g\frac{\partial \eta}{\partial x} + \frac{\tau_{bx}}{\rho_0} - fV - \frac{A_h}{H}\left(\frac{\partial^2}{\partial x^2}UH + \frac{\partial^2}{\partial y^2}UH\right) = 0 \\ M_y \equiv \frac{\partial V}{\partial t} + U\frac{\partial V}{\partial x} + V\frac{\partial V}{\partial y} + \frac{\partial}{\partial x}\left(\frac{1}{H}\int_{-h}^{\eta} (u-U)\,(v-V)\,dz\right) + \frac{\partial}{\partial y}\left(\frac{1}{H}\int_{-h}^{\eta} (v-V)^2 dz\right) + \\ g\frac{\partial \eta}{\partial y} + \frac{\tau_{by}}{\rho_0} + fU - \frac{A_h}{H}\left(\frac{\partial^2}{\partial x^2}VH + \frac{\partial^2}{\partial y^2}VH\right) = 0 \end{aligned} \tag{5.2}$$

where: x, y are the horizontal cartesian coordinates;

t is time;

u, v are the horizontal velocities;

U, V are the depth-averaged horizontal velocities;

η is the elevation;

g is gravity;

H is the total depth;

τ_{bx}, τ_{by} are the bottom stresses;

ρ_0 is the reference density;

f is the Coriolis parameter; and,

A_h is the horizontal diffusion coefficient.

The GWCE (Kinmark, 1986, Kolar et al., 1994a) is defined as:

$$W \equiv \frac{\partial L}{\partial t} - \frac{\partial}{\partial x}HM_x - \frac{\partial}{\partial y}HM_y + GL = 0 \tag{5.3}$$

where G [s^{-1}] is an arbitrary constant.

The GWCE is solved with a semi-implicit, three-time-step method where linear terms are treated implicitly, and non-linear terms are taken at the middle time step. The mass matrix is stationary and only needs to be inverted once. A weak formulation is used at flow-imposed boundaries, displaying flux as a natural boundary condition. At elevation-imposed boundaries, the GWCE is discarded, and elevations are imposed as essential boundary conditions. Further details of the solution procedure can be found in Luettich et al. (1991) and Kolar et al. (1994b).

The GWCE formulation has three major advantages for finite element models relative to most primitive equation formulations. First, in the absence of advective accelerations, it propagates and damps the $2\Delta x$ waves while being very accurate for longer waves (e.g., Lynch, 1978, Kinmark, 1985). Second, the solutions of the elevation and the velocities are naturally uncoupled, thus the equations can be solved sequentially. Third, the GWCE mass matrix is time-independent, and therefore only needs to be inverted once. The GWCE formulation is therefore stable and efficient relative to other eulerian finite element methods to solve the shallow water equations.

The major drawback of the GWCE formulation is its sensitivity to the GWCE parameter - G (e.g., Myers and Baptista, 1995): values that are "too small" disrupt mass conservation, while values that are "too large" are unable to prevent $2\Delta x$ oscillations. The approach of Kolar et al. (1994a) to guide the choice of G is used in section 5.3.2.

Once elevation is known from the solution of (5.3), the 3D momentum equations are solved for the horizontal velocities. The vertical direction is represented in a σ-coordinate system (r,s,σ,τ), defined as:

$$\begin{aligned} r &\equiv x \\ s &\equiv y \\ \sigma &= \frac{z-\eta}{H} \\ \tau &\equiv t \end{aligned} \tag{5.4}$$

where z is the vertical cartesian coordinate and $\sigma \in [-1,0]$. In complex notation, the momentum equations can be written:

$$\frac{\partial \gamma}{\partial \tau} + if\gamma - \frac{1}{H}\frac{\partial}{\partial \sigma}\left(A_v \frac{\partial \gamma}{\partial \sigma}\right) = F - A_d \tag{5.5}$$

where $i=(-1)^{1/2}$, $\gamma = u+iv$ is the horizontal velocity and A_v is the vertical eddy viscosity coefficient. Depth-independent terms are grouped in $F = F_x+iF_y$, where:

$$\begin{aligned} F_x &= -g\frac{\partial \eta}{\partial x} + A_h\left(\frac{\partial^2}{\partial x^2}UH + \frac{\partial^2}{\partial y^2}UH\right) \\ F_y &= -g\frac{\partial \eta}{\partial y} + A_h\left(\frac{\partial^2}{\partial x^2}VH + \frac{\partial^2}{\partial y^2}VH\right) \end{aligned} \tag{5.6}$$

We view horizontal diffusion only as a way to smooth results and improve stability. Consistent with this approach, we use a simple parameterization of horizontal diffusion: cross-terms are not included and velocities are depth-averaged.

The advective terms in (5.5) are represented by $A_d = A_{dx}+iA_{dy}$:

$$\begin{aligned} A_{dx} &= u\frac{\partial u}{\partial r} + v\frac{\partial u}{\partial s} + \theta\frac{\partial u}{\partial \sigma} \\ A_{dy} &= u\frac{\partial v}{\partial r} + v\frac{\partial v}{\partial s} + \theta\frac{\partial v}{\partial \sigma} \end{aligned} \tag{5.7}$$

where θ is related to the vertical velocity w as:

$$\theta = \frac{1}{H}\left(w - (\sigma+1)\frac{\partial \eta}{\partial t} - u\left(\frac{\partial \eta}{\partial x} + \sigma\frac{\partial H}{\partial x}\right) - v\left(\frac{\partial \eta}{\partial y} + \sigma\frac{\partial H}{\partial y}\right)\right) \tag{5.8}$$

Equation (5.5) is solved with the boundary conditions:

$$\left.\frac{A_v}{H}\frac{\partial \gamma}{\partial \sigma}\right|_{\sigma=-1} = c_d|\gamma(-1)|\gamma(-1) \qquad \left.\frac{\partial \gamma}{\partial \sigma}\right|_{\sigma=0} = 0 \tag{5.9}$$

where c_d is a dimensionless friction coefficient.

In addition, the vertical derivative of the continuity equation is solved for θ (Lynch and Naimie, 1993):

$$H\frac{\partial^2\theta}{\partial\sigma^2} = -\frac{\partial}{\partial\sigma}\left(\frac{\partial}{\partial r}uH + \frac{\partial}{\partial s}vH\right) \tag{5.10}$$

The solution of (5.10) rather than the continuity equation allows the enforcement of kinematic boundary conditions both at the surface and at the bottom:

$$\theta|_0 = \theta|_{-1} = 0 \tag{5.11}$$

Equations (5.5) and (5.10) are discretized in space with linear finite elements. The Galerkin weighted residual statement is applied to (5.5) at each individual vertical:

$$\int_{-1}^{0}\left(\frac{\partial\gamma}{\partial\tau} + if\gamma\right)\phi_n d\sigma + \frac{1}{H}\int_{-1}^{0} A_v\frac{\partial\gamma}{\partial\sigma}\frac{\partial\phi_n}{\partial\sigma}d\sigma = F\int_{-1}^{0}\phi_n d\sigma - \int_{-1}^{0} A_d\phi_n d\sigma + \frac{1}{H^2}\left(A_v\frac{\partial\gamma}{\partial\sigma}\right)\phi_n\Big|_{-1}^{0} \tag{5.12}$$

where ϕ_n are linear functions. A weak formulation is used for the stress term, which involves a second derivative, so the bottom and surface stresses are treated as natural boundary conditions. Depth-dependent quantities (γ, A_v and A_d) are then written as piece-wise linear functions. For instance:

$$\gamma = \sum_{m=1}^{2}\gamma_m\phi_m \tag{5.13}$$

Replacing (5.13) into (5.12) leads to a tridiagonal system of equations for each vertical. Horizontal advective accelerations at each node N are computed as, for instance:

$$\gamma\frac{\partial\gamma}{\partial r}\bigg|_N = \frac{\sum_{e=1}^{nel(N)}\sum_{k=1}^{3} A_e\gamma_e\frac{\partial}{\partial x}(\psi_{ke})\gamma_{ke}}{\sum_{e=1}^{nel(N)} A_e} \tag{5.14}$$

where *nel(N)* represents the number of horizontal elements containing node N, A_e and γ_e their area and average velocity, respectively, and ψ_{ke} the corresponding horizontal shape function. The evaluation of γ_{ke} in (5.14) will depend on the type of grid. In σ-coordinates grids, nodes are defined at planes of constant sigma, while in LSC each vertical is discretized independently. Therefore, the values γ_{ke} at neighboring verticals are either taken at specific nodes (for σ-coordinates) or linearly interpolated (for LSC). Note that, for LSC, the horizontal gradients of velocity can easily be computed in cartesian, rather than sigma, coordinates. However, we showed previously that computing these gradients in sigma-coordinates is more accurate (Fortunato and Baptista, 1995b).

Three different integrals must be computed to solve (5.12):

$$I_1 = \int_b^a \phi_n \phi_m d\sigma \qquad I_2 = \int_b^a \phi_n d\sigma \qquad I_3 = \int_b^a A_v \frac{\partial \phi_m}{\partial \sigma} \frac{\partial \phi_n}{\partial \sigma} d\sigma \tag{5.15}$$

The first two integrals are time-independent and only need to be computed once. In addition, for σ-coordinate grids, they are independent of the horizontal position. This represents an advantage of the σ-coordinates over the LSC. The use of LSC will involve either more memory requirements (if I_1 and I_2 are computed only once) or CPU time (if I_1 and I_2 are computed at each time step). In the runs presented below, the first approach was followed since memory was not a concern.

Friction is often a dominant process in shallow regions so I_3 must be evaluated accurately, even for coarse grids. Different grids are thus used for the velocity and the vertical eddy viscosity. In particular, for the eddy viscosity parameterization used in this study, the eddy viscosity grid has only three nodes per vertical, defining a linear variation in the bottom 20% of the water column and a constant value in the upper 80%. The bottom and surface values are, respectively:

$$A_{vb} = \kappa U_* z_0 \qquad A_{vs} = 0.2 \kappa U_* H \tag{5.16}$$

where κ=0.41 is the von Kármán constant, $U_*=(\tau_b/\rho_0)^{1/2}$ is the friction velocity, and z_0 is the roughness length. The direct specification of eddy viscosity is commonly used in barotropic tidal simulations (e.g., Davies and Jones, 1990, Davies and Aldridge, 1993, Foreman et al., 1995). However, it is probably not as physically realistic as higher order turbulence closure models, and it may not represent the correct non-linear generation mechanisms (Grenier et al., 1995).

5.3 Methodology

5.3.1 Boundary conditions

Eleven tidal constituents were selected for the simulations (Table 5.1). The largest constituent that we neglected is K_2, which has a maximum amplitude of 14 cm. Keeping both K_2 and the larger S_2 frequencies simultaneously would require over 182 days of simulations for harmonic analysis, which would stress our computer resources. By neglecting K_2, 36-day long simulations (including a 4-day warm-up period) were sufficient. With the three-dimensional grid used in this study, these simulations require on average 4 days of CPU and 5MB of memory on a non-dedicated 23 Mflops workstation.

Harmonic constituents from the station closest to each boundary (Cascais and V.F. Xira for the ocean and river boundaries, respectively) were used as boundary conditions for all frequencies except Z_0 (Table 5.1). Because available tidal data is not relative to the same vertical datum, the amplitudes of Z_0 extracted from the harmonic analysis are not reliable. To circumvent this problem, Z_0 elevations were imposed as zero at the ocean boundary and as an empirical function of the river flow at the upstream boundary (OFB95):

$$\eta_{Z0}(cm) = 8.2 \times 10^{-3} \times Q_R + 2.82 \tag{5.17}$$

where Q_R (m^3/s) represents the river flow. Except where otherwise noted, the average river flow of 400 m^3/s is used, leading to η_{Z0} = 6 cm. Our numerical simulations are performed for the first 36 days of 1972, where extensive tidal data is available for comparison.

Table 5.1 Boundary conditions. Amplitudes are in meters and phases are in degrees.

frequency name	ocean boundary Amp.	ocean boundary Phase	river boundary Amp.	river boundary Phase
Z_0	0.000	---	0.060	---
Msf	0.008	225.4	0.116	50.5
O_1	0.062	332.3	0.070	1.4
K_1	0.072	54.7	0.070	77.7
N_2	0.218	138.0	0.227	187.7
M_2	0.954	85.7	1.177	124.5
S_2	0.331	121.9	0.371	169.9
M_4	0.012	217.5	0.037	230.5
MS_4	0.009	323.8	0.033	228.5
M_6	0.002	196.8	0.036	37.0
$2MS_6$	0.000	---	0.035	81.7

5.3.2 The choice of G

As mentioned in Section 5.2, GWCE models are very sensitive to the choice of the parameter *G*. We estimate this parameter using the method proposed by Kolar et al. (1994a) based on dispersion analysis. We first solve:

$$\left[\frac{i}{6}(4+\alpha)\right]\omega^3+\left[\frac{i}{6}(G+\tau)\,(4+\alpha)\right]\omega^2-\left[\frac{i}{6}G\tau(4+\alpha)+\frac{ihg}{(\Delta x)^2}(2-\alpha)\right]\omega-$$
$$\left[\frac{hg\tau}{(\Delta x)^2}(2-\alpha)+\frac{hg}{(2\Delta x)^2}(\tau-G)\,\beta^2\right]=0 \tag{5.18}$$

where $i=(-1)^{1/2}$, ω is the frequency, τ [s^{-1}] is the linear friction coefficient, Δx is the grid spacing,

$$\alpha = e^{ik\Delta x}+e^{-ik\Delta x} \qquad \beta = e^{ik\Delta x}-e^{-ik\Delta x} \tag{5.19}$$

and $k \in [0,\pi/\Delta x]$ is the wave number. To derive (5.18) the linearized one-dimensional GWCE and momentum equations are written in harmonic and matrix form. A non-trivial solution of these equations exists only when the determinant (5.18) is zero. For our simulations, since the major oscillations appeared near Bugio and S. Julião, we used $\Delta x = 300$ m and $h = 5$ m. The linear friction coefficient τ was estimated using a Manning coefficient of 0.02 $m^{-1/3}s$ and a reference velocity of 1 m/s.

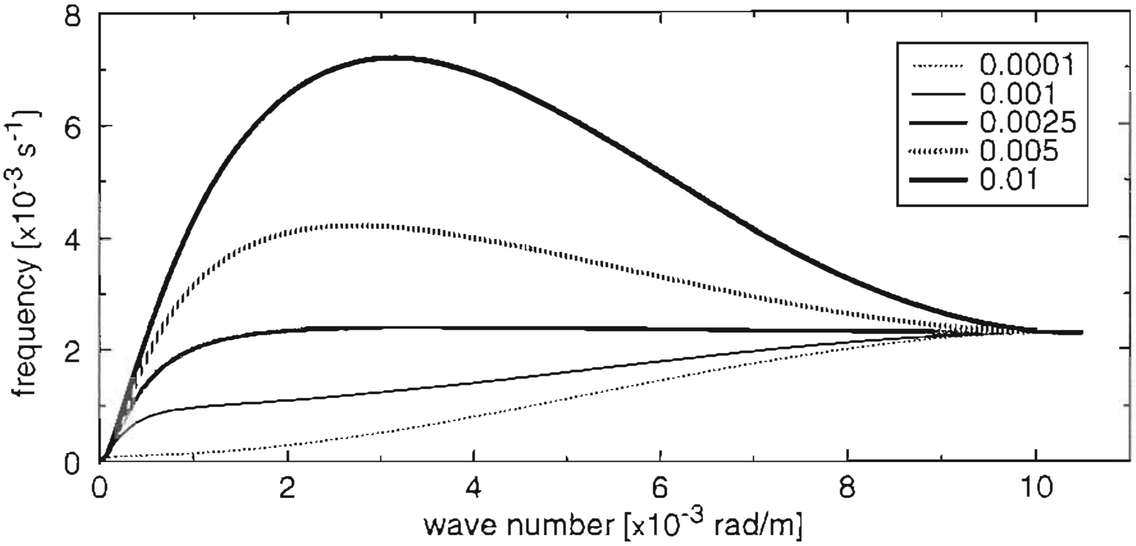

Figure 5.3 Dispersion curve for the Tagus estuary for various values of G ($h = 3$ m; $\Delta x = 300$ m).

The dispersion curve is obtained by plotting the frequency versus the wave number. A folded curve (i.e., in which the first derivative changes sign) indicates a potential for aliasing, which leads to $2\Delta x$ oscillations. Figure 5.3 shows one of the roots of (5.18) (the curves for the other two roots do not fold). Based on these results, we selected $G = 0.0025\ s^{-1}$. The runs were generally unstable with $G = 0.005\ s^{-1}$, which validates this approach. However, this approach must be used with caution. The parameters used in (5.18) must correspond to the areas most susceptible to spurious oscillations. If different critical areas lead to very different values of G, the simulations will likely suffer from mass imbalances or severe spurious oscillations.

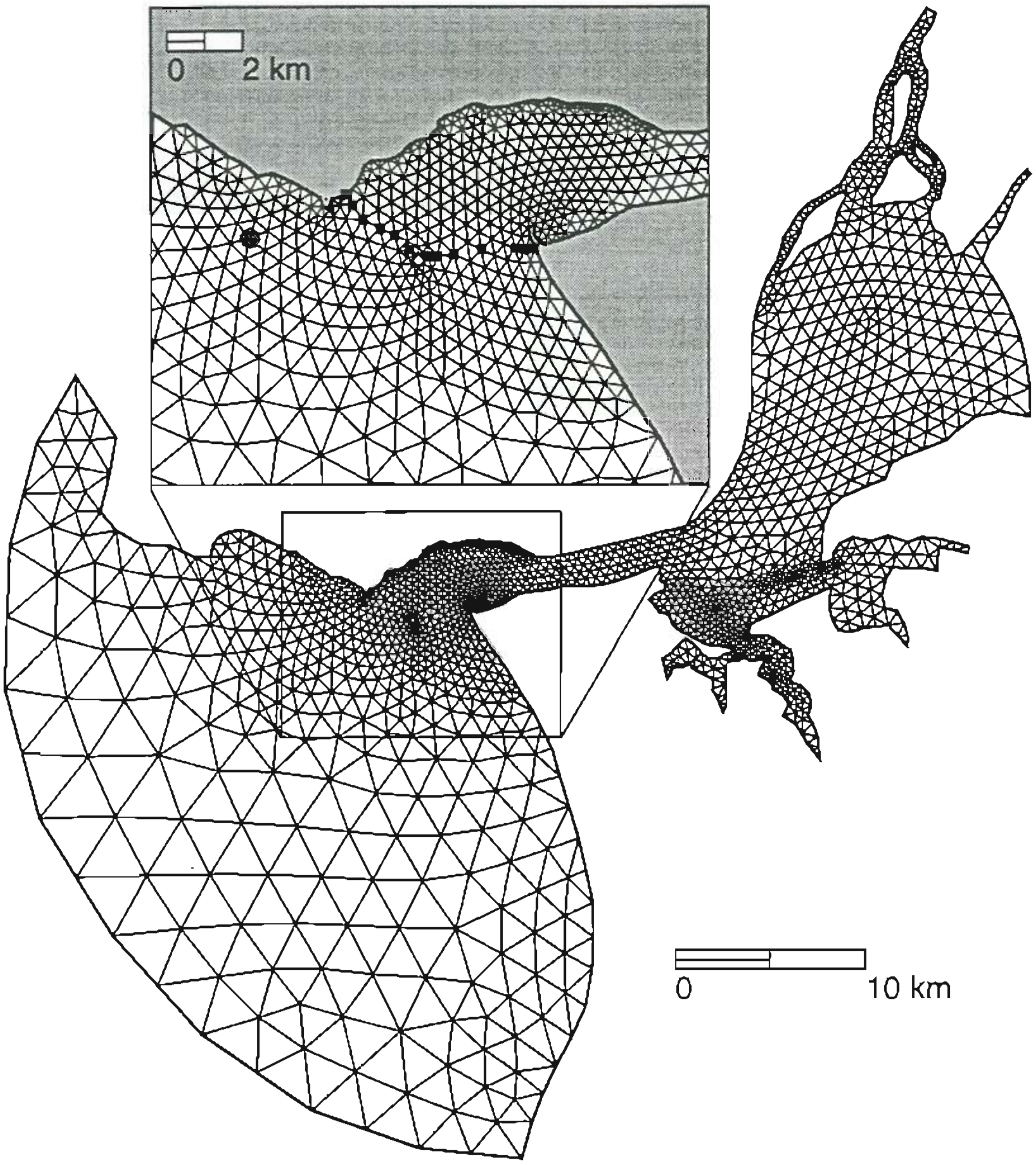

Figure 5.4 Horizontal finite element grid used in the simulations, with 1784 nodes and 3077 elements.

5.3.3 Horizontal grid

The domain extends from V.F. Xira, where elevation data exist, downstream to about 25 km seaward of the mouth, away from the influence of the tidal jet. The horizontal grid was built using the semi-automatic grid generator of Turner and Baptista (1991). In general, the grid is a compromise between the following criteria: (a) good representation of the geometry and bathymetry; (b) minimum number of nodes; (c) slow change in element size; (d) small element skewness; and, (e) enhanced refinement with the complexity of the flow. Restricting the skewness of the elements (the ratio between the largest side and the equivalent radius of the element) to a maximum of 4.3 proved to be invaluable in reducing spurious oscillations and achieving stability. Since the version of the model used in this study does not allow for inundation, the flow in the upstream reaches of the domain could not be properly represented. We decided therefore to use a coarse resolution in that area. The resulting grid has 1784 nodes, and 3077 elements with areas between 7×10^3 and 6×10^6 m^2 (Figure 5.4). Convergence studies using other models show that refining the grid leads to some accuracy gains in the tidal flat areas, but not in the mouth of the estuary (OFB95). The time step was set to 12 s to keep the Courant number below unity throughout the domain. The minimum depth was set to 2.5 m below mean sea level, corresponding to a minimum total depth of about 0.5 m on spring low water tides.

5.3.4 Vertical grid

The vertical grid was defined in a series of preliminary runs using only M_2 and its major harmonics (Z_0, M_4 and M_6). Friction parameters were set as $z_0 = 0.01$ m (as recommended by Blumberg and Mellor, 1987) and $c_d = 0.05$. The use of this relatively large friction coefficient is justified by the reduced near-bottom eddy viscosity. The horizontal diffusion coefficient was set to 10 m^2/s to avoid excessive $2\Delta x$ oscillations. For all runs, the nodes are distributed within each vertical as (Fortunato and Baptista, 1995a):

$$\sigma_i = \left(\frac{1-i}{1-N_v}\right)^4 - 1 \qquad i = 1, N_v \tag{5.20}$$

where N_v is the number of nodes at each vertical.

Three LSC grids with the same total number of vertical nodes (an average of 10 nodes per vertical) were defined, and a σ-coordinate grid with 10 nodes per vertical (grid G1) was used for comparison.

Grids G2 and G3 use the criterion proposed by Fortunato and Baptista (1995a) where the number of nodes per vertical is given by:

$$N_v = N_{vmin}\left(\frac{N_{vmax}}{N_{vmin}}\right)^{\frac{\log\Gamma/\Gamma_{min}}{\log\Gamma_{max}/\Gamma_{min}}} \tag{5.21}$$

The parameter Γ is defined at each horizontal location as:

$$\Gamma = (u_c T)/h \tag{5.22}$$

where u_c is a characteristic velocity and T is the tidal period of the major constituent (M_2). The characteristic velocity was taken as the amplitude of the M_2 depth-averaged velocity for G2 and (following Fortunato and Baptista, 1995a) as the free stream velocity U for G3:

$$U = \frac{gT}{2\pi}\sqrt{(\nabla A)^2 + (A\nabla\phi)^2} \tag{5.23}$$

where A and ϕ are the amplitude and phase of the main tidal constituent, respectively. The characteristic velocities were determined with results from the run with G1. The average number of nodes per vertical was set to 10 by varying the minimum number of nodes N_{vmin} between 3 and 5, and determining N_{vmax} by trial and error. The sensitivity to the choice of N_{vmin} was minimal, and (N_{vmin}, N_{vmax}) equal to (3,15) and (4,16) were retained for G2 (Figure 5.5a) and G3 (Figure 5.5b), respectively.

Grid G4 (Figure 5.5c) is based on an alternative criterion introduced in this study, and was motivated by the observation that the largest errors for G1 generally coincided with the areas where depth-averaged velocities were largest (Figure 5.6). The number of nodes per vertical is defined as:

$$N_v = N_{vmin} + \frac{\vartheta - \vartheta_{min}}{\vartheta_{max} - \vartheta_{min}}(N_{vmax} - N_{vmin}) \tag{5.24}$$

where ϑ is the sum of the depth-averaged velocity amplitudes for all the tidal constituents (computed with G1), and ϑ_{min} and ϑ_{max} are the minimum and maximum of ϑ, respectively. The numbers N_{vmin} and N_{vmax} are taken as 4 and 27, respectively. Again, the lower number was fixed and the upper number varied to force the average number of nodes per vertical to be 10. The consideration of all frequencies constitutes an important advantage of (5.24) over (5.21): when more than one important frequency have very different spatial patterns, (5.21) may fail to recognize some areas as critical. For instance, in the present simulations both M_2 and Z_0 velocities can be large, and in areas that do not always coincide.

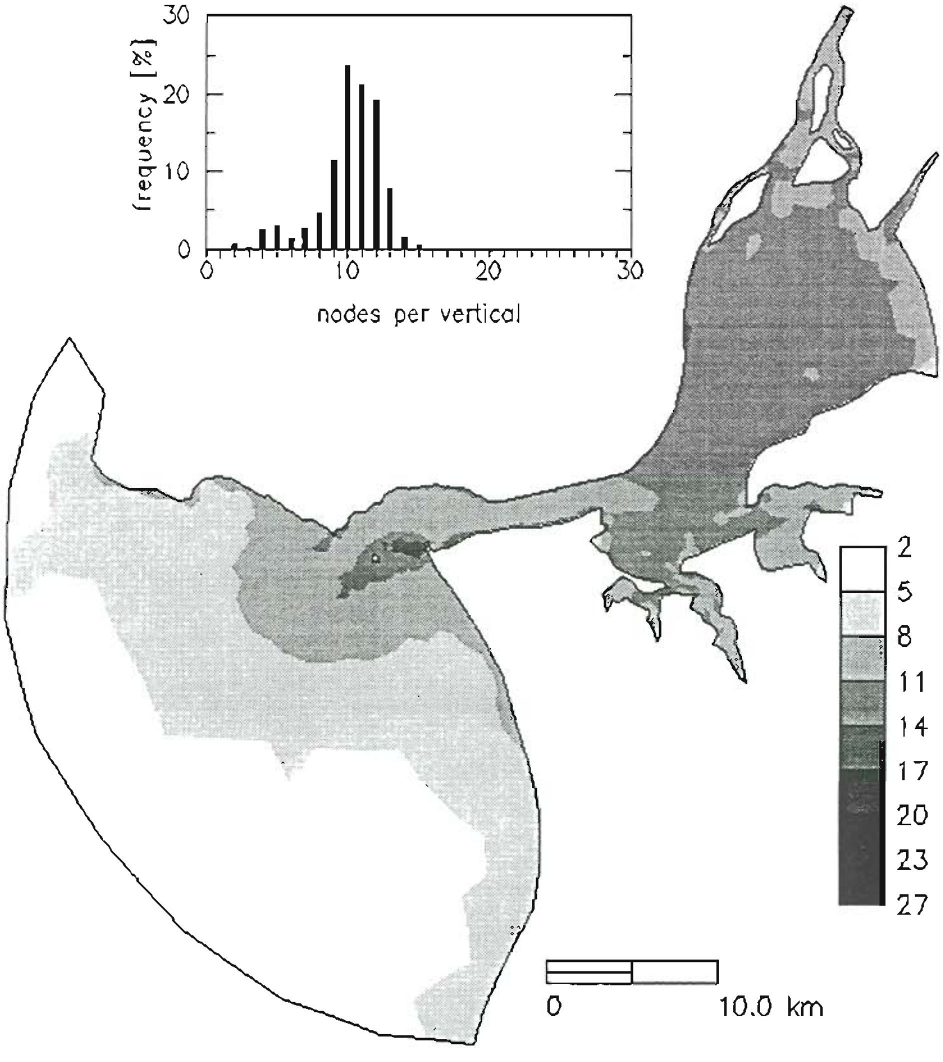

Figure 5.5a Number of nodes per vertical in localized sigma coordinates grid G2.

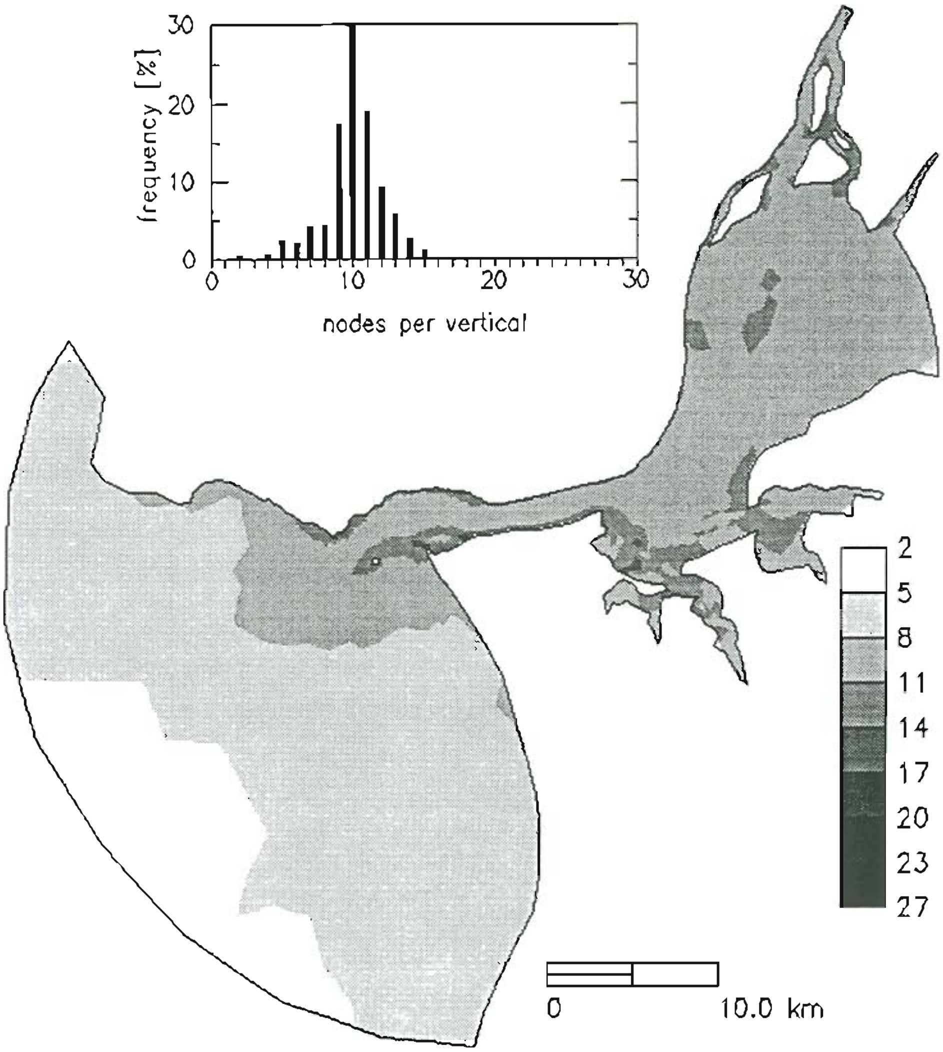

Figure 5.5b Number of nodes per vertical in localized sigma coordinate grid G3.

The performance of the grids was compared by harmonically analyzing the depth-averaged velocities at each horizontal node, and computing the root mean square error for a period of one year as:

$$\mathrm{RMS}_v = \frac{\sum_{i=1}^{N_t} \sqrt{(U_i - \tilde{U}_i)^2 + (V_i - \tilde{V}_i)^2}}{N_t} \tag{5.25}$$

where N_t is the number of time steps (taken as 17520), the time step was set to 1800 s, and the tilde represents reference results obtained with a σ-coordinate grid with 30 nodes per vertical.

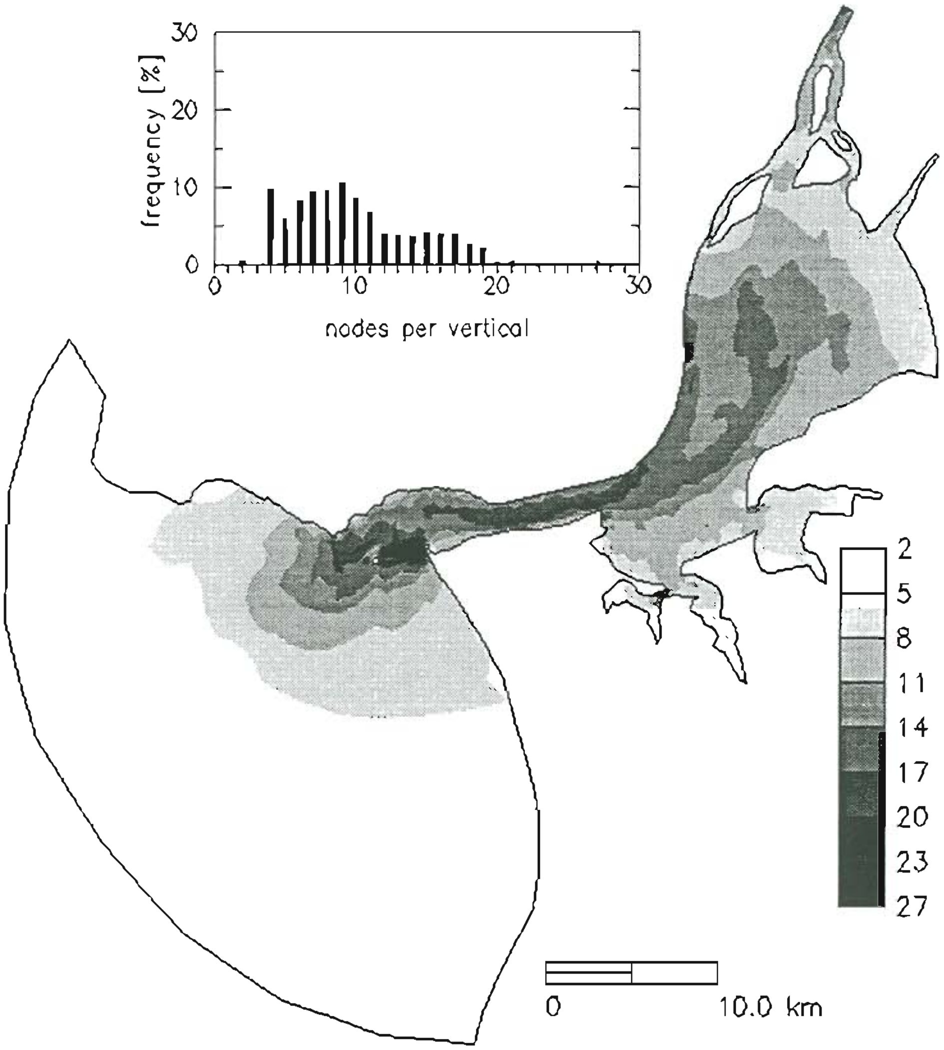

Figure 5.5c Number of nodes per vertical in localized sigma coordinate grid G4.

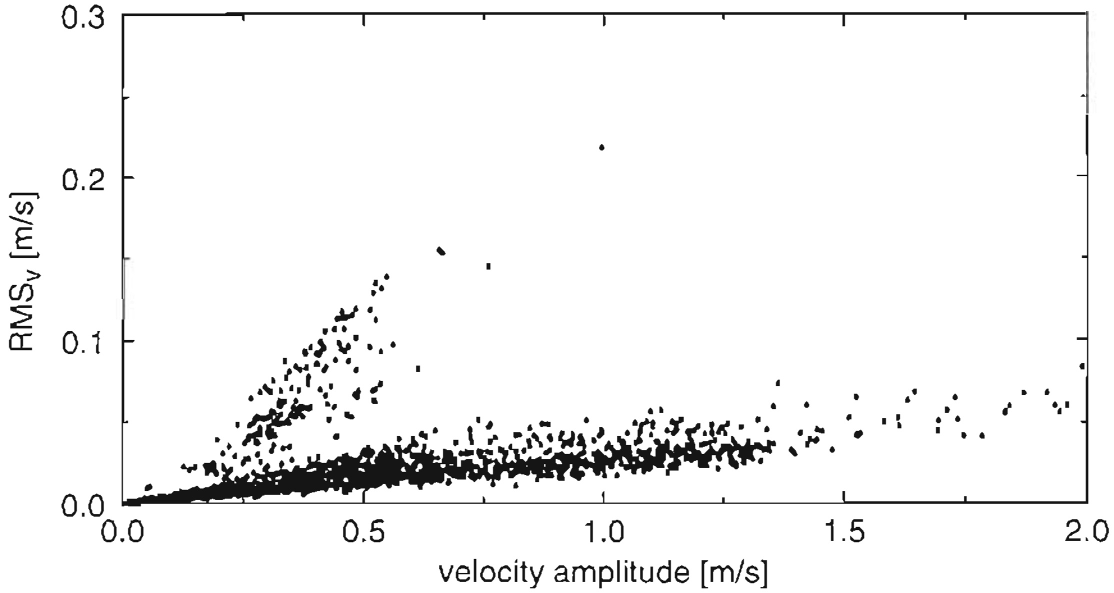

Figure 5.6 Velocity errors for grid G1 increase with velocity amplitude.

Although results from 2D vertical tests indicate that grids based on (5.21) can lead to significant gains in accuracy relative to σ-coordinate grids (Fortunato and Baptista, 1995a), G2 and G3 do not appear significantly more accurate than G1 (Figure 5.7). The criterion used to build G2 and G3 identifies some of the areas where errors are largest in G1 (e.g., the Bugio Bank), but fails to identify others (mainly the tidal jet). In the tidal jet there are large residual velocities generated by advective accelerations, suggesting that the use of (5.21) is only appropriate when all important frequencies have similar spatial distributions. This hypothesis was verified by repeating the runs without the advective terms. In this case, residual velocities were negligible in the lower estuary and G2 and G3 led to a significant accuracy improvement relative to G1.

Maximum global errors for G4 are twice as small as those for the other grids (Figure 5.7). Grid G4 is more accurate than G1 because, for barotropic tidal flows, three-dimensional effects are mostly caused by friction, which grows with the square of velocity. Areas with larger velocities should therefore exhibit stronger shear, hence requiring a finer resolution.

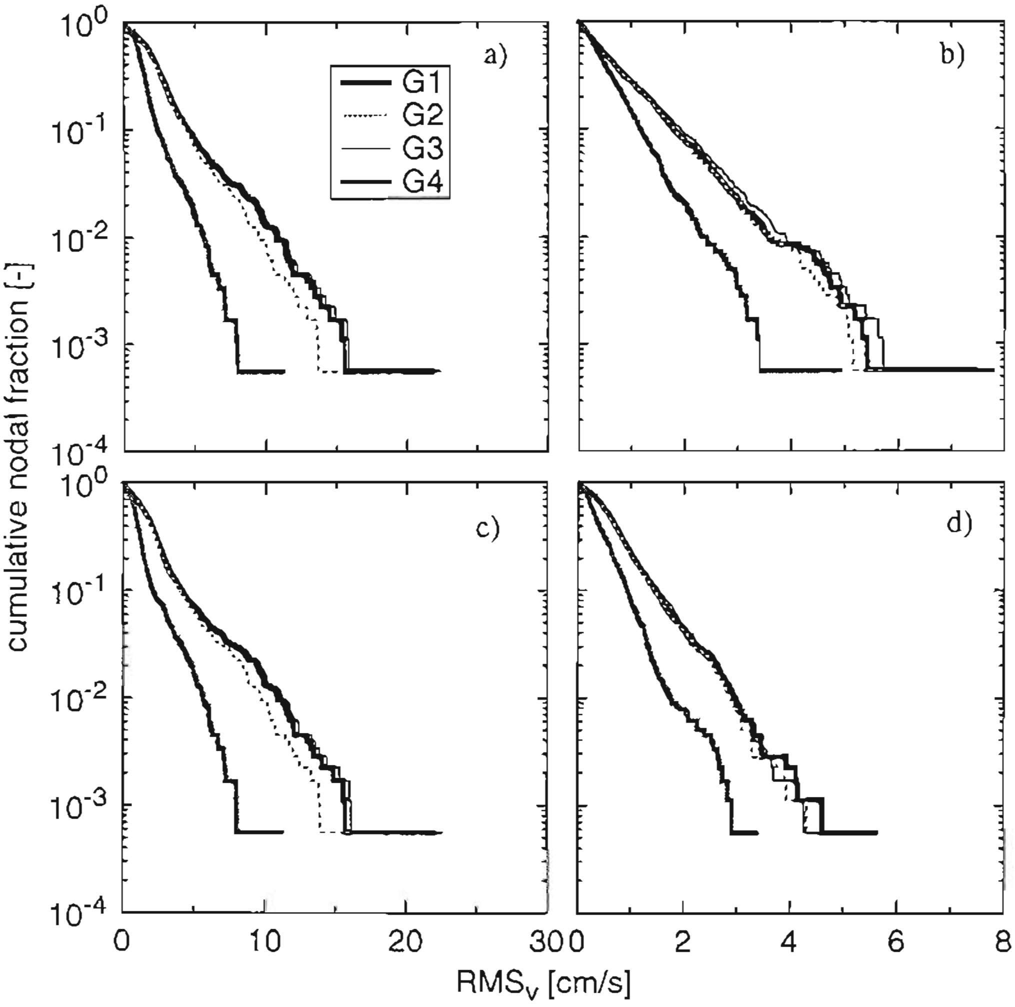

Figure 5.7 Comparison of RMS errors for different vertical grids. a) All frequencies; b) Z_0; c) M_2; d) M_4. The vertical axis represents the fraction of horizontal nodes where the error equals or exceeds the value given by the curve.

5.4 Results and Discussion

5.4.1 Model Validation

Friction parameters were set as $z_0 = 0.01$ m, $c_d = 0.05$ and $A_h = 10$ m^2/s, as in the previous Section. Results were harmonically analyzed at each node using the eleven frequencies imposed at the boundaries (Table 5.1). Root mean square errors were computed at each current meter using (5.25), and at tidal stations using:

$$\mathrm{RMS}_e = \sqrt{\frac{1}{nt}\sum_{i=1}^{nt}\left\{(\eta_i-\tilde{\eta}_i)-\left(\frac{1}{nt}\sum_{p=1}^{nt}(\eta_p-\tilde{\eta}_p)\right)\right\}^2} \tag{5.26}$$

where N_t is again taken as 17520 and the tilde now represents synthesized data. Velocities were taken at σ=-0.7, where data were collected. For the reasons stated in Section 5.3.1, Z_0 was not included in the evaluation of elevation errors.

Elevations are well represented in the lower estuary ($\mathrm{RMS}_e < 0.1$ m - Figure 5.8a). Sixth-diurnal constituents, however, are largely over-predicted (Table 5.2). Grenier et al. (1995) observed a similar over-prediction in the Bight of Abaco using the same eddy viscosity parameterization, and suggested that this result could be due to the presence of a background velocity or a residual turbulence field.

Table 5.2 Comparison of elevation data and model results. Amplitudes are in meters and phases are in degrees. Friction parameters are z_0=0.01 m and c_d=0.05.

	Observed						3D model					
	M_2		K_1		M_6		M_2		K_1		M_6	
Station	amp.	phase	amp.	phase	amp.	phase	amp.	phase	amp.	phase	amp.	phase
Cascais	0.954	85.7	0.072	54.7	0.002	196.8	0.957	86.2	0.072	55.1	0.001	179.4
P. de Arcos	0.998	92.0	0.071	54.6	0.006	277.5	0.973	92.6	0.072	58.0	0.004	147.1
Trafaria	1.038	95.5	0.069	58.2	0.007	321.1	1.010	94.9	0.072	58.6	0.008	114.2
Pedrouços	1.061	92.6	0.072	53.6	0.008	308.6	1.091	102.4	0.072	61.6	0.027	116.3
Cacilhas	1.128	96.0	0.072	56.5	0.011	309.6	1.010	94.9	0.072	58.6	0.008	114.2
Lisboa	1.138	97.1	0.071	57.2	0.011	328.3	1.082	100.5	0.072	60.8	0.020	114.0
Seixal	1.141	99.4	0.071	58.8	0.011	282.2	1.134	105.6	0.074	64.9	0.031	136.9
Montijo	1.183	98.8	0.074	59.0	0.011	269.6	1.142	106.9	0.074	65.4	0.026	130.5
Cabo Ruivo	1.207	99.5	0.072	59.4	0.013	296.4	1.136	112.0	0.073	68.3	0.030	126.1
Alcochete	1.248	104.2	0.073	62.4	0.041	283.6	1.147	119.3	0.073	76.1	0.041	121.6
Sta. Iria	1.245	109.1	0.078	62.8	0.029	328.3	1.162	124.0	0.073	78.4	0.049	127.4
Pta. da Erva	1.278	107.7	0.074	65.7	0.031	318.9	1.148	123.1	0.073	78.8	0.051	126.1
V.F. Xira	1.177	124.5	0.070	77.7	0.036	37.0	1.177	124.5	0.070	77.7	0.035	37.1

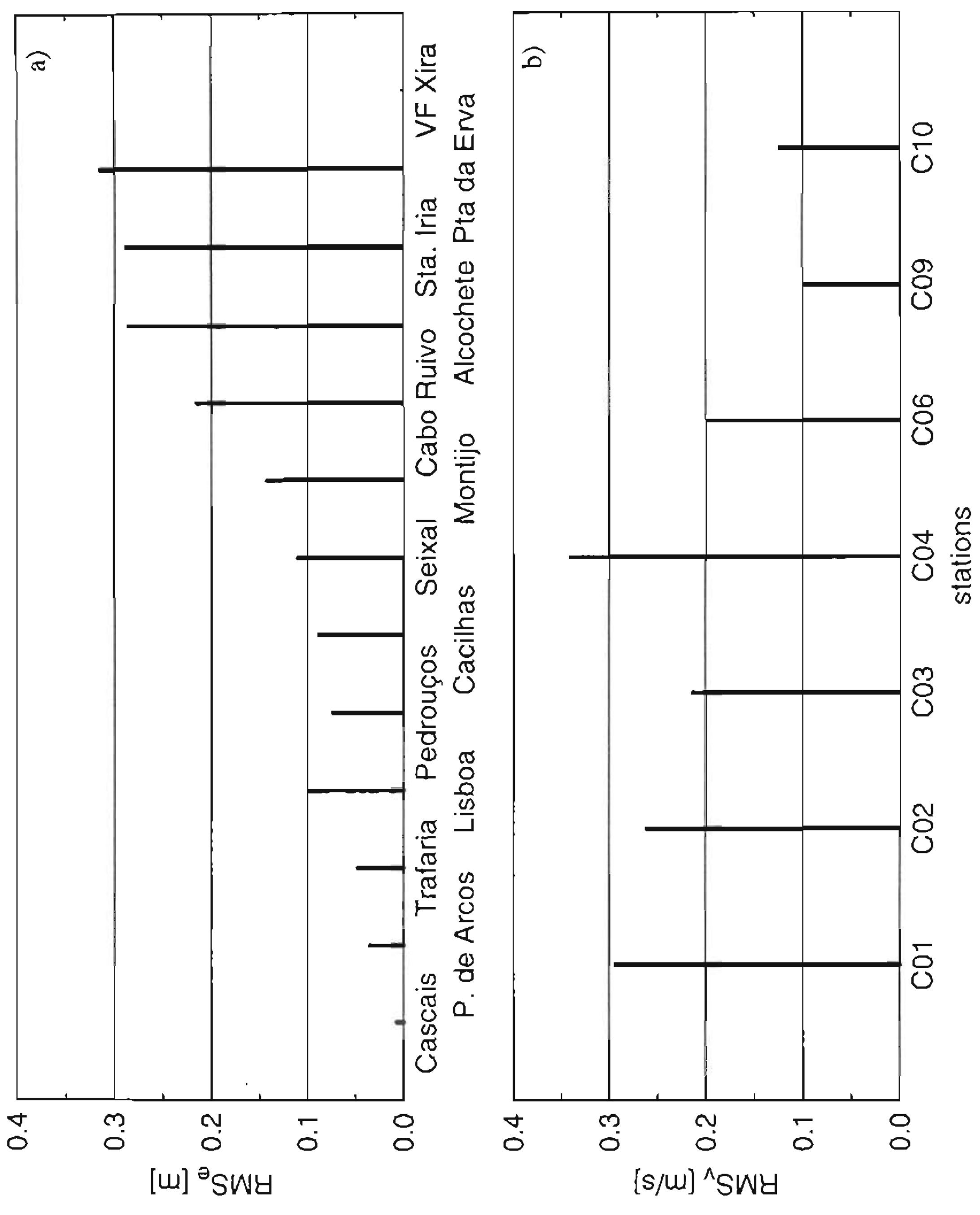

Figure 5.8 Validation results: RMS errors for a) elevations; and b) velocities.

In the upper estuary the agreement between modeled and observed elevations is not as good (0.2 m $< RMS_e <$ 0.3 m - Figure 5.8a). Comparison of our results with those of OFB95, which use finer grids, suggests that part of the error in this area is due to insufficient resolution. However, most of the error in the upper estuary is probably due to the simplified treatment of the tidal flats. As mentioned previously, the Tagus estuary has a resonance mode for a period of about eight to nine hours. Deepening the tidal flats will affect the resonance period since it is proportional to the ratio between the characteristic length and the characteristic celerity of the estuary. By deepening parts of the domain, we are increasing the characteristic celerity, thereby reducing the resonance period. This reduction will decrease the resonance effects on the semi-diurnal constituents (since the resonance period is smaller than 12 hours), thereby reducing their amplitudes. However, diurnal constituents will not be significantly affected because their period is too far from the resonance mode. This explanation is consistent with the results in Table 5.2.

RMS errors for velocities, which range from 0.1 to 0.35 m/s (Figure 5.8b), can be attributed to two major causes. First, in regions of strong velocity gradients, both the lack of precision in the position of the station or morphological changes between the time the bathymetry was surveyed (1964/67) and the time velocities were measured (1987) can lead to large errors. In particular, at station C04, where the errors are largest, the main axis of the observed M_2 ellipse is rotated by about 10 degrees relative to the data (Figure 5.9). However, computing the ellipse 200 m south of the reported position of the station (i.e., an estimate of the distance that the Bugio Bank extended northward between 1964 and 1987) reduces this difference to 1 degree. Either an error in the position of the station or the northward extension of the Bugio Bank could therefore explain part of the errors at this station. Second, the artificial deepening of the tidal flats, and the consequent increase of volume, can explain the general over-prediction of the velocities (Table 5.3 and Figure 5.9). The volume of the upper estuary (upstream of the cross-section Cacilhas/Lisboa) at mean sea level, computed with the grid shown in Figure 5.4, is 9.4×10^8 m^3 or 12.2×10^8 m^3 depending on whether a minimum depth of zero or 2.5 m is specified. This 30% increase in the volume of the estuary should lead to larger flows, specially in the stations inside the tidal jet (C01 through C06), and therefore to the over-prediction of velocities.

Table 5.3 Comparison of velocity data and model results. Amplitudes are in m/s and phases are in degrees.

		Observed		3D model (depth-average)		3D model (at σ=-0.7)	
				M_2			
Current meter		amp.	phase	amp.	phase	amp.	phase
C01	u	0.803	11	1.007	31	0.927	30
	v	0.159	9	0.209	31	0.199	32
C02	u	0.941	17	0.836	28	0.770	26
	v	0.544	39	0.238	30	0.230	31
C03	u	0.560	0	0.658	13	0.622	14
	v	0.047	157	0.052	105	0.054	113
C04	u	0.647	14	0.869	30	0.810	30
	v	0.686	14	0.645	30	0.605	30
C06	u	0.368	26	0.451	58	0.411	57
	v	0.111	358	0.139	41	0.126	42
C09	u	0.169	3	0.204	24	0.189	22
	v	0.064	147	0.049	258	0.038	255
C10	u	0.186	14	0.140	49	0.126	47
	v	0.137	5	0.232	25	0.214	24
				K_1			
Current meter		amp.	phase	amp.	phase	amp.	phase
C01	u	0.020	328	0.035	354	0.033	356
	v	0.005	348	0.008	353	0.007	353
C02	u	0.029	319	0.024	2	0.022	0
	v	0.003	280	0.007	1	0.007	2
C03	u	0.017	296	0.025	338	0.025	339
	v	0.003	73	0.005	85	0.005	87
C04	u	0.033	337	0.028	350	0.027	350
	v	0.035	337	0.019	0	0.018	359
C06	u	0.021	315	0.029	6	0.026	5
	v	0.008	271	0.011	0	0.010	0
C09	u	0.004	313	0.004	317	0.004	318
	v	0.005	207	0.002	72	0.002	68
C10	u	0.012	304	0.007	350	0.006	351
	v	0.006	255	0.008	309	0.007	309

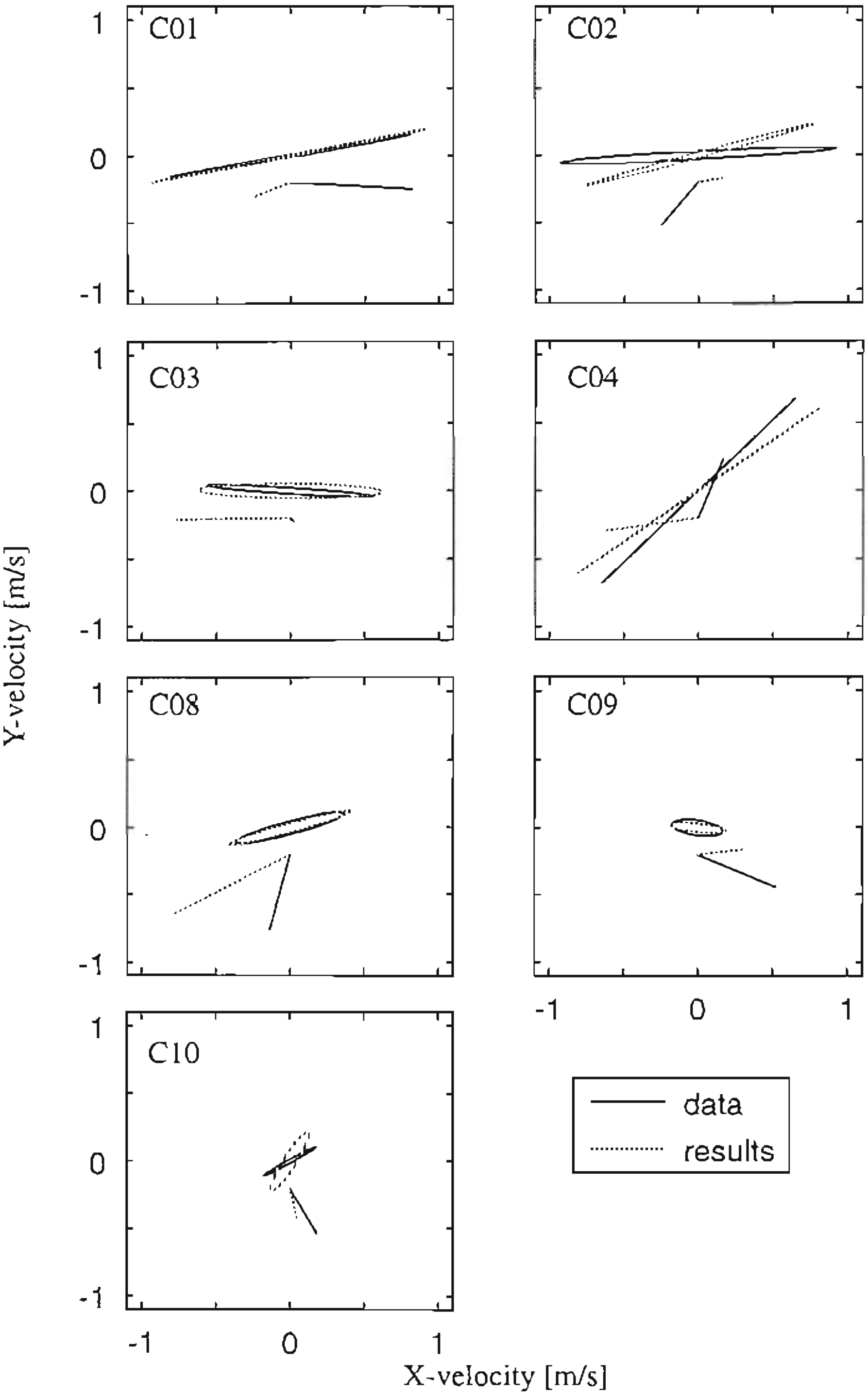

Figure 5.9 Comparison of M_2 and residual velocities at the current meter stations. Both results and data are taken at σ=-0.7. Residual velocities are multiplied by five and centered at (0., -0.2).

Finally, residual velocities agree well with data only in the coastal stations (C06, C09 and C10 - Figure 5.9). Possible reasons for the disagreement in the estuarine stations include unresolved eddies (e.g., at stations C01 and C02 due to large bridge columns, at station C04 due to the island of Bugio), incorrect bathymetry (station C04), neglected density effects, and measurement errors due to wave action.

5.4.2 Tidal dynamics

This section describes the circulation patterns and their generation in the mouth of the Tagus estuary, and discusses the implications from a water quality perspective.

Flow patterns at the mouth are very different on ebb and flood. On ebb, a tidal jet forms along the canyon prolonging the channel, with two large eddies on each side (Figure 5.10a). The eddies form near the coast, and move outward as ebb progresses. The eddies are strongest and move further away from the coast on spring tides (Figure 5.11). As the eddies move away, the currents invert near the coast. In particular, strong flood currents can be observed over the Bugio Bank while the channel currents are still ebbing. On flood, the currents over the sandbanks are large (e.g., over 2.5 m/s over the Bugio Bank), while the currents in the canyon are relatively small. As the two coastal eddies dissipate, a clockwise eddy forms inside the channel, between Paço de Arcos and Pedrouços (Figure 5.10b). This eddy forms near the southern margin of the channel and moves north until it dissipates at the end of flood.

M_2 tidal ellipses are almost rectilinear in the channel and mouth due to geometric constraints, but weak rotation effects can be observed in the bay. The largest M_2 depth-averaged velocities occur over the Bugio Bank (about 1.5 m/s) and along the main channel (up to 1.2 m/s). The phase lag between high or low water and these largest M_2 velocities is about 3 hours and 30 minutes in the Bugio Bank, and 4 hours and 25 minutes in the channel. There is therefore a strong phase lag between velocities in the channel and in the shallow areas. This phase lag, about 1 hour and 45 minutes between the channel and the northern margin and 1 hour between the channel and the Bugio Bank (Figure 5.12), is due to the difference in depths. As depths decrease, friction increases and so does the phase difference between elevation and velocities.

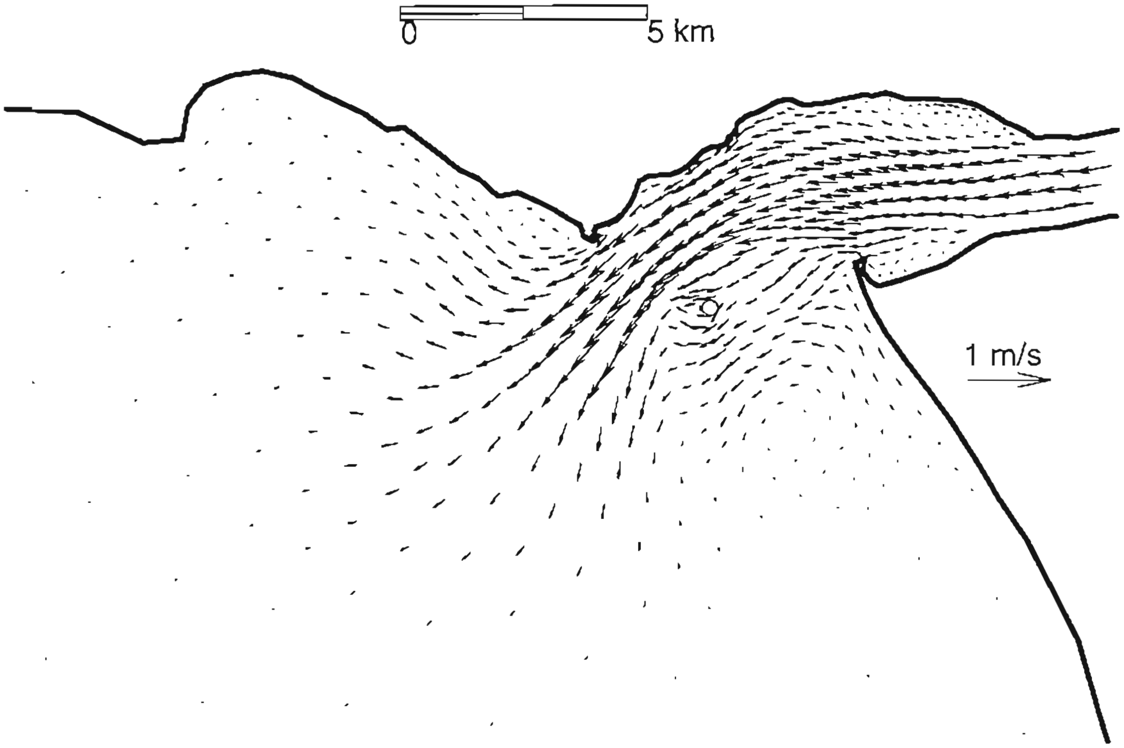

Figure 5.10a Surface currents during ebb (2:56 P.M. on January 9th). Entrainment eddies form on both sides of the tidal jet.

The eulerian residual velocities are quite large (up to 0.5 m/s over the Bugio Bank), with three well defined eddies (Figure 5.13a). An eddy develops in the mouth, between P. Arcos and Pedrouços, and two other develop on both sides of the tidal jet, the one to the north rotating clockwise, and the one to the south rotating counterclockwise. The development of two eddies downstream of inlets has been observed (e.g., Onishi, 1986) and modeled (e.g., Ridderinkhof and Zimmerman, 1990) in other systems. Residual currents point typically upstream in shallow areas, and downstream in deep areas. The other low frequency included in the model, Msf, has a pattern similar to Z_0, with two eddies forming on each side of the tidal jet. These currents reinforce residual velocities on spring tides and counteract them on neap tides, and thus explain the stronger eddies on spring tides.

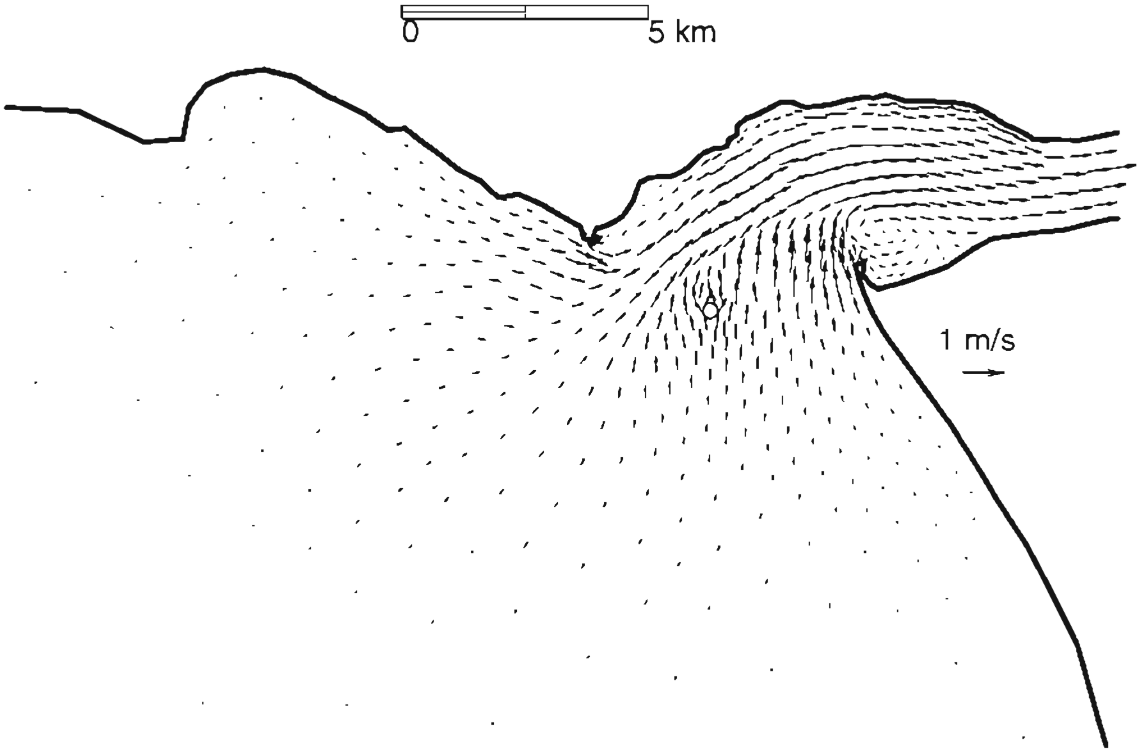

Figure 5.10b Surface currents during flood (8:32 P.M. on January 9th). An eddy forms inside the channel.

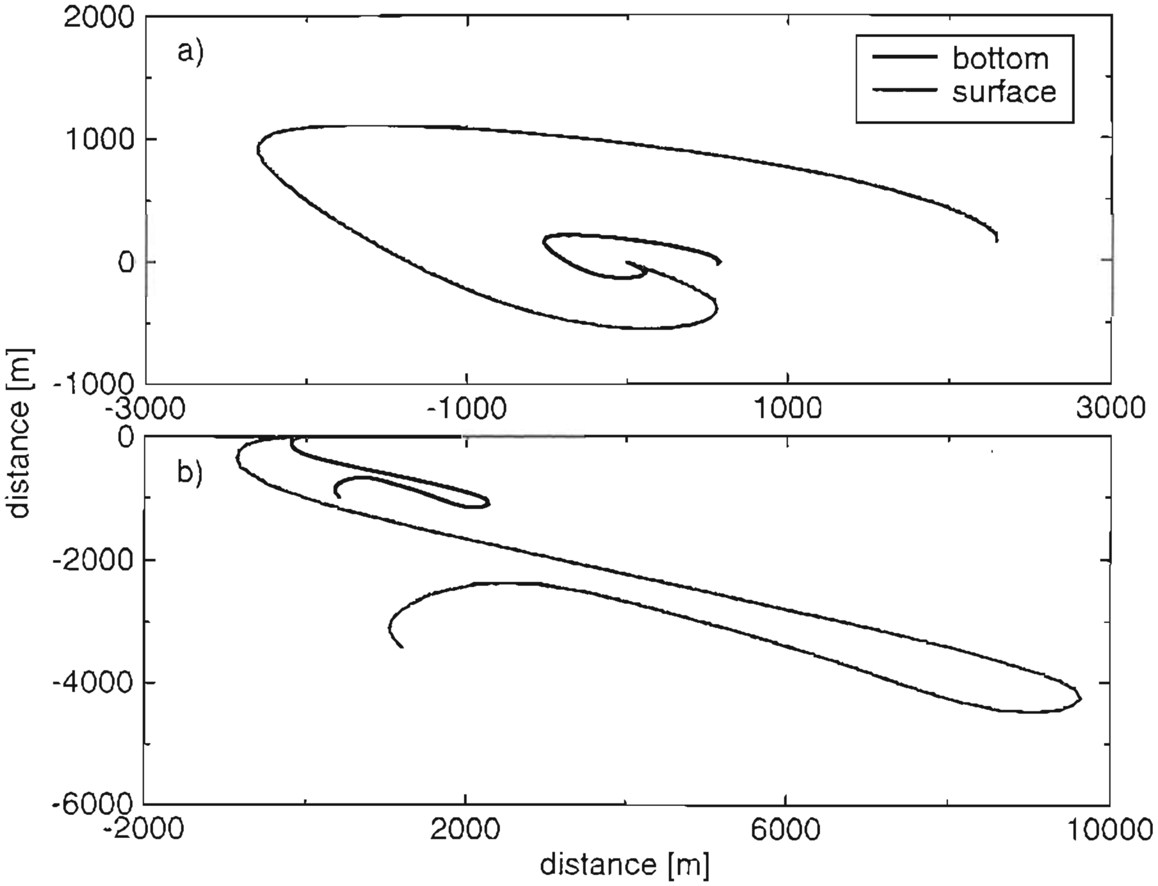

Figure 5.11 Progressive vector diagrams for the point shown in gray on Figure 5.4 for a) a neap tide, and b) a spring tide. Each curve is defined as $x(t) = \int_{t_0}^{t} u(x_0, y_0, t)\,dt$ and $y(t) = \int_{t_0}^{t} v(x_0, y_0, t)\,dt$. On a neap tide the point is inside the eddy and currents rotate always clockwise; on a spring tide, the eddy moves away from the coast, and the currents can rotate counter-clockwise on ebb.

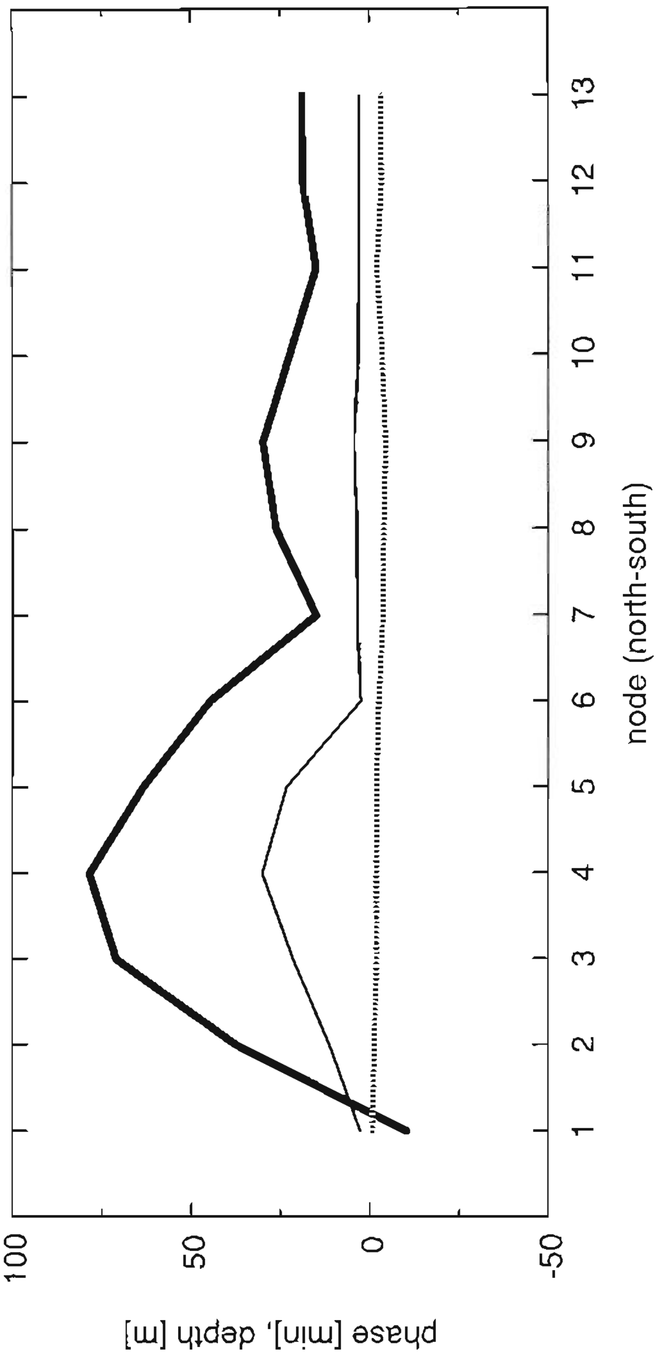

Figure 5.12 M_2 phases along the cross-section shown in Figure 5.4. Time of maximum velocity (thick line), elevation phase minus one-forth of the tidal period (dotted line), depth (thin line).

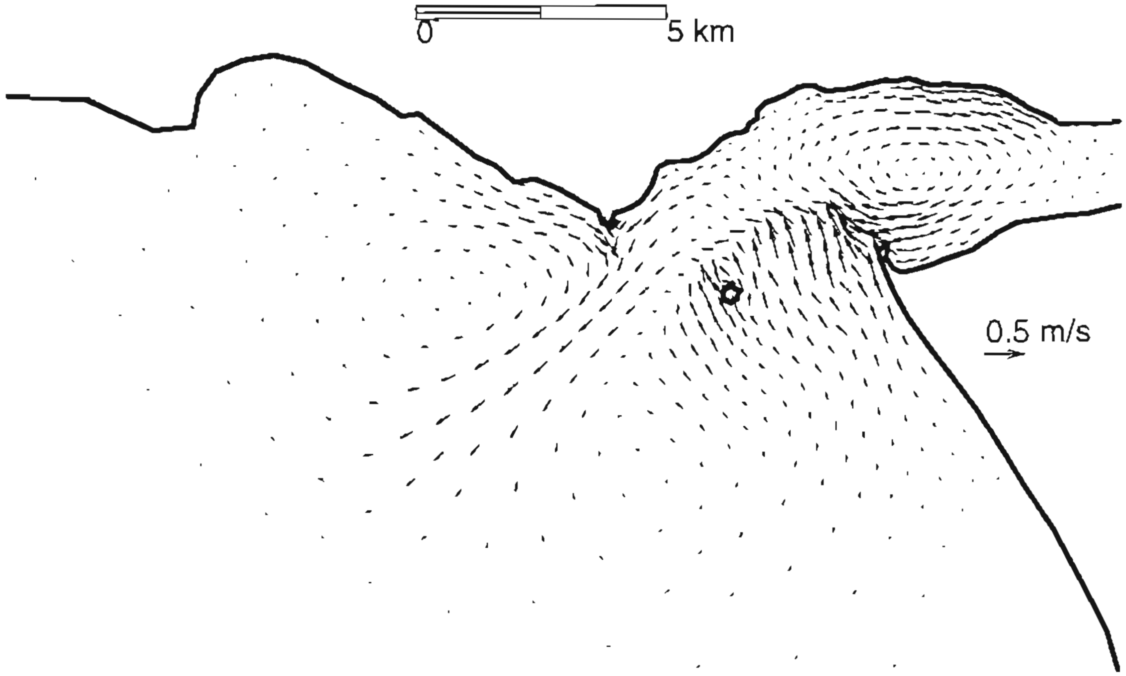

Figure 5.13a Depth-averaged eulerian residual velocities.

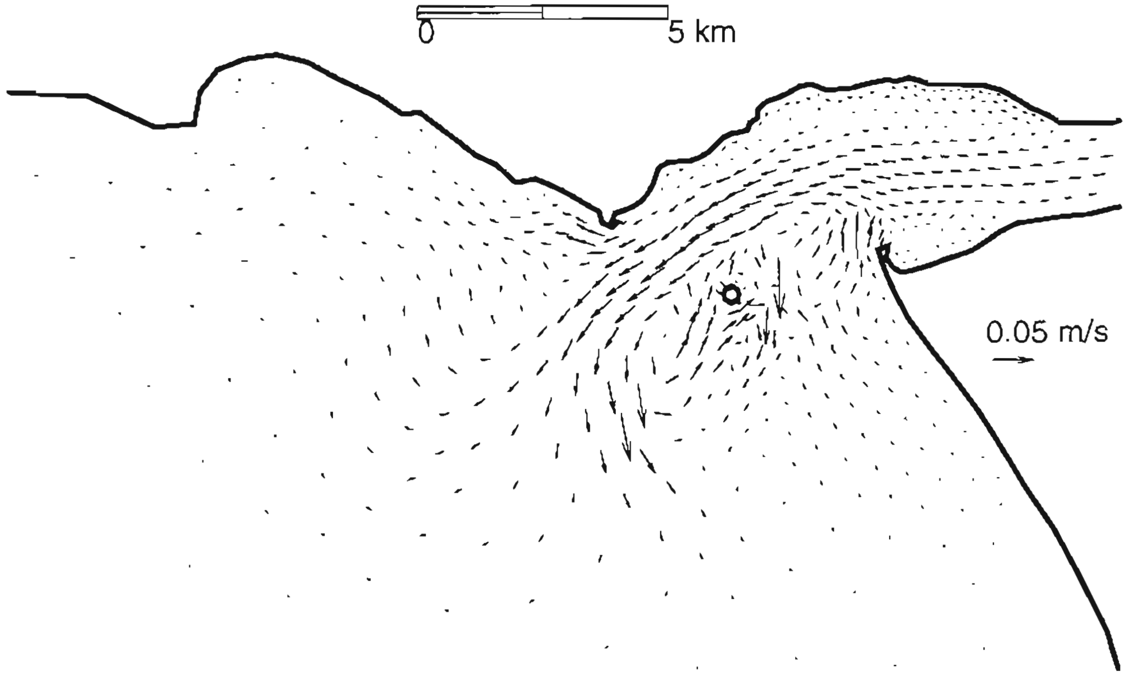

Figure 5.13b Depth-averaged eulerian residual velocities in the absence of advection.

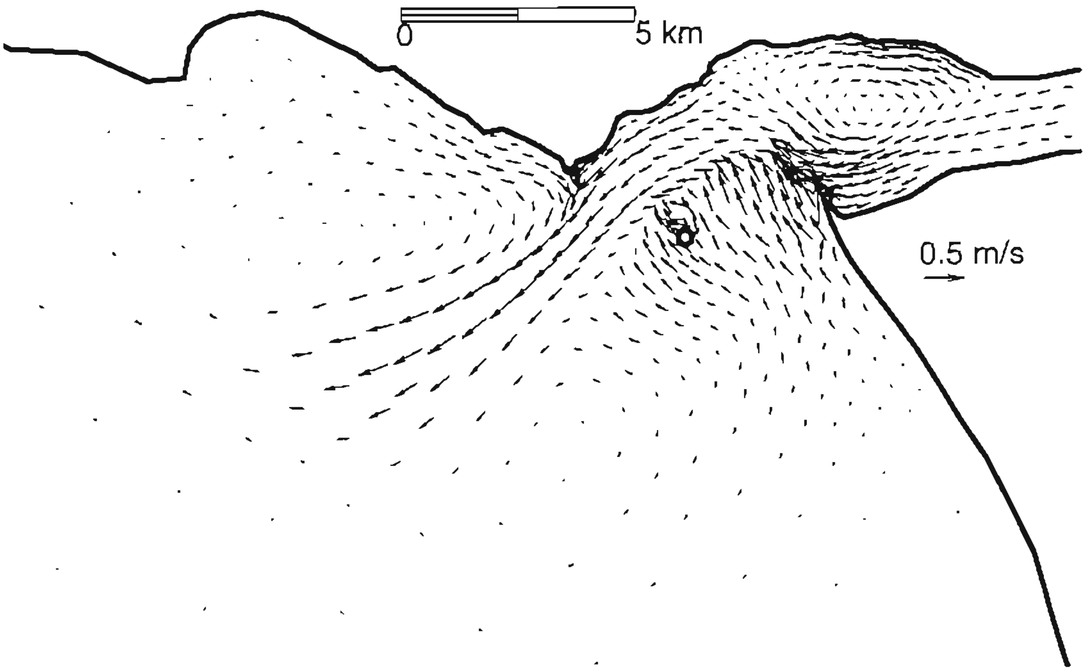

Figure 5.13c Depth-averaged eulerian residual velocities for the maximum monthly average river flow between 1971 and 1984 (4000 m^3/s).

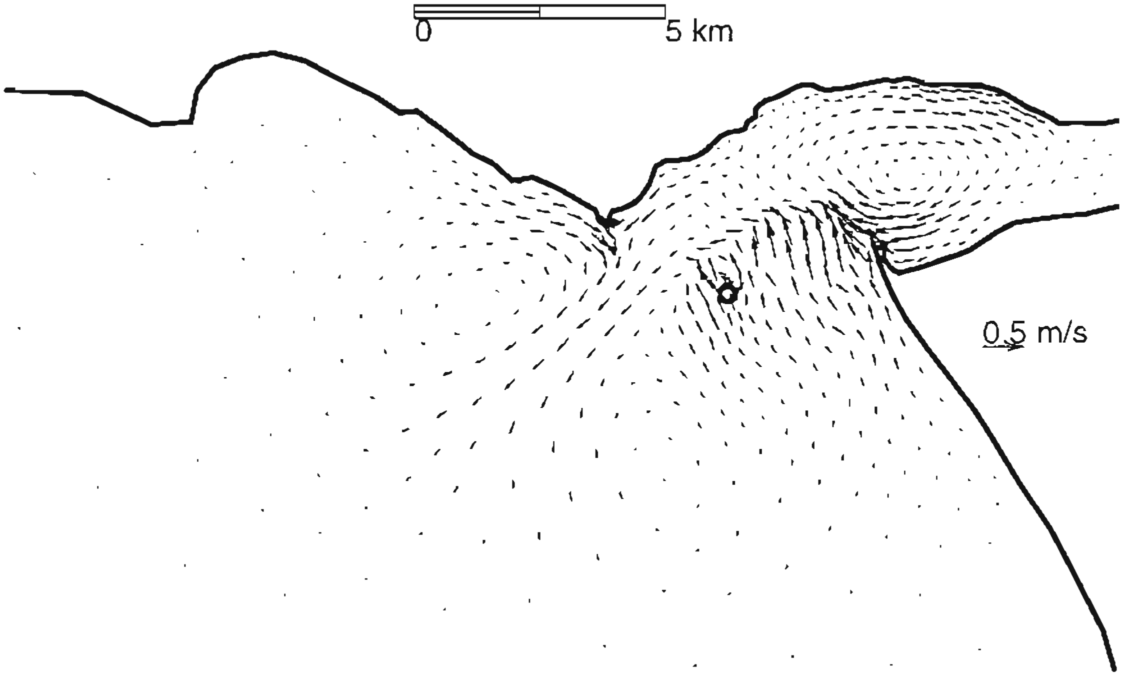

Figure 5.13d Depth-averaged eulerian residual velocities for a quasi two-dimensional simulation (see text).

The low frequency velocity field is mainly generated by advective accelerations: the fully non-linear run shows maximum depth-averaged residual velocities of 0.5 m/s (Figure 5.13a), while in a run without advection these velocities are an order of magnitude smaller and the eddies disappear (Figure 5.13b). The eddies are only mildly affected by the Coriolis force, and even a very large river flow only has a visible effect on the inside eddy (Figure 5.13c). The importance of the advective accelerations could be expected, because the velocity phase and amplitude differences between the shallow banks and the deep channel lead to large horizontal velocity gradients. To verify the importance of three-dimensional effects on the generation of residual velocities, the model was run without the momentum dispersion in the GWCE, and with the advective terms computed with the depth-averaged velocities. With these modifications, the model is equivalent to a depth-averaged model, except for the friction parameterization which remained the same as in the three-dimensional model. Results are generally similar (Figure 5.13d). The major differences occur in the tidal jet and the two associated eddies, where velocities are slightly smaller.

To further understand the importance of three-dimensional effects, we examine the spatial and temporal distribution of:

$$D_{ij} = \frac{\int_{-1}^{0} (u_i - U_i)\,(u_j - U_j)\,d\sigma}{U_i U_j} + 1 \qquad i,j = 1,2 \tag{5.27}$$

The term D_{ij} multiplies the advective fluxes U_iU_j in the conservative depth-averaged momentum equations. In depth-averaged models, D_{ij} is usually assumed equal to one, although this is strictly true only for a uniform vertical profile of velocity ($u_i = U_i$). Deviations of D_{ij} from unity are therefore a measure of the vertical variability of velocities. Values of D_{ij} were computed for $i=j=r$, where r is the direction of the local velocity, i.e.:

$$D_{rr} = D_{11}\cos^4\alpha + D_{22}\sin^4\alpha + 2D_{12}\cos^2\alpha\sin^2\alpha \tag{5.28}$$

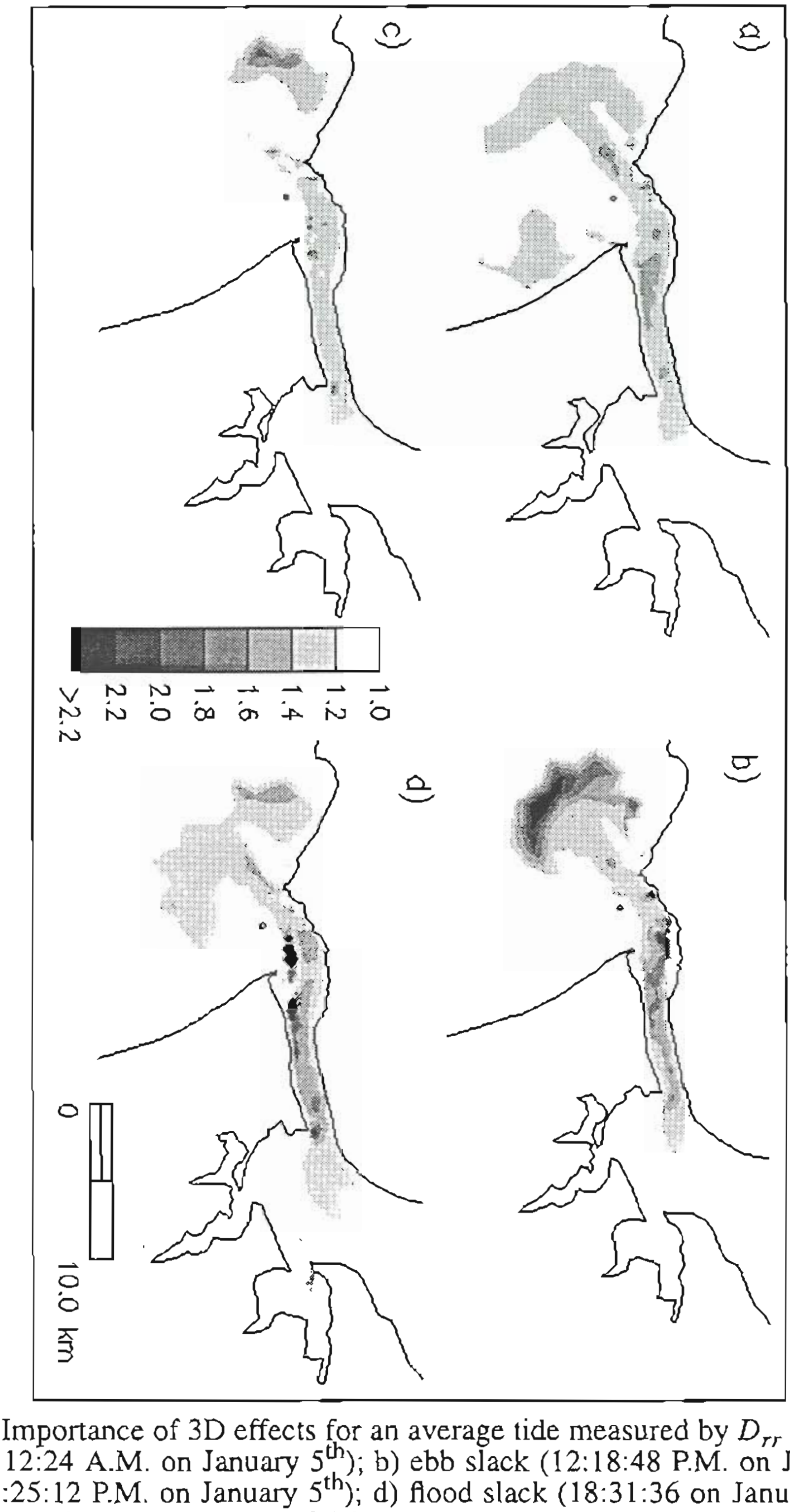

Figure 5.14 Importance of 3D effects for an average tide measured by D_{rr} (see text) at: a) high tide (9:12:24 A.M. on January 5th); b) ebb slack (12:18:48 P.M. on January 5th); c) low tide (15:25:12 P.M. on January 5th); d) flood slack (18:31:36 on January 5th). In the areas not shown D_{rr} is between 1 and 1.2.

where α is the angle between the x axis and the velocity vector, measured counterclockwise. To avoid divisions by very small numbers, D_{rr} was set to 1 for velocities smaller than 0.1 m/s. Although D_{ij} can be large at slack, its effect is negligible since it is multiplying a very small number (U_iU_j).

Values of D_{rr} computed at four instants during a tidal cycle suggest that three-dimensional effects are small in most of the domain (Figure 5.14). However, in the channel and in the tidal jet, D_{rr} can enhance the effect of advective accelerations by over 100%. Since advection is a major process in this area, three-dimensional effects cannot be neglected. The large values of D_{rr} in the channel and tidal jet also justify qualitatively the finer vertical resolution used in those areas.

Two characteristics of the flow at the mouth of the Tagus estuary promote strong mixing in the system. First, the flood-ebb asymmetries lead to exchanges between marine and estuarine waters, as the estuarine waters leaving the estuary through the canyon are partially replaced with marine water flowing in near the margins. This process, known as "tidal pumping" is common to many estuaries (e.g., Fisher et al., 1979). Second, chaotic stirring is generated in the system by the interaction between tidal and residual flows. Chaotic stirring occurs in a tidal system when the ratio of the tidal excursion over the characteristic length scale of the residual eddies is larger than O(1) (Ridderinkhof and Zimmerman, 1990, Ridderinkhof and Loder, 1994). Under these circumstances, a particle samples very different parts of the eddy (or eddies) during a tidal cycle, making the trajectory very sensitive to the initial position. Furthermore, this stirring increases with the ratio between the residual and tidal velocities (Ridderinkhof and Zimmerman, 1990). Chaotic stirring can therefore be expected at the mouth of the Tagus, where the tidal excursion is larger than the three main eddies, and residual currents are relatively strong.

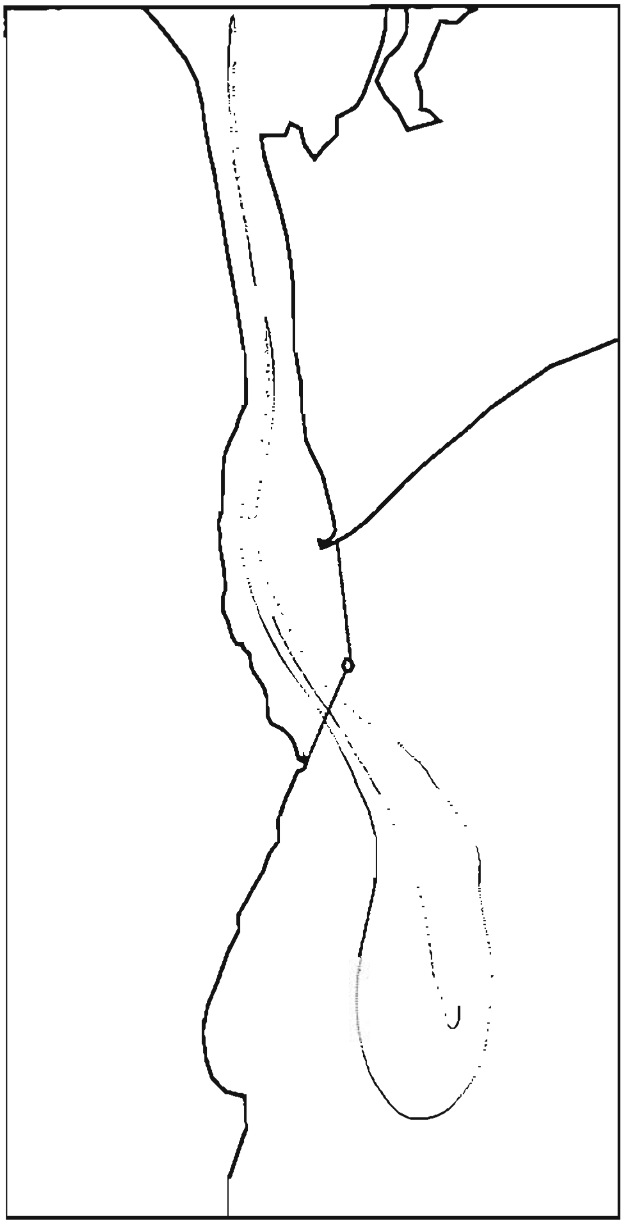

Figure 5.15a Mixing in the mouth of the Tagus estuary. 2771 particles initially located along the gray line were released at high tide (3:45 A.M. on January 1st, 1972) and followed for one M_2 tidal cycle. The dots represent their final position and illustrate the chaotic stirring and the mass exchanges between estuarine and coastal waters.

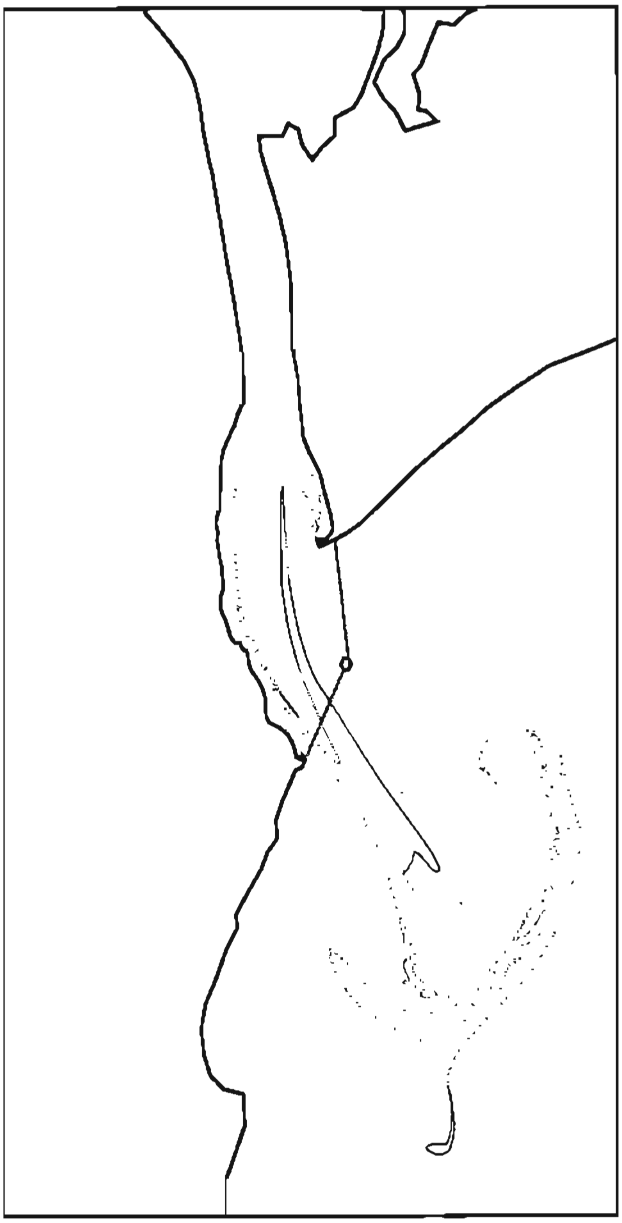

Figure 5.15b Same as Figure 5.15a, but the particles were released at mid-ebb (9:45 A.M. on January 1st, 1972). The effect of chaotic stirring is particularly clear.

The two processes are illustrated by the behavior of a large number of particles carried by the depth-averaged flow. The particles were initially distributed across the mouth of the estuary, at intervals of about 2 m from each other. They were released during a spring tide at high water (Figure 5.15a) and mid-ebb (Figure 5.15b) and were followed for one M_2 tidal cycle using a very accurate particle tracking model (Oliveira and Baptista, 1995). The model uses an accuracy-controlled fourth-order Runge-Kutta tracking algorithm and a very small closure error (10^{-7} m) to prevent error accumulation.

After one M_2 cycle the particles released at high tide were spread out over 25 km (Figure 5.15a). The particles initially located on the main channel moved seaward, while those initially close to the coast or over the sandbank moved deep inside the estuary. This behavior shows that marine waters enter the estuary close to the coast, thus enhancing the flushing of the estuarine waters and reducing residence times. However, these results must be interpreted with caution, since depth is not considered in particle tracking. Residual fluxes into the estuary occur typically in shallow areas whereas outward residual fluxes occur over the canyon. Even though residual velocities into the estuary can be quite large (Figure 5.13a), outward fluxes predominate (Figure 5.16). Fluxes of marine waters into the estuary are therefore less important than suggested by the particle tracking.

Two clear indications of chaotic nature of the trajectories are the strong dependence of lagrangian velocities on the release time (as suggested by the different final positions of the particles in the two figures) and the stretching and folding of the initially straight lines. This stretching and folding was accentuated for the particles released at mid-ebb (Figure 5.15b). In particular, the particles initially over the Bugio Bank were trapped in the flood eddy (Figure 5.10b) and rotated several times until the eddy dissipated and they were flushed out. Clearly, chaotic stirring constitutes a very efficient mixing process in this area.

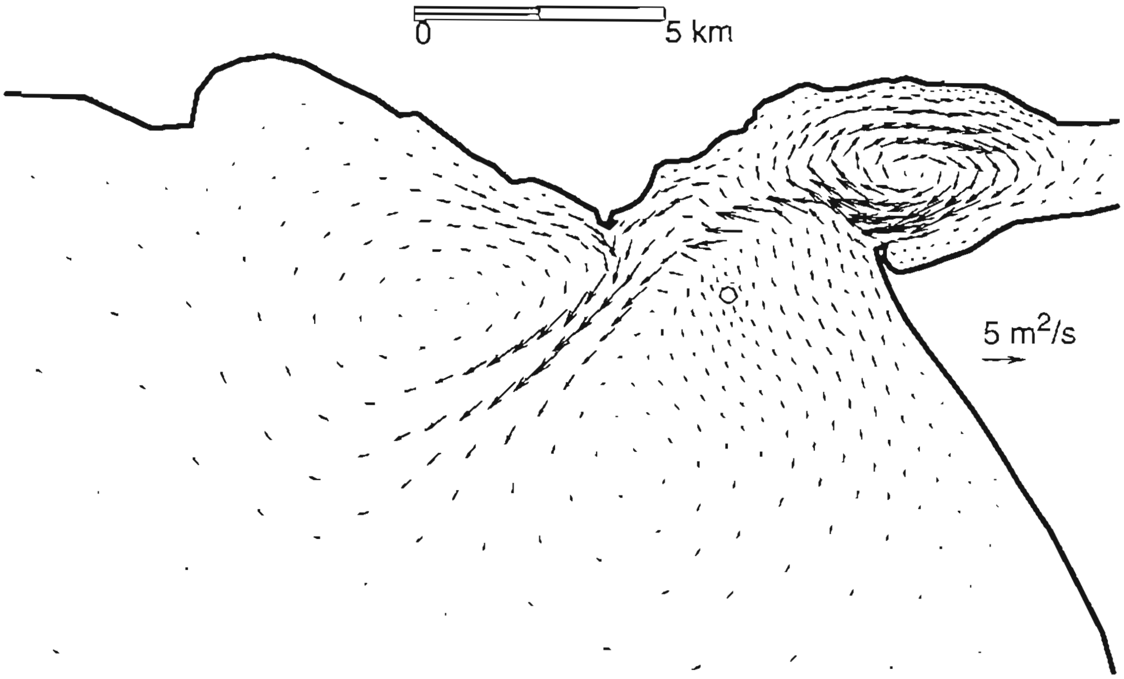

Figure 5.16 Residual fluxes, obtained through harmonic analysis of (UH,VH).

5.5 Summary

The application of a three-dimensional hydrodynamic model provided new insights into the complex barotropic circulation at the mouth of the Tejo estuary. Of particular interest are the generation of residual currents by advective accelerations and the importance of three-dimensional effects. In turn, these residual currents generate intense mixing by tidal pumping and chaotic advection. Both advective and three-dimensional effects should therefore be included in any hydrodynamic model used as a basis for a water quality model for this area.

A recently proposed method for the vertical discretization of shallow water models, the localized sigma coordinates, was applied for the first time in a fully three-dimensional situation. To take advantage of the flexibility of this method, two criteria for the horizontal distribution of the total number of nodes were evaluated. One criterion, previously proposed by Fortunato and Baptista (1995a), led to results similar to those obtained with an equivalent sigma coordinate grid, and was shown to be inappropriate when advective accelerations are important. However, with an alternative criterion introduced in this study, the maximum errors with the LSC grid were only half those obtained with the equivalent sigma coordinate grid. This study establishes therefore the LSC as an attractive alternative to the traditional sigma coordinates commonly used in shallow water models.

This study encourages new developments. From a water quality perspective, we are now investigating the effects of tidal pumping and chaotic advection on residence times in the Tagus estuary. From a hydrodynamics perspective, some aspects of our simulations should be improved. The major limitation of this study was the simplified treatment of the tidal flats which increased the volume of the estuary, leading to the over-prediction of velocities and the under-prediction of semi-diurnal tides in the upper estuary. We are currently applying two inundation models which will hopefully improve accuracy. Another significant limitation of this study, which we will address in the future, is the neglect of baroclinic effects. While arguably these effects are small during spring tides and during low river flow, they will be important at times and will affect residual currents.

References

Andreae, M.O., Byrd, J.T. and P.N. Froelich, Jr., 1983. Arsenic, Antimony, Germanium and Tin in the Tejo Estuary, Portugal: Modeling a Polluted Estuary, *Environ. Sci. and Technol.*, 17: 731-737.

Castanheiro, J.M., 1986. Distribution, Transport and Sedimentation of Suspended Matter in the Tejo Estuary, in *Estuarine Processes: an Application to the Tagus Estuary*, Secretaria de Estado do Ambiente e Recursos Naturais, Lisboa, 75-90.

Davies, A.M. and J.N. Aldridge, 1993. A Numerical Model Study of the Parameters Influencing Tidal Currents in the Irish Sea, *J. Geophys. Res.*, 98: 7049-7067.

Davies, A.M. and J.E. Jones, 1990. Application of a Three-Dimensional Turbulence Energy Model to the Determination of Tidal Currents on the Northwest European Shelf, *J. Geophys. Res.*, 95: 18143-18162.

Defant, A., 1960. *Physical Oceanography*, Vol. 2, Pergamon Press, New York, 598 pp.

DGRHA, 1986. *Monografias Hidrológicas dos Principais Cursos de Água de Portugal Continental*, Direcção Geral dos Recursos e Aproveitamentos Hidráulicos, Lisbon, Portugal.

Fisher, H.B., E.J. List, R.C.Y. Koh, J. Imberger and N.H. Brooks, 1979. *Mixing in Inland and Coastal Waters*, Academic Press, 483 pp.

Foreman, M.G.G., R.A. Walters, R.F. Henry, C.P. Keller, and A.G. Dolling, 1995. A Tidal Model for Eastern Juan de Fuca Strait and the Southern Strait of Georgia, *J. Geoph. Res.*, 100: 721-740.

Fortunato, A.B. and A.M. Baptista, 1994. Localized Sigma Coordinates for the Vertical Structure of Hydrodynamic Models, in *Estuarine and Coastal Modeling III*, M.L. Spaulding, et al. (editors), Amer. Soc. Civ. Eng., 323-335.

Fortunato, A.B. and A.M. Baptista, 1995a. Vertical Discretization in Tidal Flow Simulations, *Int. J. for Num. Met. in Fluids* (in press).

Fortunato, A.B. and A.M. Baptista, 1995b. Evaluation of Horizontal Gradients in Sigma-Coordinate Shallow Water Models, *Atmos.-Ocean* (in review).

Grenier, Jr., R.R., R.A. Luettich, Jr. and J.J. Westerink, 1995. A Comparison of the Nonlinear Frictional Characteristics of Two-Dimensional and Three-Dimensional Models of a Shallow Water Embayment, *J. Geophys. Res.*, 100: 13,719-13,735.

Kinmark, I.P.E., 1986. *The Shallow Water Equations: Formulation, Analysis and Application*. Lecture Notes in Engineering, 15, Springer-Verlag, Berlin, 187 pp.

Kolar, R.L., J.J. Westerink, M.E. Cantekin and C.A. Blain, 1994b. Aspects of Nonlinear Simulations Using Shallow Water Models Based on the Wave Continuity Equation, *Computers and Fluids*, 23: 523-538.

Kolar, R.L., W.G. Gray, J.J. Westerink and R.A. Luettich, Jr.,. 1994a. Shallow Water Modeling in Spherical Coordinates: Equation Formulation, Numerical Implementation, and Application, *J. Hydraulic Res.*, 32: 3-24.

Lima, C., J.M. Martin, M. Meybeck and P. Seyler, 1986. Mercury in the Tagus Estuary: an Acute or Obsolete Problem, in *Estuarine Processes: an Application to the Tagus Estuary*, Secretaria de Estado do Ambiente e Recursos Naturais, Lisbon, Portugal, 413-454.

Luettich, Jr., R.A., J.J. Westerink and N.W. Sheffner, 1991. *ADCIRC: An Advanced Three-Dimensional Circulation Model for Shelves, Coasts and Estuaries. Report 1: Theory and Methodology of ADCIRC-2DDI and ADCIRC-3DL*, Department of the Army, US Army Corps of Engineers.

Lynch, D.R., 1978. *Finite Element Solution of the Shallow Water Equations*, Ph.D. Thesis, Princeton University.

Lynch, D.R and C.E. Naimie, 1993. The M_2 Tide and its Residual on the Outer Banks of the Gulf of Maine, *J. Phys. Ocean.*, 23: 2222-2253.

Martins, M., T. Calvão and H. Figueiredo, 1983. *Estudo Ambiental do Estuário do Tejo. Estudo de Qualidade de Água. Resultados Referentes à Observações Sinópticas em 1982.* CNA/Tejo 30 - REL 27, Ministério da Qualidade de Vida, Lisbon, Portugal.

Myers, E.P. and A.M. Baptista, 1995. Finite Element Modeling of the July 12, 1993 Hokkaido Nansei-Oki Tsunami, *Pure and Applied Geophysics*, 144 (3/4): 1070-1103.

Oliveira, A. and A.M. Baptista, 1995. *VELA User's Manual*, OGI-CCALMR Software Documentation Series, Oregon Graduate Institute of Science & Technology, Portland, Oregon, (in preparation).

Oliveira, A., A.B. Fortunato and A.M. Baptista, 1995. Tidal Propagation in the Tagus Estuary (Portugal), (in preparation).

Oliveira, I.B.M., 1993. Port of Lisbon Improvement of the Access Conditions Through the Tagus Estuary Entrance, in *Proc. Coastal Eng. Conf.*, Amer. Soc. Civ. Eng., New York, 2745-2757.

Onishi, S., 1986. Roles of Large Scale Eddies in Mass Exchanges Between Coastal and Oceanic Zones, in *Physics of Shallow Estuaries and Bays*, J. van de Kreeke (editor), Springer-Verlag, 168-177.

Phillips, N.A., 1957. A Coordinate System Having Some Special Advantages for Numerical Forecasting, *J. Meteor.*, 14: 184-185.

Ridderinkhof, H. and J.W. Loder, 1994. Lagrangian Characterization of Circulation over Submarine Banks with Application to the Outer Gulf of Maine, *J. Phys. Ocean.*, 24: 1184-1200.

Ridderinkhof, H. and J.T.F. Zimmerman, 1990. Residual Currents in the Western Dutch Wadden Sea, in *Residual Currents and Long-Term Transport*, R.T. Cheng (editor), Springer-Verlag, 93-104.

Ridderinkhof, H. and J.T.F. Zimmerman, 1992. Chaotic Stirring in a Tidal System, *Science*, 258: 1107-1111.

Silva, M.C. and E.M. Oliveira, 1995. *EXPO'98: Hydrodynamic Modelling of the Tagus Estuary*, Report 174/95 - NET, Laboratório Nacional de Engenharia Civil, Lisbon, Portugal (in Portuguese).

Turner, P.J. and A.M. Baptista, 1991. *ACE/gredit User's Manual. Software for Semi-Automatic Generation of Two-Dimensional Finite Element Grids*, OGI-CCALMR Software Documentation Series SDS2, 91-2.

Vale, C. and B. Sundby, 1987. Suspended Sediment Fluctuations in the Tagus Estuary on Semi-diurnal and Fortnightly Time Scales, *Estuarine, Coastal and Shelf Science*, 25: 495-508.

Vieira, J.R., 1988. *Tagus Estuary Entrance. Mathematical Modeling of the Hydrodynamic Regimen*, Report 239/88 - NE, Laboratório Nacional de Engenharia Civil, Lisbon, Portugal (in Portuguese).

Westerink, J.J., R.A. Luettich, Jr., A.A. Blain and N.W. Sheffner, 1992. *ADCIRC: An Advanced Three-Dimensional Circulation Model for Shelves, Coasts and Estuaries. Report 2: User's Manual for ADCIRC-2DDI*, Department of the Army, US Army Corps of Engineers.

CHAPTER 6

Conclusions

6.1 Major Contributions

Over the past few years, the large errors generated in the evaluation of baroclinic pressure gradients in presence of steep slopes have led to severe misunderstandings. In particular, Haney (1991) claimed that sigma coordinate ocean models were only conditionally consistent due to a problem of "hydrostatic consistency". **Our work (Chapter 3) and others (Deleersnijder and Beckers, 1992, Mellor et al., 1994) shows that hydrostatic inconsistency does not correspond to a numerical inconsistency and explains the source of the misunderstandings**. The apparent inconsistency results from the cancelation, under certain conditions, of the truncation errors in Δx and in $\Delta\sigma$. When this cancellation occurs, refining either Δx or $\Delta\sigma$ alone leads to the asymptotic increase of the overall error. More importantly, the large errors result from coarse horizontal resolutions. Pycnoclines are often quasi-horizontal. In presence of steep topography, there can be a strong difference between the inclinations of the pycnoclines and the planes of constant sigma. In this situation, part the vertical gradients are resolved by the horizontal, rather than the vertical, grid. Since the horizontal grid seldom takes into account the need to evaluate horizontal gradients in the internal mode, the horizontal resolution can be too coarse and lead to large errors. Similarly, evaluating horizontal velocity gradients in z-coordinates can be highly inaccurate because streamlines tend to follow planes of constant sigma (Appendix 3). The resolution of the horizontal grid should therefore reflect the presence of steep topography, which it usually does not. **With the guidelines proposed in**

Chapter 3 to define the appropriate horizontal resolution, it is now possible to avoid the large errors in the evaluation of baroclinic pressure. However, this approach is practical only for models using unstructured grids in the horizontal, and other approaches should be used for finite difference models.

In all their simplicity, the Localized Sigma Coordinates are probably the most interesting and lasting concept introduced in this work. While the use of unstructured grids in the horizontal direction has been gaining acceptance over the years, only structured grids have been used in the vertical. **The LSC approach is the first to allow the number of nodes per vertical to vary from point to point**, and can therefore be considered a natural extension to the use of unstructured grids in the horizontal. Together with the criteria we developed to distribute horizontally the total number of nodes, **this flexibility proved highly attractive both in 2D (Chapter 4) and 3D (Chapter 5) simulations, leading to substantial accuracy improvements relative to the traditional sigma coordinate approach** (for a similar number of nodes). As we simulate increasingly complex flows, the vertical resolution will necessarily increase. With traditional structured grids, this finer resolution will be strongly limited by computational costs. Because they allow the representation of fine features of the flow while modeling large domains, the LSC should become even more useful in the future.

Due to large computational costs and the lack of guidelines on the appropriate vertical resolution, three-dimensional tidal simulations are often under-resolved in the vertical direction. **We presented the first systematic study for the vertical discretization in tidal flow simulations, and the resulting optimal grid compared favorably with grids previously proposed.** While several nodal distribution laws have been available for several years, none has been systematically tested like the β grid introduced here. Also, while the idea that vertical resolution should increase with shear is not new, there hadn't been any attempt to quantify that increase, even if only in an approximate way. We demonstrated the strong dependency of errors on local flow properties, and showed how to take those properties into account to build more accurate grids (Chapter 4).

6.2 Directions for Further Research

As pointed out in Chapter 1, much remains to be done in both the physical and the numerical aspects of three-dimensional shallow water models. The physical description of the processes is clearly the most complex issue to address. These processes are very difficult to study in a laboratory due to the space scales involved: on the one hand, the horizontal scales are very large (e.g., the wavelength of a semi-diurnal tide in a depth of 10 m is over 400 km), preventing the use of real scale models; on the other hand, the vertical scales are relatively small, forcing scale models to use excessive distortion (i.e., different horizontal and vertical scales), thus preventing the correct representation of turbulent processes. The only alternative is therefore to use field sites, with all the inherent difficulties (lack of control on the experiments, combination of many different processes, cost of the instrumentation). Fortunately, due to the periodic nature of tides, comprehensive data sets can be obtained over the years, providing that atmospheric conditions (e.g., wind, solar radiation) are not a key factor.

From a numerical perspective, there is also much to be done in three-dimensional flow models. Our experience with the Generalized Continuity Wave Equation formulation was somewhat disappointing. Although it is certainly more robust than eulerian primitive equation formulations, its sensitivity to the non-physical parameter G (in terms of accuracy, stability and mass conservation) is a major drawback. This problem could be minimized by making G space-dependent, because the value of this parameter is loosely related to the equivalent linear friction coefficient λ. Since λ can vary in space by several orders of magnitude, it is reasonable to make G vary in space as well. A simple option would be to make G inversely proportional to the local depth: the product λh should have a narrower range of variation than λ alone. Alternatively, a preliminary run could be used to estimate λ as a function of space, and that function used to impose G. In any case, this space dependence would have little effect on the computational performance since the mass matrix would still be stationary.

The use of LSC and the good results obtained with the simple criteria for barotropic tidal flows developed in previous chapters encourages the development of new criteria for vertical discretization. The methodology used in Chapter 3 could be applied to wind-driven and baroclinic flows with some modifications. For instance, the presence of two boundary layers in wind-driven flows would probably force us to use a nodal distribution law with two, rather than one, parameter, and the Coriolis term would probably need to be included due to its importance in the formation of the Ekman boundary layer. The lack of consensus on the form of the eddy viscosity profile for these types of flows would also introduce additional degrees of freedom.

As we try to simulate more and more complex systems, especially in cases where stratification plays a major role, time-independent grids are not likely to be an acceptable choice. Although very little work has been done on the vertical refinement needed across a pycnocline, it is clear that the suppression of turbulence by buoyancy can lead to very high shear and therefore require a very fine resolution. Since there is no way of knowing *a priori* where the pycnocline will be located, and its position may vary strongly in space and time (e.g., at the tip of a salt wedge), using time-independent grids can easily lead to unsustainable computational costs. Also, when modeling the passage of a storm surge over a large domain, it would be very expensive to adequately refine the surface layer over the whole path of the storm surge. The use of adaptive grids, a natural extension of LSC, may therefore be the best way to obtain the necessary resolution at an affordable cost.

The use of adaptive grids in the vertical is, at least conceptually, straightforward. Since it is essentially a one-dimensional problem, there is no need to triangulate each time the grid is changed. Also, since the vertical diffusion term is treated implicitly, the time step does not have to change with the resolution. Criteria to create and eliminate nodes have been used in many fields, and can easily be adapted for our purposes. Nodes can be added or removed when a given norm goes outside some user-specified bounds (*h-methods*). Alternatively, the number of nodes can be fixed in time at a given vertical, but their position can adapt to flow conditions (*r-methods*). This approach was described by Lynch and Werner (1991) for a shallow water model. Possible norms include estimates of truncation errors (e.g., Berger, 1985), residuals (e.g., Carey, 1995) and differences between the values of the prognostic variable at two consecutive nodes (e.g., Yeh et al., 1992).

References

Berger, M.J., 1985. Adaptive Mesh Refinement for Hyperbolic Equations, *Lectures in Applied Math.*, 22: 31-40.

Carey, G.F., 1995. Mesh Generation, a Posteriori Error Estimation and Mesh Refinement, in *Quantitative Skill Assessment for Coastal Ocean Models*, D.R. Lynch and A.M. Davies (editors), Amer. Geoph. Union, Washington, 15-29.

Deleersnijder, E. and J.-M. Beckers, 1992. On the Use of the σ-Coordinate System in Regions of Large Bathymetric Variations, *J. Mar. Syst.*, 3: 381-390.

Lynch, D.R. and F.E. Werner, 1991. Three-Dimensional Hydrodynamics on Finite Elements: Part II: Non-Linear Time Stepping Model, *Int J. Num. Methods in Fluids*, 12: 507-533.

Mellor, G.L, T. Ezer and L.-Y. Oey, 1994. The Pressure Gradient Conundrum of Sigma Coordinates Ocean Models, *J. Atmos. Oceanic. Technol.*, 11, 4: 1126-1134.

Yeh, G.-T., J.-R. Chang and T.E. Short, 1992. An Exact Peak Capturing and Oscillation-Free Scheme to Solve Advection-Dispersion Transport Equations, *Water Resources Res.*, 28: 2937-2951.

APPENDIX 1

Application of RITA_{2v}

A1.1 Introduction

This appendix describes the use of RITA2v, a two-dimensional, laterally-averaged shallow water model. The input and output formats are described in the next two sections, **Input File Structure** and **Output**. **Choosing the Input Parameters** is intended to help a beginner running RITA2v, mainly by providing realistic ranges for the various parameters. Finally, **Examples of Application** describes the inputs and outputs for two applications.

To run RITA_{2v} type:

rita2v *file1 file2 [-o [nskip]] [-i [outini]]*

The meaning of the parameters is as follows:

- *file1*, *file2* are the names of the input files (see Section A1.2).
- *-o* is the output option:

-e: elevations in ACE_1 format (Turner, 1991);

-v: depth averaged velocities in ACE_1 format;

-q: fluxes in ACE_1 format;

-u j: horizontal velocity profile at node *j* in ACE_1 format;

-w j: vertical velocity profile at node *j* in ACE_1 format;

-x j: velocity deviations (u') profile at node *j* in ACE_1 format;

-f: elevations and velocities at all the nodes in ACE/vis format (Baptista and Turner, 1991).

- *nskip* is the number of time steps between outputs (the default is 1);
- *-i* is a flag to create an initial and boundary conditions file every *outini* time steps and at the end of the run. If *outini* is not specified, the file will only be created at the end.

Typing simply "rita2v" will write out information on how to run the model to the screen.

An user friendly program (data) is available to create simple input files for $RITA_{2v}$.

A1.2 Input Files Structure

At least three input files are needed to run *$RITA_{2v}$*:

- *file1*.grd (grid file);
- *file2*.par (parameter file);
- *file2*.ibo (initial and boundary conditions file).

Depending on the options defined in the parameter file, other input files may be needed:

- *file2*.den (density field file);
- *file2*.tsu (bottom deformation file);
- boundary time histories of elevation or flow.

file1 and *file2* are defined as *CHARACTER*5*.

A1.2.1 Grid File

- File identifier
- ***nhnodes, npel***: nhnodes is the number of horizontal elements. npel is the number of nodes per element; in the present version of *$RITA_{2v}$*, only linear elements are accepted, so npel is assumed to be 2.

- *xl(i), yl(i), h(i), b(i); i=1, nhnodes:* cartesian coordinates, depth and width at each horizontal node.
- *id:* dimension (1 - 1D, 2 - 2D).
- *sigma(i); i=1*, total number of vertical nodes; if *id=2*: for each horizontal node, the vertical position of the vertical nodes bellow, from the bottom (σ=*-1*) up (σ=*0*).

A1.2.2 Initial and Boundary Conditions File

- File identifier.
- *ibt1, ibt2:* type of boundary condition imposed on the left and right sides, respectively. The options are:

  1 - imposed elevations with tidal frequencies;
  2 - imposed fluxes with tidal frequencies;
  3 - transmissive boundary;
  4 - imposed elevations with time series; and,
  5 - imposed fluxes with time series.
- *nfreq1, nfreq2:* number of frequencies on the left and right sides, respectively. If *ibti* > 2, the value is ignored.
- *amp1(i), phase1(i), freq1(i); i=1, nfreq1*; if *ibt1<3*: amplitudes (*m*), phases (*degrees*) and frequencies (*Hz*) for the left boundary.
- *filebc;* if *ibt1>3*: name of the left boundary file.
- *amp2(i), phase2(i), freq2(i); i=1, nfreq*2; if *ibt2<3*: amplitudes (*m*), phases (*degrees*) and frequencies (*Hz*) for the right boundary.
- *filebc;* if *ibt2>3*: name of the right boundary file.
- *ics:* 0 - cold start;1 - warm start (velocities); 2 - warm start (flows); 3 - warm start (velocities and u'); 4 - warm start (flows and u').
- *itrans;* if *ics=0*: number of time steps for transition. A linear ramp function is applied to the boundary conditions for the first itrans time steps to ensure a smooth transition.
- *eta1(i), eta2(i), u2(i); i=1, nhnodes; if ics=1*: initial conditions for the external mode. Elevations at two time steps and depth-averaged velocities.
- *eta1(i), eta2(i), q(i); i=1, nhnodes; if ics=2*: initial conditions for the external mode. Elevations at two time steps and flows.
- *u'(j,i); i = 1, nhnodes; j = 1, nvnodes(i); if ics = 3 or 4:* initial conditions for the internal mode.

A1.2.3 Parameter File

- File identifier.
- *g:* gravitational constant.
- ***nsteps, dt, theta:*** number of time steps, time step for the external mode, time discretization factor for the GWCE.
- ***gg, ggb:*** wave equation coefficient in the domain, and at the boundaries.
- ***ifric:*** 1 - non-linear friction; 0 - linear friction (only for 1D version).
- ***rho0, rhoa, wind, iden, itsu:*** density of water (kg/m3), density of air (kg/m3), wind speed (m/s); baroclinic switch (0 - constant density; 3 to 5: baroclinic pressure computed with different formulations); tsunami switch (itsu<0 - off; itsu>0 - the bottom deformation occurs in itsu time steps).
- ***id, alpha, ise, iform, ifits:*** dimension (1 - 1D, 2 - 2D) - note that *id* was previously defined in the grid file; time discretization coefficient for the internal mode; number of external steps per internal step; formulation for the advective terms (from -1 to 4); first internal time step.
- ***avmn:*** minimum eddy viscosity.
- ***xlam0(i), visc(i);*** *i=1,* ***nhnodes;*** *if ifric=0:* linear friction coefficient, horizontal eddy viscosity.
- ***cmann(i), visc(i);*** *i=1,* ***nhnodes;*** *if ifric=1, id=1*: Manning coefficient, horizontal eddy viscosity.
- ***cmann(i), visc(i), cd(i);*** *i=1,* ***nhnodes;*** *if id=2:* Manning coefficient, horizontal eddy viscosity, bottom stress coefficient for the internal mode.

A1.2.4 Density File

- File identifier.
- *rho(j,i); i = 1, nhnodes; j = 1, nvnodes(i); if iden =1 or 2:* initial density field.

A1.2.5 Bottom Deformation File

- File identifier.
- ***bdef(i);*** *i = 1,* ***nhnodes;*** *if itsu > 0:* bottom deformation (positive values represent uplifts).

A1.2.6 Boundary Files

- ***time, bc***; as many lines as needed: time and imposed value (elevation or flux); time is in seconds and must start at zero.

A1.3 Output

$RITA_{2v}$ allows three types of output:

- visualization output for ACE_1;
- visualization output for ACE/vis;
- global spacial output.

A1.3.1 Output for ACE_1

All the output options (see Introduction), except -f have a binary format compatible with ACE_1. The output is written directly to the screen, but can be redirected to a file. The format is:

- 17;
- number of nodes in the grid;
- position of the nodes (x or sigma);

for each time step:

- time;
- value of the variable at each node.

All the variables have four bytes.

A1.3.2 Output for ACE/vis

When the output option -f is selected, the binary file *file2*.vis is created with the following format:

- 14;
- number of time steps in the file: (nsteps-ifits)/nskip;

For each time step:

- time;
- elevations at all the vertical nodes;
- horizontal velocities at all the vertical nodes;

- vertical velocities at all the vertical nodes.

All the variables have four bytes.

A1.3.3 Global Spacial Output

An initial and boundary conditions file named *file2*.iboN can be created with the option *-i*. It has the same format as the initial and boundary conditions files, so that a new run can be started where the previous one ended. Velocities, rather than flows, are written out, regardless of the input file (i.e., *ics* takes the value of 1 for 1D runs, and 3 for 2D runs).

A1.3.4 Error Messages

At the beginning of each run, the input files are checked for basic inconsistencies. When an error is detected, an error message is written to the screen and the run is interrupted. If the model is being run from ACE_1, Figure A1.1 pops up on the screen:

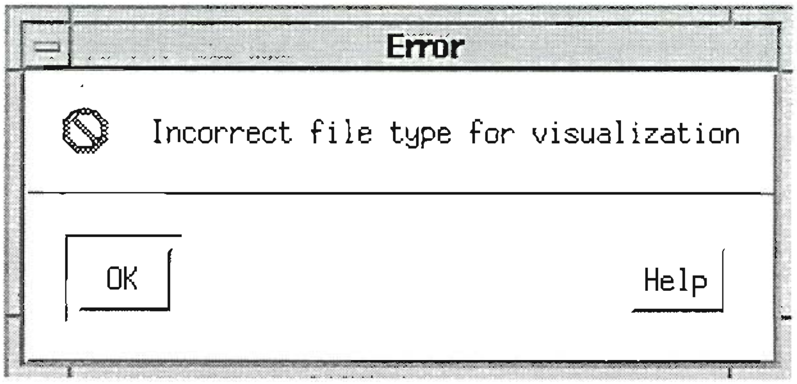

Incorrect file type for visualization

Figure A1.1 Error message in ACE_1.

In this case the model should be rerun from the screen so that the message can be read.

The possible error messages are as follows:

- Check your file *filename*

The input file *filename* does not exist.

- Check your number of nodes:

nhnodes = [*nhnodes*]

MXNOD = [*MXNOD*]

The number of horizontal nodes (*nhnodes*) in file *file1*.grd is larger than the corresponding dimensions of the matrices (*MXNOD*). Change the parameter file, *rita2v.cmn*, and compile the model again.

- Number of vertical nodes exceeds MXSI

The number of vertical nodes in at least one vertical in file *file1*.grd is larger than the corresponding dimensions of the matrices (*MXSI*). Change the parameter file, *rita2v.cmn*, and compile the model again.

- You specified 2D in the PARAMETER file, but your grid is 1D

There is an inconsistency between the parameter file, which specifies a 2D run and the grid file, which specifies a 1D grid. Change one of them.

- Problem with parameter file

The parameter file does not contain information for all the nodes.

- Problem with initial and boundary conditions file

The initial and boundary conditions file does not contain information for all the nodes.

- Your boundary conditions file is not long enough

One of the time series boundary files does not contain enough information for the whole run (this is checked during the time stepping, rather than in the beginning of the run).

- Wave Equation matrix inversion: ind = [*ind*]
- 1D momentum equation matrix inversion: ind = [*ind*]

The inversion of the matrix for the GWCE or the 1D momentum equation failed because the equations were not linearly independent. This indicates that there is a serious error in your inputs that was otherwise undetected.

A1.4 Choosing the Input Parameters

A1.4.1 Space and Time Discretization

The choice of the horizontal grid and external time step are determined by two dimensionless numbers:

- the Courant number:

$$Cu = \frac{\sqrt{gh}\Delta t}{\Delta x} \tag{A.1}$$

- the dimensionless wave length:

$$\lambda = \frac{\sqrt{gh}T}{\Delta x} \tag{A.2}$$

The Courant number should in general be kept slightly below 1, although larger values can be used when the elevation is small relative to the total depth. Formal analysis (e.g. Luettich et al., 1991) indicates that the dimensionless wavelength for the shortest wave that one wants to resolve (period T) should not be less than 30 or 40. However, in presence of strong bathymetric variations, larger values should be used (Luettich and Westerink, 1994).

Two time discretization parameters have to be specified in the parameter file. *theta* is the time discretization parameter for the wave equation, and should vary between 0 and 1. Kinnmark (1985) shows that it must be larger or equal to 0.5 for stability, and Westerink et al. (1992) recommend the use of 0.7. The other time discretization parameter, *alpha*, is used in the internal mode. A value of 0.5 (Crank-Nicholson) has been used with good results.

Guidelines for the vertical discretization are given in Fortunato and Baptista (1995) and Davies (1991).

It is possible to set the internal mode time step larger than the external mode's by setting *ise* larger than 1. Some authors use time steps in the internal mode one (e.g. Galperin and Mellor, 1990) or even two (e.g., Blumberg and Mellor, 1987) orders of magnitude larger than in the external mode. Limited tests with $RITA_{2v}$ suggest that *ise* should not exceed 3; a value of 1 has been used in most applications.

A1.4.2 Physical and Numerical Parameters

1. The GWCE coefficient (*gg*)

A good choice of the GWCE coefficient is of the utmost importance for the good behavior of the model: too large, and the results will be plagued with spurious oscillations, characteristic of models based on the primitive equations; too small and mass conservation will not be ensured. As a rule of thumb, *gg* should be taken as the maximum linear friction coefficient (Westerink et. al., 1992). For a non-linear run,

$$\approx C_f u|_{max} \qquad or \qquad gg \approx C_D u_b|_n \tag{A.3}$$

2. The GWCE coefficient at the boundary (*ggb*)

Theoretical and numerical studies suggest that better mass conservation is achieved if the GWCE coefficient takes a larger value at the boundary than in the domain (Kolar et. al., 1992). However we have generally used *ggb=gg* with good results. Note that this only affects boundaries where the elevations are imposed.

3. The advection and baroclinic pressure formulation (*iform*)

This input parameter may vary between -1 and 4, and it determines how the advective terms are treated:

iform = -1: advection is neglected both in the internal and external modes;

iform = 0: advection is neglected in the internal mode only;

iform = 1: only the depth average component of the advective term is included in the internal mode;

iform = 2: for the purpose of computing advection in the internal mode, the velocity is assumed to be the product of the depth averaged velocity with a function that depends only on depth and time;

iform = 3: standard sigma formulation; note that in this case the number of nodes has to be constant for every vertical;

iform = 4: the horizontal gradients of depth dependent quantities are computed in a cartesian coordinate system;

iform = 5: the horizontal gradients of depth dependent quantities are computed in sigma coordinates, but the number of nodes per vertical does not have to be constant as the necessary values at neighboring verticals are interpolated;

The baroclinic pressure term is computed with formulation 3, 4 or 5, consistent with the advection formulation. Note therefore that, if the baroclinic mode is selected, *iform* has to be 3 or 4.

4. The first internal time step (*ifits*)

If the internal mode is warm started, this variable should equal 1; otherwise, it should be at least 2. For computational efficiency, it may be useful to do a warm up period in 1D before activating the internal mode.

5. The transition steps (*itrans*)

In order to allow a smooth start, it is possible to specify a number of transition time steps (itrans). During this period, the forcing functions (wind and boundary conditions) are multiplied by a linear ramp function. As a rule of thumb, the duration of the transition period should be about the double of the time needed for a wave to propagate from one end of the domain to the other, i.e.,

$$itrans \approx \frac{2L}{\Delta t \sqrt{g h_c}} \tag{A.4}$$

where L represents the length of the domain, and h_c a characteristic depth.

6. The minimum vertical eddy viscosity (*avmn*)

This value is generally used to ensure that eddy viscosity does not go below the molecular viscosity of water (10^{-6} m^2/s). A larger value may be used for stability reasons.

7. The horizontal eddy viscosity (*visc*)

Physically, the horizontal eddy viscosity is negligible compared to the vertical eddy viscosity in shallow waters conditions. However, this term was included in the model since it is sometimes used for stability reasons. It must be noted though that large values of this coefficient (larger than around 1 m^2/s for typical coastal conditions) may also significantly damp the solution.

8. The linear friction coefficient (*xlam0*)

Even though bed friction is better parametrized by a quadratic than a linear function, the former has better stability properties, and therefore may be useful in some cases. The linear coefficient can be related to the Manning coefficient by:

$$xlam0 \approx \frac{(cmann)^2 g}{h^{4/3}} |\bar{u}_c| \tag{A.5}$$

where h is the mean depth, and $\bar{u}_c$ a characteristic depth averaged velocity. For tidal applications, Dronkers (1964) proposes:

$$xlam0 \approx \frac{8\,(cmann)^2 g}{3\pi h^{4/3}} \bar{u}_m \tag{A.6}$$

where $\bar{u}_m$ is the mean value of the maximum velocities in the tidal region.

9. The Manning coefficient (*cmann*)

The Manning coefficient varies with the type of bed. Table A1.1 gives a good indication for the choice of the coefficient.

Table A1.1 Typical values of the Manning coefficient (adapted from Quintela, 1981).

Bottom type	Manning coefficient ($m^{-1/3}s$)
regular soil	0.017
irregular soil	0.022
irregular soil with vegetation, rock beds	0.029
very irregular soil, stone beds	0.033
rivers with significant solid transport	0.05

10.The internal mode friction coefficient (*cd*)

The specification of c_d is not as simple because it depends on the turbulence parametrization, as well as on the distance between the bottom node and the true bottom. A possible approach is to use the logarithmic law of the wall:

$$u(\delta) = \frac{u_* ln(\delta/z_0)}{\kappa} \tag{A.7}$$

where δ is the distance from the bottom, κ is the von Karman constant, z_0 is the roughness length, and u* is the stress velocity given by:

$$u_* = \sqrt{\tau_b/\rho_0} = \sqrt{c_d}|u(\delta_b)| \tag{A.8}$$

where δ_b is the distance between the true bottom and the bottom node. An expression for c_d is obtained by combining (A.7) and (A.8):

$$c_d = \left(\frac{\kappa}{ln\left(\frac{\delta_b}{z_o}\right)}\right)^2 \tag{A.9}$$

This expression is very attractive because it is physically solid. However it leaves the modeler with the difficult task of specifying δ_b and z_0. RITA$_{2v}$ takes a simpler approach: c_d is specified directly, so the number of parameters is reduced. Table A1.2 gives the range of values of c_d found in the literature. It must be noted that the appropriate value of c_d depends on the turbulence closure model used.

Table A1.2 Values of C_d.

Reference	C_d (-)	Comments
Sternberg, 1972	0.004	Lab experiment (perm. flow)
Brown and Trask, 1980	0.035	
Blumberg and Mellor, 1987	0.0025	Minimum value
Walters, 1992	0.0025 - 0.07	Delaware Bay (calibrated)
Aldridge and Davies, 1993	0.00187 - 0.00563	Irish Sea (sensitivity analysis)

A1.5 Examples of Application

Two small examples of application are presented below. The first consists of a typical test case for depth averaged models. A closed-end channel is forced with a tidal wave. An analytical solution for the fully linear case is given by Lynch and Gray (1978) and reviewed for the 1D case by Remédio (1992). The second is a more realistic 2D application to a reservoir in the Snake river (Washington). The input files are presented, along with selected results.

A1.5.1 1D Linear Tidal Propagation

Definition of the Test

This test consists of a M_{16} tidal wave propagating in a shallow channel 80 km long and with an inclined bottom (Figure A1.2). The depths vary linearly from 15 m at the mouth to 5 m at the closed end. The amplitude of the wave, 1 cm, was chosen small compared to the depth so that the finite amplitude term was negligible and a comparison with the analytical solution was possible.

The run was cold started. The time step and grid spacing were chosen as 80s and 1000m, respectively, leading to a maximum Courant number of 0.97 and a minimum dimensionless wave length of 39. A constant linear friction coefficient of 0.00025 s^{-1} was used, and both advection and diffusion were neglected.

Input files

1. Grid file

```
grid file
81 2
0.000 0.000 5.000 1000.000
1000.000 0.000 5.125 1000.000
2000.000 0.000 5.250 1000.000
3000.000 0.000 5.375 1000.000
4000.000 0.000 5.500 1000.000
5000.000 0.000 5.625 1000.000
6000.000 0.000 5.750 1000.000
7000.000 0.000 5.875 1000.000
8000.000 0.000 6.000 1000.000
9000.000 0.000 6.125 1000.000
10000.00 0.000 6.250 1000.000
11000.00 0.000 6.375 1000.000
12000.00 0.000 6.500 1000.000
13000.00 0.000 6.625 1000.000
14000.00 0.000 6.750 1000.000
15000.00 0.000 6.875 1000.000
16000.00 0.000 7.000 1000.000
17000.00 0.000 7.125 1000.000
18000.00 0.000 7.250 1000.000
19000.00 0.000 7.375 1000.000
20000.00 0.000 7.500 1000.000
21000.00 0.000 7.625 1000.000
22000.00 0.000 7.750 1000.000
23000.00 0.000 7.875 1000.000
24000.00 0.000 8.000 1000.000
25000.00 0.000 8.125 1000.000
26000.00 0.000 8.250 1000.000
27000.00 0.000 8.375 1000.000
28000.00 0.000 8.500 1000.000
29000.00 0.000 8.625 1000.000
30000.00 0.000 8.750 1000.000
31000.00 0.000 8.875 1000.000
32000.00 0.000 9.000 1000.000
33000.00 0.000 9.125 1000.000
34000.00 0.000 9.250 1000.000
35000.00 0.000 9.375 1000.000
36000.00 0.000 9.500 1000.000
37000.00 0.000 9.625 1000.000
38000.00 0.000 9.750 1000.000
40000.00 0.000 10.000 1000.000
41000.00 0.000 10.125 1000.000
42000.00 0.000 10.250 1000.000
43000.00 0.000 10.375 1000.000
44000.00 0.000 10.500 1000.000
45000.00 0.000 10.625 1000.000
46000.00 0.000 10.750 1000.000
47000.00 0.000 10.875 1000.000
48000.00 0.000 11.000 1000.000
49000.00 0.000 11.125 1000.000
50000.00 0.000 11.250 1000.000
51000.00 0.000 11.375 1000.000
52000.00 0.000 11.500 1000.000
53000.00 0.000 11.625 1000.000
54000.00 0.000 11.750 1000.000
55000.00 0.000 11.875 1000.000
56000.00 0.000 12.000 1000.000
57000.00 0.000 12.125 1000.000
58000.00 0.000 12.250 1000.000
59000.00 0.000 12.375 1000.000
60000.00 0.000 12.500 1000.000
61000.00 0.000 12.625 1000.000
62000.00 0.000 12.750 1000.000
63000.00 0.000 12.875 1000.000
64000.00 0.000 13.000 1000.000
65000.00 0.000 13.125 1000.000
66000.00 0.000 13.250 1000.000
67000.00 0.000 13.375 1000.000
68000.00 0.000 13.500 1000.000
69000.00 0.000 13.625 1000.000
70000.00 0.000 13.750 1000.000
71000.00 0.000 13.875 1000.000
72000.00 0.000 14.000 1000.000
73000.00 0.000 14.125 1000.000
74000.00 0.000 14.250 1000.000
75000.00 0.000 14.375 1000.000
76000.00 0.000 14.500 1000.000
77000.00 0.000 14.625 1000.000
78000.00 0.000 14.750 1000.000
79000.00 0.000 14.875 1000.000
80000.00 0.000 15.000 1000.000
1
```

2. Parameter file

```
Parameter file
9.81
558 80.0000 0.7000
0.2500E-03 0.100E-01
0
1000.000 1.000 0.000E+00 0 0 -1
1 0.500 1 -1 0
0.1000E-02
0.2500E-03 0.0000E+00
0.2500E-03 0.0000E+00
0.2500E-03 0.0000E+00
0.2500E-03 0.0000E+00
0.2500E-03 0.0000E+00
0.2500E-03 0.0000E+00
0.2500E-03 0.0000E+00
0.2500E-03 0.0000E+00
0.2500E-03 0.0000E+00
0.2500E-03 0.0000E+00
0.2500E-03 0.0000E+00
0.2500E-03 0.0000E+00
0.2500E-03 0.0000E+00
0.2500E-03 0.0000E+00
0.2500E-03 0.0000E+00
0.2500E-03 0.0000E+00
0.2500E-03 0.0000E+00
0.2500E-03 0.0000E+00
0.2500E-03 0.0000E+00
0.2500E-03 0.0000E+00
0.2500E-03 0.0000E+00
0.2500E-03 0.0000E+00
0.2500E-03 0.0000E+00
0.2500E-03 0.0000E+00
0.2500E-03 0.0000E+00
0.2500E-03 0.0000E+00
0.2500E-03 0.0000E+00
0.2500E-03 0.0000E+00
0.2500E-03 0.0000E+00
0.2500E-03 0.0000E+00
0.2500E-03 0.0000E+00
0.2500E-03 0.0000E+00
0.2500E-03 0.0000E+00
0.2500E-03 0.0000E+00
0.2500E-03 0.0000E+00
0.2500E-03 0.0000E+00
0.2500E-03 0.0000E+00
0.2500E-03 0.0000E+00
0.2500E-03 0.0000E+00
0.2500E-03 0.0000E+00
0.2500E-03 0.0000E+00
0.2500E-03 0.0000E+00
0.2500E-03 0.0000E+00
0.2500E-03 0.0000E+00
0.2500E-03 0.0000E+00
0.2500E-03 0.0000E+00
0.2500E-03 0.0000E+00
0.2500E-03 0.0000E+00
0.2500E-03 0.0000E+00
0.2500E-03 0.0000E+00
0.2500E-03 0.0000E+00
0.2500E-03 0.0000E+00
0.2500E-03 0.0000E+00
0.2500E-03 0.0000E+00
0.2500E-03 0.0000E+00
0.2500E-03 0.0000E+00
0.2500E-03 0.0000E+00
0.2500E-03 0.0000E+00
0.2500E-03 0.0000E+00
0.2500E-03 0.0000E+00
0.2500E-03 0.0000E+00
0.2500E-03 0.0000E+00
0.2500E-03 0.0000E+00
0.2500E-03 0.0000E+00
0.2500E-03 0.0000E+00
0.2500E-03 0.0000E+00
0.2500E-03 0.0000E+00
0.2500E-03 0.0000E+00
0.2500E-03 0.0000E+00
0.2500E-03 0.0000E+00
0.2500E-03 0.0000E+00
0.2500E-03 0.0000E+00
0.2500E-03 0.0000E+00
0.2500E-03 0.0000E+00
0.2500E-03 0.0000E+00
0.2500E-03 0.0000E+00
0.2500E-03 0.0000E+00
0.2500E-03 0.0000E+00
0.2500E-03 0.0000E+00
0.2500E-03 0.0000E+00
0.2500E-03 0.0000E+00
```

3. Initial and boundary conditions file

```
Initial and boundary conditions file
2 1
1 1
0.00000+00 0.00000E+00 0.0000000E+00
0.10000-01 0.90000E+02 0.1792114E-03
0
0
```

Results

The model was run for 44640s (eight tidal cycles) in ACE_1. The final elevations and depth averaged velocities are shown in Figure A1.3, together with the analytical solutions. The agreement between the analytical and numerical solutions is excellent.

A1.5.2 2D Flow in a Reservoir

Definition of the Test

This test simulates the flow in a reservoir in the Snake river (Washington). The reservoir is bounded by two dams, Lower Granite (upstream) and Little Goose (downstream). It is about 55 kilometers long, with depths and widths ranging approximately from 8 to 36 meters, and 200 to 565 meters, respectively (Figure A1.4). The simulation covers the month of March 1992, during which a drawdown operation was carried out.

Elevations were specified upstream and flows downstream, both from hourly field records. The external mode solution was warm started with an approximate solution (constant flow and elevations varying linearly between the two boundaries), and the internal mode was cold started. It should be noted that it would be more appropriate to specify flows at both boundaries. This wasn't done however, due to inconsistencies in the field data.

One of the difficulties in applying RITA$_{2V}$ in a field study such as this one is to specify the grid, since the real cross-sections are obviously not rectangular. The numerical grid was specified by imposing that both the area and a "characteristic depth" should be kept at each cross-section. The characteristic depth was defined as the maximum depth after a nine point running average was used to filter each cross-section bathymetry.

Input files

1. Grid file

```
Little Goose Reservoir
 50 2 11
 421259.08453816478l 5159466.52113786247 36.4269866666666857 411.386273149869680
 422312.159126058046 5159908.75027604960 36.4242276700123639 393.607792555744936
 423394 341017613770 5160215.41633820627 34.4730569159057652 487.722453866155547
 424531.402023177769 5160173.46329783183 35.7672379334262160 459.738758392397358
 425660.851200441655 5160074.40933102462 35.0855938945472232 432.765608082777874
 426794.942744162166 5160209.94186877739 32.9780109603231324 558.824959029459365
 427935.034411788161 5160197.68603342865 32 445179510726O352 559.136521705868745
 429076.380408273893 5160154.53496584110 32.2415506351578287 533.160447265480229
 430213.458960549615 5160050.47471897304 32 4115397407572772 565.277448460554069
 431234.376049470273 5160199.67569409497 29.5915614685359358 540.126077314430745
 431925.278815887286 5161109.17339375429 28 7762024936673484 549.430445767171932
 432624.639944716648 5162010.99906565156 28.0146368358680853 556.331565065753921
 433462.623730199935 5162787.08918515779 28 1346806621361729 523.846244518043932
 434300.607515683223 5163563.17930466402 28.2547244884042605 491.360923970333829
 435296.254908168921 5163930.67719255015 27 6311710539746791 465.854239414575659
```

```
436438.352911100199 5163918.64182681032 26.3169048112740747 446.829871992933818
437580.450914031477 5163906.60646107048 25.3006780374471738 447.554192476538219
438680.172481984482 5163998.40118714329 24.9291092681785038 471.128286746093181
439487.694124796311 5164806.13969354145 26.2916549413650174 472.621653158582490
440276.961873006134 5165630.79307539389 26.9372322820054109 470.382091633761263
441020.959611331171 5166497.39567387570 25.8047143608347191 458.884796989203949
441764.957349656150 5167363.99827235751 24.6721964396640274 447.387502344646634
442181.264684665832 5168398.00113969017 27.7120065290958983 419.912651934008863
442641.869642095349 5169431.27640917152 26.1982169606231281 398.013773664240716
443284.711703270732 5170368.16686121468 23.4275821959062966 398.497961374841680
444049.574386219610 5171216.41079697944 24.6773962046090141 424.394856753520173
445056.558060273703 5171700.98598599713 23.3790971431139845 477.030472162303909
446134.199490442988 5172079.43234456237 21.3371865878531892 537.469202658688005
447252.926849136071 5172283.85282182880 20.3424585671569780 565.341167792369561
448387.230883578362 5172362.83186099119 20.1818512762892368 560.206917496474489
449524.870502989506 5172261.29962633550 21.3293086269705370 494.622904480723378
450632 927812627517 5172080.92202014383 22.0388953140560524 438.907184687200470
451556.586010086234 5171409.06769620534 20.0190480172662433 444.704731533666120
452429.156557880167 5170679.27981869038 19.1359010111882988 417.252704826605338
453213.766120985849 5169850.11821168195 20.2261595742909250 333.269893643941430
454212.514484774088 5169296.01135902759 17.9526920222074615 450.394578249427184
455340 629656296805 5169368.55248213187 17.0821277875329507 396.801476249251436
456449 379695703974 5169605.91213487834 17.1809515865364979 352.621477526176136
457525 706480401801 5169988.08140479680 18.3047615211351875 332.387536785862494
458632.146228293248 5170195.93807515316 18.1179084033810938 353.155172950273652
459774.307132528978 5170197.01842855662 16.3762963100046548 422.560458274670509
460910.601292976702 5170291.16105094366 16.3989270450147870 399.602736239399803
461993.864537066896 5170516.28850392625 17.2552331784381501 334.436742019145015
462817.779527980951 5171255.09297095053 12.4720919237015497 420.788982381039261
463646.483169550833 5170840.95708264224 13.9632306466947860 259.171179605258544
463885.809382895008 5169768.06668316294 10.1172025673089507 381.383760617250516
464723.216589323420 5169076 21327179298 11.1528172073881215 257.449809747895472
465714 458670877269 5168508.78765192255 12.1692567271455392 202.715005999035782
466705 700752431236 5167941.36203205306 10.9172143282203979 214.019826021607855
467696.942833984911 5167373 93641218264 8 2465333333333016 304.585884552104858
2
-1 000000000000000000
-0.975000000000000000
-0.950000000000000000
-0 900000000000000000
-0.800000000000000000
-0.700000000000000000
-0 600000000000000000
-0 500000000000000000
-0.400000000000000000
-0.300000000000000000
-0.200000000000000000
-0 100000000000000000
0.000000000000000000
-1.000000000000000000
-0.975000000000000000
-0 950000000000000000
-0.900000000000000000
-0 800000000000000000
-0 700000000000000000
-0.600000000000000000
-0 500000000000000000
-0.400000000000000000
-0.300000000000000000
-0.200000000000000000
-0.100000000000000000
0 000000000000000000
[...]
```

2. Parameter file

```
Little Goose Reservoir
9 8100000000000000
89160 30.0000000000000000 0.500000000000000000
0.500000000000000005E-03 0.500000000000000002E-03
1
1000 00000000000000 1.00000000000000000 0.000000000000000000E+00 0 -1
2 0.500000000000000000 1 4 2
0.100000000000000002E-05
0.350000000000000014E-01 1.000000000000000000E+00 1.000000000000000010E-01
[...]
0.350000000000000014E-01 1.000000000000000000E+00 1 000000000000000010E-01
```

3. Initial and boundary conditions file

```
Little Goose Reservoir
 5 4
 0 0
lig.flow
log.elv
 2
 -1.30454399999999993 -1.30454399999999993 -1141.00000000000000
 -1.30385975510204077 -1.30385975510204077 -1141.00000000000000
 -1.30317551020408162 -1.30317551020408162 -1141.00000000000000
 -1.30249126530612247 -1.30249126530612247 -1141.00000000000000
 -1.30180702040816310 -1.30180702040816310 -1141.00000000000000
 -1.30112277551020394 -1.30112277551020394 -1141.00000000000000
 -1.30043853061224479 -1.30043853061224479 -1141.00000000000000
 -1.29975428571428564 -1.29975428571428564 -1141.00000000000000
 -1.29907004081632649 -1.29907004081632649 -1141.00000000000000
 -1.29838579591836734 -1.29838579591836734 -1141.00000000000000
 -1.29770155102040818 -1.29770155102040818 -1141.00000000000000
 -1.29701730612244881 -1.29701730612244881 -1141.00000000000000
 -1.29633306122448966 -1.29633306122448966 -1141.00000000000000
 -1.29564881632653051 -1.29564881632653051 -1141.00000000000000
 -1.29496457142857135 -1.29496457142857135 -1141.00000000000000
 -1.29428032653061220 -1.29428032653061220 -1141.00000000000000
 -1.29359608163265305 -1.29359608163265305 -1141.00000000000000
 -1.29291183673469390 -1.29291183673469390 -1141.00000000000000
 -1.29222759183673452 -1.29222759183673452 -1141.00000000000000
 -1.29154334693877537 -1.29154334693877537 -1141.00000000000000
 -1.29085910204081622 -1.29085910204081622 -1141.00000000000000
 -1.29017485714285707 -1.29017485714285707 -1141.00000000000000
 -1.28949061224489792 -1.28949061224489792 -1141.00000000000000
 -1.28880636734693876 -1.28880636734693876 -1141.00000000000000
 -1.28812212244897961 -1.28812212244897961 -1141.00000000000000
 -1.28743787755102024 -1.28743787755102024 -1141.00000000000000
 -1.28675363265306109 -1.28675363265306109 -1141.00000000000000
 -1.28606938775510193 -1.28606938775510193 -1141.00000000000000
 -1.28538514285714278 -1.28538514285714278 -1141.00000000000000
 -1.28470089795918363 -1.28470089795918363 -1141.00000000000000
 -1.28401665306122448 -1.28401665306122448 -1141.00000000000000
 -1.28333240816326533 -1.28333240816326533 -1141.00000000000000
 -1.28264816326530595 -1.28264816326530595 -1141.00000000000000
 -1.28196391836734680 -1.28196391836734680 -1141.00000000000000
 -1.28127967346938765 -1.28127967346938765 -1141.00000000000000
 -1.28059542857142850 -1.28059542857142850 -1141.00000000000000
 -1.27991118367346934 -1.27991118367346934 -1141.00000000000000
 -1.27922693877551019 -1.27922693877551019 -1141.00000000000000
 -1.27854269387755104 -1.27854269387755104 -1141.00000000000000
 -1.27785844897959167 -1.27785844897959167 -1141.00000000000000
 -1.27717420408163251 -1.27717420408163251 -1141.00000000000000
 -1.27648995918367336 -1.27648995918367336 -1141.00000000000000
 -1.27580571428571421 -1.27580571428571421 -1141.00000000000000
 -1.27512146938775506 -1.27512146938775506 -1141.00000000000000
 -1.27443722448979591 -1.27443722448979591 -1141.00000000000000
 -1.27375297959183675 -1.27375297959183675 -1141.00000000000000
 -1.27306873469387738 -1.27306873469387738 -1141.00000000000000
 -1.27238448979591823 -1.27238448979591823 -1141.00000000000000
 -1.27170024489795908 -1.27170024489795908 -1141.00000000000000
 -1.27101599999999992 -1.27101599999999992 -1141.00000000000000
```

4. Boundary files

Due to the extent of these files only the first ten lines of the upstream file are given.

```
0.000000000000000000E+00 -1144.00060223600008
3600.0000000000000 -1158.15902553100000
7200.0000000000000 -1234.61451132399998
10800.000000000000 -1319.56505109400018
14400.000000000000 -1328.06010507099995
18000.000000000000 -1308.23831245800011
21600.000000000000 -934.455937469999981
25200.000000000000 -764.554857930000026
28800.000000000000 -1421.50569881800016
32400.000000000000 -1393.18885222800009
```

Results

Results at the boundaries are shown in Figures A.5 and 6, together with the field data. A vertical velocity profile is shown in Figure A1.7.

References

Aldridge, J.N. and A.M. Davies, 1993. A High-Resolution Three-Dimensional Tidal Model of the Eastern Irish Sea, *J. Physical Oceanography*, 23: 207-224.

Baptista, A.M. and P.J. Turner, 1991. *ACE/vis User's Manual - Software for Scientific Visualization of Estuarine and Coastal Processes*, OGI-CCALMR Software Documentation Series SDS1, 91-1, Oregon Graduate Institute of Science & Technology, Portland, Oregon.

Blumberg, A.F. and G.L. Mellor, 1987. A Description of a Three-Dimensional Coastal Ocean Model, in *Three-Dimensional Coastal Ocean Models*, N.S. Heaps (editor), Amer. Geoph. Union, Washington, D.C, 1-16.

Brown, W.S. and R.P. Trask, 1980. A Study of Tidal Energy Dissipation and Bottom Stress in an Estuary, *Estuarine, Coastal and Marine Science*, 3: 281-292.

Davies, A.M., 1991. On the Accuracy of Finite Difference and Modal Methods for Computing Tidal and Wind Wave Current Profiles, *Int. J. for Num. Methods in Fluids*, 12: 101-124.

Davies, A.M. and J.N. Aldridge, 1992. A Stable Algorithm for Bed Friction in Three-Dimensional Shallow Sea Modal Models, *Int. J. for Num. Methods in Fluids*, 14: 477-493.

Dronkers, J.J., 1964. *Tidal Computations in Rivers and Coastal Waters*, North-Holland Publishing Company, Amsterdam.

Fortunato, A.B. and A.M. Baptista, 1995. Vertical Discretization in Tidal Flow Simulations, *Int. J. for Num. Methods in Fluids* (in press).

Galperin, B. and G.L. Mellor, 1990. A Time-dependent, Three-dimensional Model of the Delaware Bay and River System. Part 1: Description of the Model and Tidal Analysis, *Estuarine, Coastal and Shelf Science*, 31: 231-253.

Kinnmark, I.P.E., 1985. *The Shallow Water Equations: Formulation, Analysis and Application*, Lecture Notes in Engineering, 15, C.A. Brebia and S.A. Orszag (editors), Springer-Verlag, Berlin, 187 p.

Kolar, R.L., W.G. Gray and J.J. Westerink, 1992. An Analysis of the Mass Conserving Properties of the Generalized Continuity Wave Equation, in *Proc. Computational Methods in Water Resources IX*, Vol. 2, T.F. Russel, et. al. (editors), 537-544.

Luettich, R.A., J.J. Westerink, 1994. Continental Shelf Scale Convergence Studies with a a Barotropic Tidal Model, in *Quantitative Skill Assessment for Coastal Ocean Models*, D.R. Lynch and A.M. Davies (editors) Amer. Geoph. Union, 349-371.

Luettich, R.A., J.J. Westerink and N.W. Scheffner, 1991. *ADCIRC: An Advanced Three-Dimensional Circulation Model for Shelves, Coasts and Estuaries. Report 1: Theory and Methodology of ADCIRC-2DDI and ADCIRC-3DL*, Department of the Army, U.S. Army Corps of Engineers.

Lynch, D.R., 1985. Mass Balance in Shallow Water Simulations, *Communications in Applied Numerical Methods*, 1: 153-159.

Lynch, D.R. and W.G. Gray, 1978. Analytical Solutions for Computer Flow Model Testing, *J. Hydraulics Division*, 104: 14105-14127.

Quintela, A.C., 1981. *Hidráulica*, Fundação Calouste Gulbenkian, Lisbon, Portugal.

Remédio, J.M.R., 1992. *RITA$_1$ - A Tool for Education and Exploratory Research on Shallow Waters*, M.S. Thesis, Oregon Graduate Institute of Science & Technology, Portland, Oregon.

Sternberg, R.W., 1972. Predicting Initial Motion and Bed Load Transport of Sediment Particles in the Shallow Marine Environment, in *Shelf-Sediment Transport*, D.P. Smith (editor), Dowden, Hutchinson, Ross, Stroudsburg, PA.

Turner, P.J., 1991. *ACE/gr User's Manual - Graphics for Exploratory Data Analysis*. OGI-CCALMR Software Documentation Series SDS3, 91-3, Oregon Graduate Institute of Science & Technology, Portland, Oregon.

Walters, R.A., 1992. A 3D, Finite Element model for Coastal and Estuarine Circulation, *Continental Shelf Research*, 12: 83-102.

Westerink, J.J., R.A. Luettich, C.A. Blain and N.W. Scheffner, 1992. *ADCIRC: An Advanced Three-Dimensional Circulation Model for Shelves, Coasts and Estuaries. Report 2: User's Manual for ADCIRC-2DDI*, Department of the Army, U.S. Army Corps of Engineers.

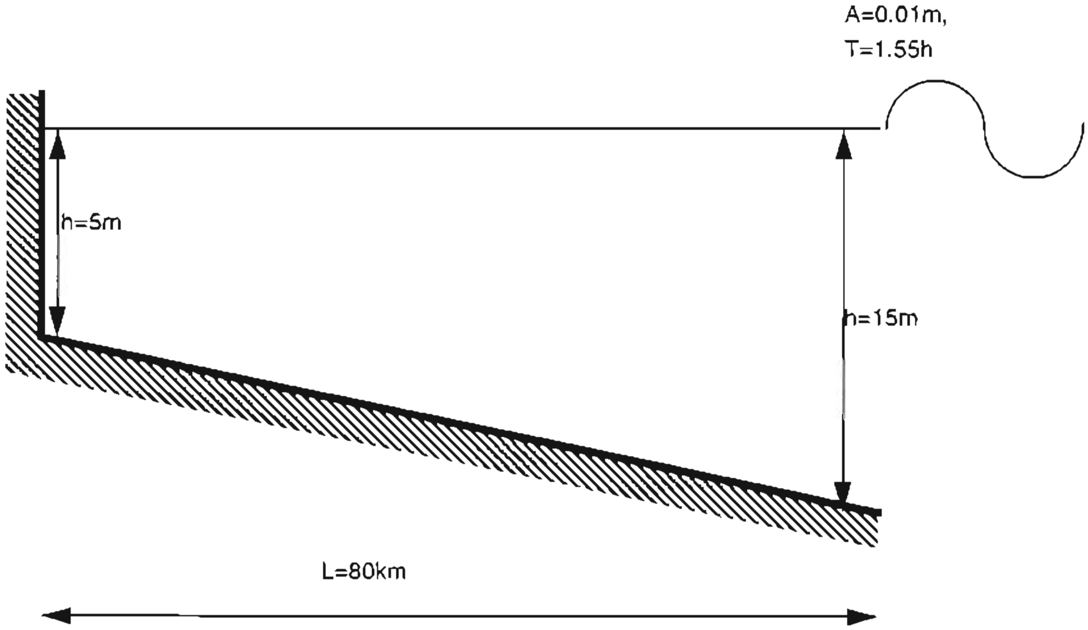

Figure A1.2 Geometry of the test case.

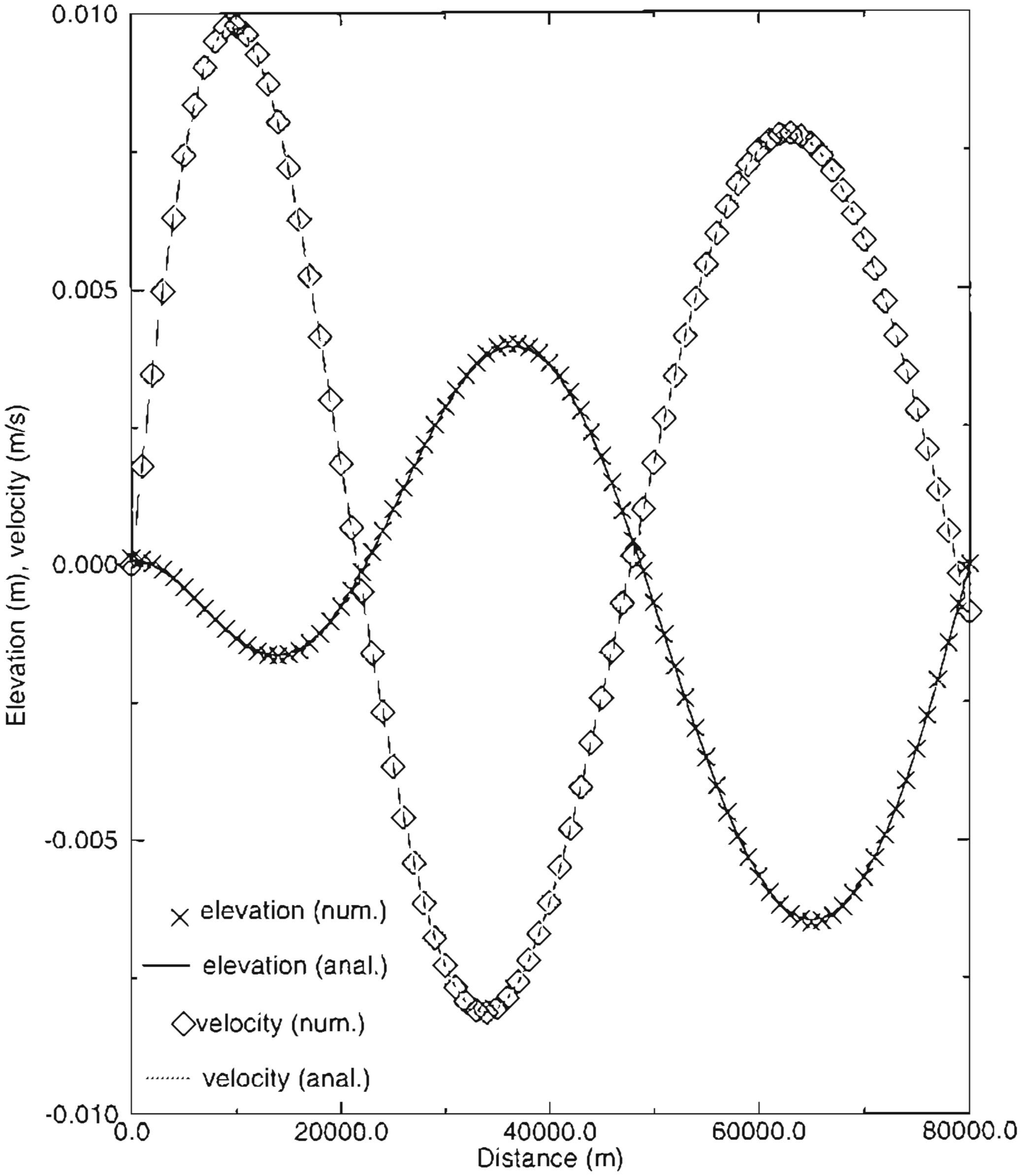

Figure A1.3 Elevations and depth-averaged velocities after eight tidal cycles.

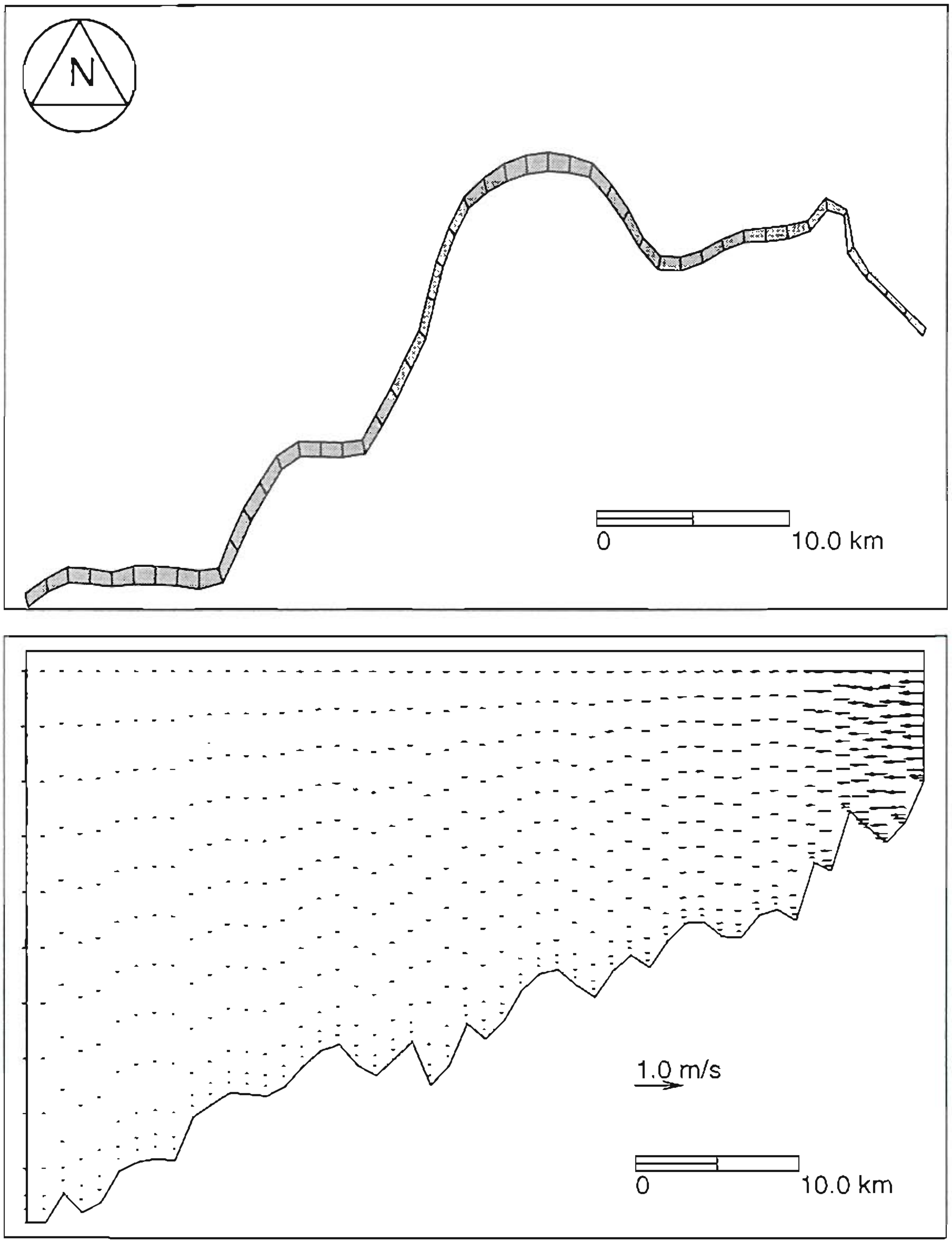

Figure A1.4 Little Goose reservoir. a) plan view; b) longitudinal section and velocities after one hour.

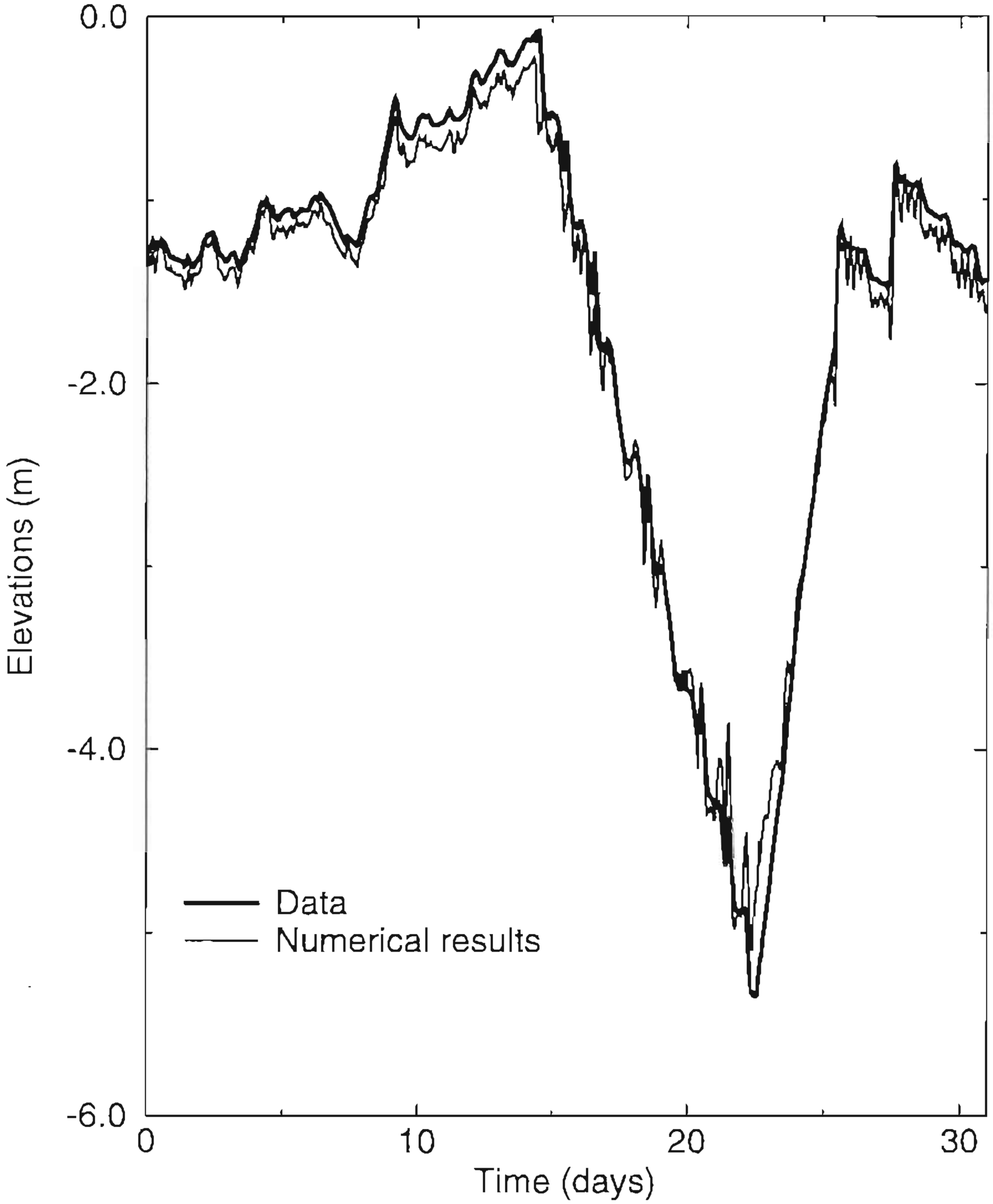

Figure A1.5 Comparison between model results and field data: elevations at Little Goose.

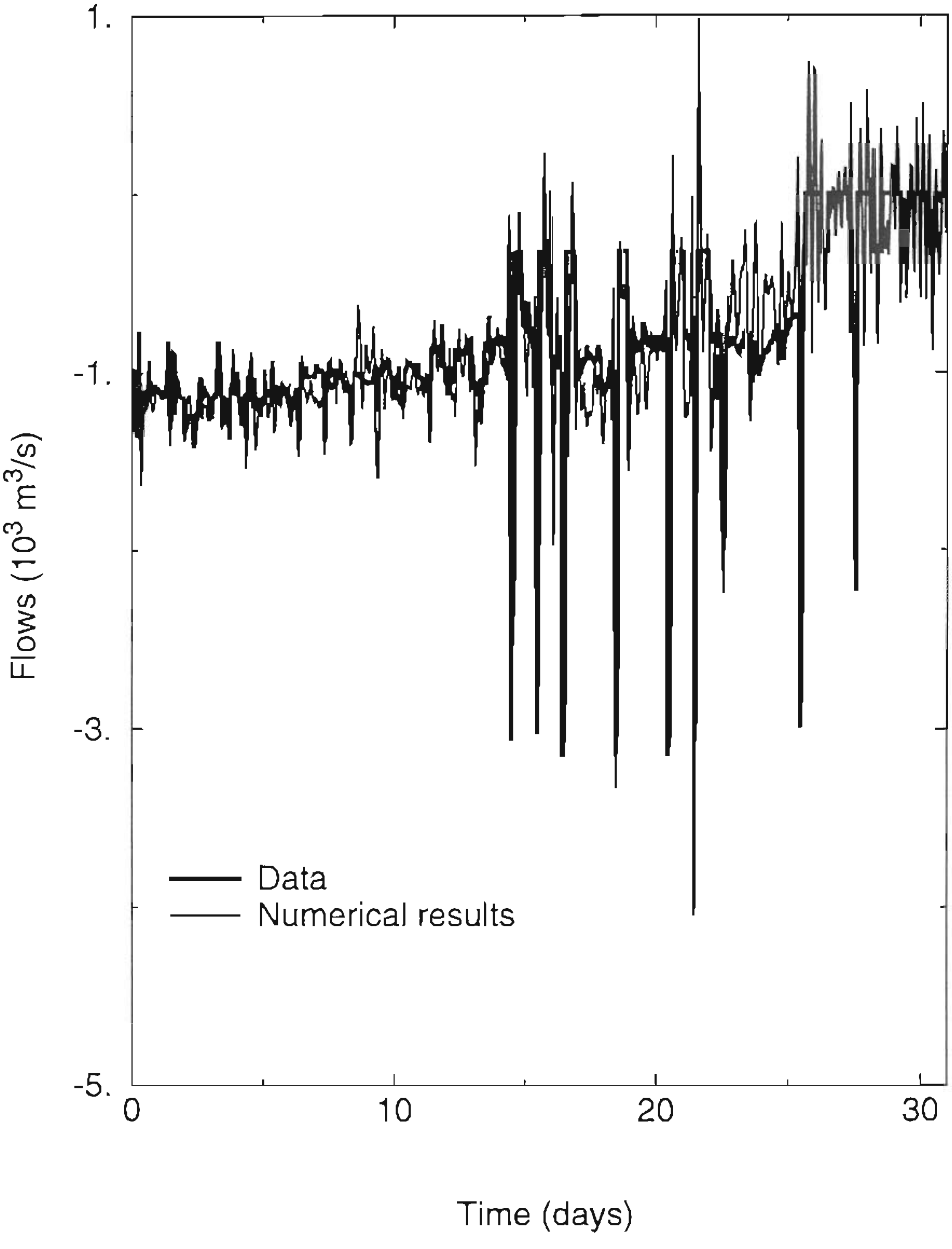

Figure A1.6 Comparison between model results and field data: flows at Lower Granite.

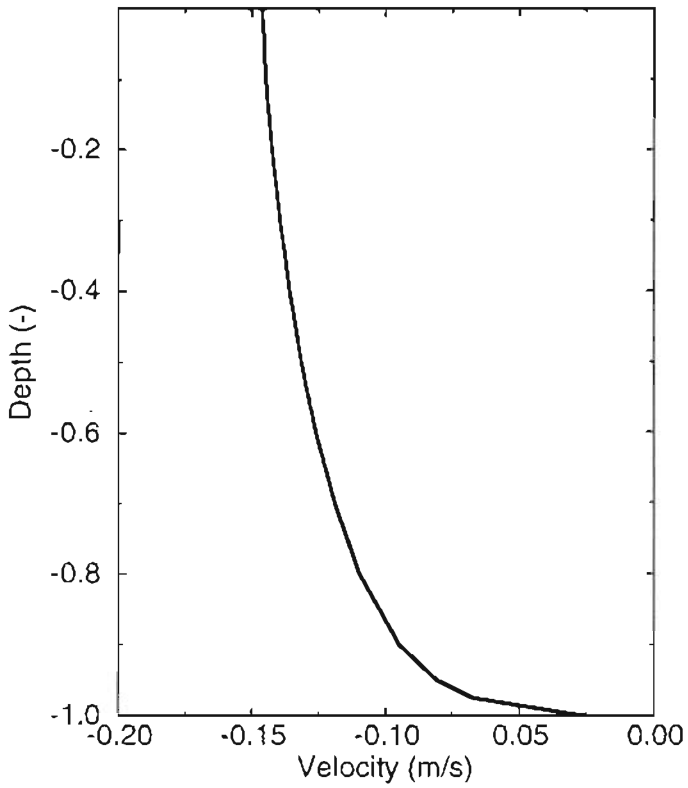

Figure A1.7 Vertical velocity profile at mid-channel (horizontal node 25), at 00:00 hours of the 2nd day.

APPENDIX 2

Brief User's Manual for ADCIRC 3D

A2.1 Disclaimer

This Appendix is intended only as a complement to other publications describing ADCIRC. The user is referred to Chapter 5 and references therein for the formulation, and to Westerink et al. (1992) for the format of most files. The model and file formats were developed by Drs. R.A. Luettich, Jr. and J.J. Westerink. The only modifications made by the author were the introduction of the localized sigma coordinates, the evaluation of advective terms in the internal mode and the solution of the 3D continuity equation. The description of the files presented below was taken from the header of the fortran code, with small modifications. This version of ADCIRC is based on version 26, release 7.

A2.2 Input Files

The version of ADCIRC described herein requires the specification of four files. In addition, the reading of several supplemental files can be triggered by certain values in the standard files.

The standard files are:

- the horizontal grid file (*fort.14*);
- the external mode parameter file (*fort.15*);
- the internal mode parameter file (*fort.17*); and,
- the vertical grid file (*fort.18*).

The first two, as well as the supplemental files, are described in Westerink et al. (1992). The others are described below.

A2.2.1 Internal Mode Parameters (fort.17)

The following input variables are required for *fort.17*. Free format is assumed.

- ***idiag***: diagnostic and warning messages types:

  0 - no (nonfatal) diagnostic output printed to units 2 or 16;

  1 - serious, nonfatal diagnostic output printed to unit 16;

  2 - serious, nonfatal diagnostic output printed to unit 16; routine diagnostic output printed to unit 2.
- ***islip, k***: slip code (o - no-slip, 1 - linear slip; 2 - quadratic slip) and slip coefficient;
- ***zos, zob***: free surface and bottom roughness;
- ***alp1, alp3***: internal mode time stepping coefficients (alp1 weights the Coriolis term, alp3 weights the vertical diffusion term);
- ***ievc, evcon***: eddy viscosity code and constant. See code header for definitions.
- ***i3dss, to3dsss, to3dfss, nspo3dss, nso3dss, nhn3dss***: station stresses output switch (0 - no output; 1 - ASCII output; 2 - binary output); number of days after which station stresses output begins; number of days after which station stresses output stops; number of time steps between outputs; number of points over the vertical to output station stresses; number of stations in the horizontal to output stresses; output to fort.41;
- ***ssout(i)***: i=1, nso3dss: sigma values of station stress output points (from -1 to 1);
- ***sshout(i)***: i=1, nhn3dss: horizontal node numbers to be used as stress output stations;
- ***i3dsv, to3dssv, to3dfsv, nspo3dsv, nso3dsv, nhn3dsv***: station velocity output switch (0 - no output; 1 - ASCII output; 2 - binary output); number of days after which station velocities output begins; number of days after which station velocities output stops; number of time steps between outputs; number of points over the vertical to output station velocities; number of stations in the horizontal to output velocities; output to fort.42;
- ***svout(i)***: i=1, nso3dsv: sigma values of station velocity output points (from -1 to 1);
- ***svhout(i)***: i=1, nhn3dsv: horizontal node numbers to be used as velocity output stations;

- ***i3dgs, to3dsgs, to3dfgs, nspo3dgs, nso3dgs***: global stresses output switch (0 - no output; 1 - ASCII output; 2 - binary output); number of days after which global stresses output begins; number of days after which global stresses output stops; number of time steps between outputs; number of points over the vertical to output global stresses; output to fort.43;
- ***gsout(i)***: i=1, nso3dgs: sigma values of global stress output points (from -1 to 1);
- ***i3dgv, to3dsgv, to3dfgv, nspo3dgv, nso3dgv***: global velocities output switch (0 - no output; 1 - ASCII output; 2 - binary output); number of days after which global velocities output begins; number of days after which global velocities output stops; number of time steps between outputs; number of points over the vertical to output global velocities; output to fort.44;
- ***gvout(i)***: i=1, nso3dgs: sigma values of global stress output points (from -1 to 1);
- ***i3dan, to3dsan, to3dfan, nspo3dan***: ancillary file (containing depth-averaged velocity, bottom stress and dispersion terms at all external mode nodes) switch (0 - no output; 1 - ASCII output; 2 - binary output); number of days after which ancillary file output begins; number of days after which ancillary file output stops; number of time steps between outputs; output to fort.45.

A2.2.2 Vertical Grid (fort.18)

- ***igc, lsc***: vertical distribution code (0 - read from fort.18; 1 - uniform grid generated; 2 - log grid generated; 3 - log-linear grid generated; 4 - double-log grid generated; 5 - β grid generated); localized sigma coordinates switch (0 - domain-wide sigma coordinates; 1 - localized sigma coordinates switch);
- ***nfen_g(i)***: i=1, number of horizontal nodes: number of nodes per vertical;
- ***sigma_g(i,j)***: i=1 (lsc=0) or i=1, number of horizontal nodes (lsc=1); j=1, nfen_g(i): nodal sigma coordinates, from the bottom (σ=-1) to the surface (σ=1).

A2.3 Output Files

The output files for the external mode are the same as those for ADCIRC-2DDI (Westerink et al., 1992). Internal mode output files are:

- station stresses (*fort.41*);
- station velocities (*fort.42*);
- global stresses (*fort.43*);
- global velocities (*fort.44*);
- ancillary output (*fort.45*).

The formats below are for binary files. Files in ASCII format are self-explanatory.

A2.3.1 Station Stresses (fort.41)

- run description, run identification, grid identification
- unit number (41);
- number of data sets;
- time interval between outputs;
- number of time steps between outputs;
- number of stations;
- number of vertical output points per station;
- for each vertical output point:
- vertical output grid (from -1 to 1);
- for each station:
- horizontal node number;
- for each output time step:
- time
- time step
- for each station:
- for each vertical output point:
- stress in X;
- stress in Y;

A2.3.2 Station Velocities (fort.42)

- run description, run identification, grid identification
- unit number (42);
- number of data sets;
- time interval between outputs;
- number of time steps between outputs;
- number of stations;
- number of vertical output points per station;
- for each vertical output point:

- vertical output grid (from -1 to 1);
- for each station:
- horizontal node number;
- for each output time step:
- time
- time step
- for each station:
- for each vertical output point:
- velocity in X;
- velocity in Y;

A2.3.3 Global Stresses (fort.43)

- run description, run identification, grid identification
- unit number (43);
- number of data sets;
- time interval between outputs;
- number of time steps between outputs;
- number of horizontal nodes;
- 0;
- for each horizontal node:
- number of output nodes per vertical;[1]
- for each horizontal node:
- for each vertical output point:
- sigma values of the output points;
- for each output time step:
- time;
- time step;
- for each horizontal node:

---

[1] even though this number is the same for all verticals in the current version, it may become variable in the future; the visualization software ACE/vis (Baptista and Turner, 1991) will allows this number to vary from one horizontal node to another.

- elevation;
- for each output point:
- stress in X;
- stress in Y;
- 0

A2.3.4 Global Velocities (fort.44)

- run description, run identification, grid identification
- unit number (44);
- number of data sets;
- time interval between outputs;
- number of time steps between outputs;
- number of horizontal nodes;
- 0;
- for each horizontal node:
- number of output nodes per vertical;[2]
- for each horizontal node:
- for each vertical output point:
- sigma values of the output points;
- for each output time step:
- time;
- time step;
- for each horizontal node:
- elevation;
- for each output point:
- velocity in X;
- velocity in Y;
- velocity in Z (velocity in sigma coordinates);

---

[2] see footnote 1.

A2.3.5 Ancillary Output (fort.45)

- run description, run identification, grid identification
- unit number (45);
- number of data sets;
- time interval between outputs;
- number of time steps between outputs;
- number of horizontal nodes;
- 0;
- for each output time step:
- time;
- time step;
- for each horizontal node:
- depth-averaged velocity in X;
- depth-averaged velocity in Y;
- bottom stress in X;
- bottom stress in Y;
- dispersion term in X;
- dispersion term in XY;
- dispersion term in Y;

References

Baptista, A.M. and P.J. Turner, 1991. *ACE/vis User's Manual. Software for Scientific Visualization of Estuarine and Coastal Processes*, OGI-CCALMR Software Documentation Series SDS1, 91-1, Oregon Graduate Institute of Science & Technology, Portland, Oregon.

Westerink, J.J., R.A. Luettich, Jr., A.A Blain and N.W. Sheffner, 1992. *ADCIRC: An Advanced Three-Dimensional Circulation Model for Shelves, Coasts and Estuaries. Report 2: User's Manual for ADCIRC-2DDI.* Department of the Army, US Army Corps of Engineers.

APPENDIX 3[1]

Modeling Near-Bottom Advective Acceleration in Surface Water Models

Abstract

This paper describes problems related to the evaluation of near-bottom horizontal velocity gradients in cartesian coordinates. An analytical model and simple scaling arguments show that computing advective accelerations in cartesian coordinates may require extremely fine horizontal grids. Numerical tests are used to confirm this conclusion and to exemplify the unrealistic velocity profiles that can be obtained due to large errors in the evaluation of the advective acceleration. It is therefore recommended that horizontal gradients of velocity be evaluated in sigma coordinates. This conclusion is in stark contrast with similar studies for the baroclinic pressure gradient, and is due to the rapid variation of the vertical gradient of horizontal velocities in the bottom boundary layer.

A3.1 Introduction

The use of sigma coordinates, wherein the height of the water column is mapped into a fixed interval, has become widespread in three-dimensional hydrodynamic models developed over the last decade (see review by Cheng and Smith 1990). The adoption of the sigma, or stretched, coordinates is explained by three important advantages relative to the older z-coordinates: (a) the resolution over depth is more uniform; (b) a smooth bot-

---

[1] published in *Proc. Int. Conf. on Computational Methods in Water Resources X*, A. Peters, et al. (editors), Kluwer Academic Publishers, 1045-1052.

tom topography can be represented; and (c) the treatment of the free surface boundary condition is straightforward.

However, there is currently some concern regarding the ability of the sigma coordinates to deal with steep topographic features. Haney 1991 showed that, in the presence of strong stratification and steep slopes, the use of sigma coordinates leads to very large errors in the evaluation of baroclinic pressure gradients. These errors are particularly troubling because they can generate moderate currents in a system that should otherwise be at rest (Walters and Foreman 1992).

To avoid this problem, several modelers have proposed computing horizontal gradients of density and/or and velocity directly in cartesian coordinates, by interpolating the values needed in planes of constant z (Sheng et al. 1990, Laible 1992, Beckmann and Haidvogel 1993). Indeed, truncation error analysis suggests that this approach may decrease the errors in the evaluation of horizontal gradients by several orders of magnitude (Fortunato and Baptista 1994). However, even though numerical experiments support this conclusion for the baroclinic pressure gradient, it will be shown in this paper that, under certain circumstances, it may be best to evaluate horizontal derivatives in sigma coordinates.

In this paper we examine the evaluation of horizontal gradients of velocities in hydrodynamic models that explicitly solve for the vertical structure of the flow. An analytical solution and scaling arguments suggest that this evaluation will be more accurate in sigma than in cartesian coordinates. Numerical results are then used to exemplify the type of errors obtained when advective accelerations are computed in cartesian coordinates. Several formulations for the treatment of near bottom velocity gradients are presented, then compared by examining velocity profiles for a wave passing over a step. The results for all formulations present a similar unrealistic behavior, in sharp contrast with those obtained from a standard sigma coordinate formulation, which are hardly distinguishable from a reference simulation.

A3.2 Analytical Solution

To isolate the errors that arise solely from evaluating horizontal gradients of velocity in cartesian coordinates, we consider a case with analytical solution. To derive the analytical solution, we write the linear momentum equation for an uniform flow in a channel:

$$\frac{\partial}{\partial\sigma}\left(A_v\frac{\partial u}{\partial\sigma}\right) = gH^2\theta \qquad \text{(A3.1)}$$

where g is the gravitational acceleration, H is the total water depth, θ is the bottom slope. Following Luettich and Westerink 1991, the vertical eddy viscosity A_v is assumed to vary linearly as $A_v=A_{v0}(\sigma+1+\sigma_0)$. A_{v0} is scaled as Hu_* ($u_*=\sqrt{\tau_b/\rho}$ is the friction velocity), or, for a uniform flow, $A_{v0}\sim H\sqrt{Hg|\theta|}$; $\sigma_0\equiv z_0/H$ is the dimensionless roughness height.

Integrating (A3.1) from a generic position σ, to the free surface (σ=0) where a no-stress boundary condition is used, we get:

$$\frac{\partial u}{\partial\sigma} = \frac{gH^2\theta}{A_{v0}}\frac{\sigma}{\sigma+1+\sigma_0} \qquad \text{(A3.2)}$$

Equation (A3.2) is integrated from the bottom (σ=-1) to a generic position to yield:

$$u(\sigma) = \frac{gH^2\theta}{A_{v0}}\left(\sigma+1+(1+\sigma_0)\,ln\left(\frac{\sigma_0}{1+\sigma_0+\sigma}\right)\right)+u_0 \qquad \text{(A3.3)}$$

where u_0 is the bottom velocity. It can be verified *a posteriori* that the sum of the horizontal and vertical advective accelerations is zero, so Equation (A3.3) is also the solution of the momentum equation including advective acceleration, coupled with the continuity equation.

The horizontal derivative can be computed as:

$$\frac{\partial u}{\partial x} = -\frac{gH\theta^2}{A_{v0}}\frac{\sigma}{\sigma + 1 + \sigma_0} \tag{A3.4}$$

Numerical approximations were computed using centered differences and Equation (A3.3), and compared against the exact solution, Equation (A3.4). The physical parameters and the velocity profile are shown in Figure A3.1.

The exact and numerical gradients of velocity are shown in Figure A3.2. Also shown in Figure A3.2 is the error in the advective term scaled by the gravitic forcing. This error was computed assuming a no-slip condition at the bottom (u_0=0), and would further increase if a more common slip condition was applied.

This figure shows that, unless the horizontal discretization is unreasonably fine (of the order of 10m), the horizontal gradient will be over-predicted by a very large amount. This error arises from the rapid variation of the second vertical derivative of the horizontal velocity near the bottom, which in turn is triggered by the variation of the eddy viscosity. If a constant eddy viscosity was selected in this simplified solution, the velocity gradient in Figure A3.2 would be linear and the numerical and analytical solutions would coincide. However, when a more realistic eddy viscosity is chosen, the second derivative of velocity decreases sharply away from the bottom, leading to large numerical errors.

Another way to look at this problem is to recognize that we have, at the bottom:

$$\left.\frac{\partial u}{\partial x}\right|_{z\,\equiv\,\text{constant}} = \left.\frac{\partial u}{\partial x}\right|_{\sigma\,\equiv\,\text{constant}} - \frac{\sigma\theta}{H}\frac{\partial u}{\partial \sigma} \gg \left.\frac{\partial u}{\partial x}\right|_{\sigma\,\equiv\,\text{constant}} \tag{A3.5}$$

In the analytical solution presented, this relation holds necessarily, since the derivative along a sigma plane is zero. In a more general case, it can be shown that this derivative is still zero at the bottom if the variations in the other horizontal direction can be neglected. In general, Equation (A3.5) is expected to hold if the bottom slope is not too small, and the bottom boundary layer is represented. When relation (A3.5) is valid, simple scaling arguments show that the discretization needed to represent the gradient on the LHS of Equation (A3.5) is much finer than that needed to represent the RHS: Equation (A3.5) can be scaled as:

$$\frac{U}{\Delta x} \gg \frac{U}{\Delta r} \Rightarrow \Delta r \gg \Delta x \tag{A3.6}$$

On the other hand, the term involving a vertical derivative in Equation (A3.5) is evaluated in the vertical grid, typically much finer than the horizontal, and therefore involves relatively small errors. Therefore, evaluating near-bottom horizontal gradients of velocity in sigma coordinates should be more accurate than in cartesian coordinates.

A3.3 Numerical Tests

A3.3.1 Alternative formulations

To evaluate horizontal gradients in cartesian coordinates while writing the equations in sigma coordinates, the necessary values at neighboring verticals are interpolated (e.g., see Fortunato and Baptista 1994). However, this is not possible near the bottom, and a special formulation is needed. Four alternatives are presented, along with the second order truncation errors E_2. The notation used is shown in Figure A3.3. The velocity at $(i+1,j)$ is assumed to be exact, even though there are errors introduced by the interpolation. These errors were studied elsewhere (Fortunato and Baptista 1994), and therefore are ignored here for simplicity. In the numerical tests, a very fine vertical grid is used near the bottom to minimize these errors.

In the first formulation (A), the velocity is interpolated along the bottom (Fortunato and Baptista 1994). The horizontal gradient is computed as:

$$\frac{\partial u}{\partial x} \approx \frac{u_{i+1,j} - (1-\alpha)\, u_{i,b} - \alpha u_{i-1,b}}{\Delta x\,(1+\alpha)} \tag{A3.7}$$

$$E_{2A} = \frac{\Delta x}{2}\frac{1-\alpha}{1+\alpha}\frac{\partial^2 u}{\partial x^2} + \alpha\theta\Delta x\frac{1-\alpha}{1+\alpha}\frac{\partial^2 u}{\partial x \partial z} - \frac{\alpha\theta^2\Delta x}{2}\frac{1-\alpha}{1+\alpha}\frac{\partial^2 u}{\partial z^2} \tag{A3.8}$$

where α is defined in Figure A3.3. The main disadvantage of this formulation is that the derivatives are not centered. In particular, it collapses into an upwind/downwind method at the bottom node.

The second formulation (*B*) is similar to that proposed by Beckmann and Haidvogel 1993. A fictitious value below the bottom is obtained by extrapolation of the vertical profile. The finite difference analog and the truncation error are:

$$\frac{\partial u}{\partial x} \approx \frac{u_{i+1,j} - \frac{\Delta z + \Delta x(1-\alpha)\theta}{\Delta z} u_{i-1,b} + \frac{\Delta x(1-\alpha)\theta}{\Delta z} u_{i-1,b-1}}{2\Delta x} \tag{A3.9}$$

$$E_{2B} = \frac{\theta\Delta x(1-\alpha)}{4}(\Delta z + \theta\Delta x(1-\alpha))\frac{\partial^2 u}{\partial z^2} \tag{A3.10}$$

Formulation *B* does not introduce horizontal numerical diffusion. However, because of the extrapolation, it is very sensitive to small errors in the nodal values when the near-bottom vertical nodal spacing is small.

Formulation *C* avoids both extrapolation and horizontal numerical diffusion:

$$\frac{\partial u}{\partial x} \approx \frac{u_{i+1,j} - u_{i-1,b}}{2\Delta x} - \frac{(1-\alpha)\theta}{4\Delta z}(u_{i,j+1} - u_{i,j-1}) \tag{A3.11}$$

$$E_{2C} = -\frac{\theta^2\Delta x(1-\alpha)^2}{4}\frac{\partial^2 u}{\partial z^2} + (\theta\Delta x(1-\alpha))\frac{\partial^2 u}{\partial x \partial z} \tag{A3.12}$$

Finally, formulation *D* is similar to formulation *C*, but further eliminates the vertical numerical diffusion. This may be very important when modeling bottom boundary layers where the vertical eddy viscosity is very small.

$$\frac{\partial u}{\partial x} \approx \frac{u_{i+1,j} - u_{i-1,b}}{2\Delta x} - \frac{(1-\alpha)\theta}{4\Delta z}(u_{i,j+1} - u_{i,j-1}) + \frac{\theta^2\Delta x(1-\alpha)^2}{4}\frac{u_{i,j+1} - 2u_{i,j} + u_{i,j+1}}{(\Delta z)^2} \tag{A3.13}$$

$$E_{2D} = (\theta \Delta x (1 - \alpha)) \frac{\partial^2 u}{\partial x \partial z} \qquad \text{(A3.14)}$$

A3.3.2 Numerical results

A 2D vertical hydrodynamic model, $RITA_{2v}$ (Fortunato and Baptista 1993) was used to compare the four alternative formulations. $RITA_{2v}$ (**RI**ver and **T**idal **A**nalysis 2D vertical) is a two dimensional, laterally averaged, baroclinic, hydrodynamic model. The external mode is solved with the Generalized Continuity Wave Equation on linear finite elements, and the internal mode can accommodate either the traditional sigma coordinate system or the more flexible localized sigma coordinates. A channel with a maximum slope of 2% (Figure A3.4) was forced with a S2 tide. The vertical eddy viscosity is parametrized as $\kappa u_*(z+z_0)$ in the lower 20% of the water column, and as constant in the upper layer (κ is the von Kármán constant (0.4), u_* the friction velocity, and z_0 a roughness height taken as 0.005m). A quadratic friction law is used, the friction coefficient being defined as $[ln((z_0+\Delta z_b)/z_0)/\kappa]^{-2}$. The domain was discretized with 61 evenly spaced nodes in the horizontal, and the time step was set to 5s. The vertical mesh is increasingly fine near the bottom in order to represent the bottom boundary layer:

$$\sigma_i = -\frac{(i-n)^p}{(1-n)} \qquad p = 0.5, \quad i = 1, \ldots, n, \quad n = 40 \qquad \text{(A3.15)}$$

The model was run for ten tidal cycles with only the external mode, then for one more tidal cycle in 2Dv mode. The final velocity profiles at x=9.5km are shown in Figure A3.5a. Profiles obtained with the traditional sigma coordinates for both the same grid, and a finer grid (301 horizontal nodes, 80 vertical) are also shown for comparison (Figure A3.5b). All four formulations in Figure A3.5a exhibit the same unrealistic behavior near the bottom, while the sigma coordinate results are hardly distinguishable from the reference results. Since the four approximations are very different, these results suggest that their common characteristic, the evaluation of horizontal gradients in cartesian coordinates, is responsible for the large errors. The test was repeated computing the horizontal gradients in sigma coordinates near the bottom (α<1), and in cartesian coordinates in the rest of the water column (formulation E). In this case, the same type of behavior is only weakly present (Figure A3.5b), supporting the idea that it is only near the bottom, where the vertical profile exhibits large vertical gradients, that evaluating horizontal derivatives in cartesian coordinates leads to large errors.

A3.4 Conclusions

This paper described problems related to the evaluation of near bottom horizontal gradients of velocity directly in cartesian coordinates. Both analytical and numerical results support the conclusion that this approach will lead to unrealistic results unless extremely fine horizontal grids are used. It is therefore recommended that the horizontal velocity gradients be computed in sigma coordinates.

This conclusion is in stark contrast with recent work on the evaluation of the baroclinic pressure term (Fortunato and Baptista 1994), for which the opposite recommendation was made. A tentative interpretation is that the gradients should be computed as much as possible in the direction along which they are smaller. This direction will clearly depend on the physical process and on the specific conditions of the problem. Typically, the direction of the near bottom flow is determined by the bathymetry, whereas the density field is basically influenced by gravity. Therefore, the gradients should be computed preferentially in sigma planes for velocity, and in horizontal planes for density. However, in some particular cases the density may exhibit a behavior similar to that discussed for velocity (e.g., density gradients determined by near bottom suspended sediments), and the flow may not follow the bottom (e.g., at the tip of a salt wedge).

References

Beckmann, A. and D.B. Haidvogel, 1993. Numerical Simulation of Flow Around a Tall Isolated Seamount. Part I: Problem Formulation and Model Accuracy, *J. Phys. Oceanography*, 23: 1736-1753.

Cheng, R.T. and P.E. Smith, 1990. A Survey of Three-Dimensional Numerical Estuarine Models, in *Estuarine and Coastal Modeling*, M.L. Spaulding (editor), Amer. Soc. Civ. Eng., 1-15.

Fortunato, A.B. and A.M. Baptista, 1993. *RITA$_{2v}$ User's Manual. 2D Vertical Hydrodynamic Model for River and Tidal Analysis. Part I - Flow Model*, OGI-CCALMR Software Documentation Series SDS7, 93-3, Oregon Graduate Institute of Science & Technology, Portland, Oregon.

Fortunato, A.B. and A.M. Baptista, 1994. Localized Sigma Coordinates for the Vertical Structure of Hydrodynamic Models, in *Estuarine and Coastal Modeling III*, M.L. Spaulding et al. (editors), Amer. Soc. Civ. Eng., 323-335.

Haney, R.L., 1991. On the Pressure Gradient Force over Steep topography in Sigma Coordinate Models, *J. Phys. Oceanography*, 21: 610-619.

Laible, J.P., 1992. On the Solution of the Three-Dimensional Shallow Waters Equations Using the Wave Equation Formulation, in *Proc. Computational Methods in Water Resources IX*, Vol. 2, T.F. Russel, et. al. (editors), 545-552.

Luettich, R.A. and J.J. Westerink, 1991. A Solution for the Vertical Variation of Stress, Rather than Velocity, in a Three-Dimensional Circulation Model, *Int. J. for Num. Met. in Fluids*, 12: 911-928.

Phillips, N.A., 1957. A Coordinate System Having Some Special Advantages for Numerical Forecasting, *J. Meteor.*, 14: 184-185.

Sheng, Y.P, H.-K. Lee and K.H. Wang, 1990. On Numerical Strategies of Estuarine and Coastal Modeling, in *Estuarine and Coastal Modeling*, M.L. Spaulding (editor), Amer. Soc. Civ. Eng., 291-301.

Walters, R.A. and M.G.G. Foreman, 1992. A 3D, Finite Element Model for Baroclinic Circulation on the Vancouver Island Continental Shelf, *J. of Marine Systems*, 3: 507-518.

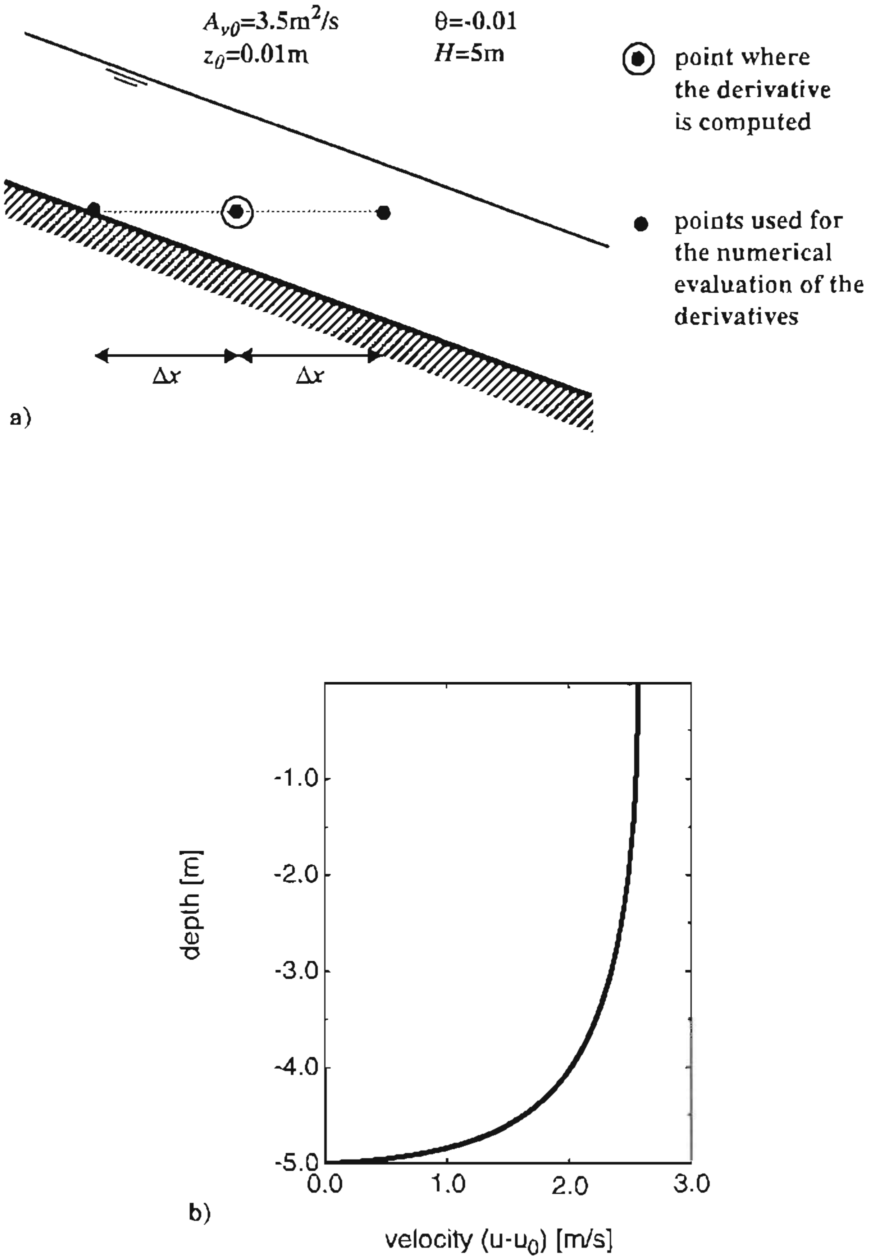

Figure A3.1 a) Parameters for the analytical solution; b) velocity profile.

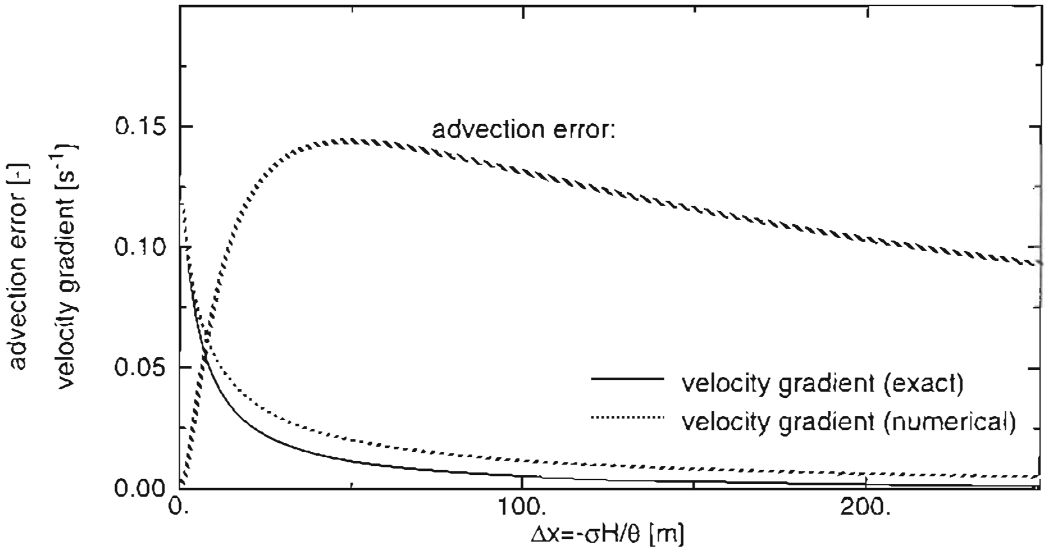

Figure A3.2 Error in the advective term scaled by the gravity forcing, and velocity gradients.

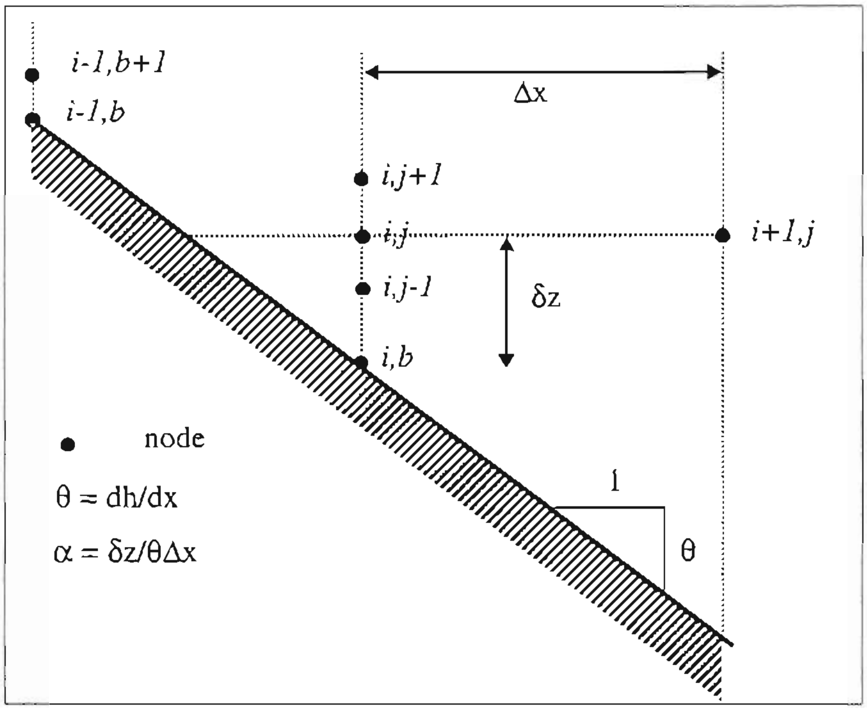

Figure A3.3 Notation

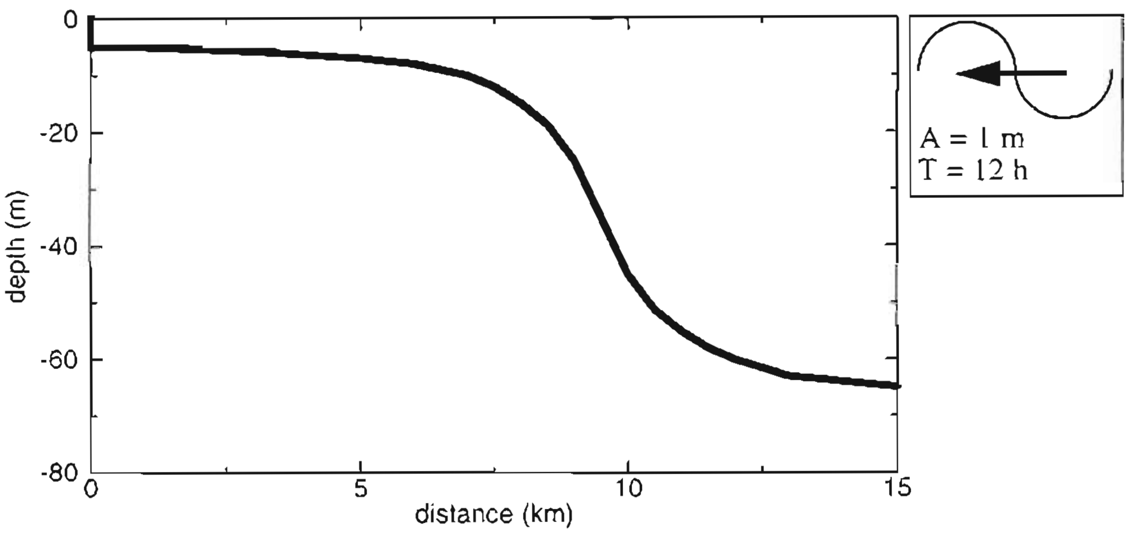

Figure A3.4 Bathymetry of the numerical test.

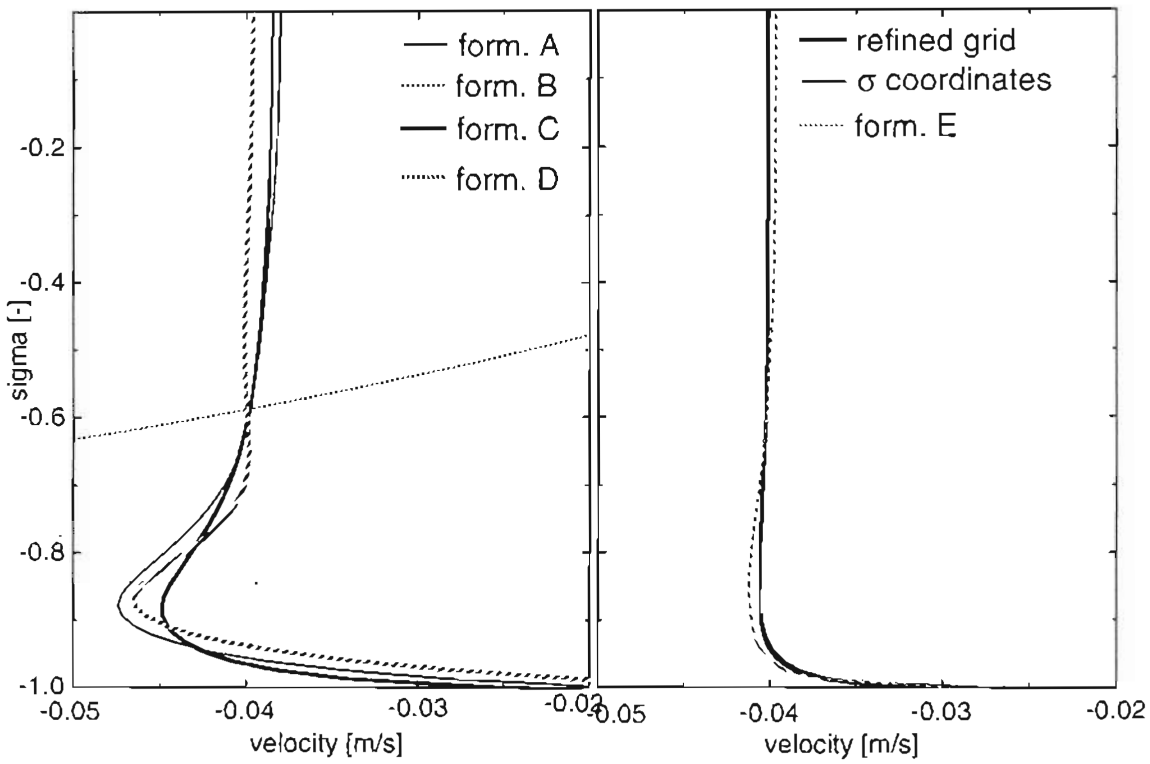

Figure A3.5 Horizontal velocity profiles at x=9.5km.

VITAE

The author was born in Lisbon (Portugal) on January 21st, 1966. He entered the Instituto Superior Técnico (Lisbon) in 1984, where he received his B.S. in Civil Engineering in 1989. He then worked for a year at the Estuaries Division of the Laboratório Nacional de Engenharia Civil, where he was introduced to estuarine and coastal dynamics.

The author came to the Oregon Graduate Institute of Science & Technology in September 1990, where he entered the Master's program in Environmental Science and Engineering. He switched to the Ph.D. program one year later and received his Ph.D. in January 1996.

Publications:

Costa, R.G., A.B. Fortunato and E.O. Oliveira, 1990. *Aeroporto Internacional de Macau. Estudos de Sedimentologia: Estudo do Regime de Marés*, Relatório 1.2, Laboratório Nacional de Engenharia Civil, Lisbon, Portugal.

Fortunato, A.F., E.O. Oliveira and R.G. Costa, 1990. *Aeroporto Internacional de Macau. Estudos de Sedimentologia: Inventário de Dados, Relatório 1.1*, Laboratório Nacional de Engenharia Civil, Lisbon, Portugal.

Fortunato, A.B. and A.M. Baptista, 1993. *RITA*$_{2v}$ *User's Manual. 2D Vertical Hydrodynamic Model for River and Tidal Analysis. Part I - Flow Model*, OGI-CCALMR Software Documentation Series SDS7, 93-3, Oregon Graduate Institute of Science & Technology, Portland, Oregon.

Fortunato, A.B. and A.M. Baptista, 1994a. Localized Sigma Coordinates for the Vertical Structure of Hydrodynamic Models, *Estuarine and Coastal Modeling III*, M.L. Spaulding, et al. (editors), Amer. Soc. Civ. Eng., 323-335.

Fortunato, A.B. and A.M. Baptista, 1994b. Modeling Near-Bottom Advective Accelerations in Surface Water Models, in *Proc. Int. Conf. on Computational Methods in Water Resources X*, in A. Peters, et al. (editors), Kluwer Academic Publishers, 1045-1052.

Fortunato, A.B. and A.M. Baptista, 1995a. Vertical Discretization in Tidal Flow Simulations, *Int J. Num. Methods in Fluids* (in press).

Fortunato, A.B. and A.M. Baptista, 1995b. Evaluation of Horizontal Gradients in Sigma-Coordinate Shallow Water Models, *Atmosphere-Ocean* (in review).

Oliveira, E.O., R.G. Costa and A.B. Fortunato, 1990. *Aeroporto Internacional de Macau. Estudos de Sedimentologia: Caracterização Hidrodinâmica da Zona Envolvente do Território de Macau. Campanha de Medição de Correntes: Especificações,* Nota Técnica 6, Laboratório Nacional de Engenharia Civil, Lisbon, Portugal.

Pearson, P., P.J. Turner, A.B. Fortunato and A.M. Baptista, 1994. *Hydrodynamic Modeling of the Snake and Columbia Rivers*, Technical Report, Center for Coastal and Land-Margin Research, Oregon Graduate Institute of Science & Technology, Portland, Oregon.